Stockholm University

Master Thesis

Degree Project in Geology 60 hp

A geochemical study of diamictite matrix in the Port Askaig Tillite Formation in western Argyll, Scotland

Martin Dahlgren

Stockholm 2020

Department of Geological Sciences
Stockholm University
SE-106 91 Stockholm
Sweden

A geochemical study of diamictite matrix in the Port Askaig Tillite Formation in western Argyll, Scotland

Abstract

This study focuses on the diamictite matrix in the Port Askaig Tillite Formation which crops out in the Garvellachs and on Islay and consists of 47 glaciogenic diamictite beds interlayered with non-glacial rocks. Measurements using handheld XRF and rock sampling for further lab-based fusion-ICP and petrographic analysis were done in 134 stations. Geochemical logs were created containing three correlated high-resolution datasets with a total of 100 ICP, 736 handheld XRF and 101 thin sections entries, altogether 24 thousand datapoints. The data was analysed using statistical and analytical methods i.a. including variables correlation, linear regression, multivariate (PCA) analysis, Fourier frequency analysis and Mann-Whitney and Kruskal-Wallis rank-tests. Stratigraphic trend-plots, bivariate / ternary diagrams and box-and-whisker plots were produced showing variation patterns within the PAF. The major-, trace- and rare earth elements were analysed and geochemical proxies representing weathering and other environmental changes as well as provenance were analysed resulting in i.a. the following detailed interpretations:

- The siliciclastic portion of the diamictite matrix has a granodioritic provenance originating from a continental volcanic arcs setting.
- The diamictites have a similar composition to the Svecofennian bedrock and Swedish till derived therefrom but have a different composition than the Rhinns complex, which is thus not a source for the PAF material.
- The limestone source for the diamictite matrix was abruptly switched-off directly after the Great Breccia.
- The analysis supports Spencer's (1971) original grouping of diamictite beds into members, but also open the possibility to further divide Member 1 into two sub-groups – M1a to cover the diamictite beds up to and including the Great Breccia and M1b starting from the Disrupted Beds up to and including the Upper Dolomites.
- Member 5 clearly deviates from the other members in its geochemical footprint, implying a shift of provenance or different transport and sorting processes for the M5 material, which raise the question if this member really represents a true glacial deposit.

Some general interpretations were also suggested:

- The source of the extrabasinal part of the PAF diamictites is the Svecofennian domain in the Baltica crustal plate located palaeogeographically to the southeast of the PAF.
- The PAF was deposited during 5 glacial cycles starting with gradual build-up of ice sheets followed by rapid meltdowns, and where the first cycle was unique in the sense of containing the multimillion years hiatus of the Snowball Earth event. The Great Breccia is interpreted as the final step in this first glacial build up. The exit from the Snowball Earth icehouse is interpreted to be through a series of possibly 5 major melting events of short durations, intermixed with somewhat longer periods when the ice managed to recover control.

Table of contents

Table of contents

List of Figures

List of Tables

1 Introduction and geological setting

1.1 Short description and aim of the study

This project focuses on the Port Askaig Tillite Formation (PAF) in western Argyll, Scotland. The PAF crops out in the Garvellachs and on Islay and consists of 47 glaciogenic diamictite beds interlayered with non-glacial rocks. The PAF provides an excellent archive of a Cryogenian glaciation (Spencer, 1971; Ali et al., 2018). This study concentrates on the matrix of the diamictite beds and selected sandstone beds, using field based XRF and conventional ICP and petrographic analysis. Compositional, petrological and geochemical variations in the diamictite matrix throughout the formation are used to interpret palaeoenvironmental factors such as weathering dynamics, sediment fluxes, early authigenesis and later post-depositional change and climate change.

The goals of this project are:

- To construct a geochemical log of the PAFs diamictites of Islay and the Garvellachs, using i) a portable XRF analyser capable of determining concentrations of heavier elements in the field, ii) conventional ICP analysis, and iii) petrographic analysis.
- To compare and interpret stratigraphic variations in matrix composition (e.g. carbonates versus igneous and meta-sediments) with variations in terms of changes in source area.
- To examine the evidence for a weathering control on silicate chemistry as expressed by the chemical index of alteration, and critically assess this index allowing for the effects of grain size on chemical composition.
- To seek evidence for local or widespread secondary changes in bulk chemistry (e.g. authigenic dolomite; selective carbonate dissolution; albitization), also utilizing others' data on clast composition.
- To interpret the depositional and paleoenvironmental history of the PAF by generalizing the findings and assess how it might relate to the Snowball Earth hypothesis.

1.2 The Cryogenian Period

1.2.1 The Cryogenian ice ages

The Neoproterozoic Era starts 1000 Ma and is succeeded 541 Ma by the Cambrian Period. The Neoproterozoic is divided into the Tonian (1000 – 720 Ma), the Cryogenian (720 – 635 Ma) and the Ediacaran (635 – 541 Ma) Periods (Cohen et al, 2019). The Cryogenian is characterized by dramatic climate shifts, with at least two major glaciations – the Sturtian and Marinoan – when Earth may have been completely covered by ice. These global glaciation events are today commonly called Snowball Earth. The Cryogenian succeeded an extended period of more than 1 Ga with a seemingly stable climate without robust evidence of glaciations.

Recent radiometric dating provide a rather well constrained start of the Sturtian glaciation at 717 Ma and an end with cap carbonates at ca 660 Ma (Rooney et al, 2015; Fairchild et al, 2018; Hoffman et al, 2017). The Sturtian was followed by a longer warm period of ca 10 – 20 Ma (Fairchild et al, 2016; Fairchild and Kennedy, 2007). The start of the subsequent Marinoan glaciation has not been ascertained, but its end 635 Ma is well documented. The Marinoan duration is estimated to be between 5 and 10 Ma (Fairchild et al, 2018; Rooney et al, 2015; Hoffman et al, 2017).

At the onset of the Cryogenian, continental crust had congregated into one supercontinent called Rodinia positioned around the equator. Rodinia was aggregated between 1300 and 900 Ma through plate-tectonic motion, most likely involving all continents existing at that time. Continental rifting started around 825 Ma, with the first major break-up of the supercontinent occurring along the western margin of Laurentia, possibly as early as 750 Ma (Li et al, 2008; Li et al, 2013).

The Cryogenian Period has left abundant evidence of a time with extreme shifts in climate impacting the entire planet. Deposits from glaciers reaching sea levels have been observed in multiple places on all palaeocontinents, several of which were judged to have been located at low latitudes at that time (Li et al, 2013). Thirty-nine locations with evidence of glaciations have been dated to the Sturtian glaciation and 48 to

the Marinoan (Hoffman et al, 2017). Evidence of the global Sturtian glaciation are i.a. found in South Australia, North-West Canada, Greenland, Namibia, Oman, Scotland and South China (Fairchild et al, 2016).

Banded iron formations which had been absent since the Great Oxygenation Event in the beginning of the Proterozoic Eon started to reappear during the Cryogenian. There is evidence of the ocean being anoxic and containing free Fe-ions during this time (Hoffman et al, 2017). $\delta^{13}C$ measurements show strong excursions in carbonate rock just below and above glacial deposits associated with the Cryogenian. Low $\delta^{13}C$ values are interpreted as being caused by drastic reduction in organic life in the oceans. Photosynthesizing cyanobacteria preferably use the lighter isotope and leave the heavier carbon in the water column which give a higher normal $\delta^{13}C$ value in a bio-producing ocean. Records of this are preserved in chemically precipitated carbonate rocks (Halverson et al, 2010). The carbon isotope data tells a story of a collapse in the photosynthesizing oceanic biota during millions of years, coupled to the global glaciation. Metazoans were first observed at the very end of the Cryogenian. Evolutionary bottlenecks linked to the recurring Cryogenian global ice ages can have impacted their evolution (Arnaud and Eyles, 2006; Hoffman et al, 1998).

1.2.2 The Snowball Earth hypothesis

J. L. Kirschvink proposed the term Snowball Earth in 1992, based on earlier ideas and modelling by W. B Harland and M. Budyko (Hoffman et al, 1998). The Snowball Earth hypothesis has been further developed and championed by P. F. Hoffman and many other scientists. Snowball Earth predicts major geological events at certain tipping points confined to relatively short geological time-periods. It is therefore in stark contrast to the Huttonian uniformitarianism with geological processes acting in the same manner and with essentially the same intensity over time, summarized by the statement "the present is the key to the past”.

At the core of the Snowball Earth hypothesis is an energy-balance model based on two main drivers for climatic change: albedo and CO_2 (Figure 1). The model includes a hysteresis between the loop of the cooling albedo and that of the warming CO_2. Once having passed a certain threshold, the albedo created by the global ice cover will assure that the whole planet will be ice covered for an extended time period. The ice cover will hinder drawdown of atmospheric CO_2 by chemical weathering and volcanic outgassing will therefore gradually increase the CO_2 concentrations in the atmosphere. When CO_2 greenhouse effects finally reaches sufficiently high levels to overcome the albedo, melting will suddenly start. From that point, the reduction in albedo will also work to hasten the climate shift from icehouse to hothouse conditions (Benn et al, 2015).

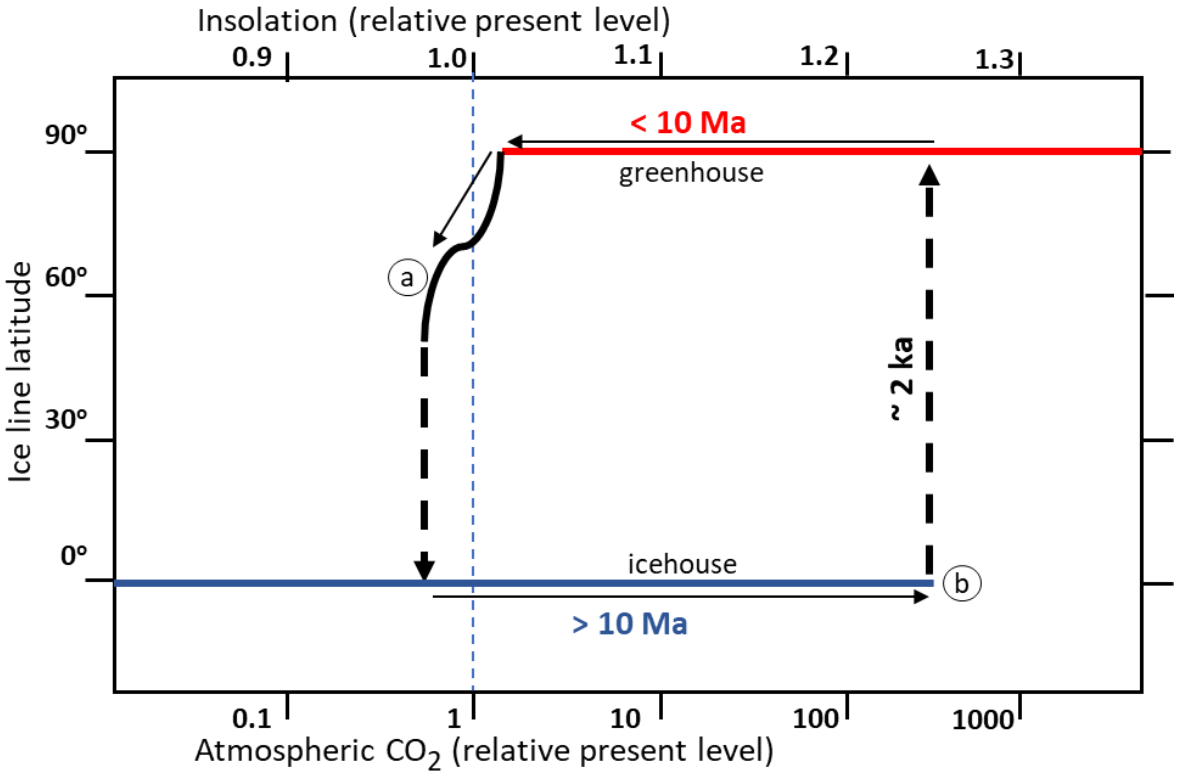

Figure 1. Simplified Snowball Earth energy balance model, redrawn after Hoffman et al (2017). The model indicates two tipping points where a) build-up of ice sheets with increasing albedo, and b) accumulation of CO_2 in atmosphere from volcanic outgassing, triggers sudden climate shifts from greenhouse to icehouse stages and back.

The Snowball Earth is thus created by a runaway albedo feedback leading to equatorial continental glaciers advancing to the sea and oceans being covered by ice. When the ice sheet pass a latitude of ca 30°, the albedo feedback will lead to the full globe being covered by ice. Equatorial seas covered by ice isolate the water column from atmospheric oxygen resulting in an anoxic and ferruginous ocean. The hydrological cycle will almost come to a stop and single cell life collapses with reduced organic production.

After millions of years with volcanic CO_2 accumulating in the atmosphere up to levels of several hundred times the present one, Earth turns suddenly into an extreme hothouse condition. When the atmospheric oxygen starts to mix into the water column, oxidation of Fe(II) builds iron formations. Aggressive chemical weathering raises alkalinity and atmospheric carbon transferred into the seas causes rapid precipitation of calcium carbonate, which builds the cap carbonate layer (Hoffman et al, 1998; Hoffman et al, 2017). The loss of biological production during the Snowball Earth explains the $\delta^{13}C$ excursion in these carbonates.

The initial trigger for driving the Earth into a Snowball Earth stage is not clear. Greenhouse CO_2 drawdown caused by extreme chemical weathering linked to the erosion of voluminous basalts in a low latitude Rodinia has been proposed as one mechanism for this (Rooney et al, 2015; Fairchild & Kennedy, 2007).

1.2.3 Predictions and contradictory observations

The Snowball Earth energy balance model predicts a synchronous and simultaneous start and end of the glacial period, and the length of one glaciation cycle shall be in the order of several million years (Hoffman et al, 1998; Hoffman & Schrag, 2002). These predictions can be tested.

The first prediction seems to hold true, where glacial deposits found on several different palaeocontinents have been age constrained to the same Sturtian period (Rooney et al, 2015). However, the second prediction of glacial cycle lengths of millions of years has been difficult to verify.

There are many examples in the Snowball Earth geological record of glacial and interglacial interlayered beds and subaerial and subaqueous deposits, which indicate the presence of dynamic ice sheets and cycles of

marine regressions and transgressions. This does not work well with an almost stopped hydrological cycle (Benn & Prave, 2006). Sequences of glacial- and interglacial deposits, with carbonate rocks followed by mudstones and tillites in repeated progression, indicate a waxing and waning ice sheet. The PAF contains ca 47 diamictite beds and Ali et al (2018) suggested the formation could have been deposited over a period of ca 10 Ma, which possibly indicates multiple and much shorter glacial-interglacial cycles. Different features such as polygonal sandstone wedges, frost-shattered clasts and gypsum pseudomorphs indicate periods with subaerial conditions. Dropstones, cross-beddings and stromatolites require open seas (Spencer, 1971; Ali et al, 2018). This implies varying depositional conditions which are not only being pro- or sub-glacial.

The original hypothesis may not provide the full answer (Klaebe et al, 2018) and the subject is intensely debated. Hoffman et al have in their 2017 paper summarized some of the above observations that contradict the original Snowball Earth hypothesis but have also tried to outline several explanations and modifications to the modelling of the Snowball Earth system which address these issues. The originally postulated shutdown of the hydrological cycle is now assumed to allow a net accumulation of ice at ca 20^{o} latitude and a net sublimation at the equator, leading to gravity induced ice flows. This would allow for the existence of ice-free terrestrial areas which i.a. could explain the subaerially formed polygonal sand-wedges observed in 13 diamictite layers within the PAF but not the occurrence of stromatolite horizons.

There exist alternative hypothesises, but none seems to provide a complete answer to all characteristics of this extreme period. Climate energy balance models have been developed that may allow water belts in low latitudes, despite the runaway effect of the albedo. Such models which allow for an active hydrological cycle would be a necessary ingredient in a Slushball Earth scenario, but they typically create unstable solutions which risk falling back into a full Snowball Earth icehouse (Hoffman et al, 2017). The Slushball Earth hypothesis has neither been able to provide falsifiable predictions (Fairchild & Kennedy, 2007).

Two other glacial hypothesises can be mentioned. The so-called Zipper-Rift Earth hypothesis posits glaciers on uplifted rift-shoulders at low latitudes (Eyles & Januszczak, 2004). The High-Tilt Earth hypothesis requires an assumed high obliquity of Earth's axis to generate glaciations at the palaeoequator. Both hypothesises have limited correlation with actual observations (Fairchild & Kennedy, 2007; Donnadieu and Ramstein, 2002).

All in all, the Snowball Earth hypothesis gives the most comprehensive explanations and applies a multidisciplinary Earth System Science perspective which integrates different processes into the model, even if several types of observations remain unexplained.

1.3 Geological setting

1.3.1 The Dalradian Supergroup

The Rhinns complex is a Palaeoproterozoic igneous bedrock of similar petrographic composition as rocks from coeval crystalline basements seen in parts of Sweden, Canada and Greenland. This could indicate a similar origin as the accretion of continental crust which took place during the Svecofennian orogeny (Webster et al, 2017). The Colonsay Group of metasedimentary rocks sits unconformably above the Rhinns complex and is overlain by the Dalradian Supergroup.

The Dalradian Supergroup was accumulated from the mid Neoproterozoic (ca 800 Ma) until beginning of the Palaeozoic (ca 540 Ma) and consists of the Grampian, Appin, Argyll and Southern Highland Groups. The PAF sits at the base of the Argyll Group just above the Lossit Formation at the top of the Appin Group. The part of the limestone formation conformably underlaying the PAF in the Garvellachs was denoted by Fairchild et al (2018) as the Garbh Eileach Formation. For the sake of simplicity this study will in stratigraphic plots refer to these underlaying limestone formations as the Lossit Formation only. Within the Argyll Group, the PAF is overlain by the Bonahaven Dolomite and the Jura Quartzite followed by other formations (Stephenson et al, 2013).

Both the Lossit / Garbh Eileach Formations below the PAF and the Bonahaven Dolomite Formation above were precipitated in warm tropical and shallow sea environments, as evidenced by the occurrence of stromatolites. This give evidence of dramatically shifting climates, going from hothouse to icehouse and then back to hothouse conditions. Negative $\delta^{13}C$ excursions have been reported in both the Bonahaven Dolomite Formation

and the limestone in the Lossit / Garbh Eileach Formations. At least a part of the anomaly in the Lossit Limestone can be explained by exchange of metamorphic fluids (Skelton et al, 2015) but the Garbh Eileach anomaly appears to be of primary origin (Fairchild et al, 2018) and is a strong indicator of a dramatic climate event.

The thickness of the Dalradian Supergroup has been estimated to 20 – 25 km and was accumulated over ca 250 Ma. To provide enough accommodation space a continuous and relatively fast subsidence was required, which possibly can be linked to the rifting during break up of Rodinia and subsequent opening of the Iapetus Ocean. The average deposition rate was thus in the range of 100 mm/ka, i.e. about 5 – 10 times higher than a typical deep-sea sedimentation rate (Jakobsson et al, 2003). Argyll Group constitutes ca 9 km of the thickness of the Dalradian Supergroup and the PAF and Jura Quartzite have thicknesses of ca 1.1 and 5 km respectively (Stephenson et al, 2013).

1.3.2 The Port Askaig Tillite Formation (PAF) stratigraphy

The PAF contains 47 diamictite beds (here called d1 to d47) interlayered with non-glacial mudstone, sandstone and dolomite beds. This 1,100 m thick formation shows an evolution from carbonate-dominated to silicate dominated clasts which were grouped into 5 members by Spencer (1971) and which can be widely correlated. The PAF is seen in 30 localities from NE Scotland to W Ireland but most prominently in the Garvellach islands and Islay. The diamictite beds have different clast lithologies, with the bottom parts primarily containing carbonate clasts from the underlaying Lossit / Garbh Eileach Formations (Ali et al, 2018; Eyles, 1988). Clasts in successively higher beds becomes more granitic silica-rich and are not plucked in situ (Ali et al, 2018; Eyles, 1988). The lower units of the PAF (below d13) are missing on Islay, which either indicates an unconformity or that the underlaying layers are not laterally continuous here. In the Garvellachs the lowest diamictite bed d1 has a conformable contact with the underlaying Garbh Eileach Formation (GEF).

Member 1 contains stacked beds of diamictite, mudstone, dolostone and sandstone, with a total thickness of ca 230 m in the Garvellachs. This member also includes four atypical layers (Spencer, 1971). The first, the Great Breccia diamictite bed (d13), contains large up to 200 m long matrix-supported clasts of dolostone (here called “rafts”) within a dolomitic matrix with varying thickness. In the Garvellach islands it is ca 40 to 50 m thick while becoming thinner to the southwest with ca 4 m on Islay (Eyles, 1988; Benn and Prave, 2006). The Great Breccia on Islay may however be a fluvial deposit which then would indicate that it may not be continuous with the Great Breccia in the Garvellachs. The rafts show signs of thrust faults and folds. Directly overlaying the Great Breccia is an up to 50 m thick bed of layered dolostone called the Main Dolomite (Ali, 2017). There are documented microbial stromatolitic structures in the Main Dolomite in the Garvellachs (Bealach an Tarabairt) which indicate warm and shallow open seas (Ali, 2017). Overlying this and separated from it by an up to 14 m thick conglomerate bed is another distinct sequence called the Disrupted Beds, containing detrital dolostone and dolostone concretions and iron-rich mudstones (Ali, 2017). The iron is mainly contained in magnetite and hematite and some siderite. The Disrupted Beds mudstone matrix has a characteristic dark blue colour and it shows soft sediment deformation features. (Arnaud and Eyles, 2002; Benn and Prave, 2006). The Disrupted Beds also contain occasional dropstones (Eyles, 1988). At the top of Member 1 is another layered dolomite bed with unconformable lower contact, possibly primary and with structures appearing to be stromatolites (Spencer, 1971; Ali, 2017). This bed is called the Upper Dolomite.

Member 1 also contains periglacial structures in several diamictite beds (Spencer, 1971; Ali et al, 2018). Spencer (1971, Table 11) listed 6 diamictite beds with numerous sandstone wedges both below and above the Great Breccia, while Ali (2017) noted sandstone wedges in two beds only in the upper part of this member. The top of the Garbh Eileach Formation which underlies d1 in the Garvellachs also contains possible periglacial structures such as sandstone wedges and frost shattered clasts (Ali, 2017).

Member 2 includes diamictite beds d19 – d32 with a total thickness of ca 160 m in the Garvellachs (Spencer, 1971). It contains stacked beds of diamictite and progressively thicker sandstone with some dolostone interbeds. At the top of this member a rhythmically laminated siltstone bed with occasional dropstones is located between thicker tidally influenced sandstone beds (Ali, 2017). This siltstone bed shows some soft sediment deformation features (Ali, 2017). The top of Member 2 contains a large unconformity, where the

overlaying beds cut down to d30 (Ali, 2017). Member 2 contains numerous periglacial features, including 10 beds with sandstone wedges and 4 beds with frost shattered clasts (Spencer, 1971; Ali, 2017).

Member 3 includes diamictite beds d33 – d38 with a total thickness of more than 210 m in the Garvellachs (Spencer, 1971). The diamictite beds are interleaved with thick tidal sandstone beds. The continuation after Member 3 can't be observed in the Garvellachs, and an unconformity can't be ruled out. Member 3 also contains periglacial features, including 3 beds with sandstone wedges and 2 beds with frost shattered clasts (Spencer, 1971; Ali, 2017).

Member 4 includes diamictite beds d39 – d44 with a total thickness of ca 230 m on Islay (Spencer, 1971). The thick diamictite beds are interleaved with thinner sandstone beds. Member 4 also contains periglacial features, including 5 beds with sandstone wedges but no beds with frost shattered clasts (Spencer, 1971; Ali, 2017).

Member 5 includes the remaining diamictite beds d45 – d47 and has a total thickness of ca 250 m on Islay (Spencer, 1971). The thin diamictite beds are interleaved with thick sandstone beds and some siltstone beds. Member 5 possibly contain 1 bed with sandstone wedges but no beds with frost shattered clast (Spencer, 1971; Ali, 2017). The diamictite beds include a few m thick conglomerate horizons with large lateral continuity, possibly of wave washed beach type (Spencer, 1971).

The diamictite layers normally have a distinct basal contact with conformable underlaying sandstone, dolostone or mudstone (Ali et al, 2018; Eyles, 1988). There is no clear evidence of erosion at these diamictite bases. There are many examples of tidal sandstones in between the diamictite beds (Ali et al, 2018). Together with the periglacial structures in the upper surfaces of the diamictites, this is interpreted as a succession of glacial-nonglacial deposits which occasionally were located in a subaerial environment (Spencer, 1971; Ali, 2017; Ali et al, 2018).

1.3.3 The PAF tectonics, age and palaeogeography

The tectonic setting for the PAF is characterized by the processes resulting in the initial opening of the Iapetus ocean. This included an unstable tectonic environment with rifting and forming of extensional basins, with listric type faulting. The tectonic setting for the build-up of the PAF was thus an extensional environment containing fault-bounded blocks and shallow basins created by the rifting (Stephenson et al, 2013; Arnaud & Eyles, 2002).

This continental basin was subject to a relatively fast subsidence which kept pace with sedimentation filling it up (Fairchild et al, 2018). However, during the extreme climatic variation of the Sturtian glaciation, this area must have experienced several sea-level changes caused by isostatic adjustment and waves of meltwater (Ali et al, 2018). Ali et al (2018) estimated an overall sedimentation rate of ca 100 – 125 m/Ma, which if valid during the deposition of the PAF would imply that it was formed within a limited period of ca 10 Ma.

During the Caledonian orogeny ca 460 – 480 Ma the rocks in the PAF were metamorphosed at greenschist facies conditions. On Islay this reached a maximum pressure of ca 1 GPa and temperature between 410 – 470 ^{o}C (Skelton et al, 1995). The Caledonian orogeny also tilted the PAF beds and folded some of the formation on Islay.

The PAF has been linked to the Sturtian glaciation ca 717 – 660 Ma, possibly at its start according to Arnaud & Eyles, (2002). Also, Benn and Prave (2006) conclude with this time. However, this date can be questioned since it would imply a quite extended period of extensional rifting before the Iapetus Ocean opened (Arnaud and Eyles, 2006). Prave et al (2009) placed the PAF within the time of the Sturtian glaciation based on $\delta^{13}C$ measurements of the Lossit / Garbh Eileach and the Bonahaven Formations correlated with other global carbonate data. These carbon anomalies bridging the PAF may be inconclusive, but subsequent strontium isotope signatures imply the same age (Sawaki et al, 2010).

The Argyll area was located at the rift zone between Baltica and Laurentia at southern subtropical latitudes during the Cryogenian Period. The estimate of the latitude at the start of the Sturtian varies between ca 30^{o} S (Benn and Prave, 2006) to ca 20^{o} S (Hoffman et al, 2012). According to a global reconstruction of

paleocontinents made by Li et al (2008) and Li et al (2013), it was located at semitropical latitudes ca 25° S at 720 Ma and somewhat further south at ca 30° S at 680 Ma. At the end of the Marinoan 635 Ma it had moved to ca 45° S. None of these reconstructions are however certain and the paleolatitude of Argyll is therefore not well constrained (Arnaud & Eyles, 2006; Fairchild & Kennedy, 2007).

Most of the surface of Islay and the Garvellachs was reworked during the Quaternary glaciations (Webster et al, 2017.) During this period, the raised beaches were formed on Garbh Eileach in the Garvellachs which is the reason why the full sequence of Members 1 – 3 are exposed in such detail there.

1.3.4 Glaciogenic sedimentary regimes

There are three mechanisms for transport and deposition of glaciogenic material (Earle, 2015):

i. Sub- or proglacial transport producing till, often with glaciotectonic structures.
ii. Glaciofluvial transport, producing better sorted material such as sand and gravel.
iii. Glaciomarine transport, producing ice rafted debris, suspension rainouts and dropstones in marine (and lacustrine) environments.

Glacial ice is an effective transporter of till when it is warm based, but less so if cold based (Ruddiman, 2014). If the PAF diamictite beds were deposited during (instead of before or after) the Snowball Earth, it thus presuppose a climate allowing for basal melting of the glacial ice.

The sedimentation rate is typically high at the ice-margin. Within ice covered sea areas sediments primarily derive from the basal melting of the sea ice (Jakobsson et al, 2014) and from iceberg transport during periods of open seas. An increase in the relative content of coarse fractions (>63 µm) is an indicator of increased contribution of ice rafted material from icebergs as compared to sea ice rafted debris (Sellén et al, 2008). The sedimentation rate under the ice margin is higher than for ice-free areas, and the rates are lowest under permanent ice (O'Regan et al, 2008).

The Antarctica Western Ross Sea region shows similar sediment structure as in the PAF. Drilling has revealed more than 1000 m thick layer of glacial-interglacial sediments representing a time of 34 Ma. The drill cores reveal sequences of facies from pelagic open water deposited mudstone, to current or wave transported sandstone, to sub- or proglacial diamictite (Dunbar et al, 2008; Wilson et al, 2012). Although the diamictite beds can be produced by different glaciomarine processes such as meltwater outwash, melt-outs and proglacial debris-flows, these have been interpreted as basal till produced by grounded ice (Wilson et al, 2012). Typical of this cycle from grounded ice to glaciomarine to open sea are disconformities associated with the diamictite beds, with erosion surfaces caused by the advancing grounded ice, truncating underlaying layers. There are at least 49 separate diamictite beds observed in the Western Ross Sea and a similar number of erosional surfaces (Dunbar et al, 2008; Wilson et al, 2012). Similar observations come from drill cores in the East Antarctica Victoria Land basin where 46 erosional unconformities were noted within the glaciomarine cycles of ice-margin advance and retreat (Naish et al, 2001). Diamictite beds combined with erosional surfaces thus seem to be a hallmark of a glacial cycle with pro- and subglacial till deposited by grounded ice.

An age model for the Western Ross Sea implies an overall relatively rapid sedimentation rate of 200 – 500 m/Ma, including the diamictite beds and as adjusted for erosional surfaces (Wilson et al, 2012). This is a factor 2 – 4 times faster than the estimates made by Ali et al (2018) for the PAF.

1.3.5 Palaeoenvironment

There has been disagreement concerning the interpretation of the palaeoenvironmental conditions under which the PAFs beds were deposited. Interpretations cover a span from i) subglacial or proglacial till deposited by grounded ice, ii) glaciomarine deposits at the ice margin, to iii) a marine slope mass flow without involvement of glacial processes (Fairchild & Kennedy, 2007).

Comparison with Quaternary examples give one interpretation of the Great Breccia as a proglacial deformation of a deep permafrozen till deposition caused by advancing grounded ice. Glaciotectonic structures including

large folds and faults closely resemble the proglacial components of sediments from grounded ice (Benn & Prave, 2006). Subsequent studies however indicate that the Great Breccia instead may have a subglacial origin. The Disrupted Beds are today interpreted as subglacial deformations with features characteristic for glaciotectonite which has been deformed but kept some of its original structure including rigid boudins and inclusions of exotic clasts indicative of ice rafting (Benn & Prave, 2006).

As an alternative, it has been proposed that the Great Breccia was formed by subaqueous debris flows caused by catastrophic failure of a carbonate platform, collapsing because of earthquakes (Arnaud & Eyles, 2002). The Great Breccia resembles other megabreccias formed in deep water marine settings as result of collapsing carbonate platforms. According to this hypothesis, there is no reason to believe that glacial processes were involved in the formation of these layers (Arnaud & Eyles, 2002).

Benn et al (2015) and Fairchild et al (2016) have found indications in Svalbard of possible Milankovitch orbital forcing in a late stage of a Snowball Earth glaciation. Milankovitch orbital forcing of glaciations is far from straightforward and requires help from coupled non-linear mechanisms such as changes in atmospheric and ocean circulation which require some understanding of palaeogeography. Since the PAF was deposited in a subtropical palaeogeography, the type of Milankovitch cycle to have an impact is the precession. Obliquity (tilt) plays a limited role at low latitudes (Hoffman et al, 2017; Ruddiman, 2014). It is noted that precession at Cryogenian had a period of ca 15 – 19 kyr (Ruddiman, 2014) as compared with the current periodicity of ca 23 kyr.

A better understanding of the depositional mechanisms for the PAFs diamictite horizons and their palaeoenvironments will lead to more accurate interpretations of climatic changes and the extent of global ice-cover during the Sturtian glaciation and could ultimately have a bearing on the validity of the Snowball Earth hypothesis. Certain questions remain unanswered including i) the number and length of the glacial-interglacial cycles (in the order of Ma according to the classical Snowball Earth hypothesis, or below 100 ka if controlled by orbital solar processes), ii) the depositional environment with deposition versus basin subsidence rates, and iii) the interplay between marine transgression and regression.

Based on the literature review presented in this Introduction and Geological Setting section and interpretation of results from the analysis of the samples from the PAF, these questions will be further addressed in section 4.4 of this report.

1.4 Review of proxies for climatic and environmental change

1.4.1 Chemical and physical weathering proxies

Several types of indexes have been proposed as proxies for chemical weathering, including CIA, PIA, WIP, CIW and STI (Price et al, 2003; Meunier et al, 2013). CIA (the Chemical Index of Alteration; Nesbitt & Young (1982)) is the most frequently used proxy for chemical weathering. Feldspar, a common mineral in the continental crust, is susceptible to chemical weathering resulting in clay minerals. Ca, Na and K are normally removed in this process, increasing the ratio between Al and these alkalis. Therefore, the ratio between Al-oxide (which remains after weathering) and the sum of Al- and above oxides contained in the sample will give an indication about the level of chemical weathering (Halverson et al, 2010). The CIA value remains relatively stable during low grade metamorphism (Nesbitt and Young, 1982). The molar ratio of Al-oxide versus the Al- plus Ca-, Na- and K-oxides is calculated as a percentage ($CIA=100x[Al_2O_3/(Al_2O_3 + CaO^* + Na_2O + K_2O)]$). Possible inclusions of Ca from carbonates in the sample will distort the result, which is why CaO^* refers to siliciclastic-bearing minerals only. McLennan (1993) proposed a method for estimating the CaO^*, setting it equal to the number of moles of Na_2O (provided the original CaO content reduced by Ca contained in apatite (based on 10/4 of P_2O_5 moles) is still larger than the number of Na_2O moles). Since feldspathic Ca typically is released earlier than Na, this can lead to an underestimation of the CIA-value. CIA is sensitive to post-depositional metasomatic alterations and results can also be impacted by sorting during transport and grain size of the deposited material.

PIA (Plagioclase Index of Alteration; Fedo et al (1995)) has the same uncertainties in the CaO* silicate fraction but eliminates possible metasomatic potassium by basing it on plagioclase weathering. It uses the formula PIA=100x[(Al_2O_3–K2O)/(Al2O3 + CaO* + Na_2O–K_2O)].

WIP (Weathering Index of Parker; Parker (1970)) is based on the individual mobilities of sodium, potassium, magnesium and calcium and is calculated as WIP=100x[(2Na_2O/0.35) + (MgO/0.9) + (2K_2O/0.25) + (CaO*/0.7)]. A higher WIP value indicates less weathering. WIP has the same uncertainties as CIA.

CIW (Chemical Index of Weathering; Harnois (1988)) is identical to CIA except for the exclusion of K_2O thus avoiding the problem of metasomatic potassium. Its formula is therefore written CIW= 100x[Al_2O_3/(Al_2O_3 + CaO* + Na_2O)].

STI (Silica – Titania Index; de Jayawardena and Izawa (1994)) was developed for strong weathering of metamorphic silicate rocks, with formula STI=100x[(SiO_2/TiO_2)/((SiO_2/TiO_2) + (SiO_2/Al_2O_3) + (Al_2O_3/TiO_2))]. A higher STI value indicates less weathering.

Repositories and time lags need to be considered where reworking during transport and shifting efficiency in transport modes from inland sources to continental margins may have a larger influence on the depositional composition, rather than climate driven change in the source of the proxy. Resolution of climate proxies is typically better than 10^5 years (Clift et al, 2014). This may be too long when studying climate variations on an orbital scale (10^4) but should suffice for geological processes such as tectonic forcing (>10^6) (Clift et al, 2014).

Weathering is intimately related with climate. Not only high temperatures but also humid conditions increase chemical weathering while an arid climate reduces it. Cold/warm versus humid/arid conditions can be evaluated with help of proxies for respectively “kaolinitic” and “illitic” environments, where Ga and Al are enriched in well-weathered aluminosilicate fractions such as kaolinite, while K and Rb are associated with the less weathered illite (Roy & Roser, 2013; Xie et al, 2018). Kaolinite typically require both warm and humid conditions to reach maturity, while illite is the diagenetic result of weathering in colder and more arid environments.

Chemical weathering typically produces clay minerals while physical weathering generates silt- and clay sized particles which thus have different geochemical compositions. Rock flour consists of fine clay-sized particles produced by glacial abrasion. Rock flour can travel long distances, either in suspension carried by water or by wind, then forming loess deposits. Ti and Zr are typically enriched in fine silt, while Al and Ga are linked to clay minerals (personal communication, Ian Fairchild, 2019). This means that these elements possibly could be used to discriminate between physical and chemical weathering. However, although chemical and physical weathering per definition are separated from each other, they do not represent opposing processes and may in practice show a correlation.

The ratio Al/Si is sometime used to assess proportions of clay versus sand. Grain size represented by increasing content of coarser fractions (>63 µm) can also be used as an indicator for increase in fluvial mass transports, but which does not necessarily need to be connected to a warmer climate.

1.4.2 Other proxies and methods

High-Field-Strength (HFS) elements and Rare Earth Elements (REE) are partitioned in melts during crystallization. However, during weathering and erosion of igneous rocks they are relatively immobile and not soluble and are typically transported in terrigenous components before sedimentation. They can therefore reflect the composition of their original source. La and Th are more common in felsic rocks while Sc and Co are more abundant in mafic ones. This is used to discriminate for their tectonic provenance (Bhatia & Crook, 1986; Lopez et al, 2005; Xie et al 2018).

Fe and Mn can serve as proxies for a redox environment. Reducing water conditions are required to maintain Fe(II) and Mn-ions in dissolved form, which require them to be isolated from atmospheric O_2, e g by thick ice covers or by a stratified ocean. Anoxic conditions existed during the Snowball Earth glaciations. Mn-ions

require a higher ρO_2 than Fe(II) to oxidize and precipitate (Graf et al, 1994), which makes the trend of $MnO/Fe2O_3$(T) an indicator of redox conditions.

Certain processes in the Earth System have periodicity, such as e.g. solar orbital forcing of climate, and which therefore can leave signals in a geochemical log. Time-series analysis is used to identify and quantify such periodic features in datasets. Here Fourier analysis is a powerful tool that is easily adapted to use in R-programming for statistical computing (Crockett, 2019). A complicated wave form can be represented by a linear combination of sinusoids of different periods – the Fourier series. The time and intervals of a fluctuating trend-line can thus be uniquely transformed to frequencies and phases, which are easier to work with when it comes to periodic patterns. The Fourier transform generates amplitude spectrums for the frequencies which helps identify possible underlying periodicity in the data. The transform also generates a power spectrum which represents the relative proportion of the time-series variance explained by each frequency.

2 Methodology

2.1 The methodological strategy

The main objective has been to build a comprehensive dataset showing lithological and geochemical variations in the PAF. Focus has been to cover the matrix of the diamictite beds, but also to correlate the data with variations in clast lithologies measured by others.

The dataset is of composite type with correlated inputs from two overlapping localities – the Garvellachs covering diamictite beds d1 to d38 and Islay covering d13 to d47 – and three complementary source types – field XRF geochemical data, ICP lab-analysed geochemical data and thin section microscopy with point-counted lithologies. Correlation of this data with clast lithologies measured by others was assured by utilizing synchronized site locations.

The data-logs primarily show the trend over the total sequence of the PAF, but in addition measurements were also made of intrabed variations over some individual beds.

Additional data were acquired from selected sandstone beds and from certain siltstone and dolostone beds at and just below the Disrupted Beds.

This methodology has resulted in a high-resolution composite geochemical and lithological log of the diamictite matrixes from the PAFs stratigraphic column, consisting of 5 100 data points generated by Inductively Coupled Plasma (ICP) analysis, 17 664 data points generated by X-Ray Fluorescence (XRF) spectrometer analysis and 808 thin section point-count data points (Table 1). The methods used for handling these data are described in section 2.4 below.

ICP measurements			
Member	**Garvellachs**	**Islay**	**Total**
5		8	8
4		17	17
3	15	7	22
2	17	6	23
1	23	7	30
sum	**55**	**45**	**100**
51 registrations per ICP measurement = 5 100 data points			

XRF measurements			
Member	**Garvellachs**	**Islay**	**Total**
5		69	69
4		102	102
3	132	52	184
2	137	45	182
1	163	36	199
sum	**432**	**304**	**736**
24 registrations per XRF measurement = 17 664 data points			

Thin sections			
	Garvellachs	**Islay**	**Total**
Thin sections	57	44	101
8 registrations per TS point count = 808 data points			

Table 1. Measurements by location and PAF member. This study is based on three datasets from 100 ICP analysis, 736 portable XRF measurements and point-counts from 101 thin sections – altogether about 24 thousand data points.

2.2 Description of field measurements

2.2.1 Sampling localities in the Garvellachs and Islay

The fieldwork was done in the Garvellachs islands in June 2019 and Islay in October 2019. Measurements and acquisition of rock samples were done from a total of 134 field stations of which 85 in Garvellachs and 49 in Islay. A list of field stations with GPS coordinates and stratigraphic position is given in Table 2 for the Garvellachs and Table 3 for Islay. The station locations are shown on an Ordnance Survey map for the Garvellachs (Figure 2) and two geological maps for Islay (Figures 3 and 4). The GPS accuracy was estimated to be 5 m by comparing with GPS measurements done by others for stone measurement locations, which also correspond to the instrument reported accuracy of 3 – 4 m.

station	date	location	diamictite horizon	stratigraphic level	sample no	XRF no	stone measurement no	GPS N	GPS W
1	2019-06-05	Garbh Eileach, E coast	d1		19-G-25	3-9	1	56°14.941'	005°45.075'
2	2019-06-05	Garbh Eileach, E coast	d1	2 mts above base	XRF only	10		56°14.944'	005°45.076'
3	2019-06-05	Garbh Eileach, E coast	d1	1 mt below top	XRF only	11		56°14.932'	005°45.073'
4	2019-06-05	Garbh Eileach, E coast	d1		19-G-26	12-16	13	56°14.937'	005°45.072'
5	2019-06-05	Garbh Eileach, E coast	d1		19-G-27	17-22	55	56°14.941'	005°45.074'
6	2019-06-05	Garbh Eileach, E coast	d2		19-G-28	23-27	23	56°14.933'	005°45.051'
7	2019-06-05	Garbh Eileach, E coast	d3		19-G-29	28-32	56	56°14.918'	005°45.058'
8	2019-06-05	Garbh Eileach, E coast	d5		19-G-30	34-38	58	56°14.912'	005°45.037'
9	2019-06-05	Garbh Eileach, E coast	d6		19-G-31	39-43	59	56°14.905'	005°45.037'
10	2019-06-05	Garbh Eileach, E coast	d7		19-G-32	44-49	14	56°14.893'	005°45.026'
11	2019-06-05	Garbh Eileach, E coast	d8		19-G-33	50-54	67	56°14.888'	005°45.032'
12	2019-06-05	Garbh Eileach, E coast	d9	middle	XRF only	55-59		56°14.882'	005°45.039'
13	2019-06-05	Garbh Eileach, E coast	d10	middle	XRF only	60-64		56°14.873'	005°45.029'
14	2019-06-05	Garbh Eileach, E coast	d11	3 mts above base	XRF only	65-69		56°14.866'	005°45.023'
15	2019-06-05	Garbh Eileach, E coast	d11	1 mt below top	XRF only	70-74		56°14.843'	005°45.016'
16	2019-06-05	Garbh Eileach, E coast	d12	middle	19-G-34	75-80		56°14.840'	005°45.028'
17	2019-06-06	Garbh Eileach, E coast	d13	middle	19-G-35	2-6	2 + 15	56°14.808'	005°45.016'
18	2019-06-04	Eileach an Naoimh	disr. beds		XRF only	9-12			
19	2019-06-06	Garbh Eileach, E coast	disr. beds		19-G-38	17-21	185	56°14.754'	005°45.065'
20	2019-06-06	Garbh Eileach, E coast	disr. beds		19-G-39	22-26	186	56°14.745'	005°45.062'
21	2019-06-04	Eileach an Naoimh	d14		19-G-13	13-17	69	56°13.023'	005°48.943'
22	2019-06-06	Garbh Eileach, E coast	d14		19-G-40	27-31	44	56°14.736'	005°45.066'
23	2019-06-04	Eileach an Naoimh	d15		19-G-14	19-23	70	56°13.044'	005°48.895'
24	2019-06-06	Garbh Eileach, E coast	d15		19-G-41	32-36	22	56°14.735'	005°45.074'
25	2019-06-06	Garbh Eileach, E coast	d16		19-G-42	37-41	24	56°14.723'	005°45.080'
26	2019-06-06	Garbh Eileach, E coast	d17	middle	19-G-43	42-46		56°14.719'	005°45.079'
27	2019-06-06	Garbh Eileach, E coast	d18		19-G-44	47-51	43	56°14.721'	005°45.072'
28	2019-06-04	Eileach an Naoimh	d19	2 mts above base	19-G-15	24-28		56°13.048'	005°48.875'
29	2019-06-06	Garbh Eileach, E coast	d19		19-G-45	52-56	21	56°14.700'	005°45.074'
30	2019-06-06	Garbh Eileach, E coast	d20		19-G-46	57-61	40	56°14.686'	005°45.082'
31	2019-06-06	Garbh Eileach, E coast	d21		19-G-47	62-66	20	56°14.678'	005°45.083'
32	2019-06-04	Eileach an Naoimh	d22		XRF only	2-8		56°13.135'	005°48.632'
33	2019-06-06	Garbh Eileach, E coast	d22		19-G-48	67-72	41	56°14.678'	005°45.077'
34	2019-06-06	Garbh Eileach, E coast	d23	linear bottom-up	XRF only	73		56°14.672'	005°45.084'
35	2019-06-06	Garbh Eileach, E coast	d23	linear bottom-up	XRF only	74			
36	2019-06-06	Garbh Eileach, E coast	d23	linear bottom-up	XRF only	75			
37	2019-06-06	Garbh Eileach, E coast	d23	linear bottom-up	XRF only	76			
38	2019-06-06	Garbh Eileach, E coast	d23	linear bottom-up	XRF only	77			
39	2019-06-06	Garbh Eileach, E coast	d23	linear bottom-up	XRF only	78			
40	2019-06-06	Garbh Eileach, E coast	d23	linear bottom-up	XRF only	79			
41	2019-06-06	Garbh Eileach, E coast	d23	linear bottom-up	XRF only	80		56°14.669'	005°45.090'
42	2019-06-06	Garbh Eileach, E coast	d24		19-G-49	81-85	19	56°14.667'	005°45.082'
43	2019-06-06	Garbh Eileach, E coast	d25	linear bottom-up	XRF only	86		56°14.664'	005°45.080'

Table 2:1. Station list (part 1 of 2) from field measurements in the Garvellachs islands. Unique sample and measurement identification numbers are linked to each station point. This consist of ID for samples used for ICP analysis and thin sections, portable XRF log measurement numbers and stone measurement numbers used by A. Spencer and K. Chew in their

compilation of diamictite clast types and quantities. A. Spencer gave support to identify correct stratigraphic levels of the station points.

station	date	location	diamictite horizon	stratigraphic level	sample no	XRF no	stone measurement no	GPS N	GPS W
44	2019-06-06	Garbh Eileach, E coast	d25	linear bottom-up	XRF only	87			
45	2019-06-06	Garbh Eileach, E coast	d25	linear bottom-up	XRF only	88			
46	2019-06-06	Garbh Eileach, E coast	d25	linear bottom-up	XRF only	89		56°14.657'	005°45.084'
47	2019-06-04	Eileach an Naoimh	d26'		19-G-16	29-33	157	56°13.208'	005°48.432'
48	2019-06-04	Garbh Eileach, E coast	d26		19-G-23	68-72	18	56°14.651'	005°45.094'
49	2019-06-04	Garbh Eileach, E coast	d26		19-G-24	73-77	38	56°14.656'	005°45.086'
50	2019-06-04	Garbh Eileach, E coast	d27-29		19-G-22	63-67	37	56°14.631'	005°45.123'
51	2019-06-04	Eileach an Naoimh	d27-29		19-G-17	34-38	3	56°13.288'	005°48.292'
52	2019-06-04	Garbh Eileach, E coast	d27-29		19-G-21	59-62	35	56°14.622'	005°45.127'
53	2019-06-04	Garbh Eileach, E coast	d29		19-G-19	44-48	151	56°14.619'	005°45.147'
54	2019-06-04	Garbh Eileach, E coast	d29		19-G-19	49-53	154	56°14.618'	005°45.147'
55	2019-06-04	Garbh Eileach, E coast	d27-29		19-G-20	54-58	17	56°14.613'	005°45.155'
56	2019-06-04	Garbh Eileach, E coast	d30		19-G-18	39-43	16	56°14.605'	005°45.173'
57	2019-06-03	Garbh Eileach, E coast	d31		19-G-12	60-64	33	56°14.585'	005°45.206'
58	2019-06-03	Garbh Eileach, E coast	d32		19-G-11	54-58	32	56°14.584'	005°45.212'
59	2019-06-03	Garbh Eileach, SE coast	d33		19-G-9	42-46	45	56°14.532'	005°45.341'
60	2019-06-03	Garbh Eileach, SE coast	d33		19-G-9	47	45	56°14.532'	005°45.341'
61	2019-06-07	Garbh Eileach, W coast	d33-35	middle	XRF only	2-6		56°14.248'	005°46.632'
62	2019-06-07	Garbh Eileach, W coast	d33-35	2 mts above base	19-G-50	17-21		56°14.271'	005°46.595'
63	2019-06-07	Garbh Eileach, W coast	d33-35	8 mts above base	XRF only	22-26		56°14.260'	005°46.603'
64	2019-06-03	Garbh Eileach, SE coast	d34		19-G-10	48-52	46	56°14.512'	005°45.352'
65	2019-06-07	Garbh Eileach, W coast	d33-35	top of d34	XRF only	7-11		56°14.242'	005°46.597'
66	2019-06-03	Garbh Eileach, Harbour	d35		19-G-1	2-6	7	56°14.465'	005°45.756'
67	2019-06-03	Garbh Eileach, Harbour	d35		19-G-2	7-11	6	56°14.464'	005°45.764'
68	2019-06-07	Garbh Eileach	d33-35	bottom of d35	XRF only	12-16		56°14.218'	005°46.600'
69	2019-06-03	Garbh Eileach, Harbour	d36		19-G-4	12-16	28	56°14.438'	005°45.811'
70	2019-06-03	Garbh Eileach, Harbour	d36		19-G-3	17-21	47	56°14.435'	005°45.811'
71	2019-06-07	Garbh Eileach, W coast	d36		XRF only	37-41	82	56°14.249'	005°46.495'
72	2019-06-03	Garbh Eileach, Harbour	d37		19-G-5	22-26	29	56°14.424'	005°45.807'
73	2019-06-03	Garbh Eileach, Harbour	d37		19-G-6	27-31	30	56°14.421'	005°45.808'
74	2019-06-07	Garbh Eileach, W coast	d37		XRF only	47-51	11	56°14.211'	005°46.510'
75	2019-06-03	Garbh Eileach, Harbour	d38		19-G-7	32-36	31	56°14.411'	005°45.810'
76	2019-06-03	Garbh Eileach, Harbour	d38		19-G-8	37-41	147	56°14.406'	005°45.789'
77	2019-06-07	Garbh Eileach, Harbour	d38	middle	XRF only	52-56		56°14.205'	005°46.485'
78	2019-06-07	Garbh Eileach, Harbour	d38	test of instrument	XRF only	62-74		56°14.404'	005°45.806'
79	2019-06-06	Garbh Eileach, E coast	d13 raft	caravan raft	19-G-36	7-11		56°14.811'	005°45.024'
80	2019-06-06	Garbh Eileach, E coast	d13 raft	bath tube raft	19-G-37	12-16		56°14.808'	005°45.021'
81	2019-06-08	Chuli	d13 raft		19-G-55			56°14.268'	005°47.025'
82	2019-06-07	Garbh Eileach, SE coast	d32.5 (sandst)	12 mts below top sandstone	19-G-51	27-31		56°14.278'	005°46.614'
83	2019-06-07	Garbh Eileach, SE coast	d35.5 (sandst)	middle of sandstone	19-G-52	32-36		56°14.259'	005°46.504'
84	2019-06-07	Garbh Eileach, SE coast	d36.5 (sandst)	middle of sandstone	19-G-53	42-46		56°14.226'	005°46.521'
85	2019-06-07	Garbh Eileach, SE coast	38.5 (sandst)	8 mts above base sandstone	19-G-54	57-61		56°14.228'	005°46.374'

Table 2:2. Station list (part 2 of 2) from field measurements in the Garvellachs islands. For comments, please refer to Table 2:1.

station	date	location	diamictite horizon	stratigraphic level	sample no	XRF no	stone measurement no	GPS N	GPS W
1	2019-10-14	P Askaig	d40		19-IS-01	2-6	90	55°50.985'	006°06.357'
2	2019-10-14	P Askaig	d40		19-IS-02	8-12+13	91	55°51.009'	006°06.382'
3	2019-10-14	P Askaig	d40		19-IS-03	14-18+19	95	55°51.045'	006°06.370'
4	2019-10-14	P Askaig	d41		19-IS-04	20-24	96	55°51.079'	006°06.345'
5	2019-10-14	P Askaig	d41	lateral measurement, W	19-IS-05	26-30	97	55°51.113'	006°06.360'
6	2019-10-14	P Askaig	d41	lateral measurement, mid	19-IS-06		97	55°51.113'	006°06.360'
7	2019-10-14	P Askaig	d41	lateral measurement, E	19-IS-07	33	97	55°51.113'	006°06.360'
8	2019-10-14	Caol Ila	d43		19-IS-08	34-38	89	55°51.134'	006°06.360'
9	2019-10-14	Caol Ila	d44		19-IS-09	40-44	88	55°51.212'	006°06.423'
10	2019-10-14	Caol Ila	d44		19-IS-10	50-54	87	55°51.215'	006°06.386'
11	2019-10-14	P Askaig	d39		19-IS-11	57-61	134	55°50.927'	006°06.419'
12	2019-10-14	P Askaig	d39	15 mts above bottom M4	19-IS-12	63-67	133	55°50.923'	006°06.396'
13	2019-10-14	P Askaig	d38	top of M3	19-IS-13	69-73	135	55°50.896'	006°06.409'
14	2019-10-15	Torrabus	d13	bottom of d13	19-IS-14	3-7	136	55°51.273'	006°07.836'
15	2019-10-15	Torrabus	d25		19-IS-15	9-13+19		55°51.311'	006°07.933'
16	2019-10-15	Torrabus	member 2	sandstone bed	19-IS-16	14-18+20		55°51.309'	006°07.935'
17	2019-10-15	Torrabus	d28		19-IS-17	21-25		55°51.354'	006°07.952'
18	2019-10-15	W L nam Ban	d33		19-IS-18	27-32+33		55°51.411'	006°07.990'
19	2019-10-15	W L nam Ban	member 3	sandstone bed	19-IS-19	34-38		55°51.437'	006°08.007'
20	2019-10-15	W L nam Ban	member 3	sandstone bed	XRF only	40-42		55°51.524'	006°07.984'
21	2019-10-15	W L nam Ban	d39		XRF only	43-45		55°51.554'	006°08.064'
22	2019-10-15	W L nam Ban	d39		19-IS-20	46-50	143	55°51.610'	006°07.946'
23	2019-10-15	NW L nam Ban	d41		19-IS-21	52-56		55°51.789'	006°08.001'
24	2019-10-15	SW Ardnahoe L	d42		XRF only	58-61		55°51.904'	006°07.968'
25	2019-10-15	SW Ardnahoe L	d42		XRF only	62-64		55°51.904'	006°07.968'
26	2019-10-15	W Ardnahoe L	member 4	sandstone below top of M4	19-IS-22	65-69+70		55°51.972'	006°07.887'
27	2019-10-15	W Ardnahoe L	d44	top of M4	19-IS-23	71-75	144	55°51.998'	006°07.796'
28	2019-10-15	W L nam Ban	d39		19-IS-24	77-81+82		55°51.495'	006°08.381'
29	2019-10-16	Con Tom	d45	boulder from d45	19-IS-25	2-6+7	close 145	55°52.510'	006°07.014'
30	2019-10-16	Con Tom	d45	boulder from d45	19-IS-26	8-12	close 145	55°52.503'	006°07.013'
31	2019-10-16	Con Tom	member 5	sandstone bottom of M5	19-IS-27	14-18		55°52.505'	006°07.026'
32	2019-10-16	Con Tom	member 5	sandstone within d46	19-IS-28	20-24+25		55°52.530'	006°07.069'
33	2019-10-16	Con Tom	member 5	sandstone just above d47	19-IS-29	26-30+31		55°52.608'	006°07.089'
34	2019-10-16	Con Tom	member 5	sandstone top of M5	19-IS-30	32-36+37		55°52.638'	006°07.080'
35	2019-10-16	Con Tom	member 5	sandstone bottom of M5	19-IS-31	38-42+43		55°52.440'	006°07.004'
36	2019-10-16	Con Tom	d47		19-IS-42			55°52.608'	006°07.089'
37	2019-10-17	Am Meall	d21		19-IS-32	2-6	140	55°49.506'	006°06.152'
38	2019-10-17	Am Meall	d21		19-IS-33	8-12+14	139	55°49.500'	006°06.152'
39	2019-10-17	Am Meall	d29		19-IS-34	15-20+21	141	55°49.539'	006°06.174'
40	2019-10-17	C Loisgte	d34		19-IS-35	22-26+27	102	55°49.270'	006°06.807'
41	2019-10-17	C Loisgte	member 3	sandstone, 3rd bed in M3	19-IS-36	28-32		55°49.285'	006°06.793'
42	2019-10-17	C Loisgte	d37		19-IS-37	34-38+39	close 104	55°49.359'	006°06.736'
43	2019-10-17	C Loisgte	member 3	sandstone	19-IS-38	40-44		55°49.265'	006°06.851'
44	2019-10-17	Dun Boraraic	d15		19-IS-39	47-51	94	55°48.975'	006°07.540'
45	2019-10-17	Dun Boraraic	dis. beds	ironstone bed	19-IS-40	53-57		55°49.001'	006°07.611'
46	2019-10-17	Dun Boraraic	dis. beds	dolostone concretions	19-IS-41	59		55°49.001'	006°07.611'
47	2019-10-14	Lossit	below dis. beds	dolostone bed	19-IS-43			55°48.438'	006°07.804
48	2019-10-14	Lossit	below dis. beds	sandstone bed above dolst	19-IS-44			55°48.438'	006°07.804
49	2019-10-14	Lossit	below dis. beds	dolostone bed above sandst	19-IS-45			55°48.438'	006°07.804

Table 3. Station list from field measurements in Islay. For comments, please refer to Table 2:1.

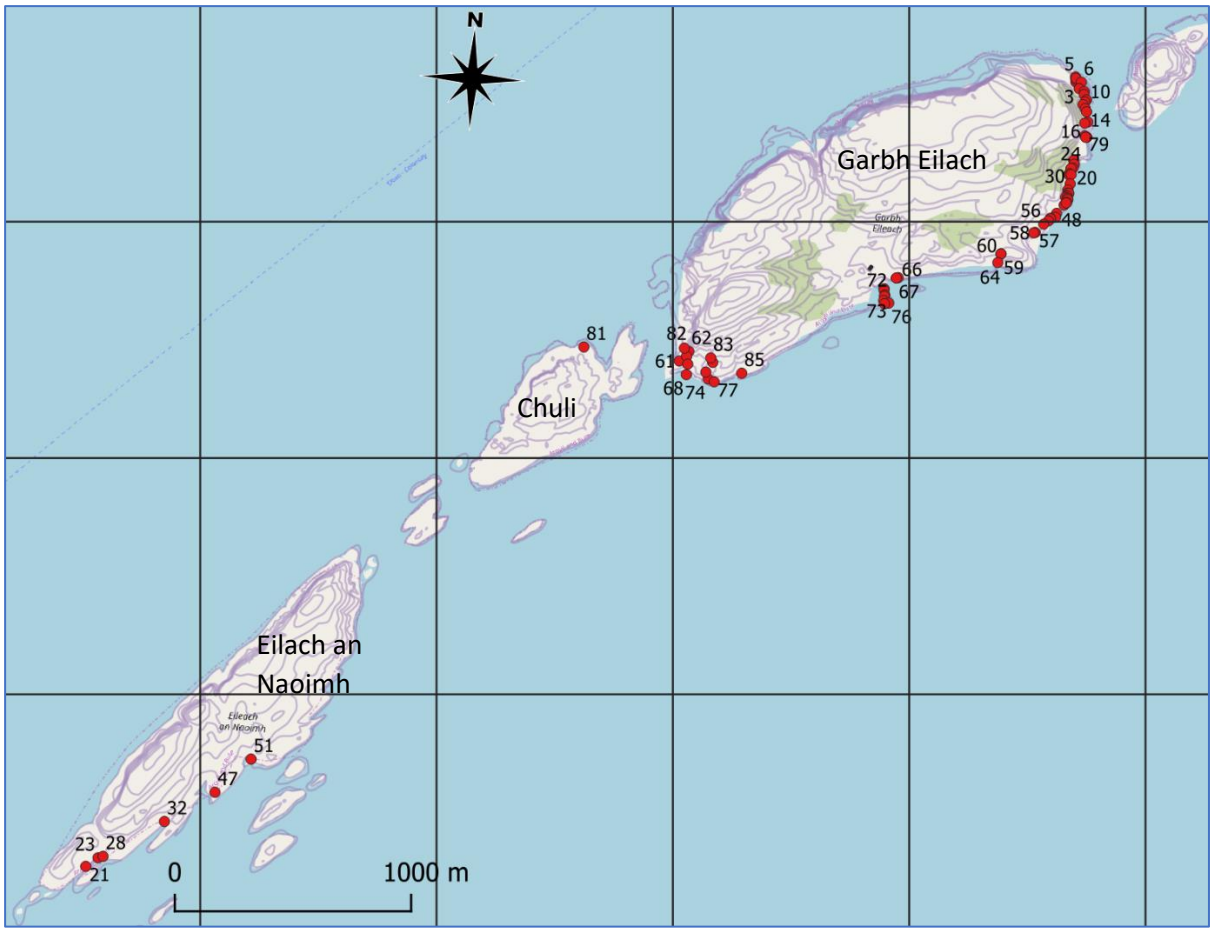

Figure 2. Garvellachs site measurement stations, June 2019. Station numbers' GPS coordinates were imported with help of QGIS 3.6 into an Ordnance Survey map of the Garvellachs islands. The reference coordinate system used is British National Grid / OSGB 1936.

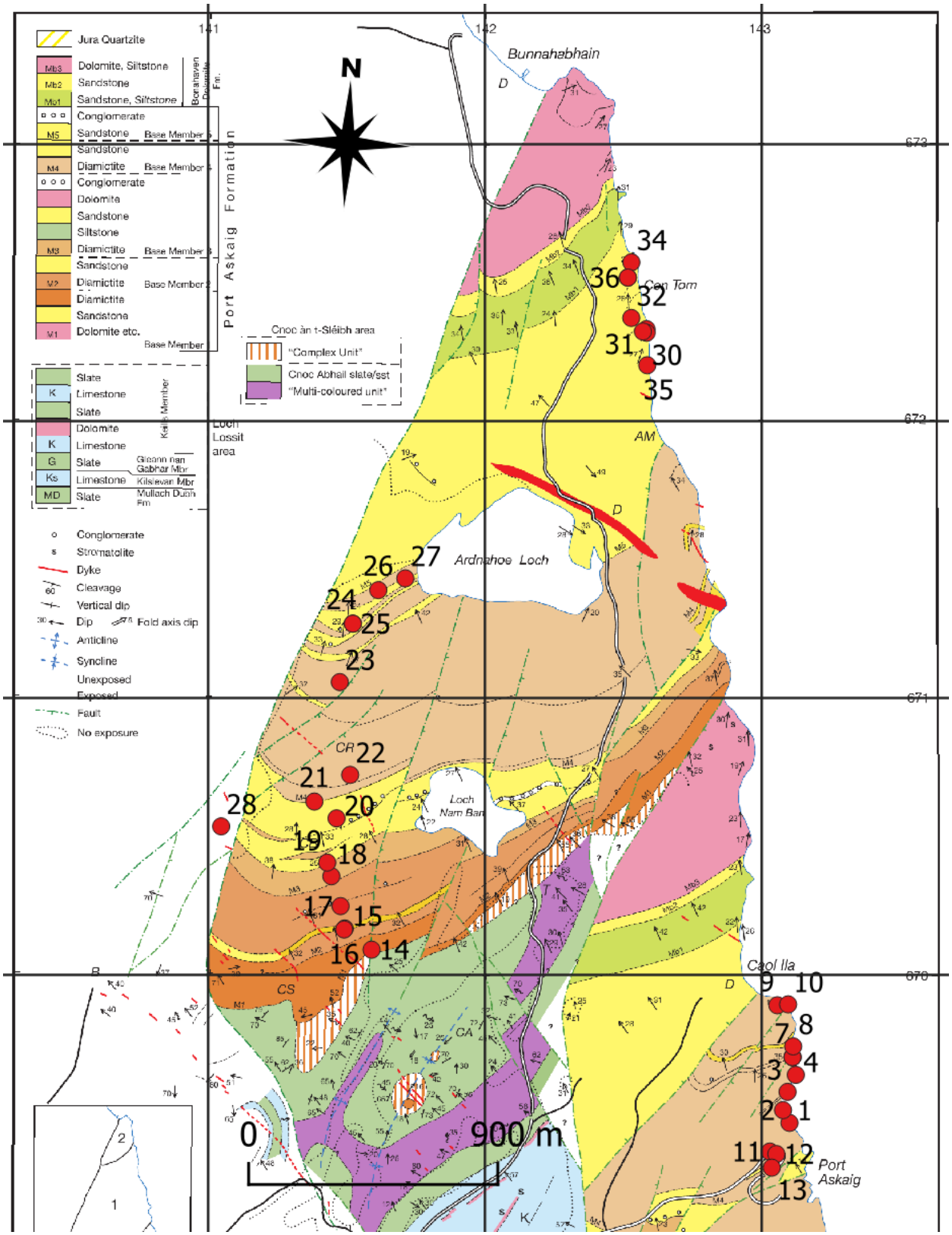

Figure 3. North Islay site measurement stations, October 2019. Station numbers' GPS coordinates were imported with help of QGIS 3.6 into an Ordnance Survey map of Islay together with A. Spencer's 2020 updated geological map covering the PAF on Islay (A. Spencer, personal communication, 2020). The reference coordinate system used is British National Grid / OSGB 1936.North Islay.

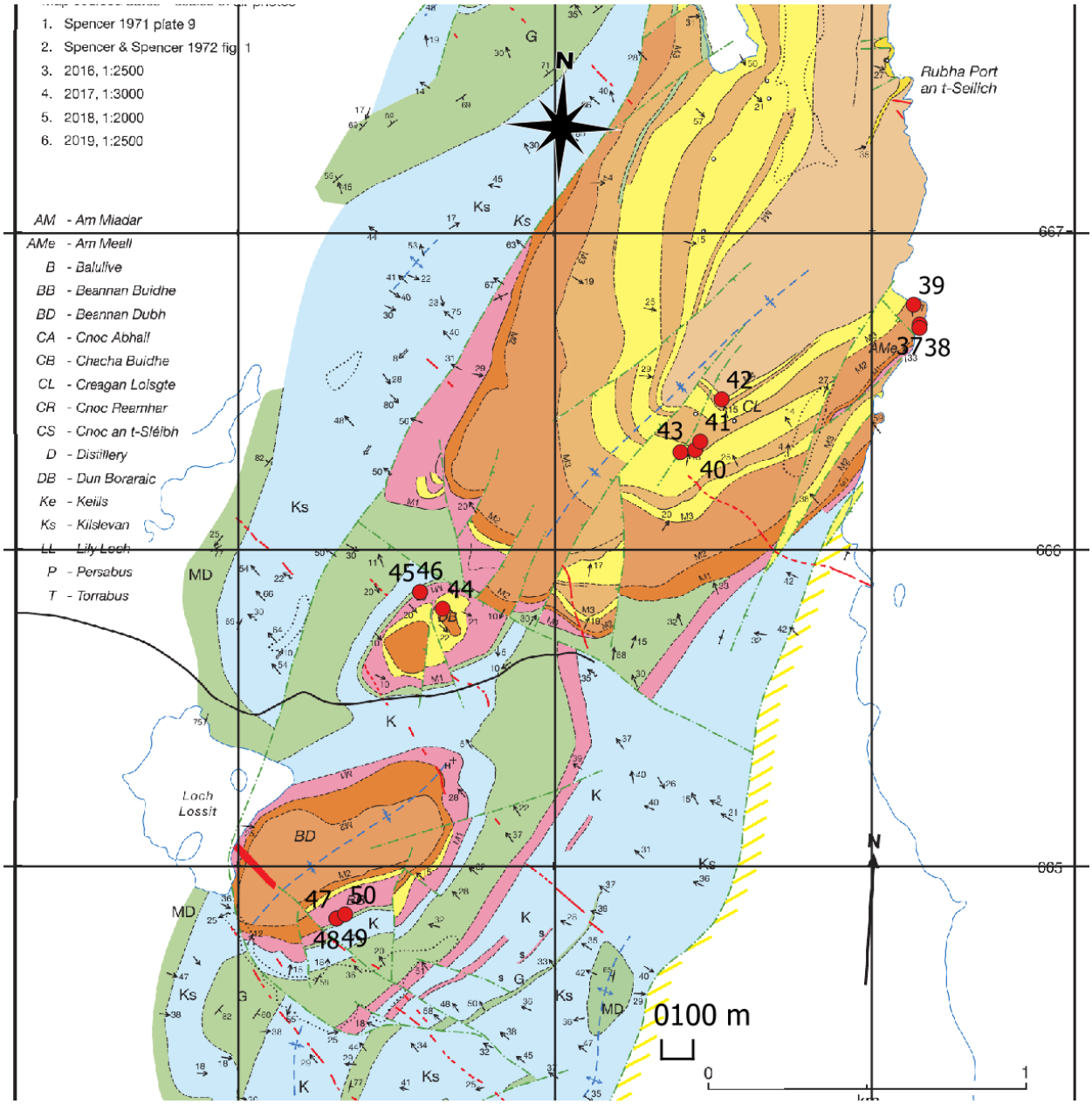

Figure 4. South Islay site measurement stations, October 2019. For comments, please refer to Figure 3.

2.2.2 Stratigraphic level of samples

The correct stratigraphic position of all samples was confirmed on site by A. Spencer who provided invaluable help during both field excursions. Figure 5 shows the stratigraphic positions of acquired rock samples which later were used for ICP analysis and preparation of thin sections for microscopy. Figure 6 shows the stratigraphic positions of site measurement using portable XRF.

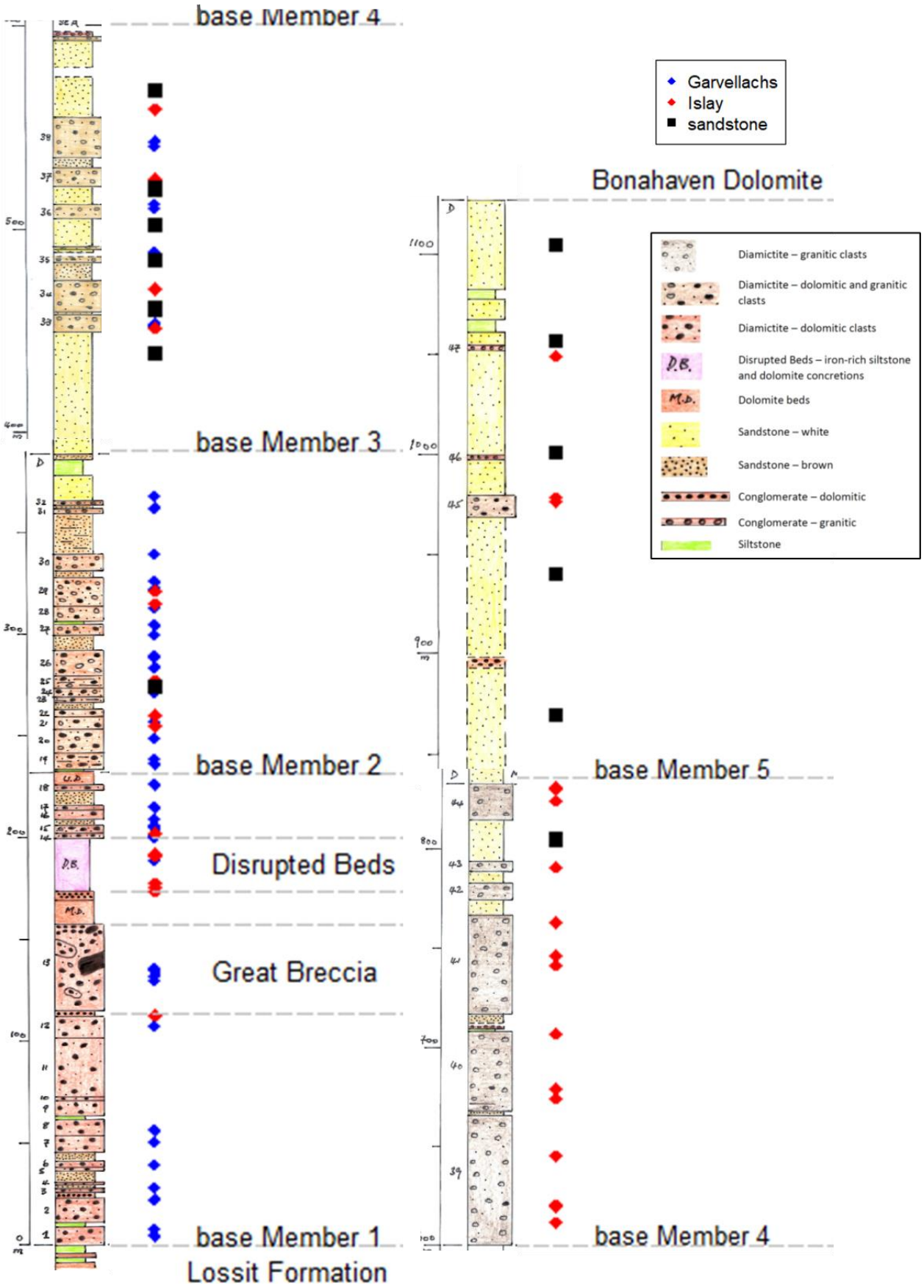

Figure 5. ICP samples and corresponding thin sections stratigraphic positions within the PAF. The stratigraphic column with legend was prepared by A. Spencer from field observations in the Garvellachs (Member 1 – 3) and Islay (Member 4 – 5) (received in personal communication, 2020).

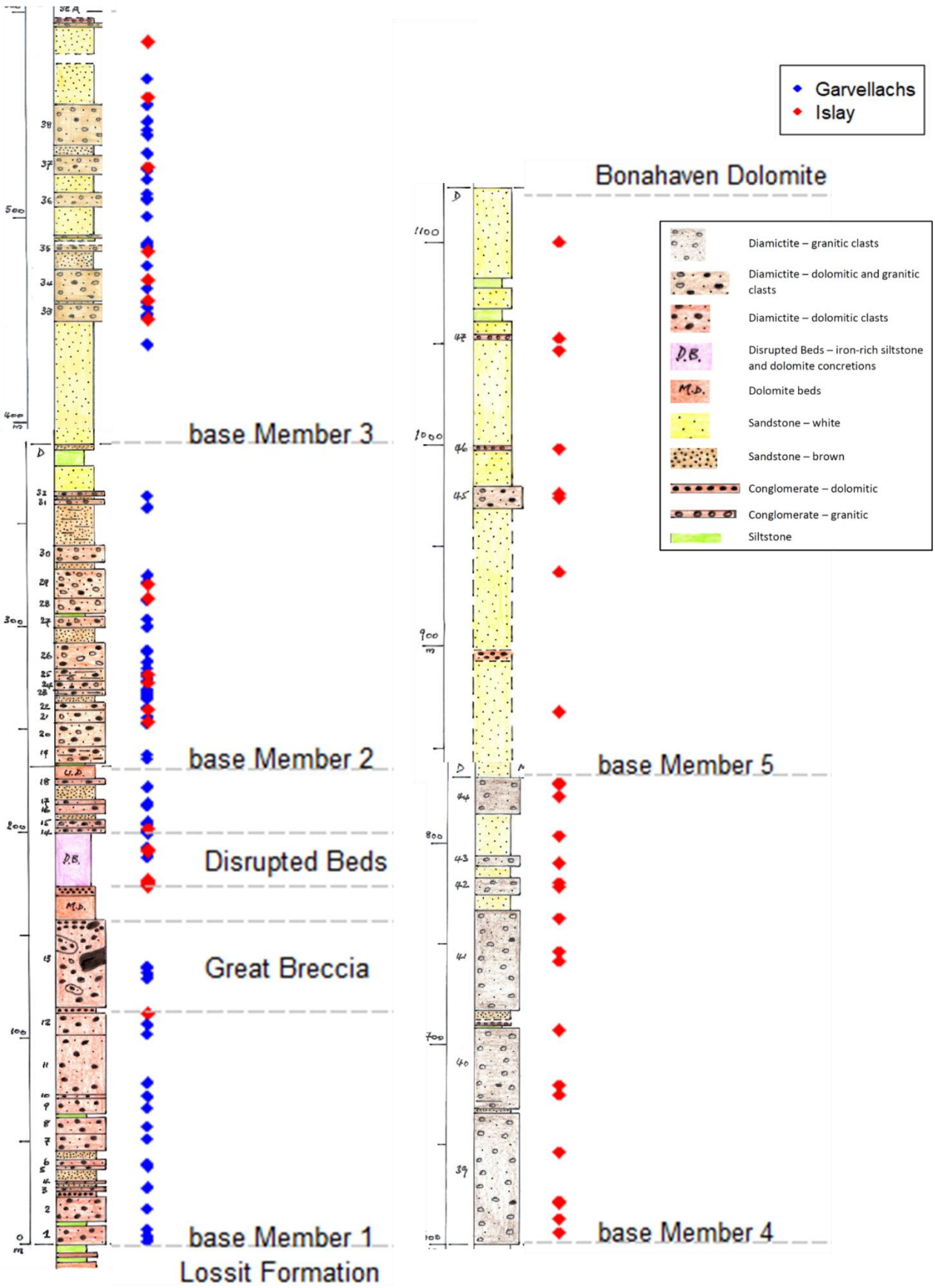

Figure 6. XRF measurements stratigraphic positions within the PAF. For comments and legend, please refer to Figure 5.

2.2.3 Sampling and field measurement methodology

Rock specimens were primarily collected from two lithologies: 79 samples from diamictites and 14 samples from sandstones. The diamictite samples were as far as possible taken from the matrix part of the rocks, although some undetected inclusions of smaller clasts in the groundmass could not be excluded. Three of the diamictite matrix samples are atypical, coming from the matrix of large rafts within the Great Breccia, and thus have a lower original stratigraphic position than their host.

In addition to the diamictite and sandstone samples, 4 rock specimens were taken from the siltstone and dolostone in the Disrupted Beds and 3 specimens from a ca 2 m thick sequence of dolostone – mudstone – sandstone just below the Disrupted Beds.

Geochemical field measurements were done on all locations where rock specimens were collected and in a large number of intermediate locations. This was done with the X-ray fluorescence (XRF) method. By bombarding the sample with high energy X-rays, electrons in the constituent atoms are exited and emit characteristic secondary fluorescent radiation when falling back into their normal states. By sampling the energy states of the secondary emissions, the quantity of elements in the sample can be calculated. A portable XRF analyser of type Olympus Innov-X Delta was used for these field measurements. Further descriptions of the XRF method and the measurement device is available in the User Manual for the Olympus Delta™ Innov-X Analyzers (PN_103201, Rev_A: June/2010) and in Kleine et al (2016) paper.

The XRF analyser has a lower sampling area (ca 1 cm diameter) and wider confidence interval of reported data than larger XRF stationary units. Its penetration depth is ca 1 – 3 mm (Kleine et al, 2016) which can be a limiting factor. The absolute values of XRF element measurements are distorted by the amount of air between the detector muzzle and the sample surface. This is especially the case when the rock surface is uneven, strongly weathered or fractured. However, since the atmosphere mainly consists of light elements (N_2 and O_2), such measurement distortions lead to some increase of reported light elements (LE) but rather small % error within the actual proportions of elements detected.

Lighter elements and elements in lower concentrations are more difficult to detect using XRF analysers. In the actual field location, Al, P, S and Cl were only occasionally detected and their data contain high percentages of uncertainty. Si being a relatively light element also suffers from this, but since the total amount of Si in the samples is relatively high, uncertainty was kept at an acceptable level. Mg and Na were never detected.

The reported XRF data are uncertain both as regards random variations in the instrument sampling and analysis of data, but also because of small variations in exact positioning of the device. For future field measurements, it is recommended to regularly make field tests of the aggregated confidence interval of the data. This can e.g. be done by making repeated measurements on the same exact location. If making 20 repeated measurements at the same spot, the total variation in data for each reported element would give an estimate of a 5% confidence interval for each such element.

Field observations were also made of periglacial structures such as sandstone wedges and frost shattered stones and of marine indicators such as tidal influenced cross bedded sandstone. Stromatolites in carbonate beds were also observed in the Garbh Eileach Formation below the PAF.

2.3 Description of lab analysis

2.3.1 Sample preparation and ICP chemical elements analysis

The 100 collected rock specimens from the Garvellachs and Islay were each cut into 3 pieces using a diamond-saw. One piece was saved as a control specimen and for other possible future analyses, one ca 2x5 cm chip was used for preparation of thin sections for microscopy, and the last piece was used for the ICP-analysis. Care was taken to exclude weathered materials. The piece intended for ICP-analysis was crushed in a jaw crusher and milled to fine powder in a vibratory disc mill before shipment to an external laboratory for analysis. The cutting, crushing and milling were done in Stockholm University Geo Sciences laboratory.

The ICP chemical analysis was performed by Activation Laboratories Ltd, Ancaster, Ontario, Canada, using a combination of lithium metaborate/tetraborate fusion ICP for whole rock and ICP-MS for trace elements. Lithium metaborate and lithium tetraborate were mixed with the sample in graphite crucibles and fused in induction furnaces at 1150 °C. The fused crucible was dropped into a mixture of 5% nitric acid. The resultant molten mixture was dissolved resulting in total metal useful for lithogeochemistry including major oxides and trace elements including REE and other high field strength elements. The diluted fused samples were analysed by Perkin Elmer Sciex ELAN 6000, 6100 or 9000 ICP/MS. Calibration was performed using 10 synthetic calibration standards. A set of 10 certified reference material was run before and after every batch of samples. Duplicates were fused and analysed every 17 samples. The instrument was recalibrated after every 2 trays of samples. Accuracy is typically in the 1-3% range provided the analyte is greater than 100 times the detection limit.

2.3.2 Thin sections microscopy

The thin sections were prepared by Vancouver Petrographics, Langley, British Columbia, Canada from chips cut from rock samples. The thin sections were analysed in the microscopy lab at Stockholm University. Point counts of the following 8 mineral groups were made on 100 thin sections: quartz, feldspar, carbonates (calcite and dolomite), muscovite, biotite, chlorite, opaque (pyrite, hematite, magnetite, chalcopyrite) and others (not classified).

Average crystal sizes were estimated and the typical mineral in the groundmass were noted for each sample. Foliation and similar crystal arrangements were noted as well as other observations of interest, such as the possible occurrence of microcline, albite and alterations at the rims and within crystals (Figures 7 – 9).

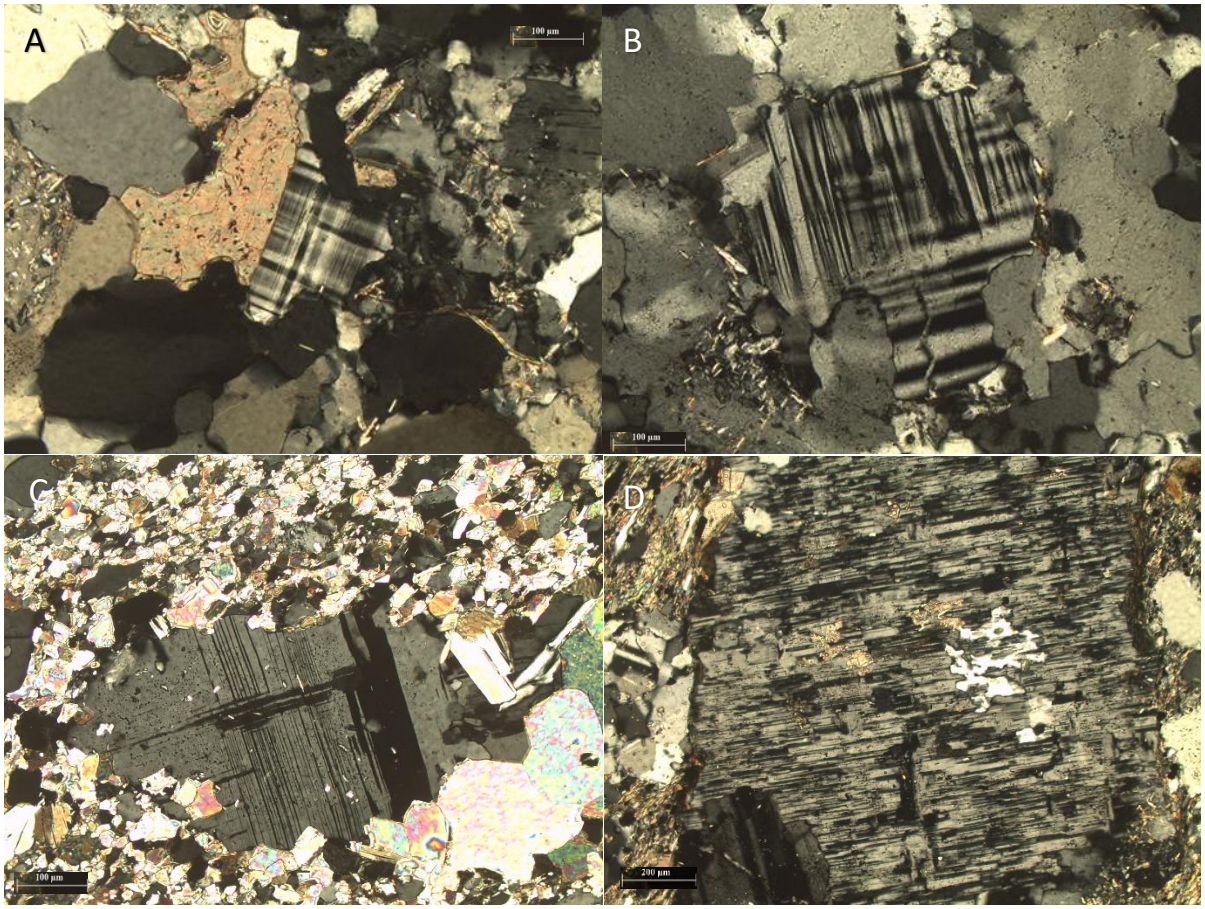

Figure 7. Microscope photos showing microcline in thin section nos. 19-G-51 from sandstone bed above d32 (A), 19-G-53 from sandstone bed above d36 (B), 19-G-13 from d14 (C) and albite in 19-G-24 from d26 (D), all from Garbh Eileach. XPL, magnification A, B and C 20x and D x10.

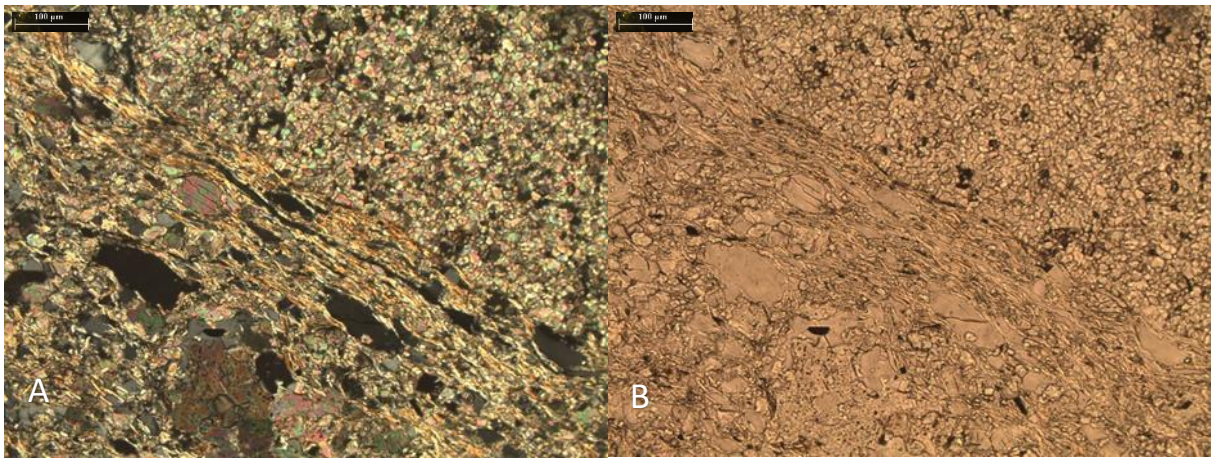

Figure 8. Microscope photos showing recrystallization resulting from metasomatic fluids in thin section no. 19-G-30 from diamictite matrix in d5, Garbh Eileach. XPL (A) and PPL (B), magnification 20x.

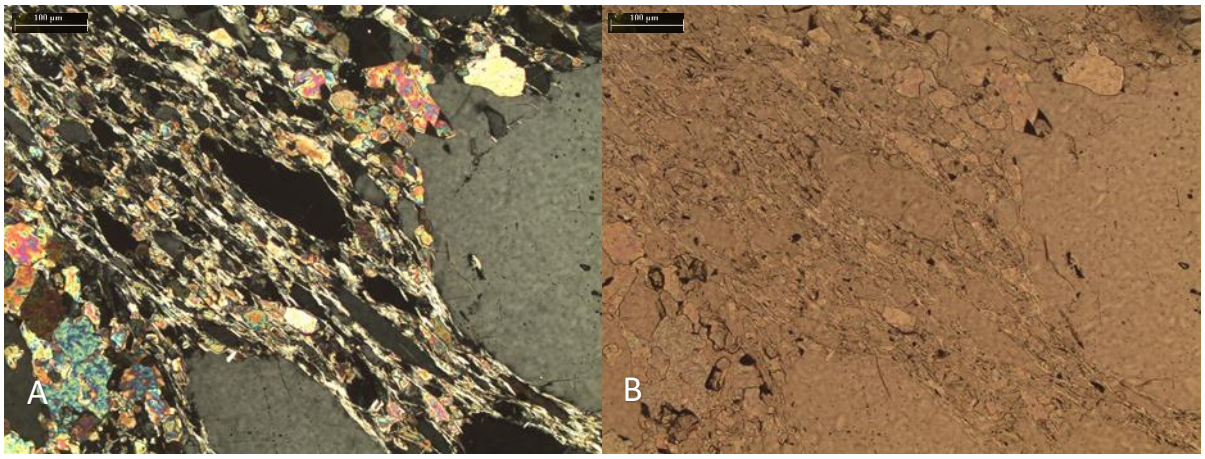

Figure 9. Microscope photos showing crystal foliation pattern in thin section no. 19-G-41 from diamictite matrix in d15, Garbh Eileach. XPL (A) and PPL (B), magnification 20x.

Selected thin sections with high percentage of opaque minerals were selected for study in reflected light. This enabled identification of individual crystals of pyrite, hematite and chalcopyrite (Figure 10).

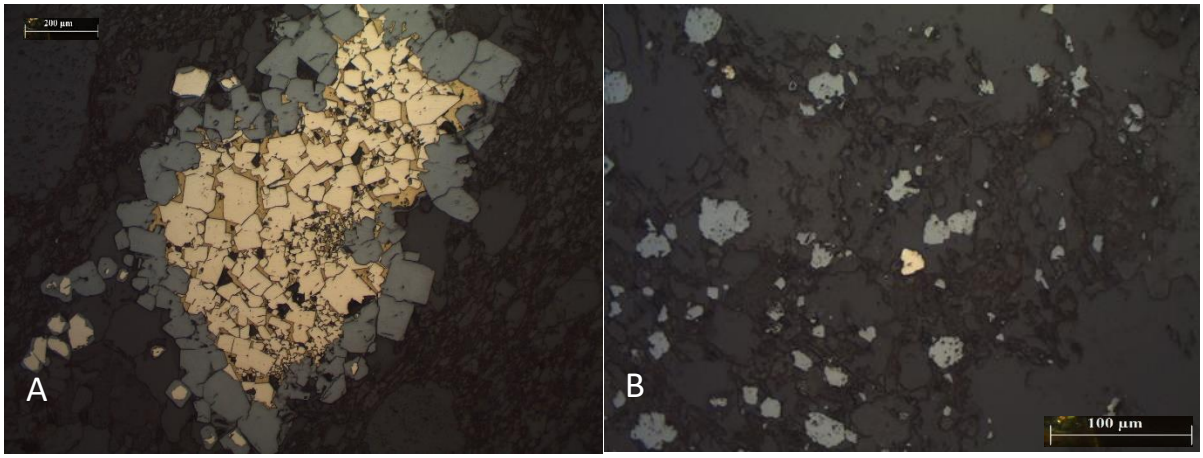

Figure 10. Microscope photos showing pyrite in centre surrounded by hematite with intergrown chalcopyrite in thin section no. 19-G-41 from diamictite matrix in d15 (A), plus grains of euhedral hematite and single light-yellow pyrite in centre in thin section no. 19-G-45 from diamictite matrix in iron-rich d19 (B), both from Garbh Eileach. Reflected light, magnification 10x respectively 40x.

2.4 Data handling

2.4.1 Preparation and presentation of data

The number of the diamictite bed (d1 – d47), the relative stratigraphic position (%-number showing the relative height within the PAFs total of 1100 m), the number of the member (M1 – M5) and the location (Garvellachs or Islay) were linked to the data belonging to each sample.

Data point outliers were reviewed using box-and-whisker plots as shown in example in Figure 11. Since none of the observed outliers could be linked to measurement errors or other anomalies and in order not to risk introducing bias into the data, no outliers were removed from the dataset.

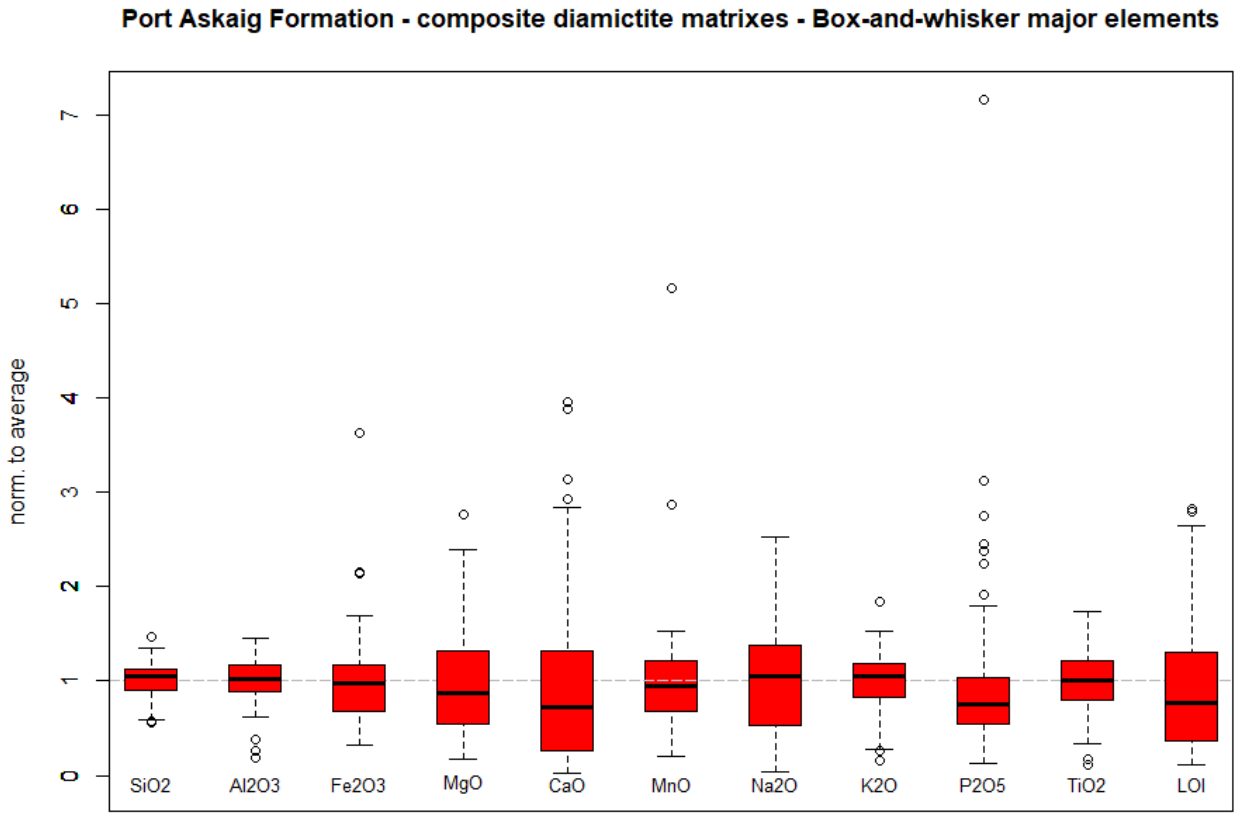

Figure 11. Box-and-whisker plot of major elements from the PAF diamictite matrix dataset showing the interquartile range in red, median as black bar, "whiskers" extending to the most extreme data point not more than 1.5 times the interquartile range, and outliers as open circles. Data for each element have been normalized to their respective averages. Outliers are defined to be data outside the "whiskers". The largest observed Fe_2O_3 outlier is in d19, the largest outlier in P_2O_5 is coupled to the same high Fe_2O_3 value in d19 and all CaO outliers belong to the carbonate rich member 1.

Data points not detected were recorded as "<[detection limit]" in the ICP geochemical log and "ND" (Not Detected) in the XRF geochemical log. In both logs these data points were deleted which means that they did not enter statistical computations such as calculations of means, variances, correlation factors etc. Alternative approaches would be to set such not detected values to zero or to 50% of their respective detection limits. This would have increased the information content of the dataset, but also uncertainty if failure to detect such data points were caused by other reasons than low concentrations. Failure to detect an individual value of an element typically increase with decreasing relative concentrations, but for XRF data also with lower atomic weight of the element.

In the graphical presentation of data, each individual data point is typically shown as a point, but in some few cases they have been displayed as points connected by lines to emphasize an interlinked trend.

Geochemical data plotted as trend over the stratigraphic column of the PAF are normally shown vertically. Thus position 0% (base of d1) represent the bottom of the stratigraphic column bordering EAF and 100% (sandstone

bed above d47) represent the top of the PAF below the Bonahaven Dolomite. However, in some cases the data have been shown as a horizontal progression following the implicit time arrow from left to right.

2.4.2 Statistical analyses applied

Statistical analysis was performed using program package R version 3.5.1 (2018-07-02), provided by The R Foundation for Statistical Computing.

The following types of statistical and analytical methods were used: i) check for linear association of pairs of variables (statistical correlations), ii) dependent variables response to one or more explanatory variables (simple and multiple linear regression), iii) deconvolving groups of variables using multivariate statistical analysis (principal components analysis – PCA), iv) comparison of two or more samples of variables to check if they originate from the same distribution (using Mann–Whitney respectively Kruskal–Wallis rank tests, similar to parametric methods such as ANOVA), v) investigation of possible cyclicity in the data (Fourier frequency analysis giving amplitude and power spectrums, and autocorrelation lag calculations), vi) analysis of distribution patterns (using box-and-whisker plots) and vii) test if data follows normal distributions (quantile checks).

The results of the statistical analyses have been displayed i.a. in i) data tables, ii) trend plots (in some cases supplemented with trendlines from linear regression), iii) bivariate plots, iv) ternary diagrams, v) spider diagrams with data normalized to standard values, vi) discrimination diagrams, vii) scree plots and viii) box-and-whisker plots.

2.4.3 Normalization of data

The average concentrations compiled by McLennan (2001) for the Upper Continental Crust (UCC) have been used when normalizing the PAFs geochemical datasets to standard values. UCC has been chosen instead of another often used standard, Post-Archean Australian Shale (PAAS), because i) the average composition of the non-carbonate glacial clay in the matrix of the PAF diamictite is expected to primarily originate from the unroofed crystalline bedrock below the Dalradian sedimentary cover, and ii) the profile of the PAFs Rare Earth Elements (REE) follows UCC better than PAAS.

In some comparisons, the PAF data have been normalized to concentrations excluding carbonates. Here the weight% (wt%) sum of all elements divided by wt% sum of all elements less wt% sum of MgO, CaO and LOI (representing primarily CO_2) for each sample is used to normalize the remaining elements of that sample. This will somewhat overestimate the carbonate content by also including CaO in anorthite feldspar, some non-carbonate minerals containing Mg and some light compounds such as OH burnt away in LOI. Alternative methods, such as using CO_2 mole content from LOI as representative for carbonates, were discarded since the fluctuating proportions of limestone and dolomite would introduce larger uncertainties.

When comparing trends of different elements in the same plot, the elements were normalized to their respective averages. Variations in element concentrations over the height of the stratigraphic column in such plots are thus seen as percentage shifts around their average values.

Normalization of elements to exclude LOI in the ICP dataset and to exclude LE in the XRF dataset were considered but discarded. LOI primarily consists of CO_2 as will be seen in the Result section and therefore a normalization to exclude carbonates (if any) is more useful. LE contains light elements where Al, Mg and Na together with C in carbon dioxide in carbonates constitute a considerable share of its relative weight. To normalize data excluding LE would thus be based on unknown mixes of their related minerals.

2.4.4 Data precision and reliability

Variability in studied parameters may be masked by poor reliability in the data, leading to erroneous interpretations. Uncertainty in the data comes from different sources. Systematic errors set the data accuracy level and random errors the precision level. Both internal factors such as measurement instruments accuracy

and precision as well as external factors such as site disturbances and human errors may impact the reliability of the data.

Risks of systematic errors (accuracy) are mitigated by calibrating measurement instruments to standardized samples with known geochemical compositions. The portable XRF was calibrated against a metal test-disc at the beginning of each workday. The ICP measuring instrument was calibrated against 10 standardized reference samples before each batch of tests.

The size of the random errors (precision) needs to be known to evaluate the reliability of the data. The portable XRF's data-log provide a confidence interval for the precision of measurements. Similarly, Activation Laboratories indicate a detection limit for the precision of their analyses. With this information the range of precision of the instruments and laboratory analysis can be assessed, but it does not necessarily cover all aspects of random errors. Therefore, the total range of precision has also been estimated by conducting repeated measurements on same samples, which was done with the portable XRF in one site location in the Garvellachs and with the ICP method on 5 duplicate samples. The results concerning the precision are presented below in Table 4 for ICP data and Tables 5 and 6 for XRF data.

Analyte Symbol	SiO2	Al2O3	Fe2O3(T)	MnO	MgO	CaO	Na2O	K2O	TiO2	P2O5	Total
Unit Symbol	%	%	%	%	%	%	%	%	%	%	%
Detection Limit	0,01	0,01	0,01	0,001	0,01	0,01	0,01	0,01	0,001	0,01	0,01
Detection limit precision (relative to analyte average wt%)	0,02%	0,1%	0,2%	1,8%	0,2%	0,1%	0,7%	0,4%	0,3%	5,6%	0,01%
Average wt% (5 duplicate samples)	60,2	7,8	4,2	0,05	4,4	7,6	1,4	2,4	0,37	0,18	99,998
Mean precision from 5 duplicate samples (+/-)	0,9%	0,9%	0,9%	0,5%	1,1%	1,6%	2,7%	2,5%	1,0%	10,7%	0,5%
Upper bound of mean precision (95% one-sided confidence interval)	1,5%	1,5%	1,6%	1,1%	1,9%	2,3%	3,8%	3,4%	1,5%	25,1%	0,9%

Analyte Symbol	Sc	Be	V	Ba	Sr	Y	Zr	Cr	Co	Ni	Cu	Zn	Ga
Unit Symbol	ppm	ppm	ppm	ppm	ppm	ppm	ppm	ppm	ppm	ppm	ppm	ppm	ppm
Detection Limit	1	1	5	2	2	1	2	20	1	20	10	30	1
Detection limit precision (relative to analyte average ppm)	17%	57%	10%	0%	1%	7%	1%	13%	16%	89%	44%	67%	10%
Average ppm (5 duplicate samples)	6,0	1,8	49	1022	217	15,2	147	156	6,4	22,5	22,5	45,0	9,9
Mean precision from 5 duplicate samples (+/-)	0,0%	0,0%	2,0%	2,1%	0,7%	2,2%	4,1%	3,1%	5,7%	20,0%	0,0%	9,5%	2,7%
Upper bound of mean precision (95% one-sided confidence interval)			3,4%	3,2%	1,3%	4,8%	5,2%	7,5%	12,5%	39,1%		22,4%	7,8%

Analyte Symbol	Ge	Rb	Nb	Mo	Ag	Sn	Cs	Hf	Ta	Tl	Pb	Th	U
Unit Symbol	ppm	ppm	ppm	ppm	ppm	ppm	ppm	ppm	ppm	ppm	ppm	ppm	ppm
Detection Limit	1	2	1	2	0,5	1	0,5	0,2	0,1	0,1	5	0,1	0,1
Detection limit precision (relative to analyte average ppm)	78%	3%	15%	23%	83%	89%	33%	5%	19%	31%	63%	2%	8%
Average ppm (5 duplicate samples)	1,3	70,7	6,6	8,7	0,6	1,1	1,5	3,7	0,5	0,3	8,0	5,4	1,3
Mean precision from 5 duplicate samples (+/-)	0,0%	2,0%	4,7%	12,6%	16,8%	16,7%	5,5%	2,5%	6,7%	0,0%	5,6%	5,1%	3,1%
Upper bound of mean precision (95% one-sided confidence interval)		3,6%	10,2%	34,0%	18,1%	44,2%	9,0%	5,3%	14,6%		10,9%	7,4%	6,7%

Analyte Symbol	La	Ce	Pr	Nd	Sm	Eu	Gd	Tb	Dy	Ho	Er	Tm	Yb	Lu
Unit Symbol	ppm	ppm	ppm	ppm	ppm	ppm	ppm	ppm	ppm	ppm	ppm	ppm	ppm	ppm
Detection Limit	0,1	0,1	0,05	0,1	0,1	0,05	0,1	0,1	0,1	0,1	0,1	0,05	0,1	0,01
Detection limit precision (relative to analyte average ppm)	0,5%	0,2%	1,0%	0,5%	2,7%	6,2%	3,1%	19,6%	3,4%	17,2%	5,8%	19,7%	5,8%	3,7%
Average ppm (5 duplicate samples)	20,9	42,17	4,873	18,41	3,68	0,812	3,23	0,51	2,95	0,58	1,73	0,254	1,72	0,271
Mean precision from 5 duplicate samples (+/-)	3,9%	4,5%	4,8%	3,7%	4,2%	2,6%	4,8%	3,1%	4,1%	10,7%	4,7%	3,7%	5,7%	1,9%
Upper bound of mean precision (95% one-sided confidence interval)	5,9%	6,3%	6,8%	6,3%	7,5%	5,5%	7,4%	8,9%	6,3%	25,5%	9,4%	7,0%	9,8%	3,4%

Table 4. ICP data precision analysis. The table is grouped into main, trace and rare earth elements and provide information about data precision relating to ICP detection limitations and total precision estimated from repeated measurements. Detection limit precision = average weight of samples / detection limit. Mean precision from 5 duplicate samples = average of absolute values of 5 relative differences from duplicate measurements on same sample. Upper bound of mean precision (95% confidence level) = mean precision + SD of relative differences x t-value for 5% one sided confidence interval / square rote of n=5.

For elements in the ICP dataset which are in low concentrations, such as Be, Ni, Cu, Zn, Ge, Mo, Ag, Sn, Cs, Tl and Pb, the detection limit imposes restrictions on reliability. Overall assessment of precision from duplicate samples analysis furthermore raises questions for P_2O_5, Mo and Ho. Since P_2O_5 appears in larger concentrations together with Fe_2O_3 and Ho belongs to the generally more abundant REE group, they are kept in the ICP

dataset, but remaining elements with low reliability are left out from further analysis. In summary, all major elements and REE plus following trace elements from the ICP analysis are used in the continued work: Sc, V, Ba, Sr, Y, Zr, Cr, Co, Ga, Rb, Nb, Hf, Ta, Th and U.

Analyte symbol	Al	Si	P	S	Cl	K	Ca	Ti	V	Mn	Fe	Ni
Unit Symbol	%	%	%	%	%	%	%	%	%	%	%	%
Atomic mass	27,0	28,1	31,0	32,1	35,5	39,1	40,1	47,9	50,9	54,9	55,8	58,7
Average wt% (all samples)	8,41	26,57	0,54	0,421	7,070	1,93	1,66	0,27	0,034	0,05	3,37	0,925
Mean precision (+/-)	24,0%	3,4%	23,5%	14,6%	7,4%	2,3%	5,4%	10,6%	28,9%	16,1%	1,9%	26,3%
Upper bound of mean precision (95% one-sided confidence interval)	25,2%	3,7%	24,8%	15,5%	8,6%	2,4%	6,1%	11,2%	29,8%	17,2%	1,9%	31,8%

Analyte symbol	Cu	Zn	As	Rb	Sr	Y	Zr	Mo	Pb	Th	U	LE
Unit Symbol	%	%	%	%	%	%	%	%	%	%	%	%
Atomic mass	63,5	65,4	74,9	85,5	87,6	88,9	91,2	95,9	207,2	232,0	238,0	
Average wt% (all samples)	0,013	0,006	0,002	0,008	0,009	0,002	0,015	0,002	0,005	0,005	0,007	61,28
Mean precision (+/-)	25,4%	15,7%	25,1%	5,1%	5,4%	16,7%	3,8%	27,7%	17,3%	27,6%	27,6%	1,1%
Upper bound of mean precision (95% one-sided confidence interval)	27,3%	16,4%	27,0%	5,3%	5,7%	17,2%	4,0%	28,7%	18,4%	28,3%	33,3%	1,2%

Table 5. XRF instrument data precision. The table shows all elements except for those only intermittently reported by the instrument and provides information about data precision relating to the instrument precision. Mean precision = average relative instrument precision calculated from all XRF measurements for each element. Upper bound of mean precision (95% confidence level) = mean precision + SD of relative precisions x t-value for 5% one sided confidence interval / square rote of n (=number of total reported readings for each element). The table also provides information about atomic mass and average weight for each element from which it can be inferred that heavier and more abundant atoms have better reported precisions.

The overall precisions estimated from repeated XRF measurements on same sample on site (Table 6 below) have a good correspondence with indicated instrument precision (Table 5 above) for most of the elements. S and Cl have higher than average concentrations in the sample used for the repeated site measurements and show a markedly better precision here.

Analyte symbol	Si	S	Cl	K	Ca	Ti	V	Mn	Fe	Cu	Zn	As
Unit Symbol	%	%	%	%	%	%	%	%	%	%	%	%
Number of site-test measurements	11	11	11	11	11	11	1	10	11	4	11	2
Average wt% (all site-test measurements)	11,2	0,75	30,0	1,30	0,37	0,18	0,023	0,012	3,08	0,0028	0,0026	0,0011
Instrument mean precision for test measurements (+/-)	3,1%	4,9%	1,0%	1,8%	3,5%	9,7%	32,2%	24,8%	1,2%	29,2%	17,1%	28,6%
95% conf intervall for site measurement results (+/-)	2,2%	1,7%	1,0%	1,6%	3,0%	5,3%		16,1%	0,7%	18,7%	12,5%	42,8%

Analyte symbol	Rb	Sr	Y	Zr	Pb	Th	LE
Unit Symbol	%	%	%	%	%	%	%
Number of site-test measurements	11	11	11	11	4	3	11
Average wt% (all site-test measurements)	0,0077	0,0046	0,0015	0,015	0,0012	0,0029	53,10
Instrument mean precision for test measurements (+/-)	3,9%	4,3%	13,7%	2,6%	28,7%	31,5%	0,8%
95% conf intervall for site measurement results (+/-)	1,9%	2,8%	9,9%	1,5%	24,9%	10,8%	0,5%

Table 6. XRF site tested precision analysis. The table shows data from those elements which gave reported values in the site test and provides information about total precision from repeated measurements. The instrument mean precision was calculated from the reported precision in same manner as in Table 5, but only for the actual number of test measurements. A 95% confidence interval was also calculated based on the site measurement results of weights for each element = mean weight + SD of weights x t-value for 2.5% (giving a two-sided confidence interval of 5%) / square rote of n (number of readings for each element from site test). Instrument reported precisions and the 95% confidence intervals from repeated site measurements show good correspondence.

The elements Mg, Cr, Co, Se, Ag, Cd, Sn, Hf, Ta, W, Hg and Bi in the XRF dataset were deleted from the outset because they were not possible to detect at all or only very rarely. The following elements show extremely poor instrument precisions: Al, P, V, Ni, Cu, As, Mo, Th and U. In the repeated measurements on same sample on site, the overall estimate of precision show poor values for V, Mn, Cu, Zn, As, Pb, and Th. These elements are left out from further analysis, except for Al and Mn which, as important components in different geochemical proxies, are kept in the dataset (although interpreted with caution). Although Cl give an

acceptable precision, it primarily reflects the influence of sea sprayed salt and adds no value to the data. In summary, the following data from the XRF site measurements are used in the continued analysis: Al, Si, S, K, Ca, Ti, Fe, Rb, Sr, Y, Zr and LE.

2.4.5 Correlation between datasets

Correlations of XRF versus ICP data show acceptable covariance for Fe, Ca and Sr but none for Al (Table 7). This confirms that the portable XRF is usable for measuring certain selected elements. Measurements from Garvellachs generally have a better correspondence then those from Islay, which can be attributed to higher concentrations of these elements in Members 1 – 3.

The XRF data were also normalized to [100/(100-LE)] and to [100/(100-Cl)] to eliminate the effect of dilution of varying quantities of undetected elements respectively chlorine from sea spray. This recalculated XRF data were again correlated versus ICP data (Table 7). The LE normalized correlations are of similar or lower values while the chlorine-free correlations improve for most of the elements. This supports the reasoning in section 2.4.3 why not to recalculate the XRF data on a LE-free basis. However, the quality of the XRF data improves by eliminating the chlorine dilution.

	Si	Al	Fe	Ca	K	Ti	Sr	Y	Zr	Rb
correlation ICP - XRF	0,44	-0,02	0,81	0,81	0,45	0,37	0,70	0,51	0,53	0,60
Garvellachs samples	0,69	-0,01	0,88	0,81	0,70	0,35	0,60	0,58	0,66	0,83
Islay samples	0,38	-0,30	0,45	0,43	0,16	0,37	0,77	0,41	0,46	0,33
corr. ICP - XRF (norm. to 100-LE)	0,52	0,06	0,73	0,86	0,41	0,33	0,61	0,28	0,35	0,41
Garvellachs samples	0,53	-0,25	0,76	0,88	0,40	0,12	0,54	0,04	0,31	0,41
Islay samples	0,39	0,14	0,64	0,32	0,42	0,57	0,54	0,51	0,63	0,45
corr. ICP - XRF (norm. to 100-Cl)	0,31	0,19	0,88	0,83	0,70	0,74	0,82	0,77	0,71	0,87
Garvellachs samples	0,56	0,21	0,86	0,91	0,77	0,76	0,84	0,79	0,69	0,91
Islay samples	0,20	-0,03	0,84	-0,03	-0,11	0,55	0,85	0,71	0,82	0,48

Table 7. The correlation coefficients between XRF and ICP datasets. The covariance between these two sets of variables was calculated using the Pearson product-moment method giving the linear relationship as a coefficient between -1 to +1. The table lists the correlation for the whole PAF, for Garvellachs and for Islay separately. The XRF data were also normalized to eliminate LE (proportion of undetected elements) and to eliminate chlorine (where Cl tends to be added by sea spray) using the formulas $X_i*100/(100-LE_i)$ and $X_i*100/(100-Cl_i)$where X_i, Cl_i and LE_i signify the respective element, LE and Cl values in sample number [i].

Correlation coefficients have also been calculated between ICP and quantity of minerals given by point-count of thin sections for corresponding samples (Table 8). This show some expected covariance between major elements and the minerals they primarily are associated with. Quartz correlates with SiO_2, carbonates with CaO, MgO and LOI, feldspar with Na_2O and opaque (hematite, magnetite, pyrite) correlate with Fe_2O_3 and P_2O_5. Muscovite show some correlations with Al_2O_3 and K_2O. For trace elements correlations exist between Cr and quartz, Ga and Rb with muscovite and Sr with carbonates. In summary, this validates the result of the point-count of minerals in thin samples.

	CHLORITE	OTHER	FELDSPAR	BIOTITE	OPAQUE	QUARTZ	MUSCOVITE	CARBONATE
SiO2	-0.01	-0.16	0.42	0.13	0.00	0.88	0.24	-0.83
Al2O3	0.05	-0.09	-0.15	0.38	0.22	-0.07	0.64	-0.24
Fe2O3(T)	0.05	0.09	-0.40	0.30	0.71	-0.32	0.14	0.11
MnO	0.02	0.12	-0.24	-0.21	-0.11	-0.41	-0.30	0.49
MgO	0.00	0.21	-0.32	-0.17	-0.08	-0.80	-0.34	0.81
CaO	-0.01	0.13	-0.31	-0.27	-0.20	-0.77	-0.42	0.84
Na2O	-0.21	0.02	0.58	0.22	0.03	0.41	0.28	-0.51
K2O	0.20	-0.11	-0.35	0.34	0.15	-0.16	0.59	-0.11
TiO2	0.05	-0.07	-0.47	0.33	0.33	-0.42	0.45	0.13
P2O5	0.00	0.10	-0.25	0.26	0.47	-0.10	0.13	-0.03
LOI	0.00	0.16	-0.32	-0.27	-0.17	-0.80	-0.40	0.85
Sr	0.07	0.10	-0.30	-0.20	-0.11	-0.64	-0.39	0.71
Zr	0.07	-0.08	-0.33	0.32	0.17	-0.07	0.46	-0.14
Cr	-0.09	-0.06	0.43	0.03	-0.16	0.80	0.05	-0.67
Ga	0.06	-0.09	-0.28	0.42	0.28	-0.16	0.60	-0.14
Rb	0.22	-0.11	-0.41	0.36	0.15	-0.25	0.53	-0.01

Table 8. The correlation coefficients between point counts of minerals in thin sections and corresponding ICP elements. Positive correlations >0.5 are marked with blue and negative correlations <-0.6 are marked with green.

3 Results

3.1 Major elements geochemistry

The major elements in the ICP dataset were normalized to UCC average concentrations (McLennan, 2001) with results shown in Figure 12. The average composition of the PAFs diamictites stays close to UCC, with the exception of Na_2O which is depleted to ca 30% of the UCC value. The Garvellachs and Islay averages differ for CaO and MgO, which is explained by the absence of the carbonate rich d1 – d12 in Islay. The data are presented with colours shifting from red nuances in the lower diamictite up to blue at the top of Member 5. This indicates an upward increase in concentrations of SiO_2, Al_2O_3 and Na_2O and a corresponding decrease of CaO and MgO. The largest variations in concentrations are seen in CaO and Na_2O. In contrast, Si-, Al and Ti-oxides show a more modest variation which indicates a rather steady supply of detrital components.

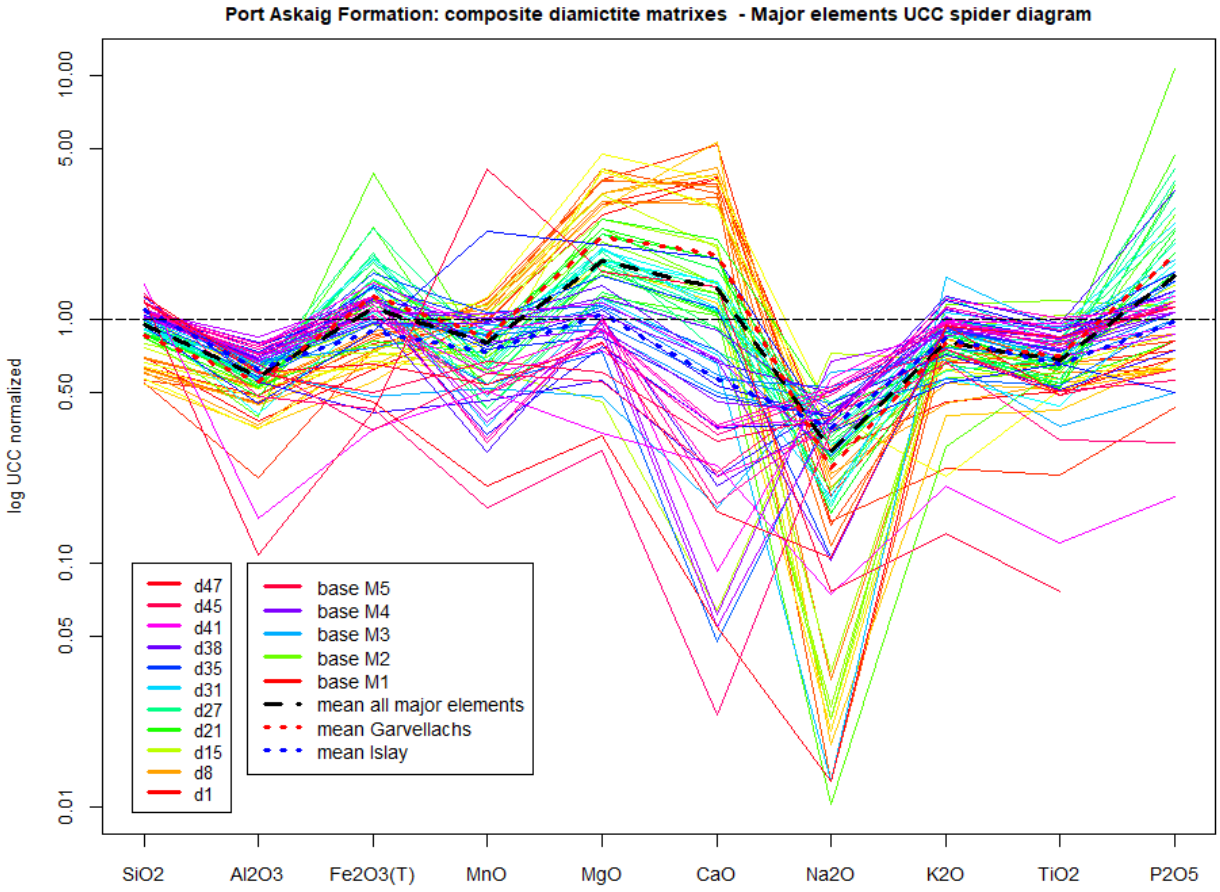

Figure 12. UCC normalized spider diagram covering major elements from the PAF diamictite matrix ICP dataset. The diamictite beds are gradational coloured from red in lower units (d1) to blue in upper units (d47). Average of Garvellachs, Islay and all samples are marked with dotted and dashed lines (see legend in plot). The vertical scale is logarithmic. UCC standard values (McLennan, 2001) are marked with a horizontal line at vertical position 1.0.

The major elements were also normalized to concentrations excluding the carbonate components CaO, MgO and LOI representing CO_2. The result was then again normalized to the UCC standard (McLennan, 2001) as seen in Figure 13 resulting in a diamictite average which stays even closer to UCC. The variation between upper and lower quartiles for major elements excluding MgO and CaO were on average reduced from 48% to 40% in the carbonate free set. However, the variation in MnO increased which indicates a connection with the carbonates.

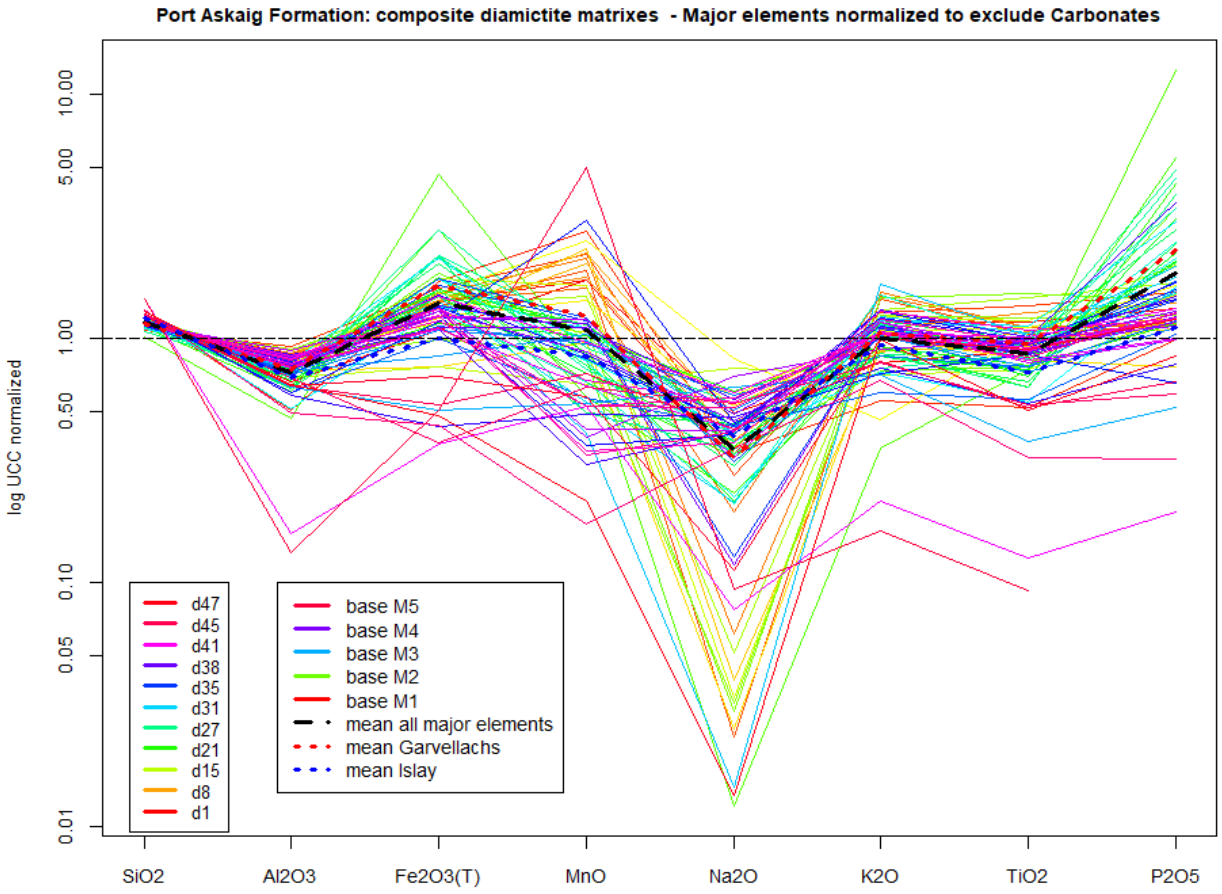

Figure 13. UCC normalized spider diagram covering major elements on a carbonate free basis. For other comments, please refer to Figure 12.

Linear correlations between major elements from the ICP dataset are given in Table 9. The absence of correlation between SiO_2 and Al_2O_3 indicates that Si-oxide is not primarily controlled by aluminosilicates but included as detrital quartz or silica cementation. The positive correlation between K_2O and Al_2O_3 suggests that K-feldspar or micas (illite and muscovite) are the primary hosts for K and Al. The negative correlation between CaO versus SiO_2 means that calcium resides in carbonates and not in siliciclastic minerals. This is further confirmed by the remarkably high correlation (r=0.95 – 0.98) between LOI and MgO respectively CaO which also indicates that the component burnt away on ignition mainly was CO_2 from the carbonates. Furthermore, correlation between CaO and MgO indicate that the carbonate primarily is dolomite. The absence of correlation between P_2O_5 and Al_2O_3 indicates that P is not associated with clays. The correlation P_2O_5 with Fe_2O_3 (T) is instead typical for late Proterozoic iron formations where oxidation of Fe(II) acts as a sink for phosphorus (Young, 2002; Hoffman & Schrag, 2002). The medium-low correlation between MnO and the carbonates indicates that manganese also is found in other minerals.

	SiO2	Al2O3	Fe2O3(T)	MnO	MgO	CaO	Na2O	K2O	TiO2	P2O5	LOI
SiO2	1.00	0.39	-0.05	-0.25	-0.94	-0.92	0.39	0.28	0.02	0.00	-0.95
Al2O3		1.00	0.17	-0.53	-0.51	-0.63	0.44	0.86	0.81	-0.02	-0.59
Fe2O3(T)			1.00	-0.18	-0.09	-0.20	-0.04	0.13	0.33	0.91	-0.18
MnO				1.00	0.35	0.37	-0.24	-0.47	-0.32	-0.18	0.37
MgO					1.00	0.90	-0.40	-0.38	-0.14	-0.10	0.95
CaO						1.00	-0.44	-0.50	-0.31	-0.17	0.98
Na2O							1.00	0.08	0.11	-0.10	-0.47
K2O								1.00	0.78	-0.07	-0.45
TiO2									1.00	0.11	-0.24
P2O5										1.00	-0.17
LOI											1.00

Table 9. Internal correlation coefficients between major elements from the PAF diamictite matrix ICP dataset. Positive correlations >0.7 are marked with blue and negative correlations <-0.7 are marked with yellow.

Several of the major elements in the ICP dataset do not have a normal (Gauss) distribution. This may impact the validity of parametric statistical comparisons of e g ANOVA type. Figures 14 – 17 show normal quantile plots for four examples: SiO_2, Al_2O_3, CaO and K_2O. CaO has a right-skewed distribution, Al_2O_3 a left-skewed distribution, SiO_2 has a more uniform ("fat tailed") distribution than a normal distribution and only K_2O shows a reasonable closeness to a normal distribution.

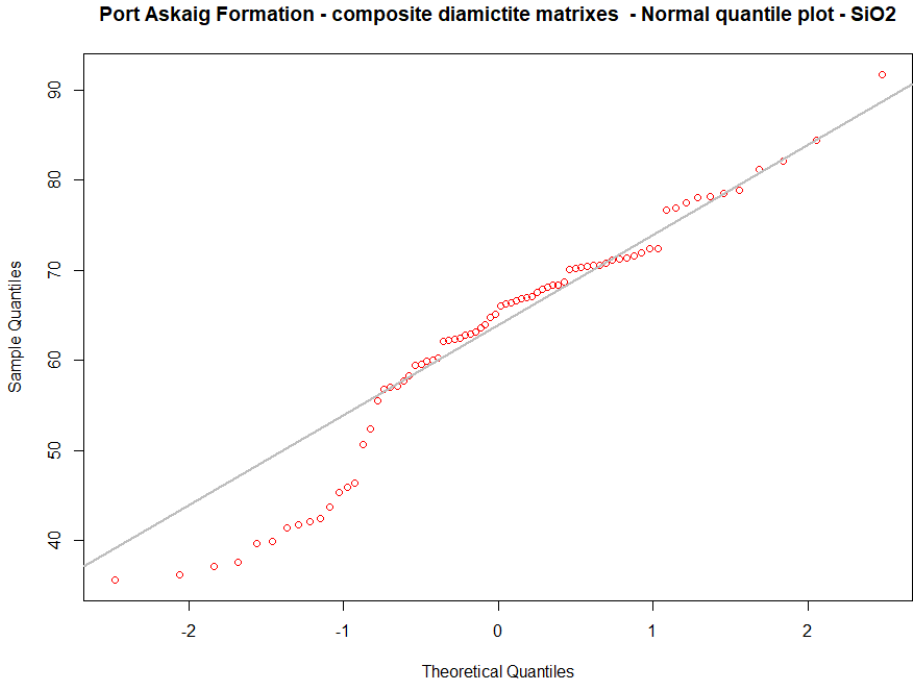

Figure 14. Test if SiO_2 follows a normal distribution. Simulated normal quantile data (theoretical quantiles) are plotted versus actual sample data (sample quantiles). A variable with a perfect normal (Gauss) distribution plots on a straight line. Data staying above the straight line in both upper and bottom parts indicates a right-skewed distribution while data staying below the line in both upper and bottom parts indicate a left-skewed distribution. Data staying below the line in the bottom part and above in the upper part indicates that the distribution contains "fatter tails" than a normal distribution.

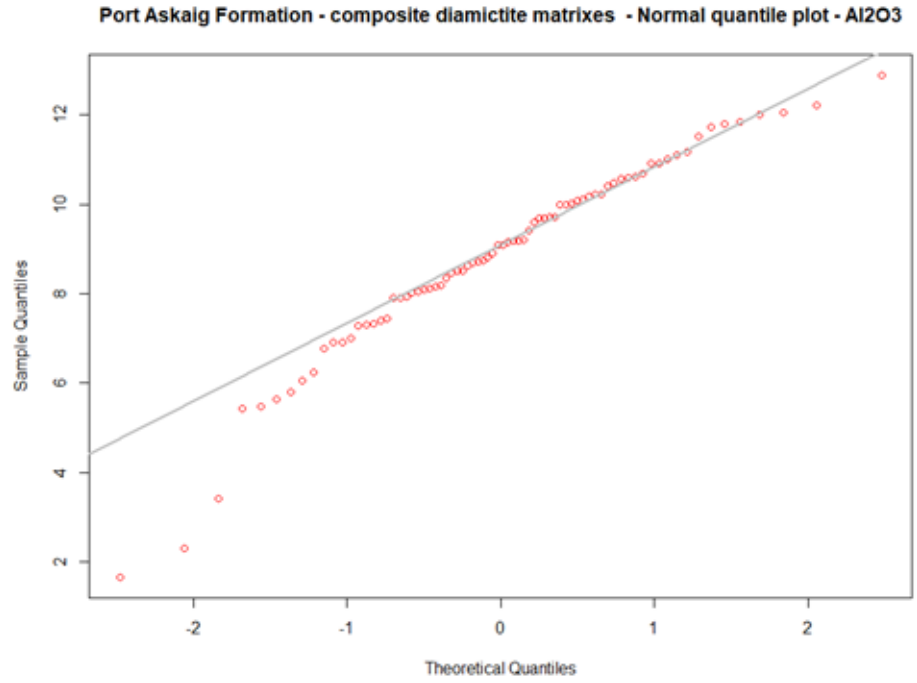

Figure 15. Test if Al_2O_3 follows a normal distribution. For comments, please refer to Figure 14.

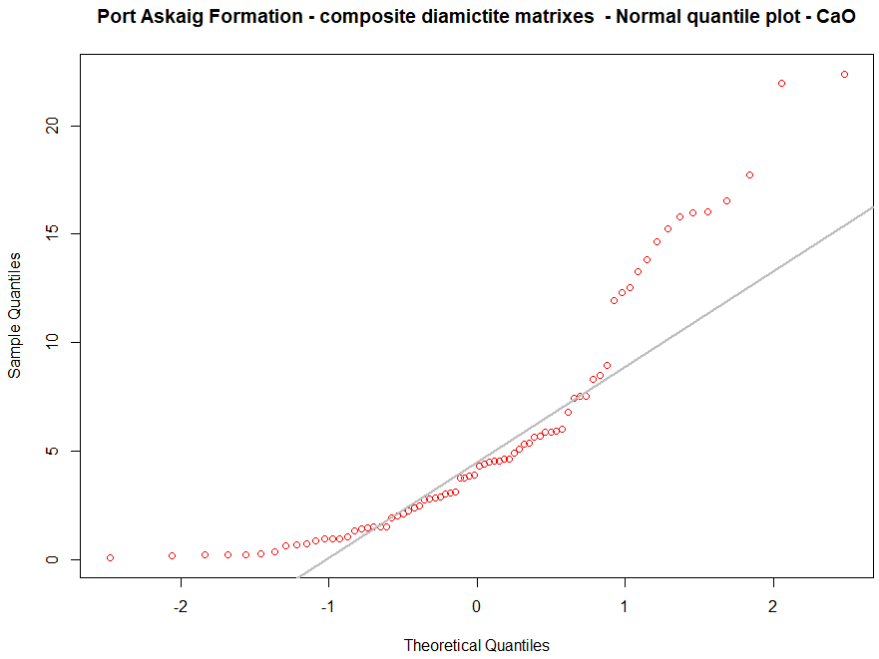

Figure 16. Test if CaO follows a normal distribution. For comments, please refer to Figure 14.

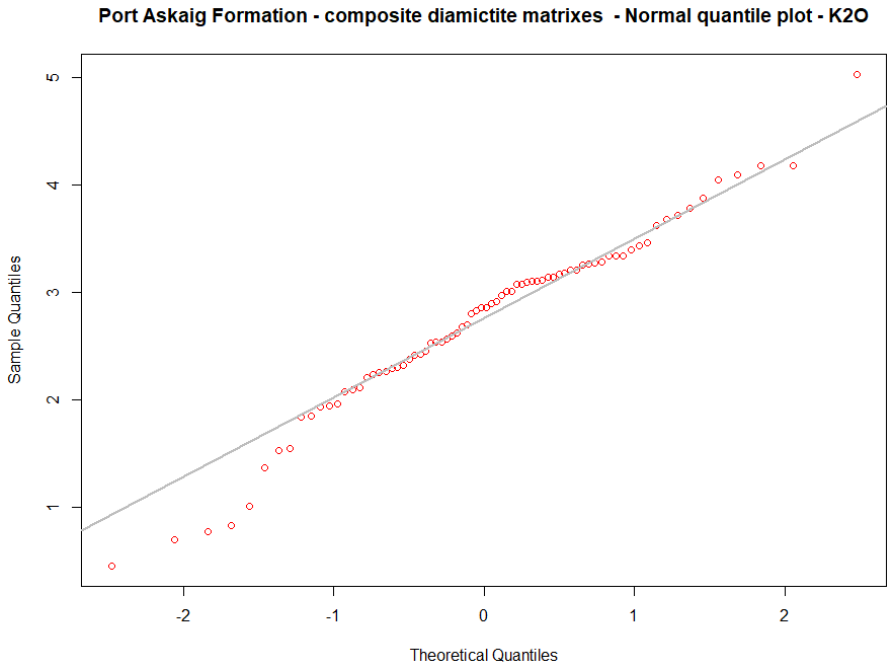

Figure 17. Test if K_2O follows a normal distribution. For comments, please refer to Figure 14.

To avoid uncertainty from non-Gaussian distributions, non-parametric rank-tests were used to compare the major element's distribution for different members in the PAF. The Kruskal-Wallis test (the non-parametric equivalent of ANOVA) was used to simultaneously compare distributions between all five members, while Mann-Whitney tests (the non-parametric equivalent of two-sample t-test) were used to compare individual members. The p-values given in Figures 18 – 27 indicate the probability that the concentrations of respective major element originate from the same source or from the same deposition process and that differences seen therefore can be attributed to pure chance. The Kruskal-Wallis p-value is exceptionally low for all elements except K_2O and TiO_2 and it can therefore with surety be ascertained that the geochemical compositions of all members cannot have the same joint source or process origin. Furthermore, the Mann-Whitney p-values generally indicate low probability that the diamictite matrix for individual members share the same

distribution. However, again K_2O and TiO_2 seem to be the exception which will be further discussed in section 4.1.

The variance in wt% within and between members and occurrence of outliers are also shown in the box-plots in Figures 18 – 27. SiO_2 gradually increases from low concentrations in M1 to a maximum in M5 while Al_2O_3 reaches its maximum in M4 and Fe_2O_3 together with P_2O_5 in M2. MgO and CaO gradually decrease from their maximums in M5 and MnO, Na_2O, K_2O and TiO_2 have less clear trend-patterns.

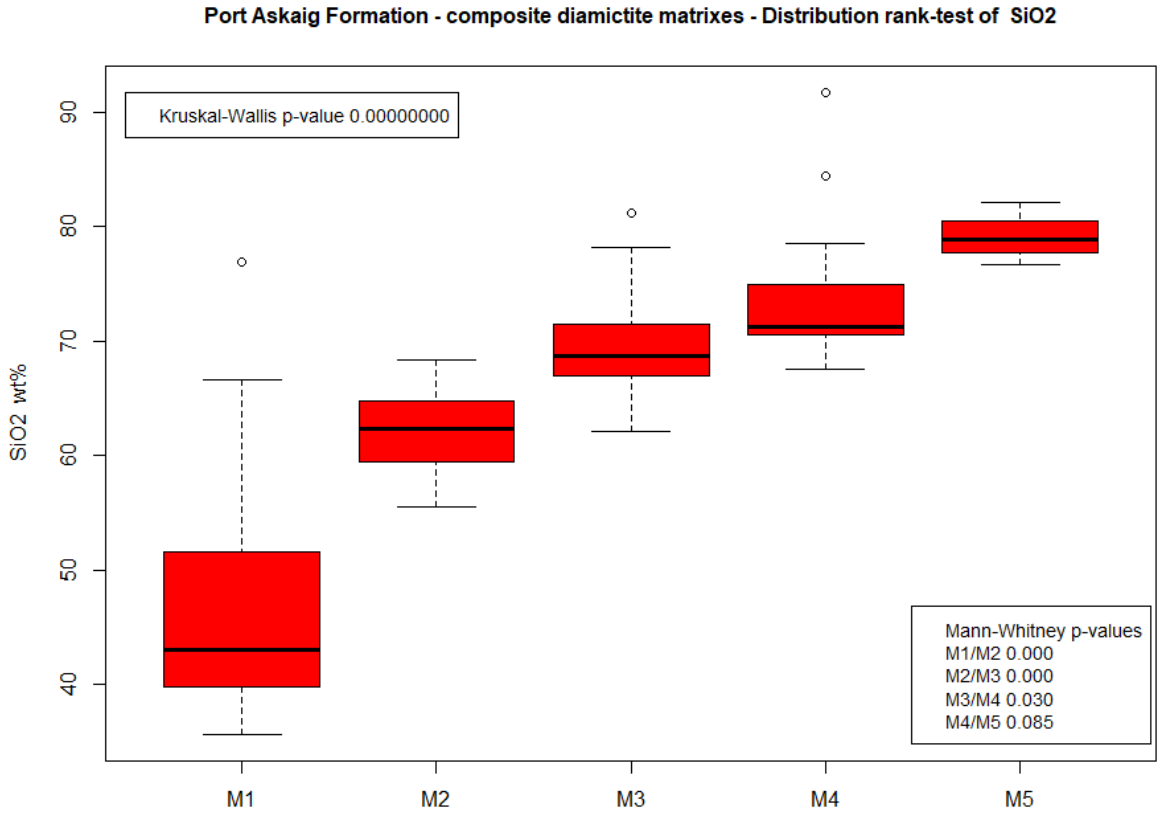

Figure 18. Kruskal-Wallis and Mann-Whitney rank-tests of SiO_2 distribution. The distribution for each member is shown in a box-and-whisker plot (for description of box-and-whisker plots, please refer to Figure 11). The Kruskal-Wallis rank test simultaneously compares distributions between all five members. The Kruskal-Wallis p-value indicates the probability that the concentrations of the tested element have the same distribution and thus originate from the same distribution source or deposition process. Mann-Whitney rank test compares the distribution for pairs of members and its p-value indicates the probability that individually compared members have the same distribution.

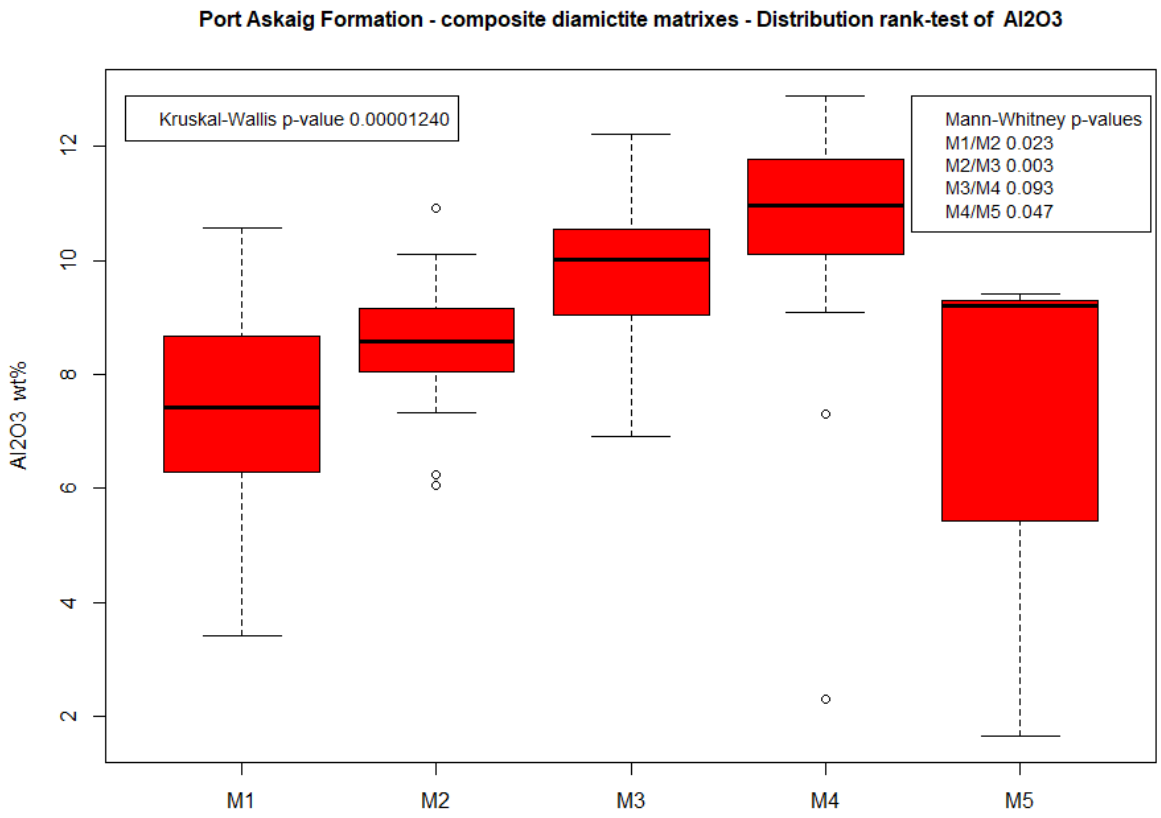

Figure 19. Kruskal-Wallis and Mann-Whitney rank-tests of Al_2O_3 distribution. For comments regarding box-and-whisker plots please refer to Figure 11 and for rank test to Figure 18.

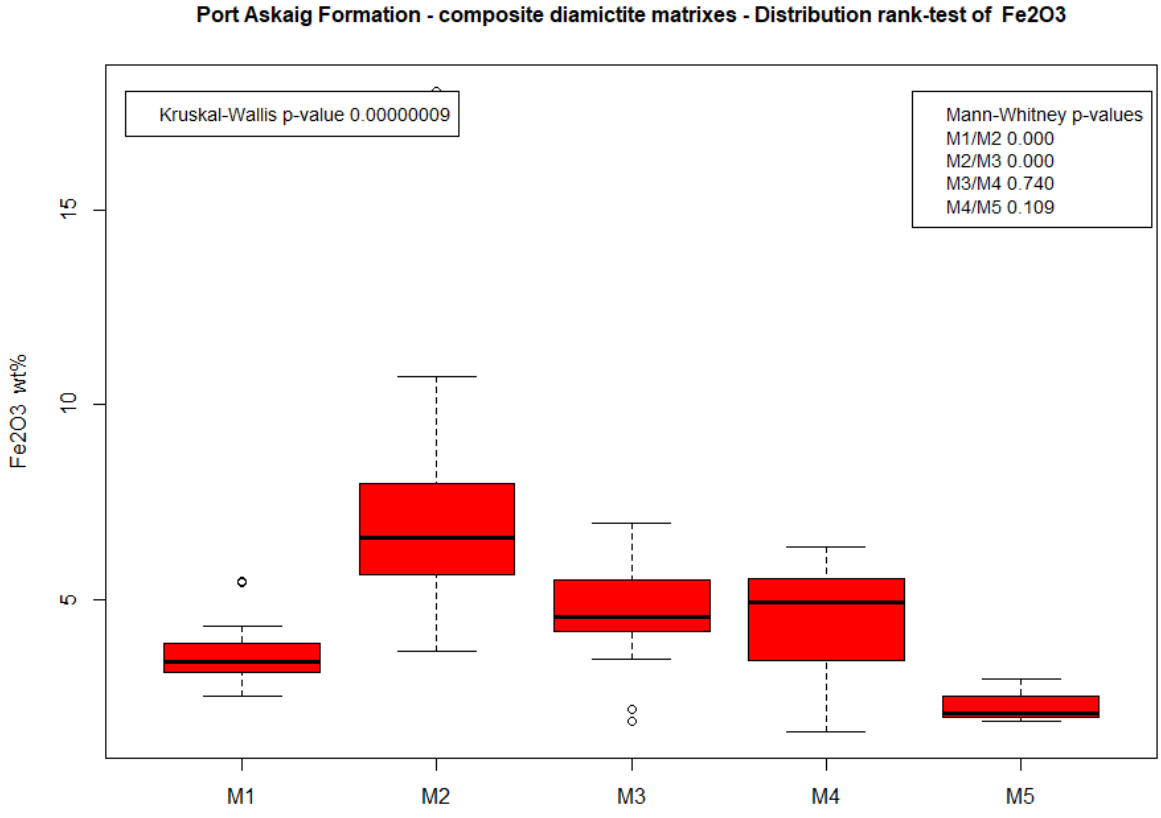

Figure 20. Kruskal-Wallis and Mann-Whitney rank-tests of Fe_2O_3 distribution. For comments regarding box-and-whisker plots please refer to Figure 11 and for rank test to Figure 18.

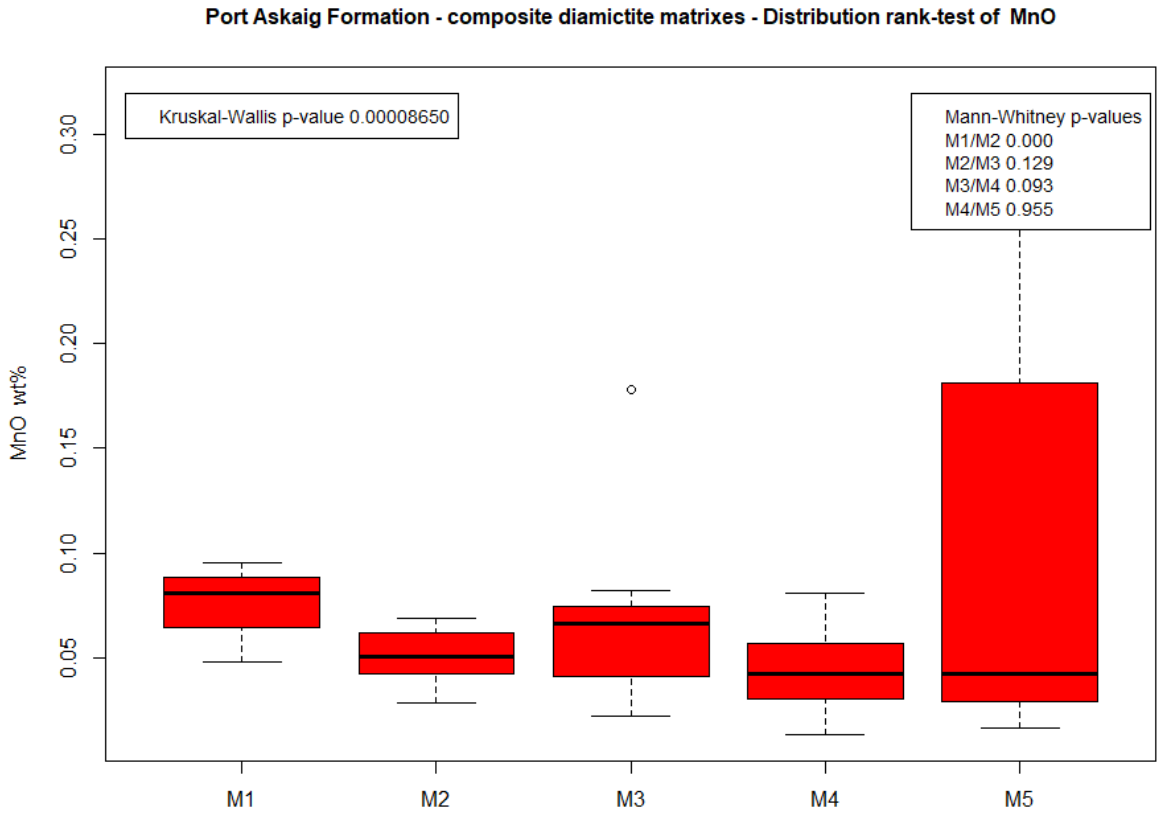

Figure 21. Kruskal-Wallis and Mann-Whitney rank-tests of MnO distribution. For comments regarding box-and-whisker plots please refer to Figure 11 and for rank test to Figure 18.

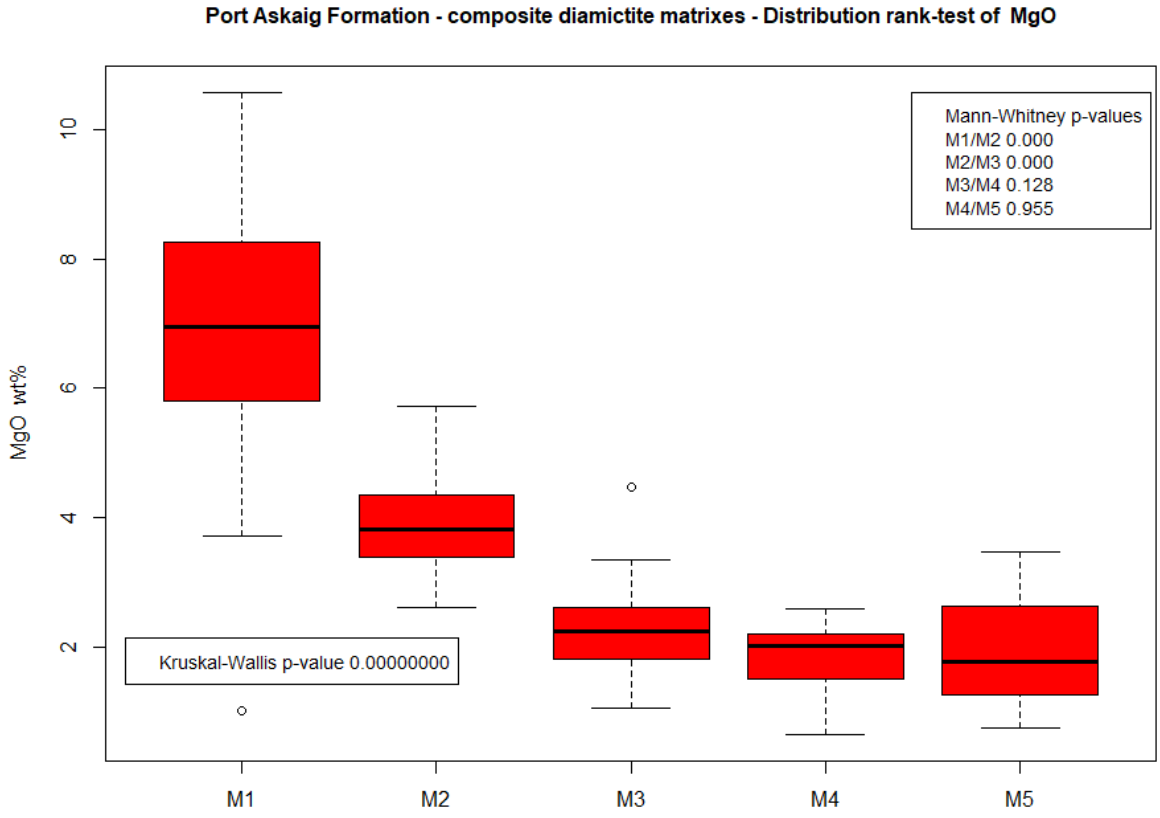

Figure 22. Kruskal-Wallis and Mann-Whitney rank-tests of MgO distribution. For comments regarding box-and-whisker plots please refer to Figure 11 and for rank test to Figure 18.

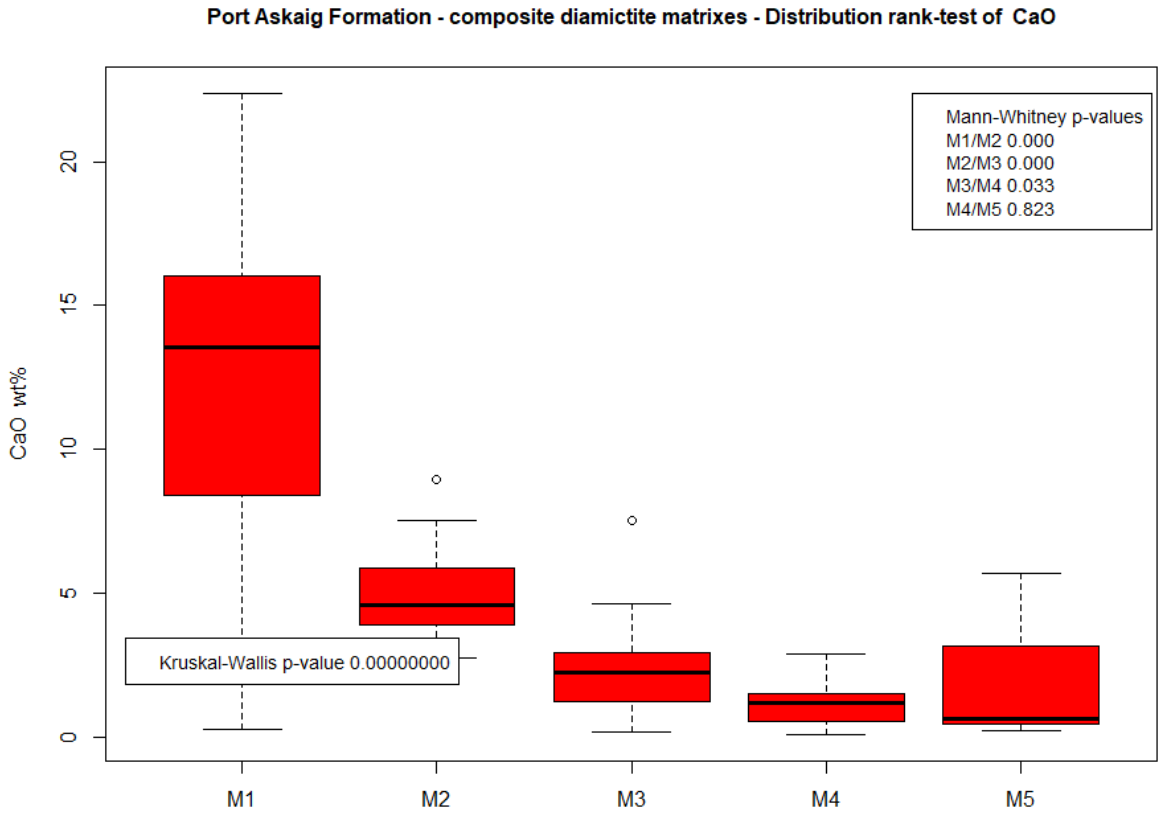

Figure 23. Kruskal-Wallis and Mann-Whitney rank-tests of CaO distribution. For comments regarding box-and-whisker plots please refer to Figure 11 and for rank test to Figure 18.

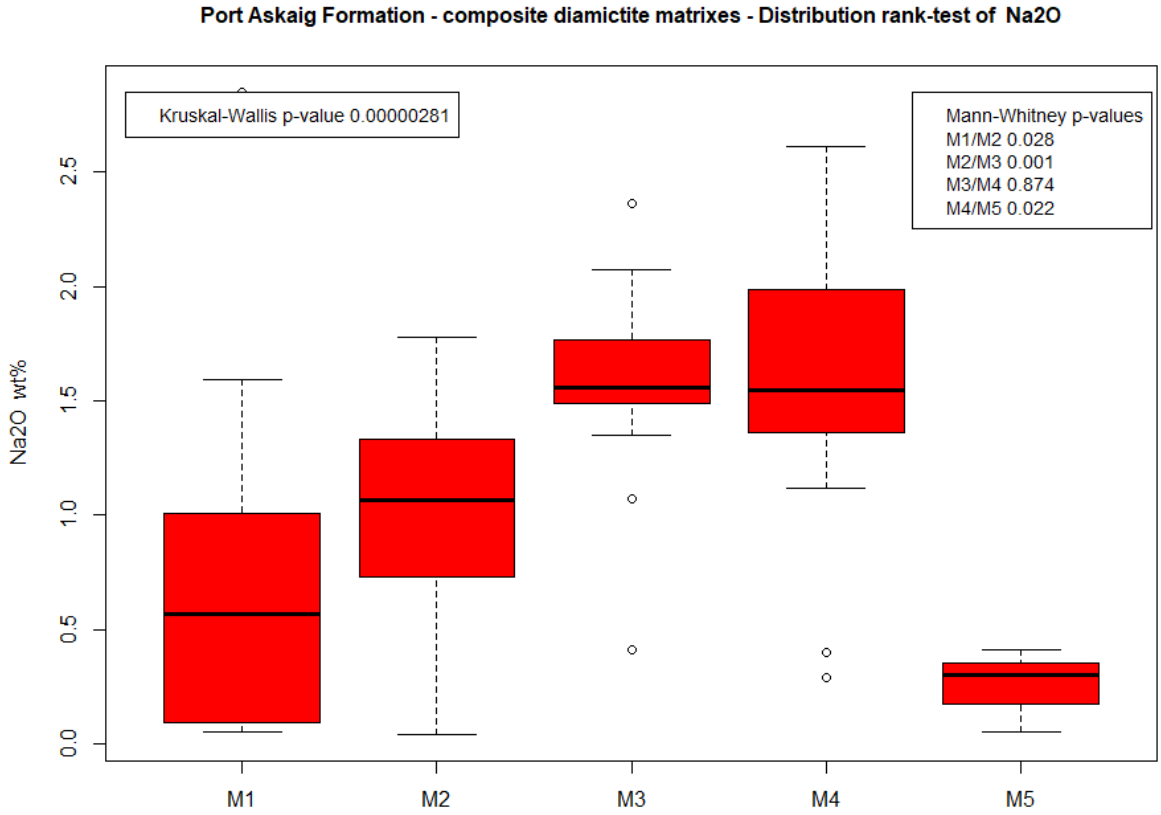

Figure 24. Kruskal-Wallis and Mann-Whitney rank-tests of Na_2O distribution. For comments regarding box-and-whisker plots please refer to Figure 11 and for rank test to Figure 18.

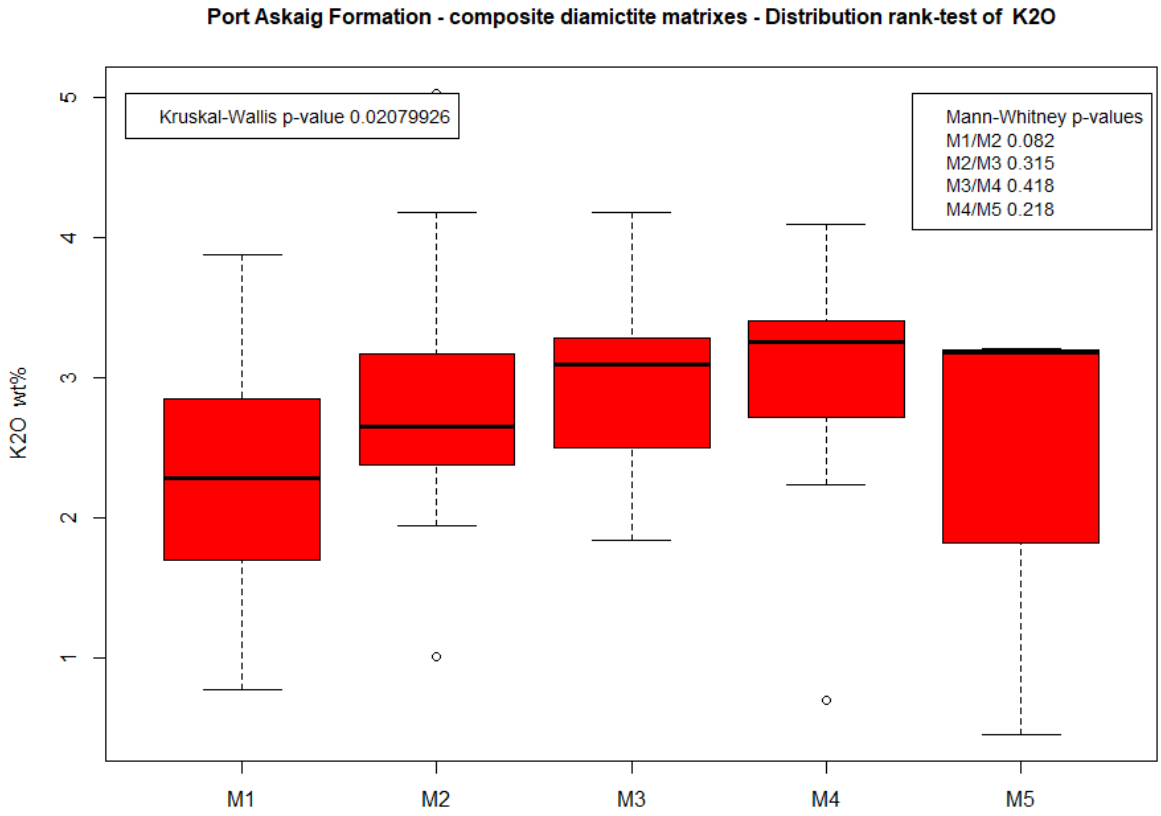

Figure 25. Kruskal-Wallis and Mann-Whitney rank-tests of K_2O distribution. For comments regarding box-and-whisker plots please refer to Figure 11 and for rank test to Figure 18.

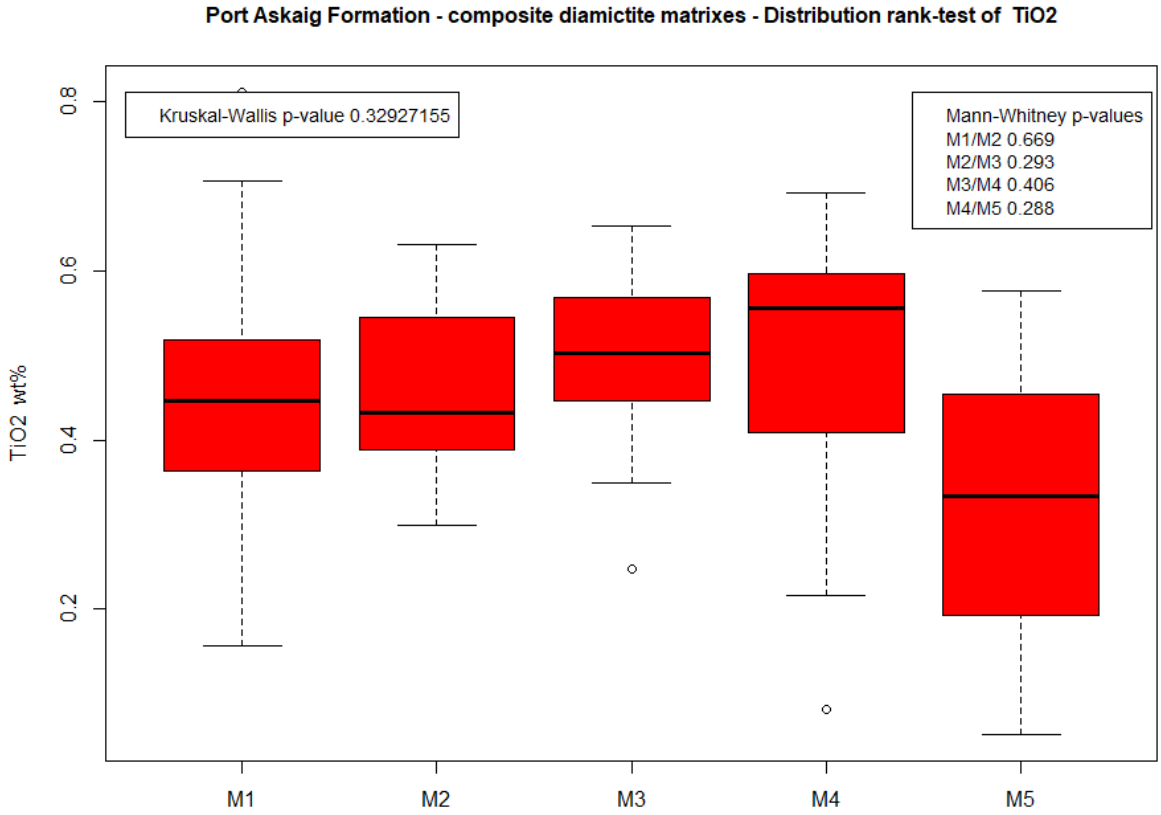

Figure 26. Kruskal-Wallis and Mann-Whitney rank-tests of TiO_2 distribution. For comments regarding box-and-whisker plots please refer to Figure 11 and for rank test to Figure 18.

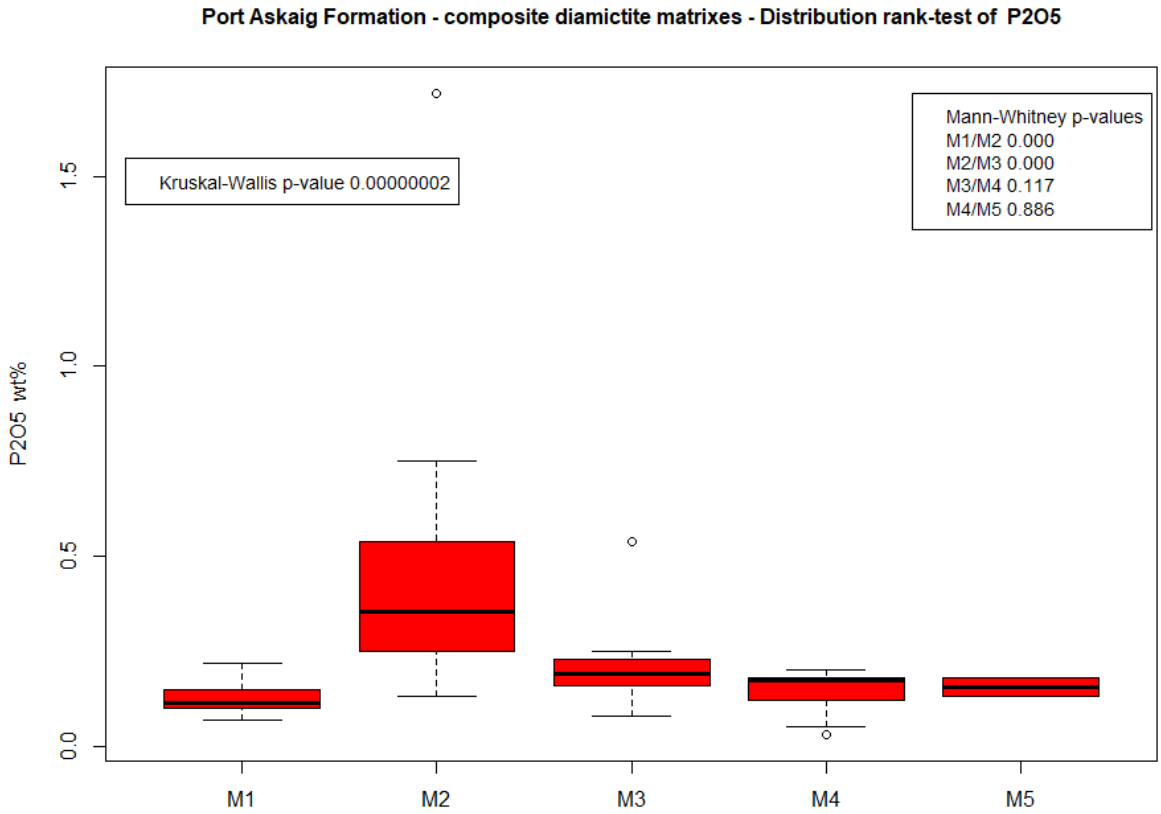

Figure 27. Kruskal-Wallis and Mann-Whitney rank-tests of P_2O_5 distribution. For comments regarding box-and-whisker plots please refer to Figure 11 and for rank test to Figure 18.

A principal component analysis (PCA) was done on the major elements, converting the dataset into a system of new artificial orthogonal (i.e. linearly uncorrelated) variables. The scree plot of the variances in the dataset (Figure 28) shows that the first five principal components account for 97%, while the remaining components each account for 1% or less. The principal loadings of the first six components (Table 10) give the conclusion that PC1 is controlled by carbonate/silicate ratios, PC2 is dominated by quartz versus Fe-, P- and Ti-oxides, while Fe- and P-oxides operate against detrital Al, K and Ti elements in PC3. Sodium respectively manganese controls PC4 and PC5 but falls below the threshold in Figure 28 and have thus low explanatory values. Based on this the PC1 is interpreted as showing the main PAF trend with a gradual replacement of carbonates by siliciclastic material, PC2 showing the influence of quartz sand versus silt, while PC3 shows the inclusion of the non-detrital Fe (which is discussed in section 4.1.1).

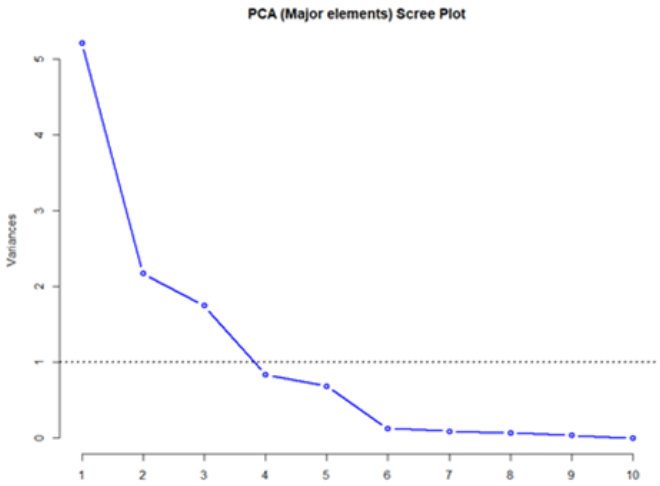

Figure 28. Scree plot showing principal components variances generated from a major elements PCA on correlations. The principal components are ordered according to their explanatory value (variance shown on the y-axis) in falling order. The most significant components are those with the highest values. The components above a certain threshold or an interpreted "elbow" in the plot are typically retained for further analysis. The horizontal line indicates one possible selection criteria called the Kaiser rule where only components with variance > 1 are retained.

	PC1	PC2	PC3	PC4	PC5	PC6
SiO2	0.35	-0.35	-0.16	0.19	0.03	-0.13
Al2O3	0.36	0.21	0.32	-0.10	-0.12	0.07
Fe2O3.T.	0.11	0.48	-0.47	-0.04	-0.17	0.20
MnO	-0.24	-0.19	-0.08	0.35	-0.86	0.15
MgO	-0.38	0.24	0.16	-0.15	-0.05	0.01
CaO	-0.41	0.14	0.13	-0.12	0.07	0.08
Na2O	0.22	-0.19	0.04	-0.84	-0.35	0.15
K2O	0.30	0.26	0.38	0.27	0.04	0.67
TiO2	0.23	0.44	0.33	0.08	-0.30	-0.66
P2O5	0.08	0.41	-0.57	-0.05	0.02	-0.01
LOI	-0.41	0.18	0.16	-0.09	0.04	0.03

Table 10. List of principal components from PCA of major elements with their respective loadings. Loadings state how much of each of the original variables goes into each principal component. Loadings are also called eigenvectors.

When projecting the main variables onto a PC1/PC2 two-dimensional diagram (Figure 29), the same correlation emerges: Ca and Mg representing the carbonates show up in IV quadrant opposite to SiO2 in the II quadrant. Fe with its partner P appears together with detrital components Al, K and Ti in the I quadrant. The Na and Mn arrows have short lengths when projected on the PC1/PC2 plane since they mainly belong in the two perpendicular components PC4 and PC5.

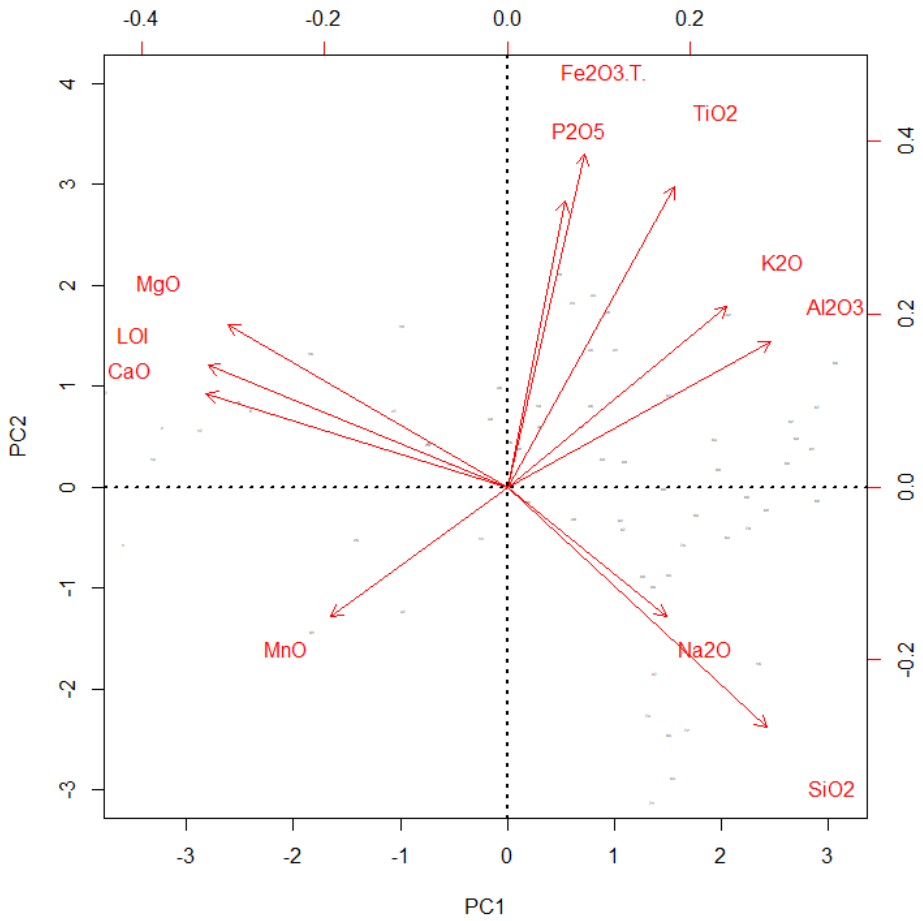

Figure 29. Projection of the main elements onto a PC1/PC2 two-dimensional biplot. The left and bottom scales refer to scores (e.g. a high PC1 score indicate that a variable can be characterized as "PC1-ish") and right and top scales refer to loadings (the amount of the original variable that goes into each principal component). Variables whose arrows point in the same direction tend to be correlated. Note that PC3 scores are not seen in this plot since PC3 is orthogonal to PC1 and PC2 and variables with high PC3 scores can thus not be distinguished here.

Figures 30 – 33 show the trends of the major elements over the stratigraphic height of the diamictite beds. The five members have approximately the same thicknesses but contain varying number of diamictites with 18 beds in M1 and only 3 in M5, which is also reflected in the density of data points.

The following general observations are noted regarding the trends of the major elements and LOI:

- The SiO_2 concentration jumps up after the Disrupted Beds and then continues to gradually increase.
- Al_2O_3 show a gradual increase but with large intrabed variations.
- Fe_2O_3 and P_2O_5 are both added to the system as from the Disrupted Beds.
- MnO has a sharp peak just above the Disrupted Beds but otherwise shows a gradual slow decrease.
- The carbonate elements CaO, MgO and LOI have the same pattern with high levels in M1, steep decreases within M2 and then lower concentrations throughout M3 to M5.
- K_2O, TiO_2 and Na_2O all show large intrabed variations and do not display distinct trends over the 5 members.

The trends of the major elements follow as expected the trends of the lithologies, with a stepwise replacement of carbonates by granitic materials in the diamictite matrixes. Several trend-shifts or irregularities can be seen at the level of the Great Breccia / the Disrupted Beds (SiO_2, Fe_2O_3, P_2O_5, Na_2O, CaO, MgO, LOI) and when entering M5 (Fe_2O_3, Al_2O_3, Na_2O).

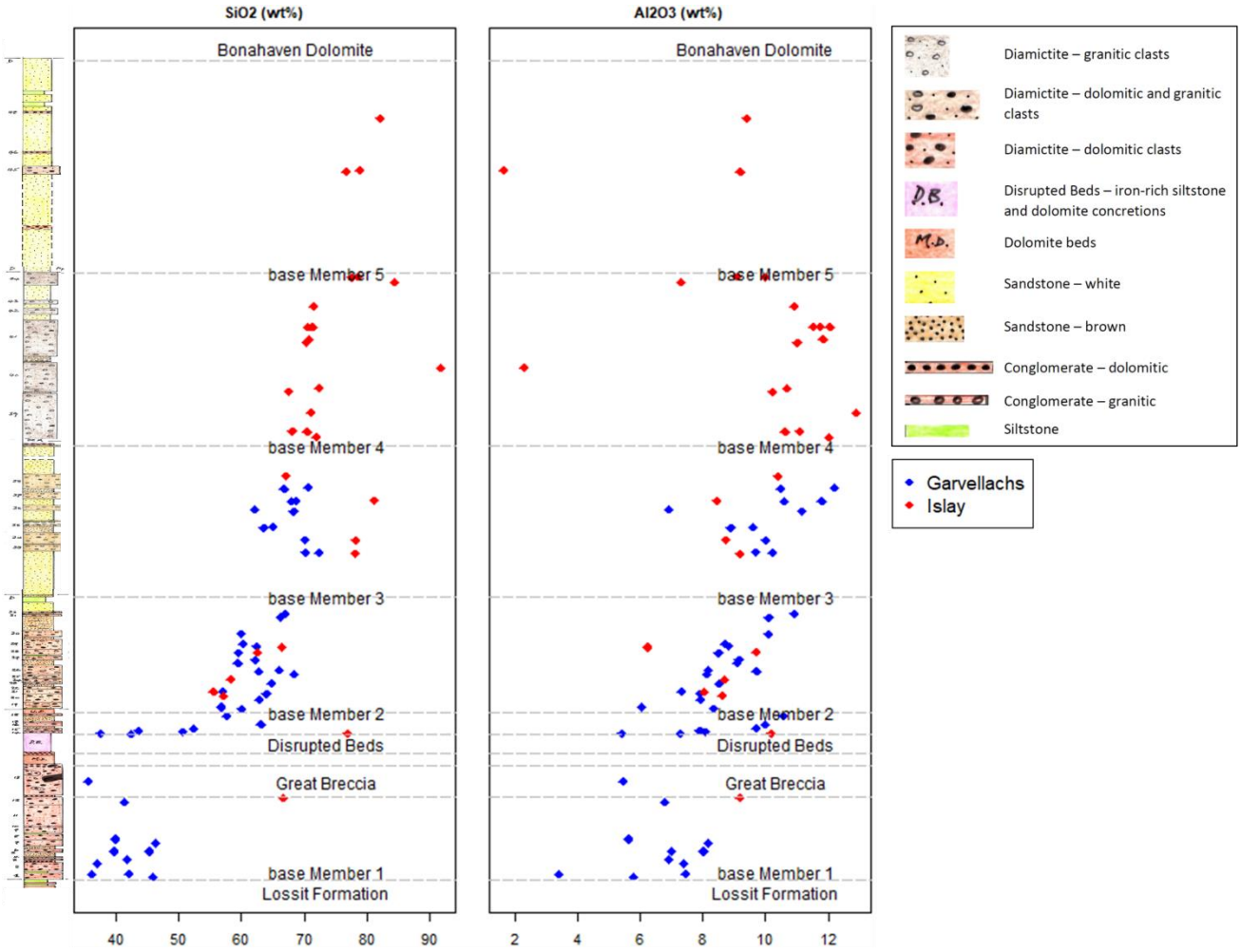

Figure 30. SiO_2 and Al_2O_3 trends over the PAFs stratigraphic column, from diamictite matrix ICP data. The wt% concentration of each element is given on the horizontal scale. The stratigraphic column with legend was prepared by A. Spencer from field observations in the Garvellachs (Member 1 – 3) and Islay (Member 4 – 5) and received in personal communication, January 2020. The legend indicates the composition of the beds in the PAF. Data from Garvellachs samples are marked blue and Islay red.

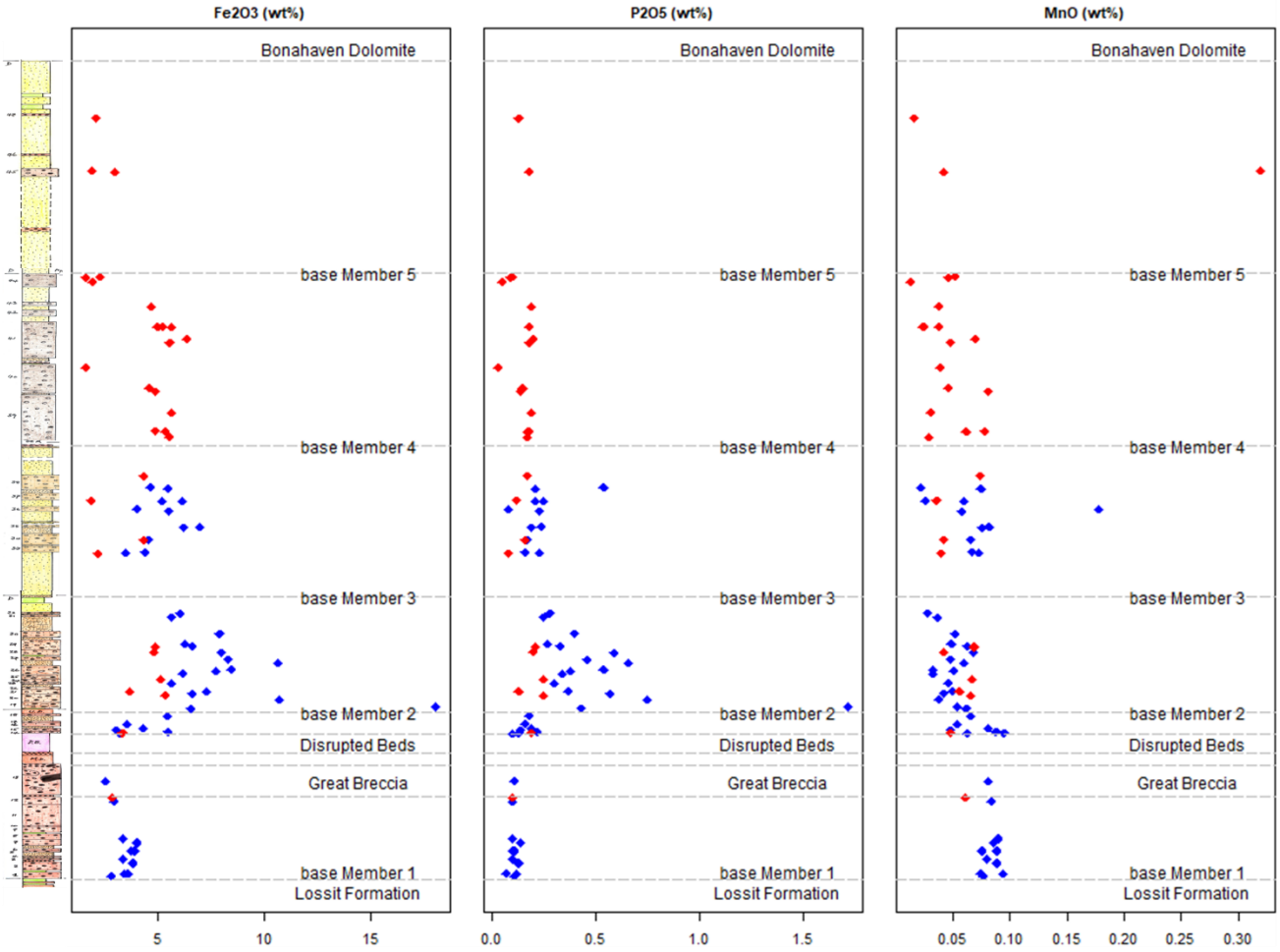

Figure 31. Fe_2O_3, P_2O_5 and MnO trends over the PAFs stratigraphic column, from diamictite matrix ICP data. For further comments, please refer to Figure 30.

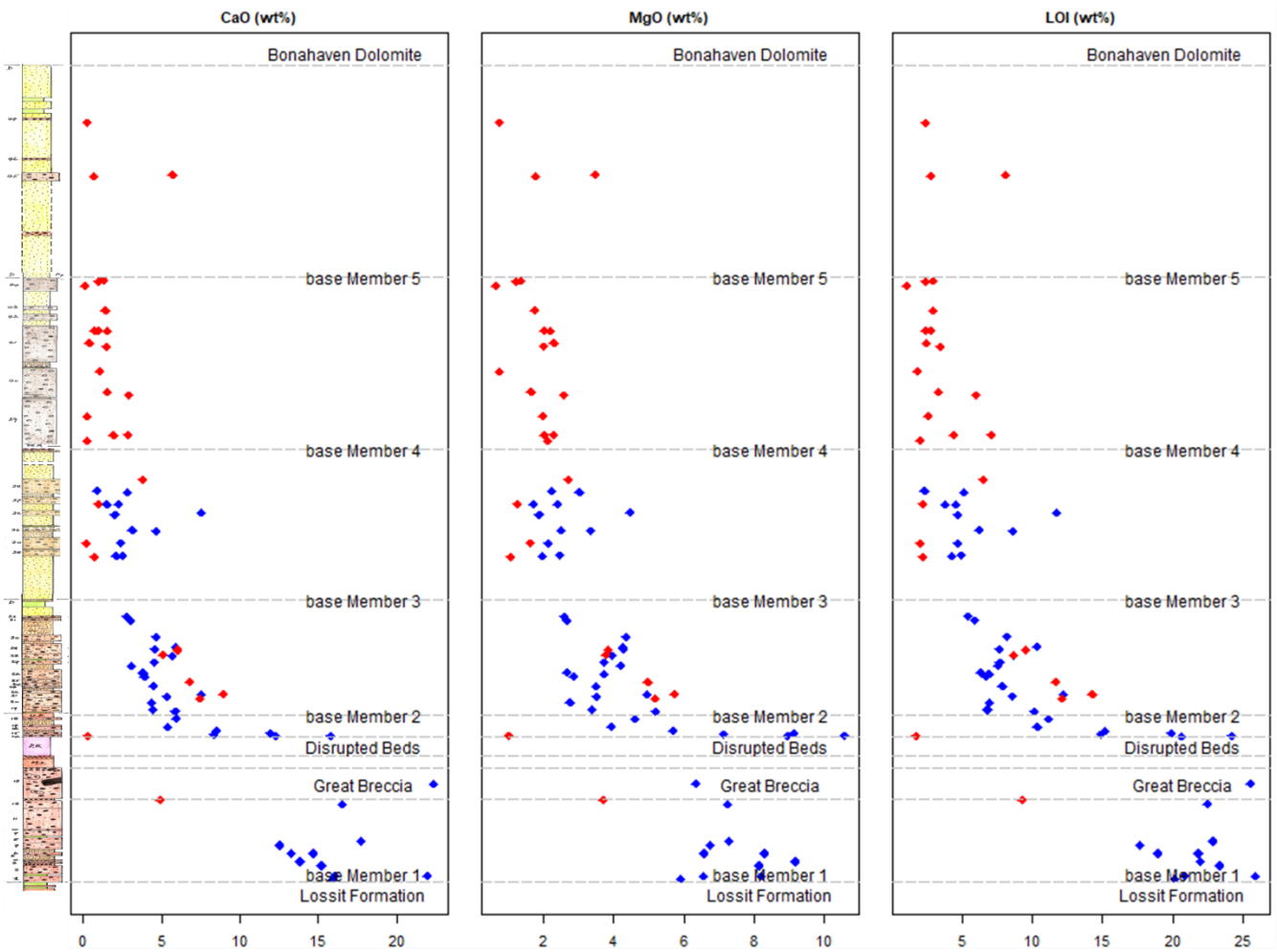

Figure 32. CaO, MgO and LOI trends over the PAFs stratigraphic column, from diamictite matrix ICP data. For further comments, please refer to Figure 30.

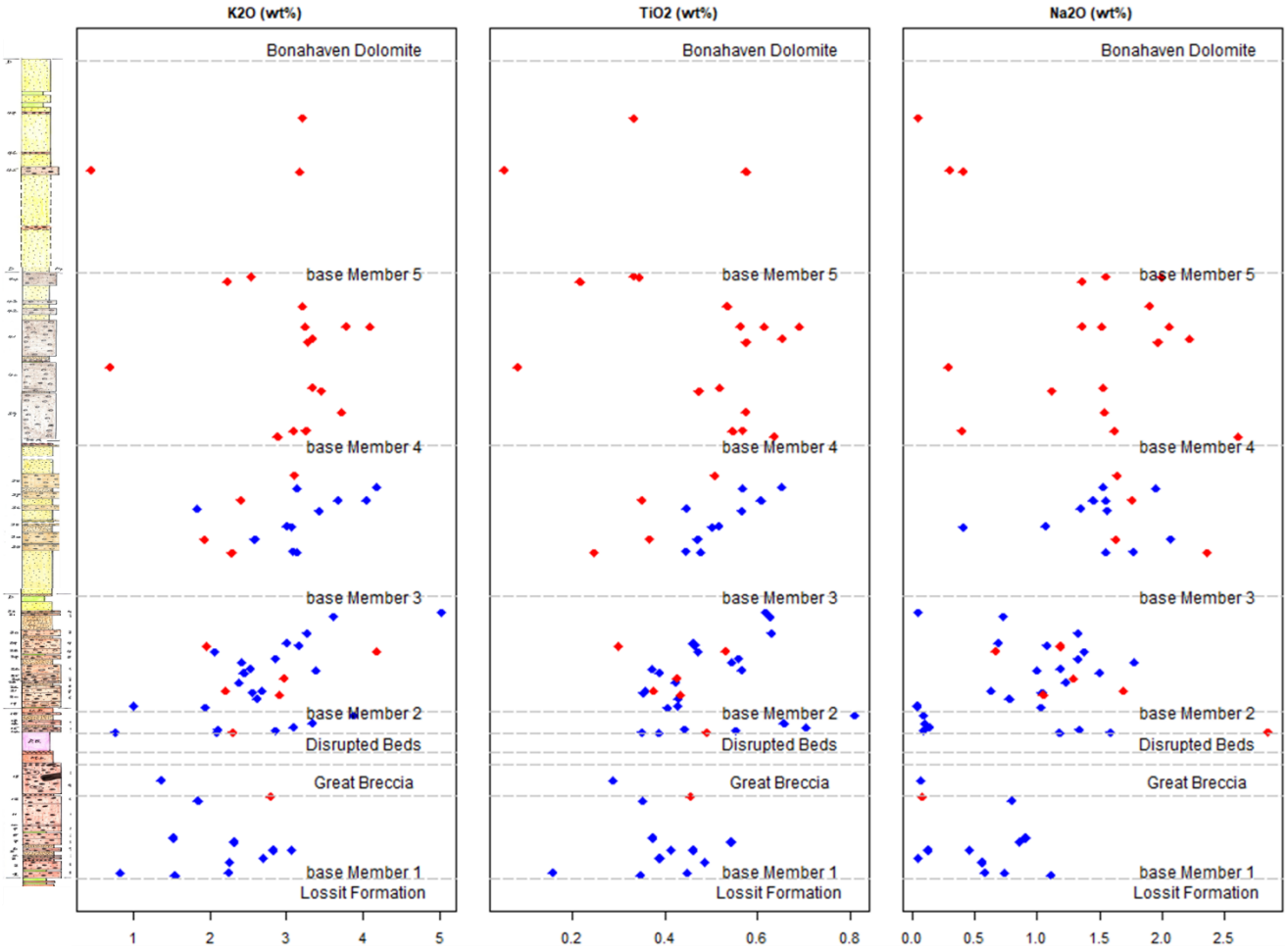

Figure 33. K_2O, TiO_2 and Na_2O trends over the PAFs stratigraphic column, from diamictite matrix ICP data. For further comments, please refer to Figure 30.

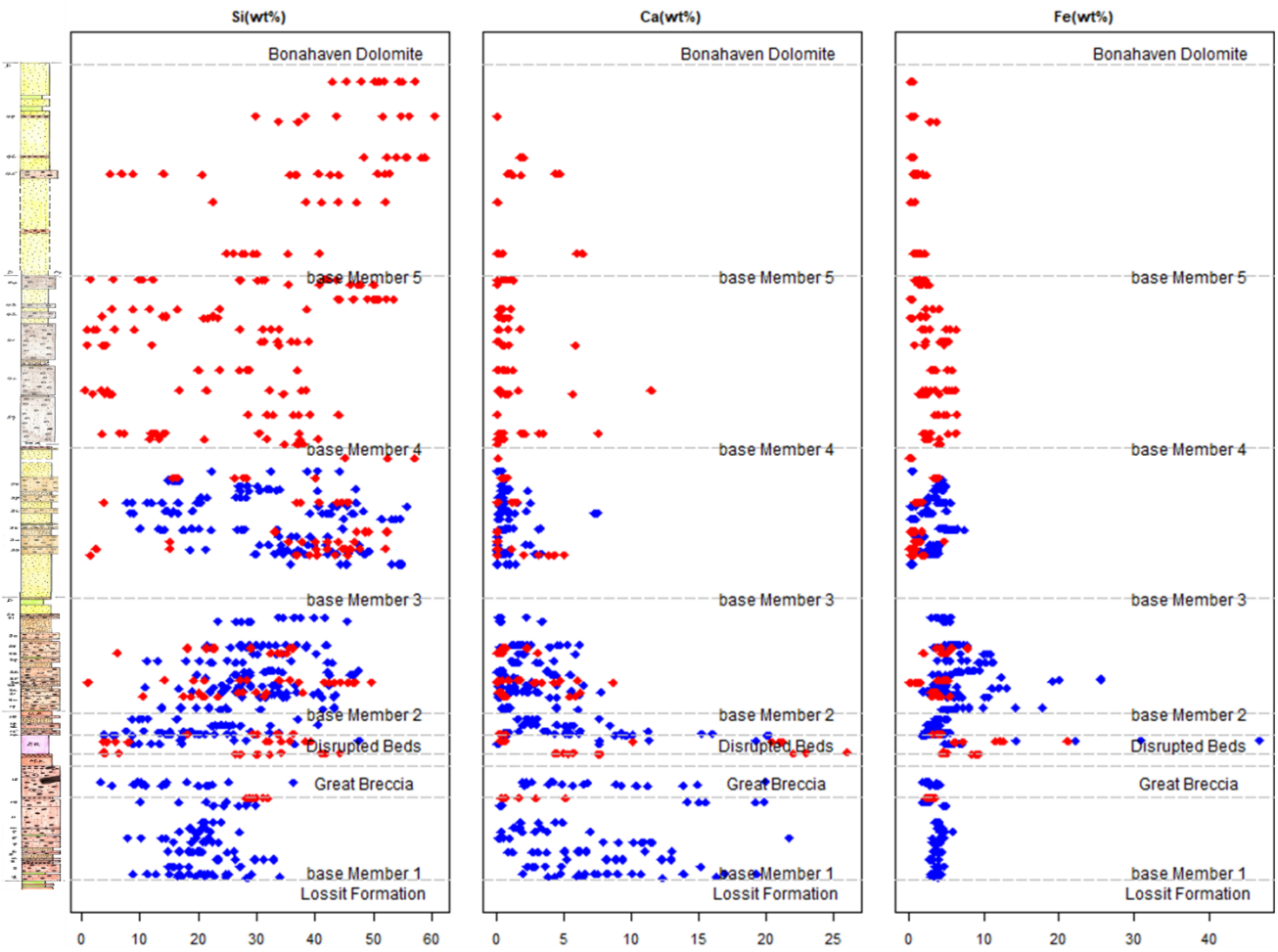

Figure 34. Si, Ca and Fe trends over the PAFs stratigraphic column, from diamictite matrix XRF data normalized to exclude Cl. The number of XRF readings are higher than in the ICP dataset but also contain a higher variability i.a. due to high proportions of undetected elements (LE). Therefore, the plotted readings shall be interpreted as "painting" a solid base and the trend can be inferred from the uppermost value at each stratigraphic level. For other comments regarding the plot, please refer to Figure 30.

Figure 34 shows the XRF dataset trends for Si, Ca and Fe, which are the major elements in this dataset with the best reliability. Similar patterns as for the ICP data can also be distinguished here, with a step-wise increase of Si after the Disrupted Beds and again in M5, high Ca concentrations in M1 and declining throughout M2, and higher levels of Fe from the Disrupted Beds and within M2.

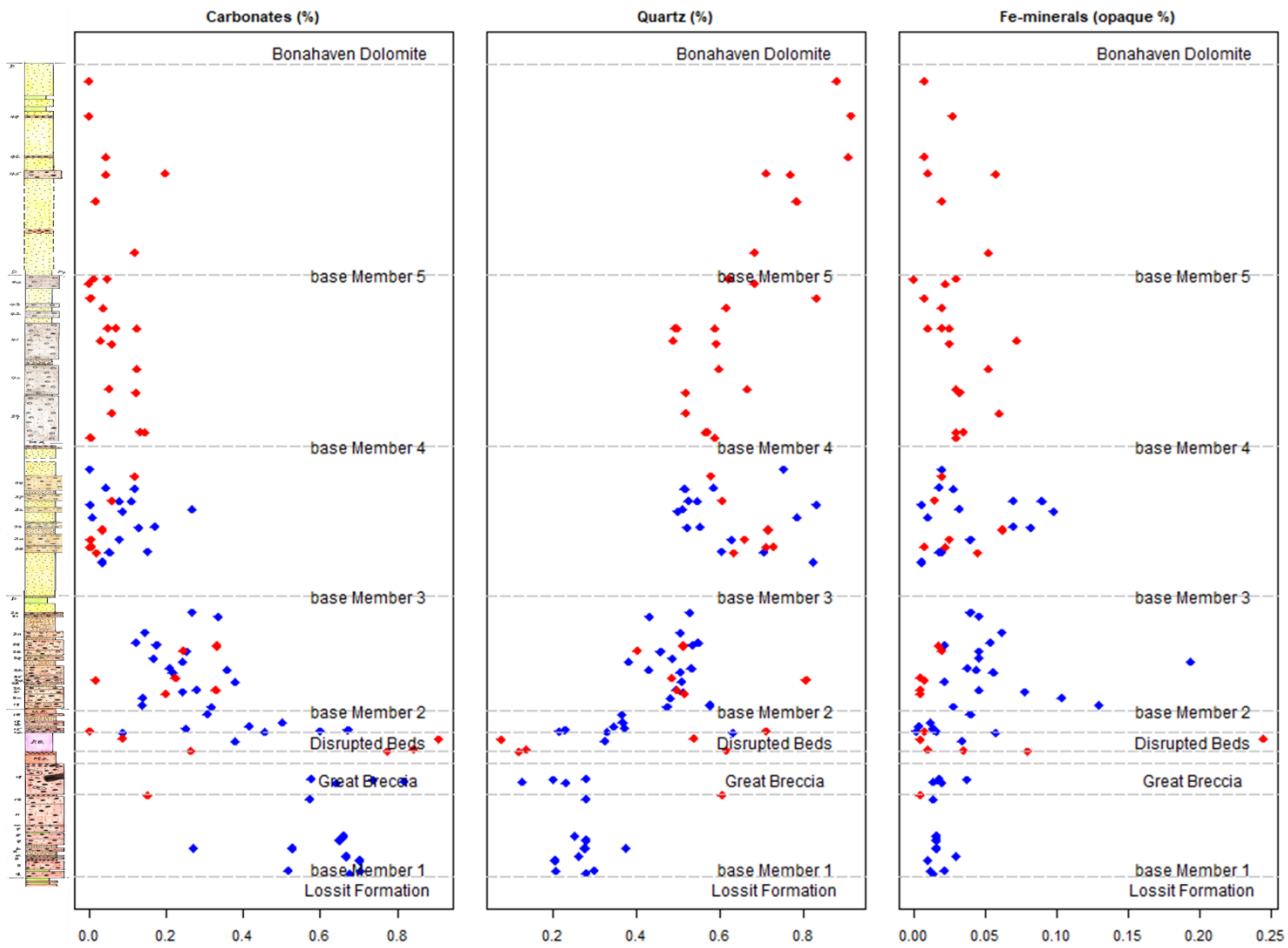

Figure 35. Carbonates, quartz and Fe-minerals (hematite, magnetite and pyrite) trends over the PAFs stratigraphic column, from the point count data from thin sections. The horizontal scale indicates the relative proportions of each lithology from 0.0 to 1.0. For other comments regarding the plot, please refer to Figure 30.

Figure 35 shows the percentage trends of carbonate-, quartz- and opaque Fe-bearing minerals in the PAF based on point-counted lithologies in thin sections. The patterns of these trends correspond to the ICP dataset trends for LOI (where carbonates are common in M1 and decline throughout M2), SiO_2 (where quartz has a step-wise increase after the Disrupted Beds and again in M5) and Fe_2O_3 (where opaque Fe-minerals are more abundant from the Disrupted Beds and within M2).

3.2 Rare earth elements geochemistry

The rare earth elements (REE) including yttrium in the ICP dataset were normalized to UCC average concentrations (McLennan, 2001) with results shown in Figure 36. The average REE + Y content in the PAF diamictites is close to UCC, indicating a detrital source. In the lower part of the chart a few negative outliers can be seen which primarily come from silica-rich beds high up in the sequence (d33, d34, d41, d44 and d45). The Garvellachs averages are somewhat above Islay's but this is explained by the said negative outliers in the higher diamictite beds which all are in Islay.

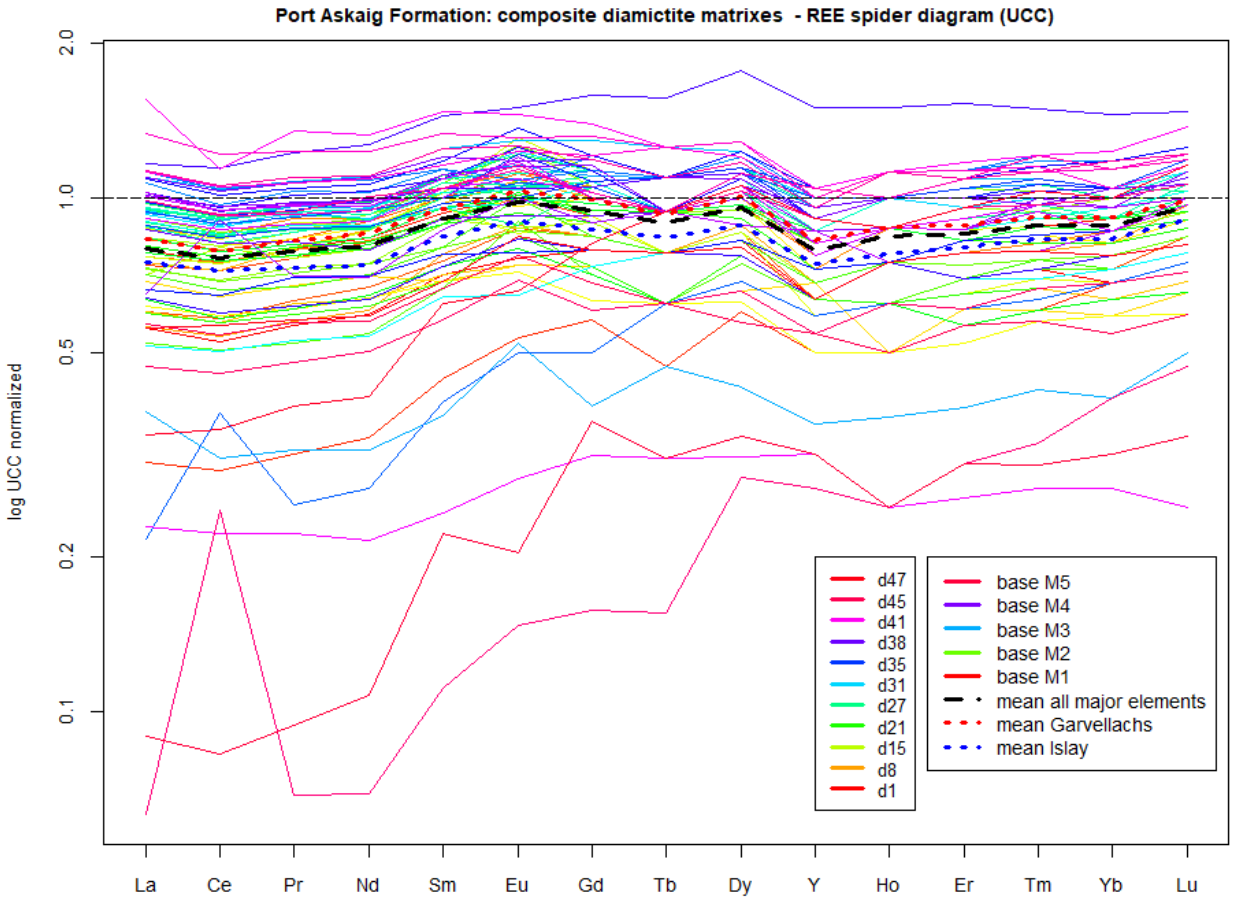

Figure 36. UCC normalized spider diagram covering REE+Y from the PAF diamictite matrix ICP dataset. For comments concerning legend and the plot, please refer to Figure 12.

The REE+Y ICP set was also recalculated on a carbonate free basis and then again normalized to UCC average concentrations (McLennan, 2001) with revised result shown in Figure 37. This resulted in an average REE+Y staying even closer to UCC. The variation between upper and lower quartiles were in average reduced from 34% to 27% in the carbonate free set.

No substantial Ce nor Eu anomaly can be inferred from the plot and there are only minor differences between the LREE and HREE segments compared to UCC.

The data are presented with colours shifting from red nuances in the lower diamictite up to blue at the top of Member 5. The general upward trend seen in Figure 36 disappears in Figure 37 and was thus caused by carbonate dilution.

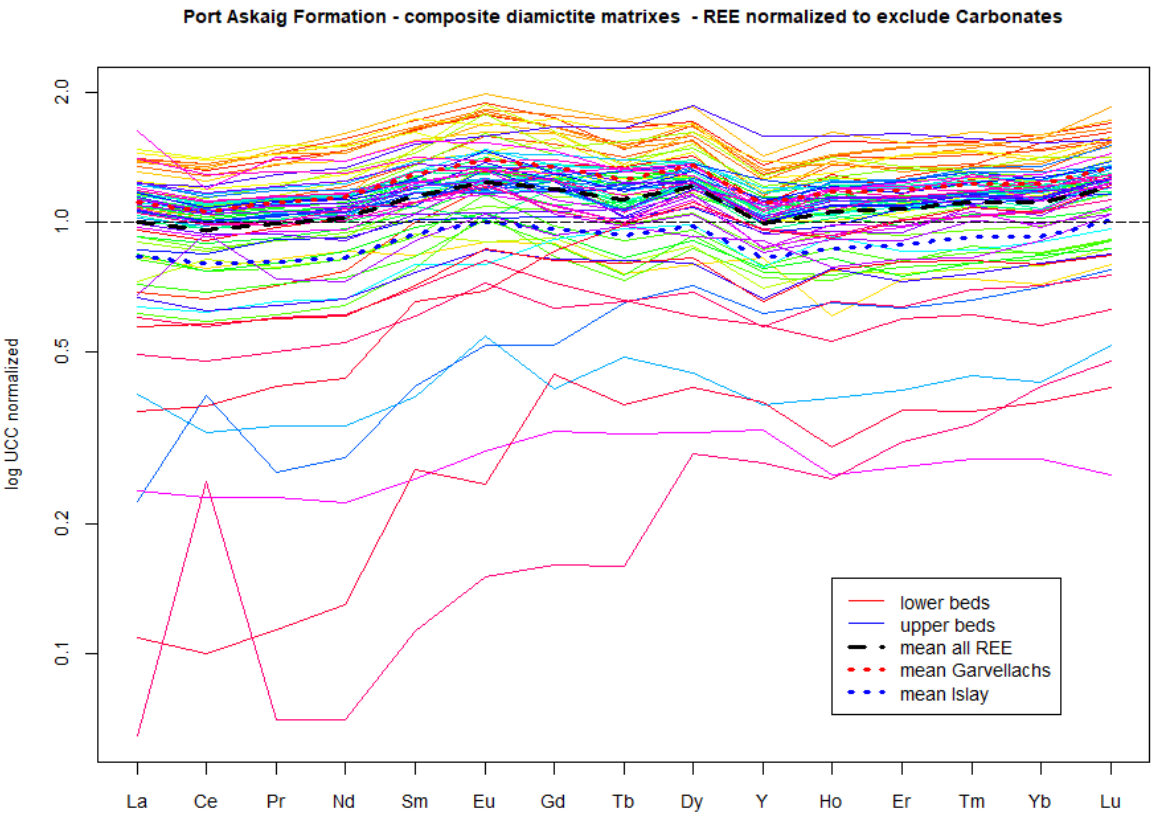

Figure 37. UCC normalized spider diagram covering REE+Y on a carbonate free basis. For other comments, please refer to Figure 12.

The internal correlations between REE+Y elements in Table 11 show strong correlation with neighbouring elements and a gradual decrease over longer distances. Correlation is thus strongest within each group of LREE and HREE and less in between these two groups.

REE+Y correlates with major elements linked to detrital clasts such as Al_2O_3, K_2O and TiO_2, but not with other major elements that possibly were added through other processes such as aggregation of carbonates or precipitation of Fe oxyhydroxides (Table 12). This implies the REE+Y are controlled by detrital components and have no legacy from ocean chemistry. It is also noted that REE+Y has no correlation with sodium.

	La	Ce	Pr	Nd	Sm	Eu	Gd	Tb	Dy	Y	Ho	Er	Tm	Yb	Lu
La	1.00	0.97	0.99	0.98	0.97	0.91	0.93	0.88	0.86	0.83	0.85	0.85	0.85	0.85	0.84
Ce		1.00	0.98	0.98	0.97	0.91	0.93	0.89	0.88	0.86	0.87	0.87	0.87	0.87	0.86
Pr			1.00	1.00	0.99	0.93	0.96	0.90	0.89	0.86	0.88	0.88	0.87	0.87	0.86
Nd				1.00	0.99	0.94	0.96	0.91	0.89	0.86	0.88	0.87	0.87	0.86	0.86
Sm					1.00	0.95	0.98	0.93	0.93	0.88	0.91	0.91	0.90	0.89	0.89
Eu						1.00	0.94	0.90	0.89	0.86	0.87	0.86	0.85	0.85	0.84
Gd							1.00	0.96	0.96	0.92	0.94	0.94	0.93	0.92	0.91
Tb								1.00	0.97	0.94	0.96	0.95	0.94	0.92	0.91
Dy									1.00	0.97	0.98	0.98	0.98	0.96	0.95
Y										1.00	0.96	0.97	0.97	0.96	0.94
Ho											1.00	0.98	0.98	0.97	0.95
Er												1.00	0.99	0.98	0.97
Tm													1.00	0.99	0.98
Yb														1.00	0.98
Lu															1.00

Table 11. Internal correlation coefficients between REE+Y from the PAF diamictite matrix ICP dataset.

	SiO2	Al2O3	Fe2O3(T)	MnO	MgO	CaO	Na2O	K2O	TiO2	P2O5	LOI
Sum REE	-0.03	0.75	0.32	-0.29	-0.11	-0.24	0.25	0.74	0.80	0.12	-0.20
Sum LREE	-0.04	0.74	0.31	-0.29	-0.09	-0.23	0.26	0.72	0.78	0.11	-0.18
Sum HREE	0.03	0.72	0.32	-0.27	-0.18	-0.28	0.17	0.74	0.80	0.18	-0.25

Table 12. Correlation coefficients between the sum of total REE+Y, light REE and heavy REE versus major elements from the PAF diamictite matrix ICP dataset. Positive correlations >0.7 for total REE are marked with blue.

The non-parametric rank-tests were used to compare the distribution of total sum of REE + Y (Figure 38) and respectively the sum of LREE (Figure 39) and HREE (Figure 40) between different members in the PAF. Since the Kruskal-Wallis p-value is low for all these sums it can therefore with surety be ascertained that the REE compositions of all five members cannot have originated from the same source or deposition process. However, the Mann-Whitney comparisons between individual members indicate that some of the members may share the same source and from the boxplots it is seen that primarily M5 deviates in the distribution of LREE. The fact that there is a clear difference between LREE and HREE in M5 and since igneous differentiation enriches LREE in felsic rocks, this would imply a shift of provenance or different transport and sorting processes for the M5 material as compared to the other members.

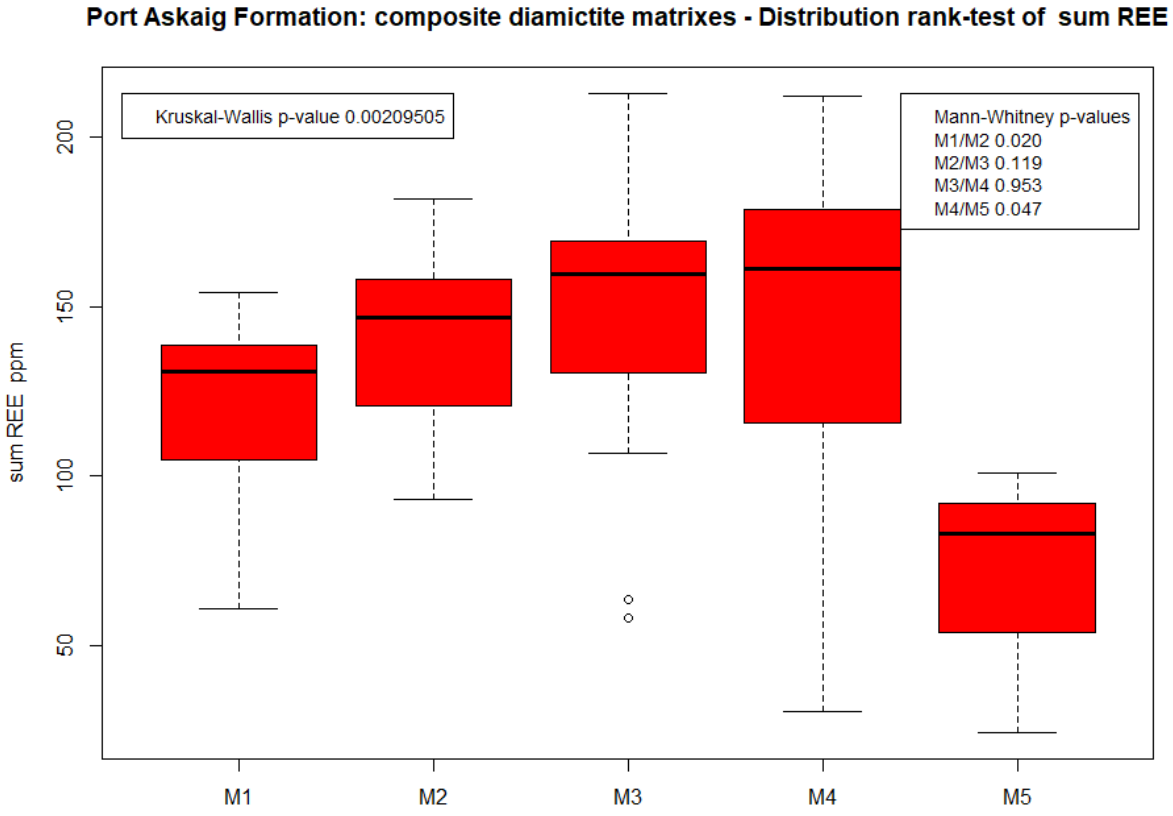

Figure 38. Kruskal-Wallis and Mann-Whitney rank-tests of sum of total REE+Y distribution. For comments regarding box-and-whisker plots please refer to Figure 11 and for rank test to Figure 18.

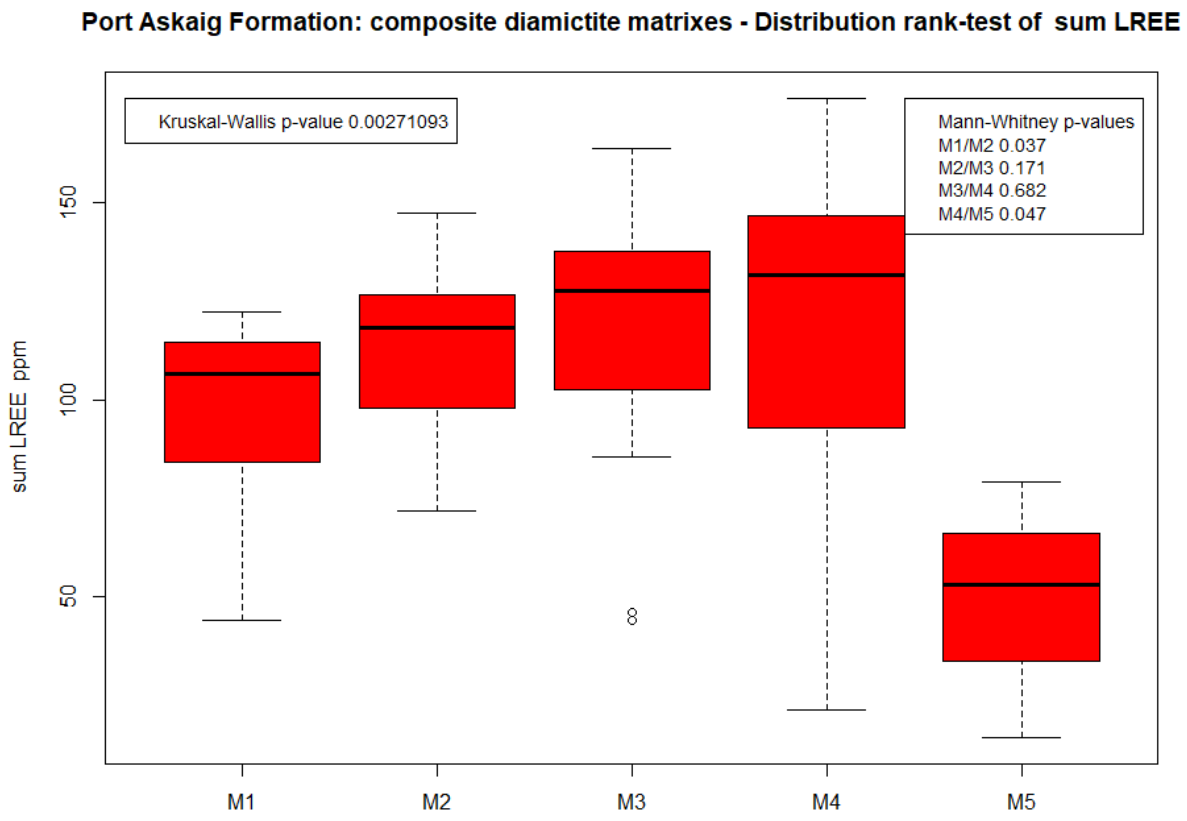

Figure 39. Kruskal-Wallis and Mann-Whitney rank-tests of sum of light REE distribution. For comments regarding box-and-whisker plots please refer to Figure 11 and for rank test to Figure 18.

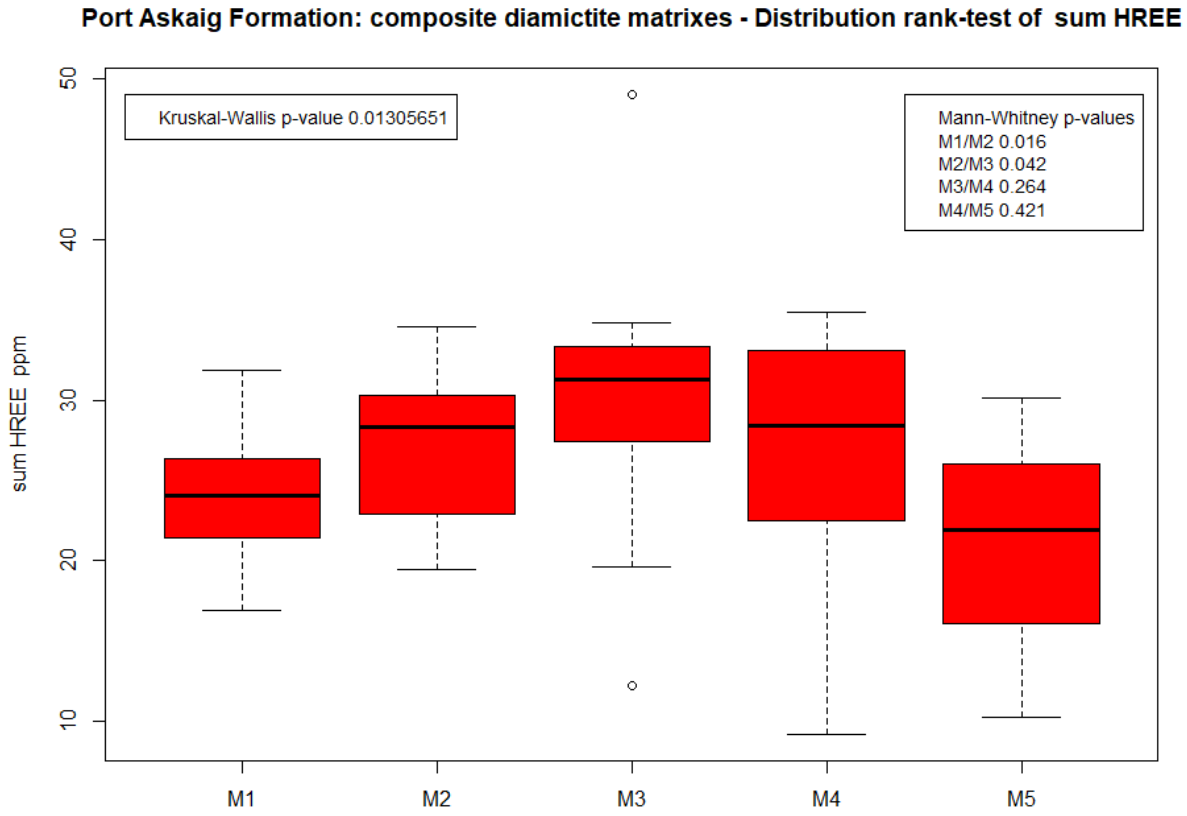

Figure 40. Kruskal-Wallis and Mann-Whitney rank-tests of sum of heavy REE distribution. For comments regarding box-and-whisker plots please refer to Figure 11 and for rank test to Figure 18.

The first two new variables of a PCA of the REE+Y explains 97% of the variance while each of the remaining new variables have a proportion of 1% or less of the total variance (Figure 41). All REE+Y participate equally in governing PC1 while LREE versus HREE have opposite weights in PC2. Eu dominates in PC3 and PC4 and Y in PC5, but these new variables have relative low explanatory weights (Table 13). In a PC1/PC2 diagram (Figure 42), all LREE appear in quadrant I while HREE show up in quadrant II.

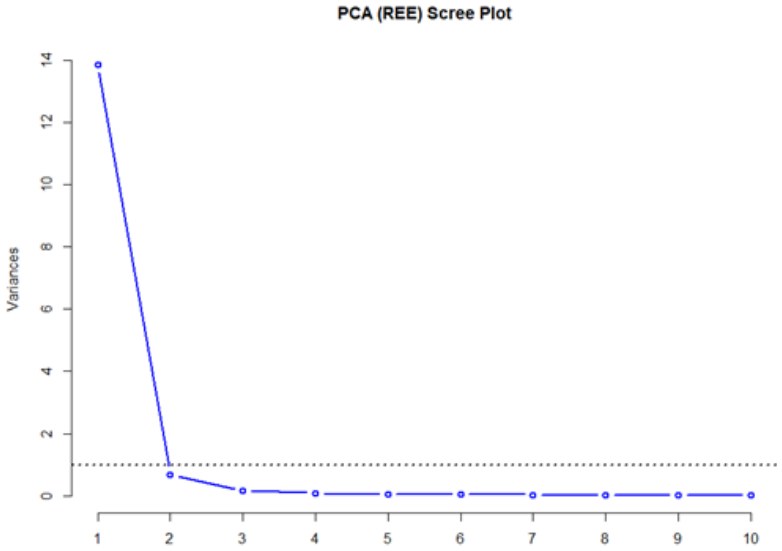

Figure 41. Scree plot showing principal components variances generated from a REE PCA on correlations. For further comments to this type of plot, please refer to Figure 28.

	PC1	PC2	PC3	PC4	PC5	PC6
La	0.252	0.364	0.303	0.078	-0.074	0.119
Ce	0.255	0.296	0.290	0.111	-0.187	-0.529
Pr	0.257	0.327	0.176	0.115	-0.006	0.083
Nd	0.257	0.329	0.045	0.042	-0.043	0.093
Sm	0.262	0.235	-0.078	-0.009	0.232	0.192
Eu	0.251	0.224	-0.559	-0.677	-0.167	-0.227
Gd	0.264	0.086	-0.237	0.077	0.286	0.480
Tb	0.260	-0.085	-0.389	0.451	0.177	-0.207
Dy	0.262	-0.198	-0.193	0.162	0.054	0.099
Y	0.256	-0.263	-0.058	0.097	-0.810	0.300
Ho	0.260	-0.234	-0.096	0.153	0.153	-0.420
Er	0.261	-0.260	0.037	0.084	-0.020	0.018
Tm	0.260	-0.273	0.156	-0.059	0.012	-0.073
Yb	0.258	-0.269	0.275	-0.235	0.106	-0.123
Lu	0.256	-0.259	0.338	-0.417	0.263	0.179

Table 13. List of principal components from PCA of REE with their respective loadings.

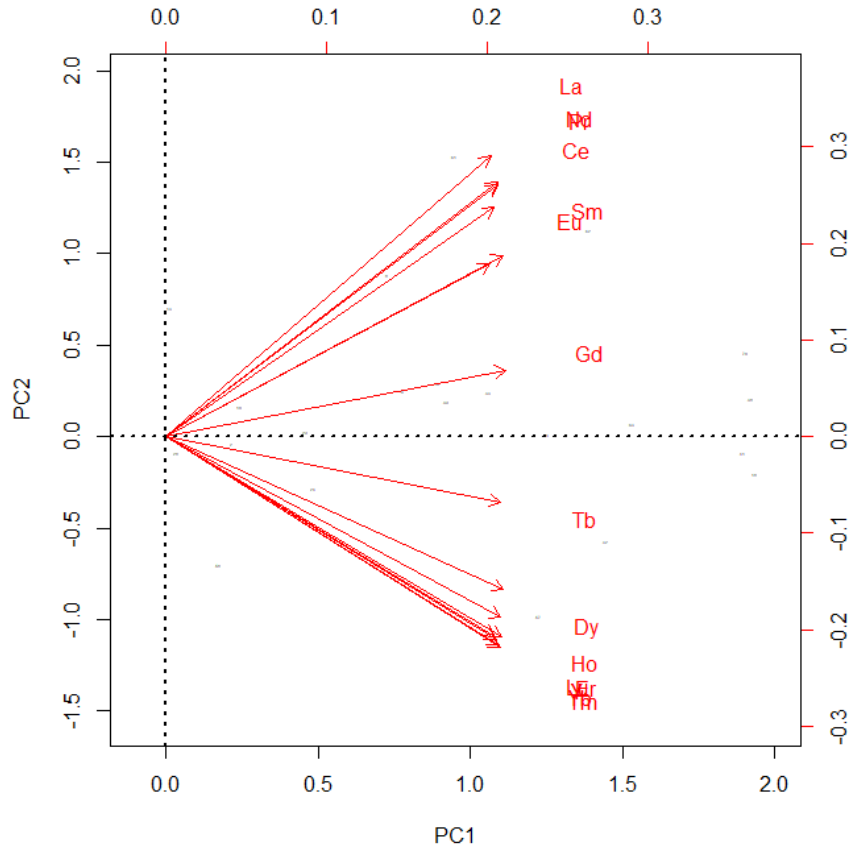

Figure 42. Projection of REE onto a PC1/PC2 two-dimensional biplot. For further comments to this type of plot, please refer to Figure 29.

Figure 43 shows the trends of sum of REE+Y and the respective ratios of La/Sm and Gd/Lu over the PAFs stratigraphic column. The ratio La/Sm was chosen to represent enrichment/depletion within LREE and Gd/Lu within HREE. The following general observations are noted regarding their trends:

- The sum of REE+Y and the ratio La/Sm increase slowly upwards in the stratigraphic column from M1 to M4.
- The ratio Gd/Lu is flat from M1 to M4 (i.e. does not increase nor decrease).
- The M5 data points are scattered in all three trend plots.

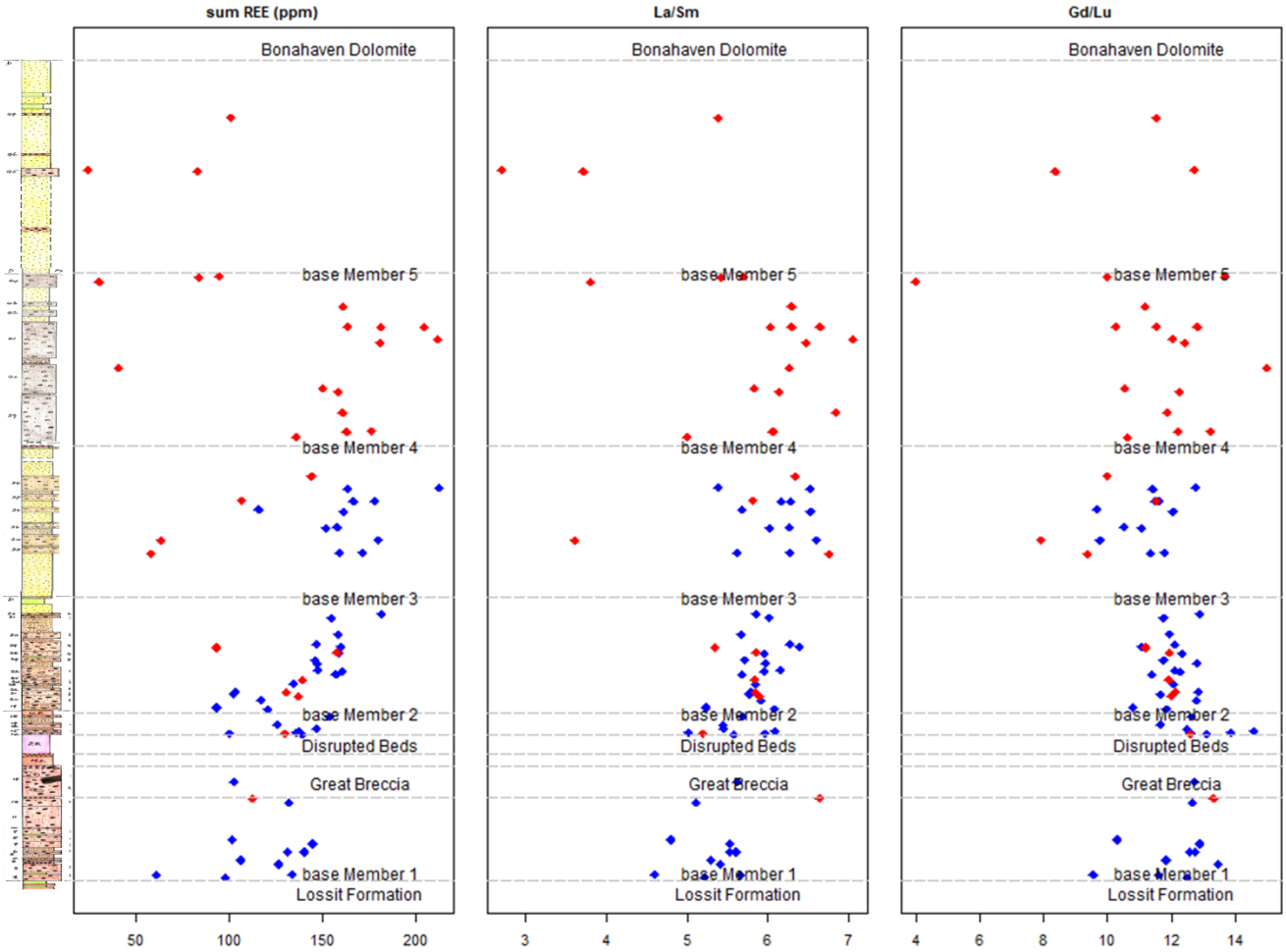

Figure 43. Total REE+Y, La/Sm and Gd/Lu ratios trends over the PAFs stratigraphic column, from the diamictite matrix ICP dataset. The ppm concentration of each element is given on the horizontal scale. For further comments to this plot, please refer to Figure 30.

3.3 Trace elements geochemistry

The trace elements in Figure 44 show that the PAF diamictites contain below average Sr and Co and above average Cr. Sr is easily released during weathering of terrigenous rocks. Neoproterozoic composites are normally depleted in Co (Gaschnig et al, 2016).

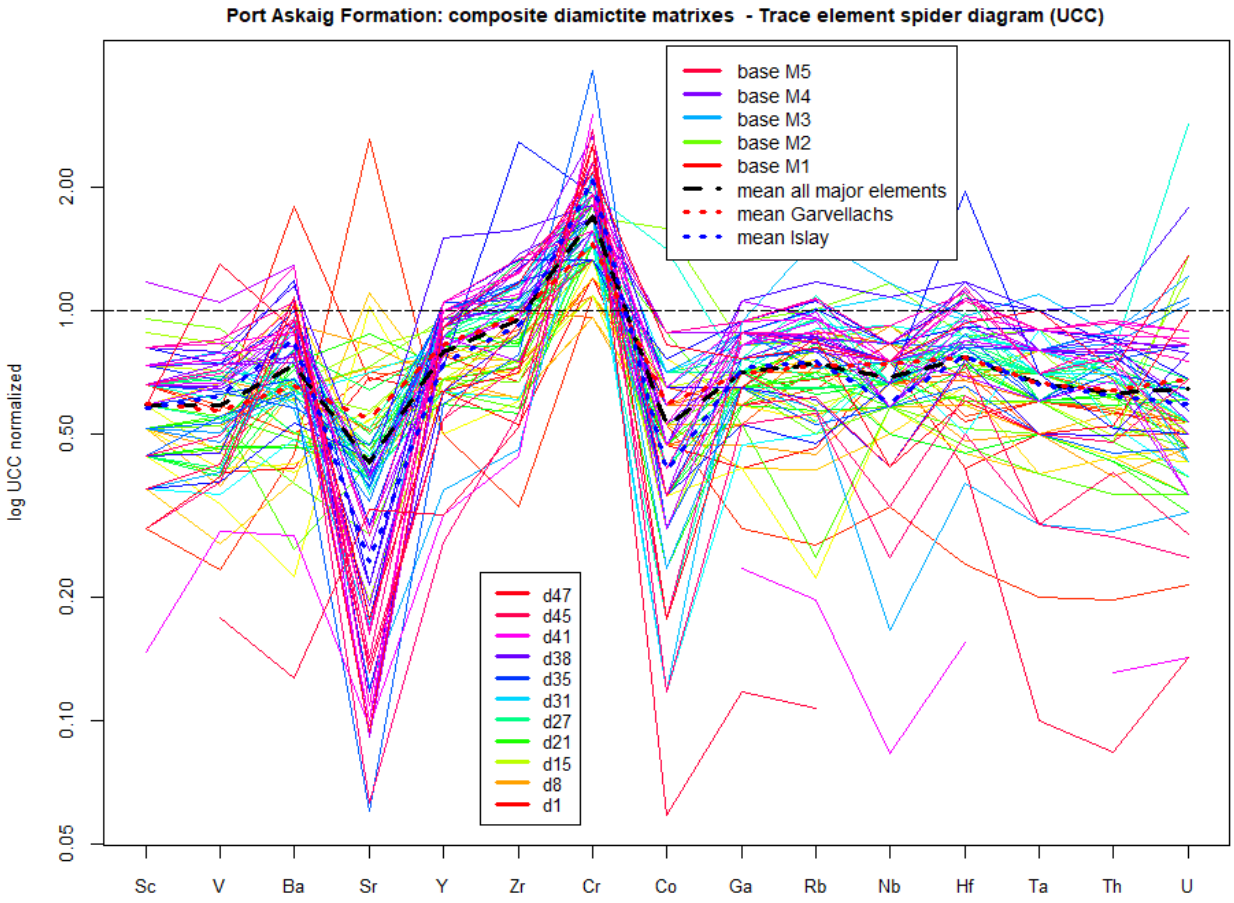

Figure 44. UCC normalized spider diagram covering trace elements over the PAFs stratigraphic column, from the diamictite matrix ICP dataset. For comments concerning the plot, please refer to Figure 12.

The trace element concentrations were also recalculated on a carbonate free basis and then again normalized to UCC average concentrations (McLennan, 2001) with revised result shown in Figure 45. The trace elements concentrations stay somewhat closer to the UCC standard with an average variation between upper and lower quartiles reduced from 44% to 40% in the carbonate free set. However, and not surprisingly, the Sr variation increased substantially in the carbonate free set.

The largest variations are seen in Sr and Co. Sr and Co clearly decrease upwards while the rest of the trace elements show a more ambiguous trend. Sr evidently is controlled by the carbonates in the dolomitic lower beds in the Garvellachs but have lower concentrations in the granitic diamictites in the upper beds on Islay.

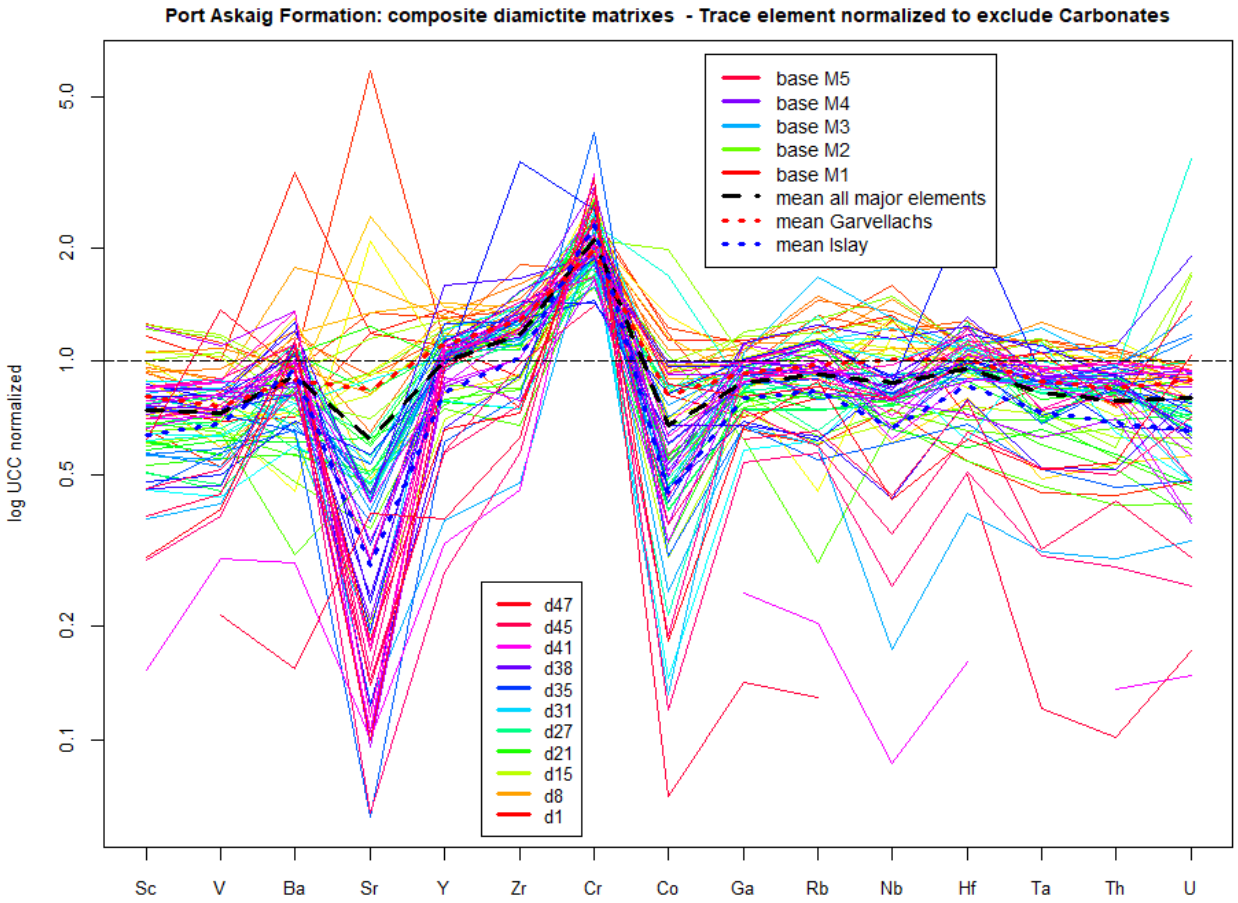

Figure 45. UCC normalized spider diagram covering trace elements on a carbonate free basis. For other comments, please refer to Figure 12.

Internal correlations calculated from the ICP dataset between trace elements and with major elements and REE are listed in Tables 14 and 15. Connections exist between following group of trace elements: Sc, V, Y, Ga, Rb, Nb, Ta and Th, and separately between Zr and Hf. These groups consist primarily of incompatible trace elements, i.e. high field strength (HFS) elements (e g Sc, Y, Zr, Nb, Hf, Ta and Th) and large ion lithophiles (LIL) elements (e g Rb). For example, Zr and Hf have almost identical cationic charge and ionic radius and Hf can thus easily substitute for Zr in zircon.

Both the LIL and HFS elements are incompatible during crystalizing of melted mantle materials. Their behaviour however differs during post-magmatic processes where HFS elements acts conservatively and are less influenced by metasomatic processes and metamorphism while LIL elements more easily substitute for major mobile elements such as potassium, sodium and calcium. Therefore, HFS elements better reflect the provenance of the diamictites while the LIL elements can give indications about post-depositional alterations such as diagenesis and metasomatism (Albarède, 2009; McLennan, 1989).

Both Rb and Sr belong to the mobile LIL elements. Their ability to substitute for major mobile elements are exemplified by their correlation with K respectively with Ca. Sr, thus being a carbonate associate, also correlates well with MgO and LOI (equal to CO_2). Since Sr is removed early from siliciclastic rocks in chemical weathering but have this high correlation with Ca, Mg and LOI, this furthermore confirms that Ca is mainly of carbonate (not siliciclastic) type.

The internally correlated group Sc, V, Y, Ga, Rb, Nb, Ta and Th show good correlation with several major elements such as Al_2O_3, K_2O, TiO_2 and with REE, which all are associated with detrital sedimentary rocks. Since these insoluble HFS elements show a good correlation with the sum of REE, this may indicate that the REE have a large terrigenous detrital source such as glacial clay

Finally, Cr has a good correlation with SiO_2 but not with other elements, indicating that it primarily is included in quartz.

	Sc	V	Ba	Sr	Y	Zr	Cr	Co	Ga	Rb	Nb	Hf	Ta	Th	U
Sc	1.00	0.84	0.35	-0.20	0.68	0.34	-0.19	0.34	0.81	0.67	0.70	0.39	0.61	0.61	0.22
V		1.00	0.41	-0.36	0.64	0.40	0.05	0.37	0.80	0.70	0.58	0.45	0.68	0.60	0.34
Ba			1.00	-0.33	0.37	0.28	0.08	0.02	0.54	0.50	0.06	0.33	0.28	0.42	0.23
Sr				1.00	-0.16	-0.31	-0.51	0.05	-0.43	-0.35	-0.04	-0.35	-0.33	-0.32	-0.14
Y					1.00	0.65	-0.17	0.30	0.80	0.75	0.73	0.67	0.78	0.89	0.54
Zr						1.00	0.08	0.17	0.55	0.50	0.46	0.98	0.58	0.65	0.38
Cr							1.00	-0.22	0.03	-0.01	-0.32	0.12	0.02	-0.08	0.06
Co								1.00	0.27	0.18	0.24	0.12	0.24	0.25	0.58
Ga									1.00	0.85	0.62	0.63	0.76	0.84	0.42
Rb										1.00	0.61	0.57	0.75	0.76	0.42
Nb											1.00	0.49	0.75	0.66	0.28
Hf												1.00	0.63	0.71	0.36
Ta													1.00	0.86	0.40
Th														1.00	0.51
U															1.00

Table 14. Internal correlation coefficients between trace elements from the PAF diamictite matrix ICP dataset. Positive correlations >0.7 are marked with blue.

	Sc	V	Ba	Sr	Y	Zr	Cr	Co	Ga	Rb	Nb	Hf	Ta	Th	U
SiO2	-0.01	0.21	0.30	-0.71	0.05	0.24	0.74	-0.16	0.31	0.20	-0.21	0.27	0.19	0.14	0.15
Al2O3	0.74	0.75	0.59	-0.49	0.72	0.53	0.10	0.20	0.97	0.82	0.48	0.62	0.70	0.80	0.39
Fe2O3.T.	0.28	0.24	-0.17	-0.05	0.32	0.15	-0.12	0.23	0.24	0.14	0.25	0.17	0.19	0.25	0.04
MnO	-0.13	-0.35	-0.41	0.26	-0.27	-0.01	-0.09	-0.10	-0.50	-0.43	0.02	-0.06	-0.34	-0.36	-0.17
MgO	-0.09	-0.30	-0.40	0.66	-0.20	-0.29	-0.64	0.10	-0.44	-0.31	0.13	-0.34	-0.26	-0.27	-0.16
CaO	-0.24	-0.44	-0.34	0.77	-0.29	-0.37	-0.62	0.03	-0.57	-0.42	-0.01	-0.43	-0.38	-0.39	-0.25
Na2O	0.04	0.06	0.29	-0.32	0.16	0.27	0.26	-0.06	0.32	0.04	-0.08	0.33	0.20	0.39	0.12
K2O	0.68	0.72	0.53	-0.41	0.73	0.52	0.01	0.15	0.88	0.98	0.57	0.59	0.74	0.75	0.38
TiO2	0.91	0.86	0.34	-0.24	0.80	0.57	-0.16	0.44	0.87	0.77	0.79	0.61	0.80	0.76	0.40
P2O5	0.10	0.07	-0.24	-0.05	0.16	-0.01	-0.07	0.18	0.05	-0.07	0.12	-0.01	-0.02	0.04	0.05
LOI	-0.18	-0.39	-0.36	0.74	-0.27	-0.35	-0.65	0.05	-0.52	-0.37	0.05	-0.41	-0.34	-0.36	-0.23
Sum REE	0.71	0.56	0.36	-0.18	0.90	0.61	-0.25	0.27	0.82	0.76	0.70	0.65	0.78	0.92	0.42

Table 15. Correlation coefficients between trace elements and major elements and total REE from the PAF diamictite matrix ICP dataset. Positive correlations >0.7 are marked with blue and negative correlations <-0.7 are marked with yellow.

The non-parametric rank-tests were used to compare the distribution of some more prominent trace elements between different members in the PAF (Figures 46 – 52). The Kruskal-Wallis p-value varies between the elements where HFS elements typically have lower values than LIL elements. This again confirms that different processes have controlled the supply of these elements through the five members. Insoluble and conservative HFS elements have followed the original distribution of detrital material while LIL elements may have been added or subtracted from the system in later metamorphism and hydrothermal alterations.

There are concentration maxima of Sr in M1, Zr in M3 and Ga in M4 but the other trace elements show less distinct trends. It is also noted that the distribution of V, Ga and Ta in M5 fluctuates greatly compared to their variation in other members.

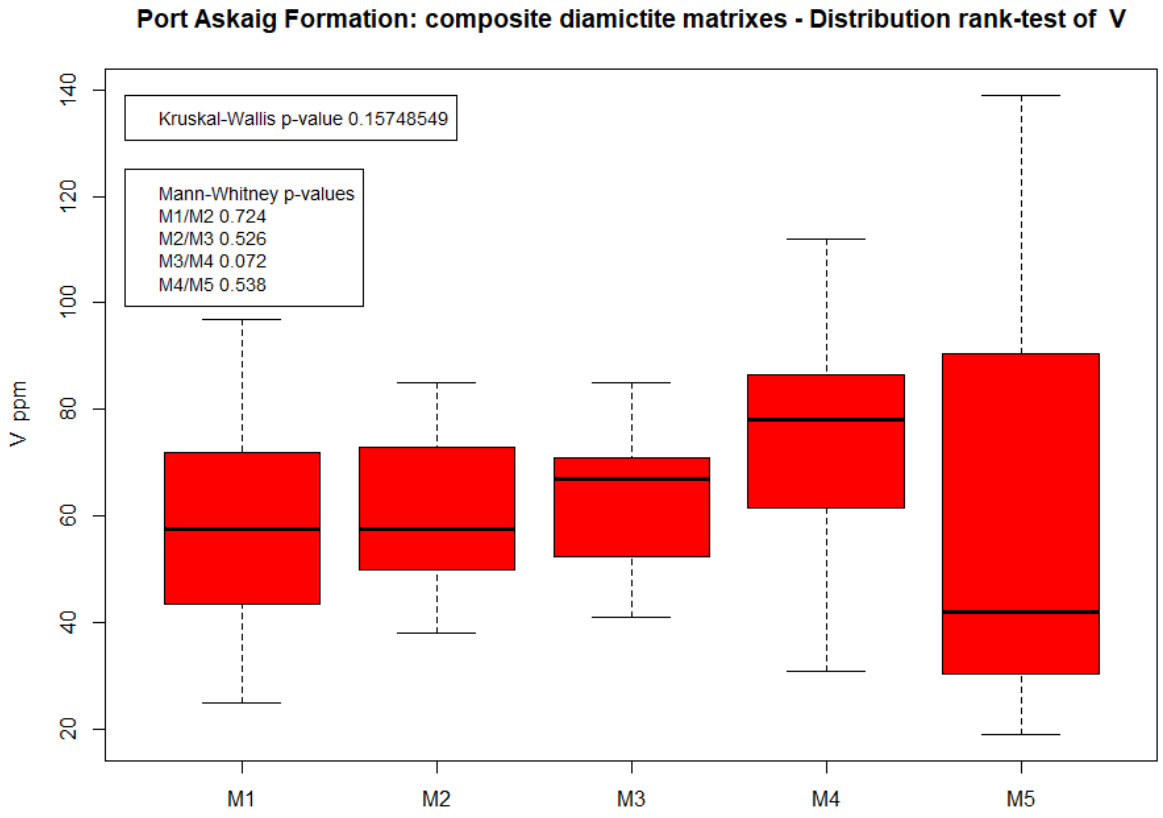

Figure 46. Kruskal-Wallis and Mann-Whitney rank-tests of V distribution. For comments regarding box-and-whisker plots please refer to Figure 11 and for rank test to Figure 18.

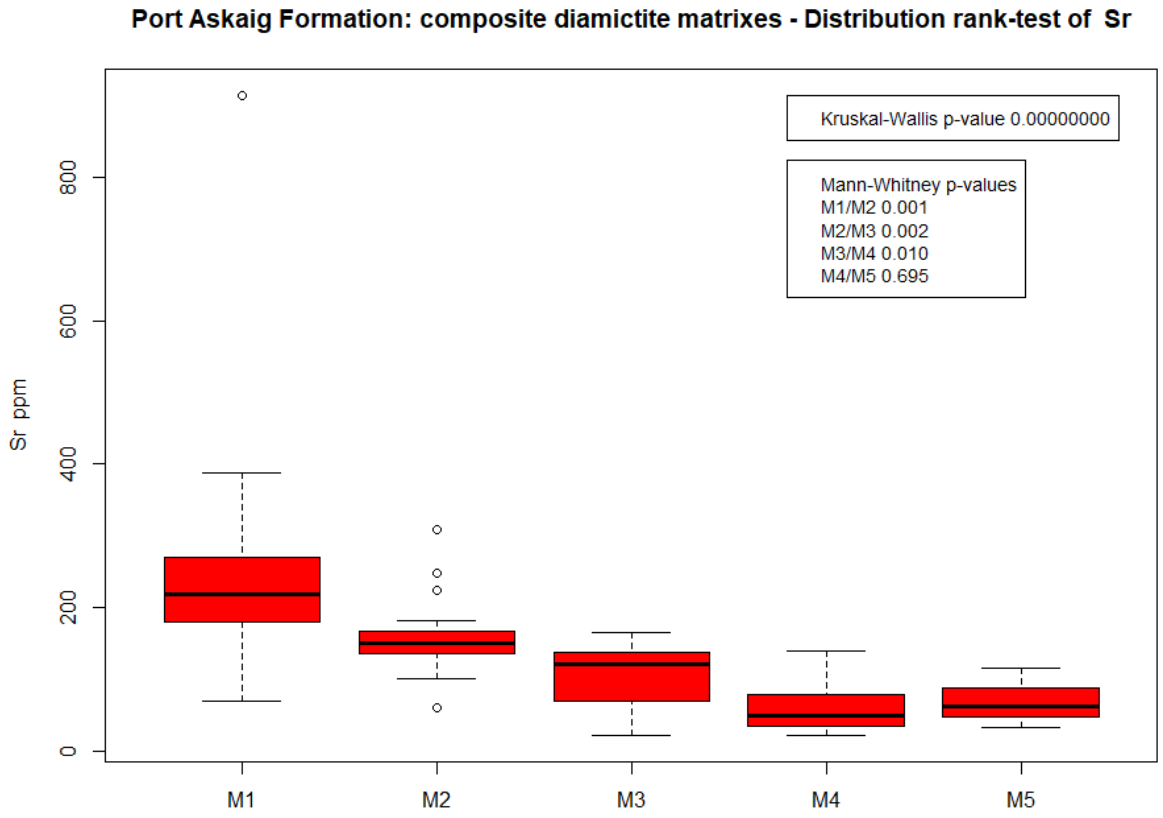

Figure 47. Kruskal-Wallis and Mann-Whitney rank-tests of Sr distribution. For comments regarding box-and-whisker plots please refer to Figure 11 and for rank test to Figure 18.

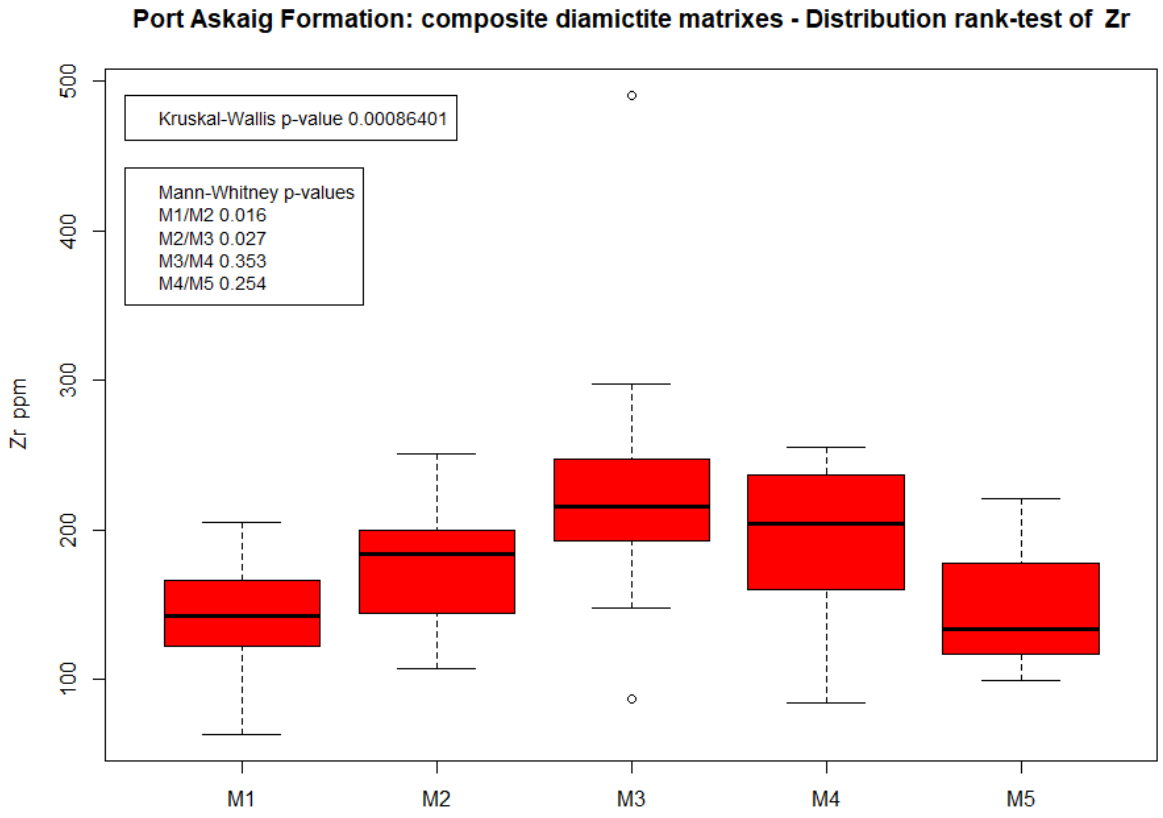

Figure 48. Kruskal-Wallis and Mann-Whitney rank-tests of Zr distribution. For comments regarding box-and-whisker plots please refer to Figure 11 and for rank test to Figure 18.

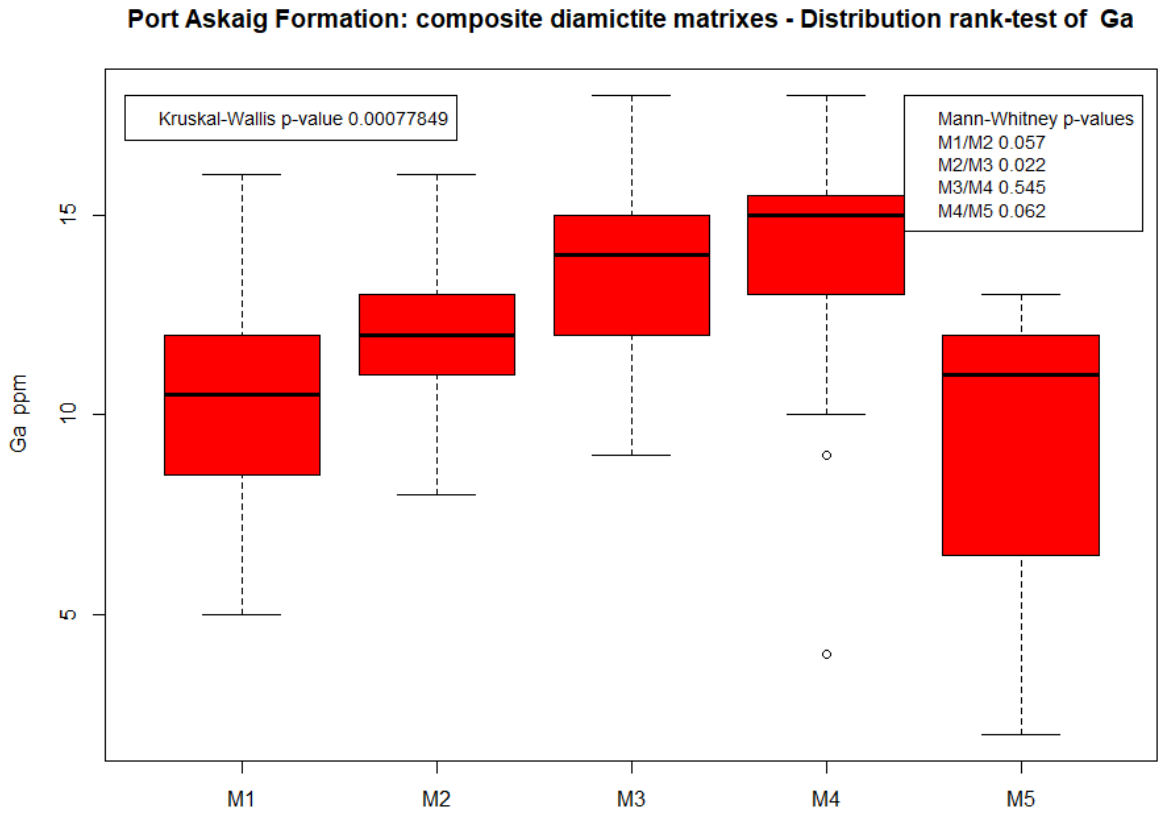

Figure 49. Kruskal-Wallis and Mann-Whitney rank-tests of Ga distribution. For comments regarding box-and-whisker plots please refer to Figure 11 and for rank test to Figure 18.

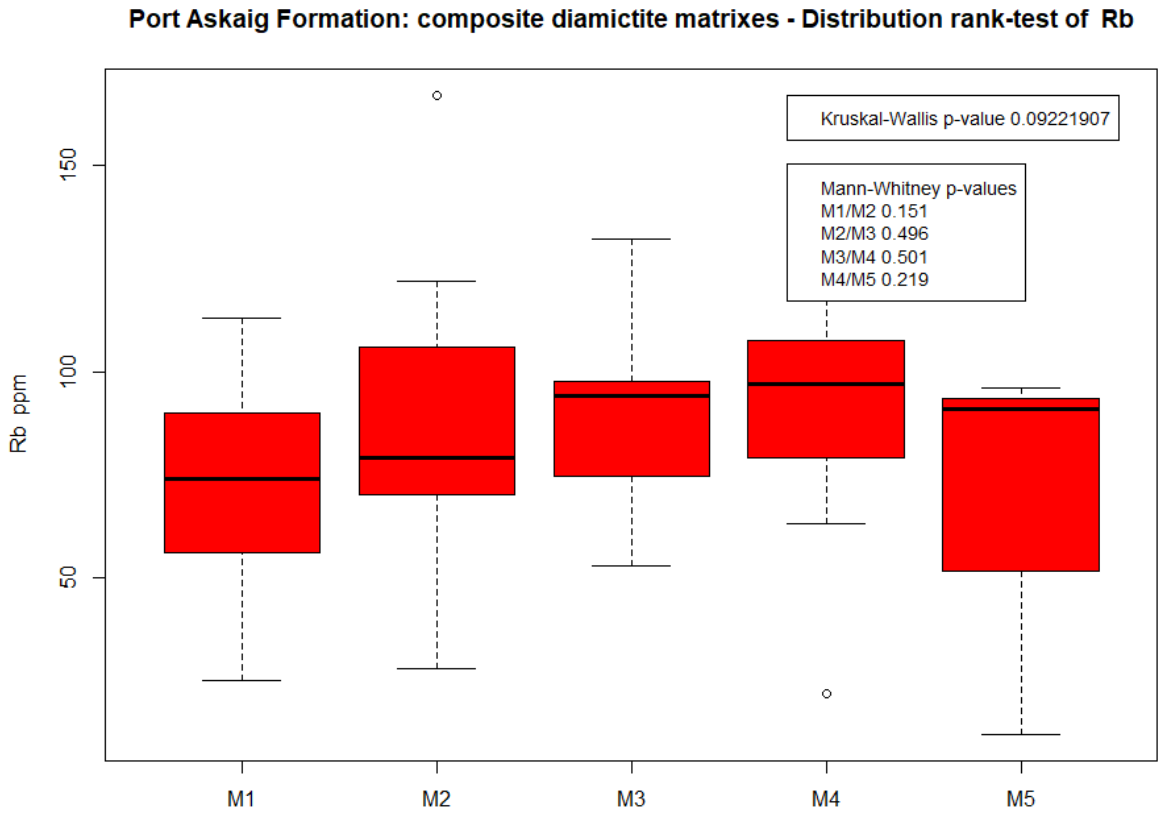

Figure 50. Kruskal-Wallis and Mann-Whitney rank-tests of Rb distribution. For comments regarding box-and-whisker plots please refer to Figure 11 and for rank test to Figure 18.

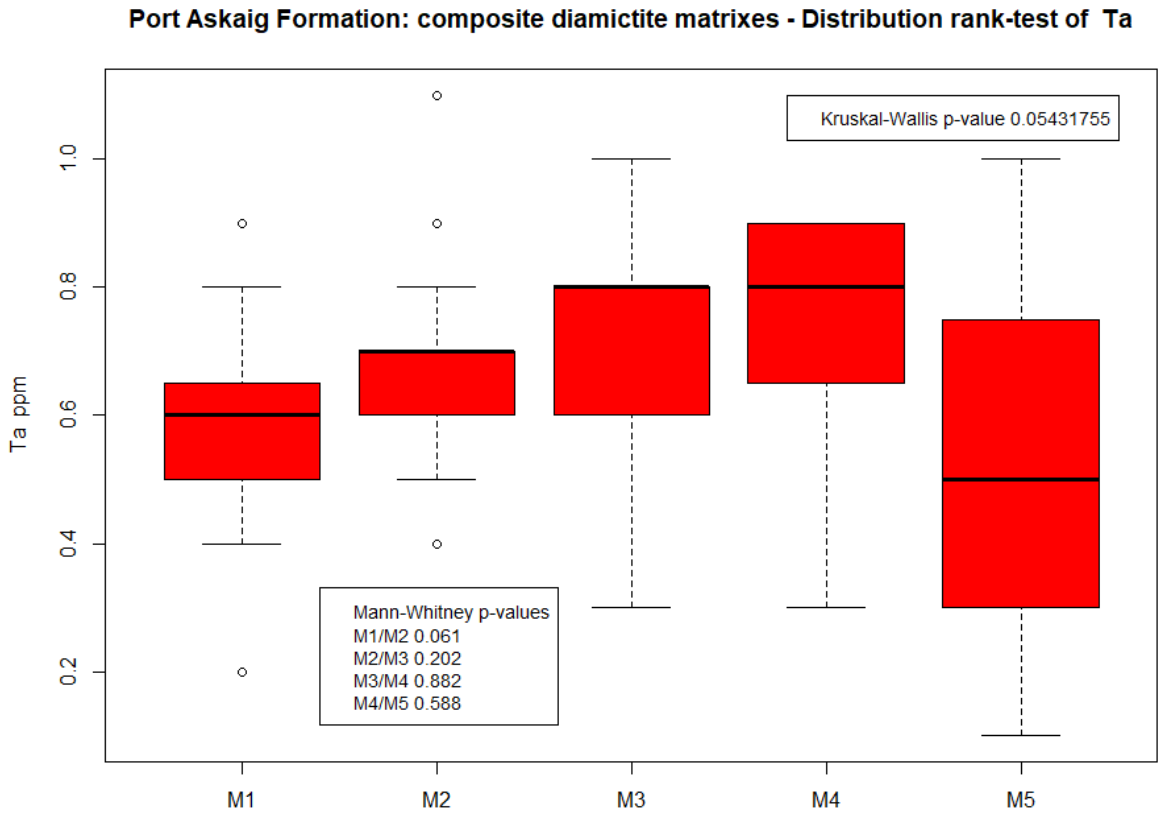

Figure 51. Kruskal-Wallis and Mann-Whitney rank-tests of Ta distribution. For comments regarding box-and-whisker plots please refer to Figure 11 and for rank test to Figure 18.

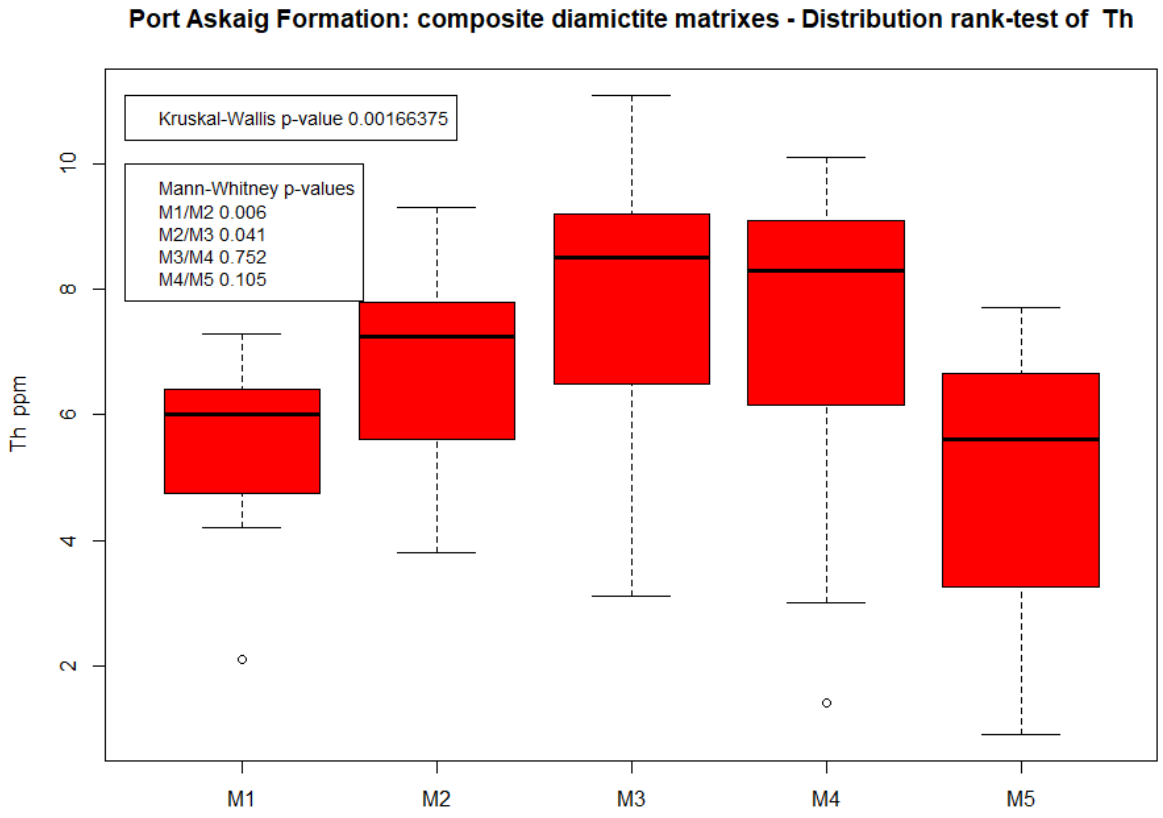

Figure 52. Kruskal-Wallis and Mann-Whitney rank-tests of Th distribution. For comments regarding box-and-whisker plots please refer to Figure 11 and for rank test to Figure 18.

A trace elements PCA does not generate new variables with strong explanatory weights since as much as six PC are needed to accommodate 90% of the total variance in the dataset as indicated by the scree plot (Figure 53). PC1 and PC2 are to some extent governed by Sr and Cr which reflects their respective correlation with carbonates and silica. PC3 is controlled by Zr, Hf and U, while PC4 is steered by Co and U and PC5 by Ba (Table 16).

When projecting the main variables onto a PC1/PC2 2-dimensional diagram (Figure 54), Cr and Sr show up alone in respective quadrants III and IV. It is noted that Zr and Hf respectively Rb and Ga stay close together and that Co, Ba and U having larger weights in e g PC4 and PC5 therefore are to be understood to be orthogonal to the PC1/PC2 plane.

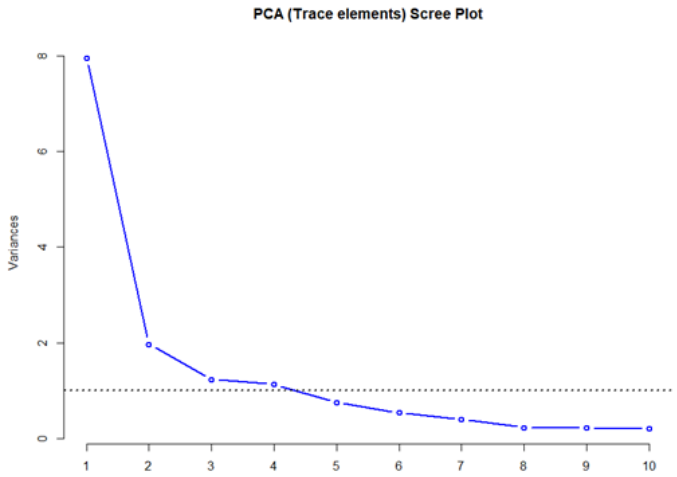

Figure 53. Scree plot showing principal components variances generated from a trace elements PCA on correlations. For further comments to this type of plot, please refer to Figure 28.

	PC1	PC2	PC3	PC4	PC5	PC6
Sc	0.291	0.175	-0.352	0.034	-0.121	0.277
V	0.285	-0.007	-0.311	0.183	-0.267	0.282
Ba	0.174	-0.225	-0.324	0.083	0.792	0.178
Sr	-0.126	0.531	0.130	-0.146	0.239	0.000
Y	0.321	0.098	0.103	-0.079	0.089	-0.218
Zr	0.252	-0.176	0.463	-0.260	0.051	0.376
Cr	-0.023	-0.589	0.060	0.274	-0.289	-0.097
Co	0.153	0.344	0.205	0.576	-0.080	0.389
Ga	0.329	-0.071	-0.199	0.034	-0.016	-0.019
Rb	0.306	-0.053	-0.179	-0.018	0.052	-0.277
Nb	0.280	0.277	-0.035	-0.210	-0.236	-0.128
Hf	0.270	-0.203	0.391	-0.267	0.034	0.322
Ta	0.319	0.048	0.015	-0.123	-0.151	-0.240
Th	0.324	-0.011	0.089	-0.092	0.069	-0.295
U	0.193	0.048	0.391	0.562	0.207	-0.347

Table 16. List of principal components from PCA of trace elements with their respective loadings.

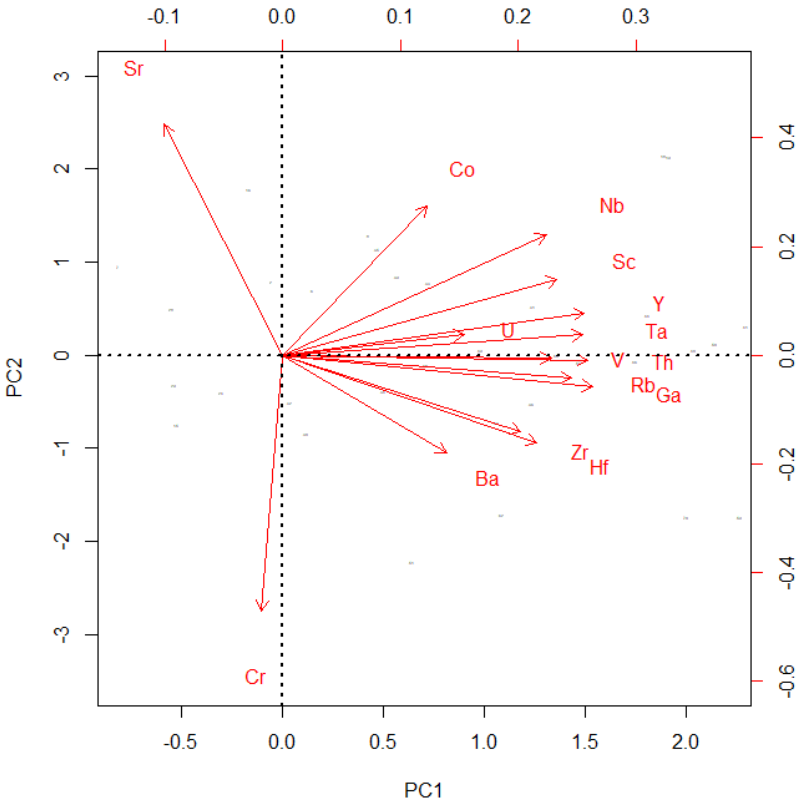

Figure 54. Projection of trace elements onto a PC1/PC2 two-dimensional biplot. For further comments to this type of plot, please refer to Figure 29.

Figures 55 – 57 show the trends of some of the trace elements over the PAFs stratigraphic column. The following general observations are noted regarding their trends:

- The carbonates associate Sr decreases as expected upwards.
- Cr follows silica with an upwards increase.
- Co do not display any distinct trend.
- There is some hint of an upward-increasing intra-member “sawtooth” trend seen in M2, M3 and M4 for V, Zr, Rb and possibly for Ga, Th, Y.
- The distribution of M5 data points shows limited resemblance with those of other members in several of the trend-plots.

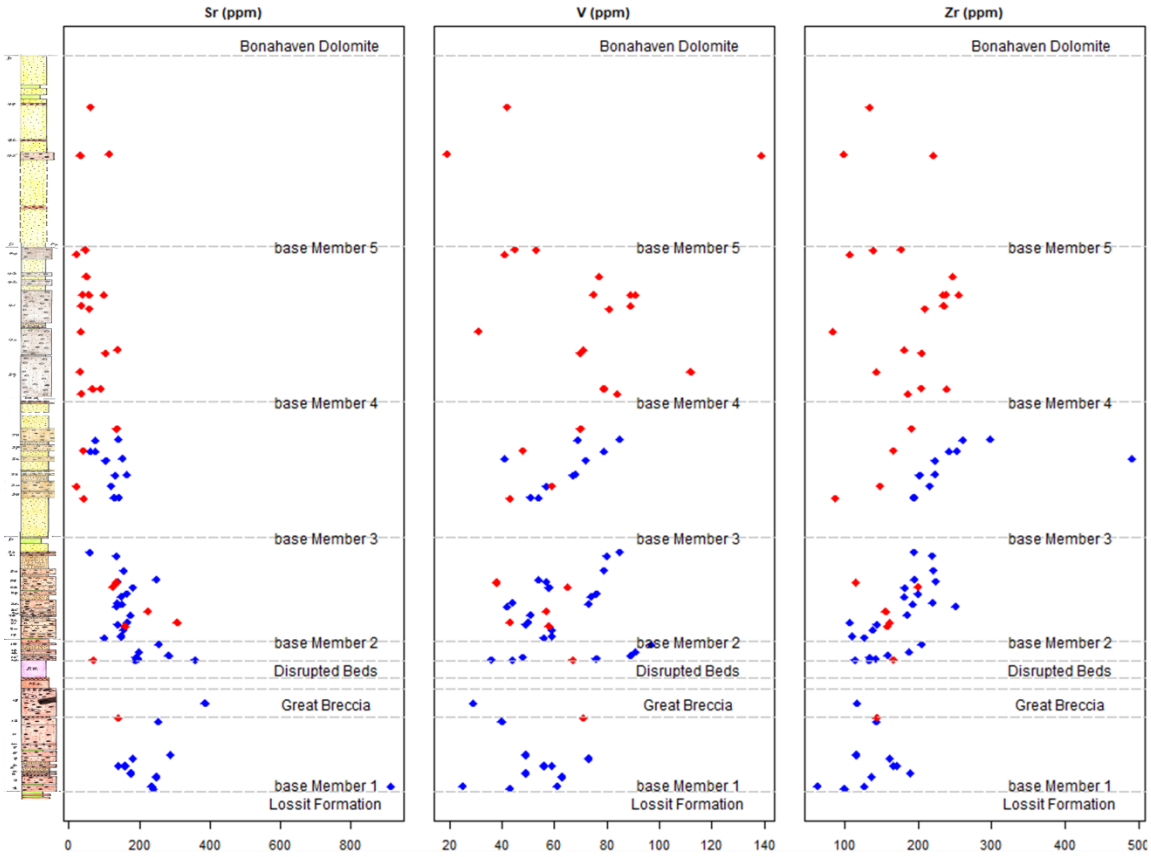

Figure 55. Sr, V and Zr trends over the PAFs stratigraphic column, from diamictite matrix ICP data. The ppm concentration of each element is given on the horizontal scale. For further comments to this plot, please refer to Figure 30.

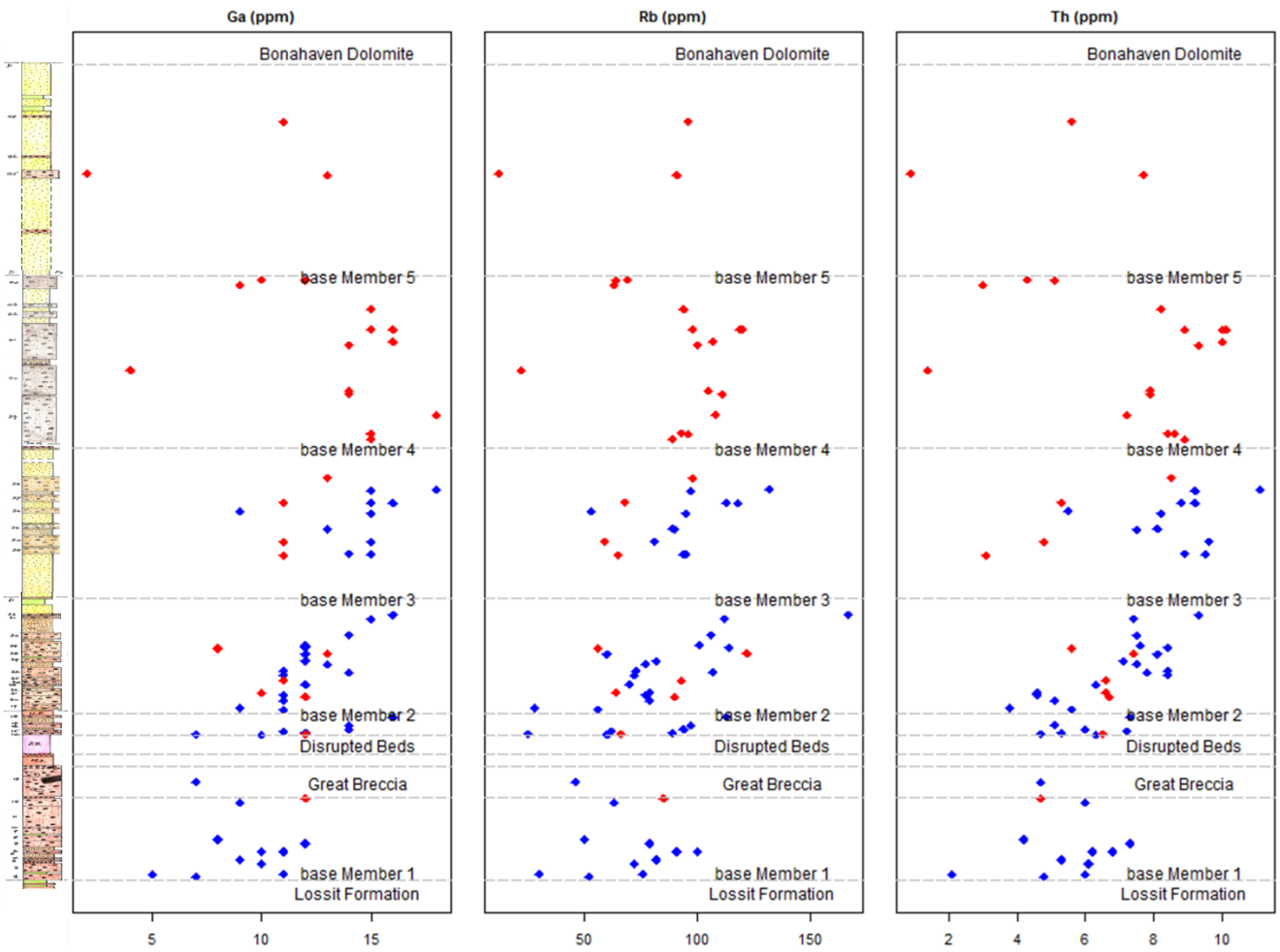

Figure 56. Ga, Rb and Th trends over the PAFs stratigraphic column, from diamictite matrix ICP data. The ppm concentration of each element is given on the horizontal scale. For further comments to this plot, please refer to Figure 30.

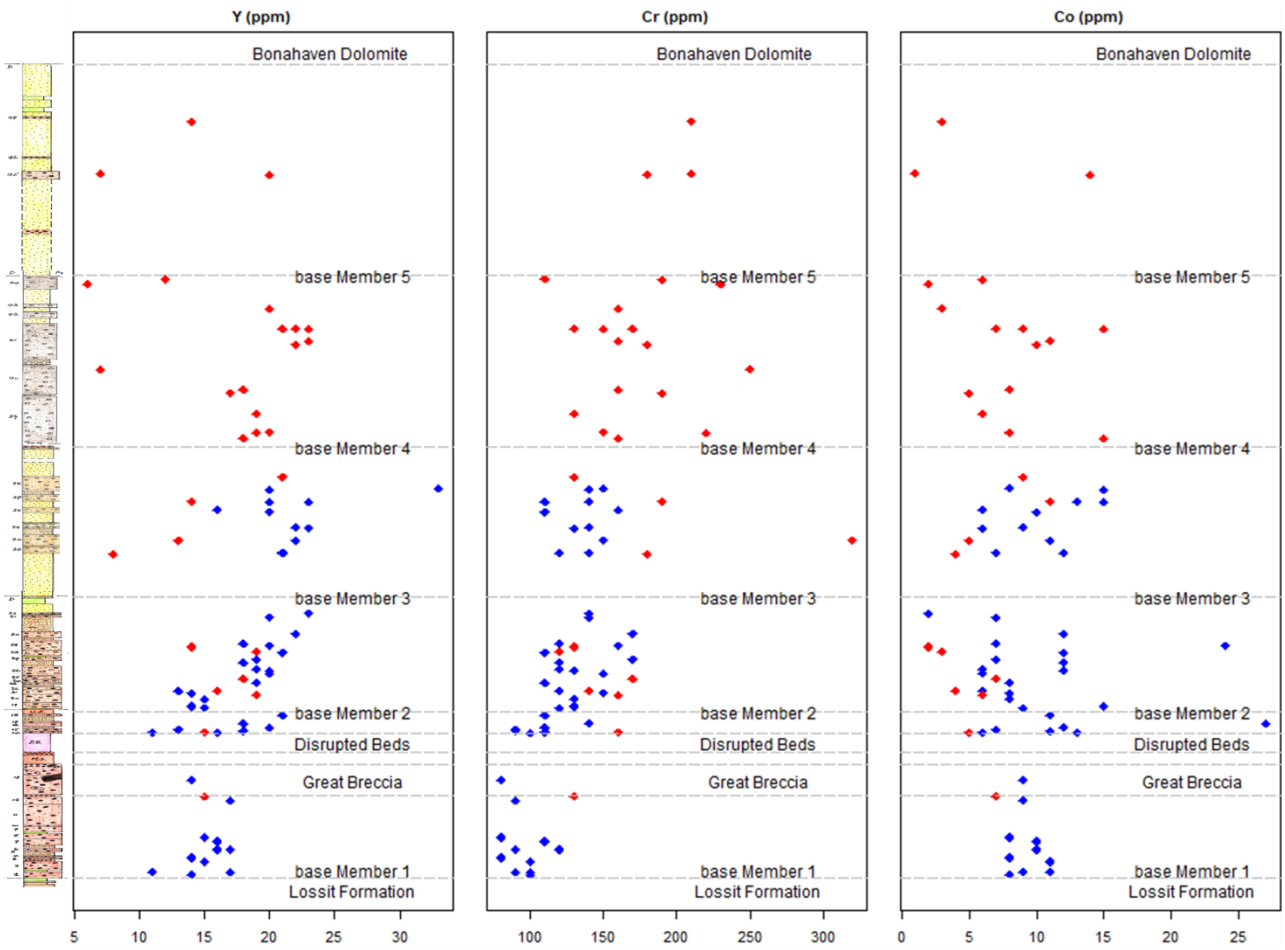

Figure 57. Y, Cr and Co trends over the PAFs stratigraphic column, from diamictite matrix ICP data. The ppm concentration of each element is given on the horizontal scale. For further comments to this plot, please refer to Figure 30.

3.4 Sandstone beds geochemistry

Fourteen samples were taken from sandstone beds: one from M2, seven from M3, one from M4 and five from M5. The stratigraphic positions of the sandstone beds are shown in Figure 5 and listed in Tables 2 and 3. Since the standard error decreases with the inverse of the square root of the number of observations, more variation is to be expected in this dataset compared to the diamictite matrix dataset.

The REE+Y in the the PAF sandstone dataset were normalized to UCC average concentrations (McLennan, 2001) with results shown in Figure 58. As expected, this shows that the sandstone beds are depleted in REE compared to UCC and thus also to the diamictite matrixes, which is attributed to quartz dilution.

There is a significant positive Eu anomaly in the sandstone beds not seen in the diamictites. Positive Eu anomalies in sedimentary rock can e.g. either be the result of precipitates from oceanic hydrothermal vents solutions or from high abundance of plagioclase from terrigenous sources. Eu may substitute for Sr in plagioclase, especially in anorthite, due to similar ionic radiuses, which leads to an Eu enrichment compared to other REE (McLennan, 1989). Since the sand grains in the PAF have a terrigenous source, the positive Eu anomaly is interpreted as a plagioclase enrichment during sedimentary sorting.

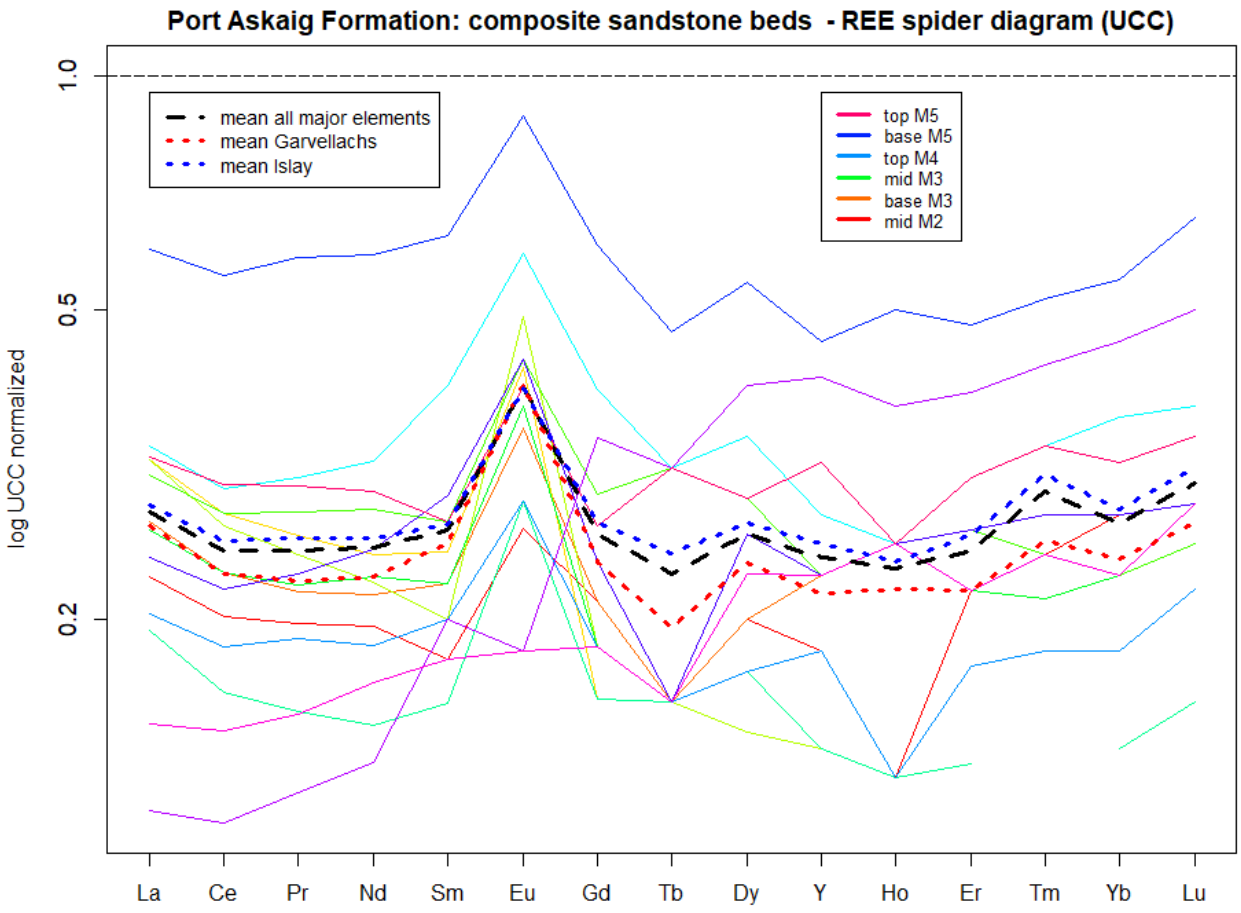

Figure 58. UCC normalized spider diagram covering REE+Y from sandstone beds in the PAF M2 – M5, with data from ICP dataset. The sandstone beds are gradational coloured from red in lower units (M2) to blue in upper units (M5). Average of all sandstone beds is shown with dashed black line (see legend in plot). The vertical scale is logarithmic. UCC standard values (McLennan, 2001) is marked with a horizontal line at vertical position 1.0. The average size of the Eu/Eu_N anomaly is ca 1.5.*

Detrital carbonates are included in the sandstone as inferred from strong correlations between MgO, CaO and LOI in Table 17 and confirmed by petroscopy. Presence of quartz grains is evidenced by the negative correlation between SiO_2 and Al_2O_3 representing aluminosiliciclastic minerals. Strong correlation between TiO_2 and REE and to some degree Zr is interpreted as sedimentary sorting of rutile and zircon as heavy minerals and inclusions of REE and Ti in zircon. Na_2O absence of correlation with other elements is noted.

	SiO2	Al2O3	Fe2O3.T.	MnO	MgO	CaO	Na2O	K2O	TiO2	P2O5	LOI	Zr	sumREE
SiO2	1.00	-0.86	-0.50	-0.13	-0.67	-0.49	-0.28	-0.62	-0.58	-0.68	-0.66	-0.05	-0.68
Al2O3		1.00	0.28	-0.32	0.30	0.02	0.52	0.72	0.34	0.54	0.24	-0.20	0.61
Fe2O3.T.			1.00	0.39	0.71	0.44	-0.15	0.20	0.57	0.78	0.70	0.33	0.54
MnO				1.00	0.62	0.76	-0.37	-0.23	0.23	0.12	0.65	0.29	-0.04
MgO					1.00	0.71	-0.37	0.36	0.75	0.63	0.92	0.49	0.65
CaO						1.00	-0.24	-0.03	0.58	0.36	0.89	0.40	0.43
Na2O							1.00	-0.06	-0.44	0.05	-0.35	-0.77	-0.29
K2O								1.00	0.50	0.26	0.22	0.25	0.73
TiO2									1.00	0.69	0.78	0.78	0.96
P2O5										1.00	0.63	0.27	0.73
LOI											1.00	0.52	0.68
Zr												1.00	0.74
sumREE													1.00

Table 17. Correlation coefficients between major elements and REE from sandstone beds in the PAF M2 – M5, with data from ICP dataset. Positive correlations >0.7 are marked with blue and negative correlations <-0.7 are marked with yellow.

The variations in concentrations of silica/aluminium ratio, Zr and HREE over members 2 – 5 are displayed in Figure 59. The difference between M5 and the other members is evident with considerably higher Si to Al content and enrichments of zircon and heavy REE. This is interpreted as meaning more mature well worked sediments have formed the M5 sandstone beds compared to more arkosic feldspar-rich immature material deposited in the M2 – M4 beds. Arkose originates from physical weathering of granitic bedrock deposited in

cold and/or arid climate whereby more extensive chemical weathering is avoided. More sorting of heavy minerals had also taken place in the M5 deposition. Different processes are thus responsible for the creation of the M5 beds as compared to the other beds.

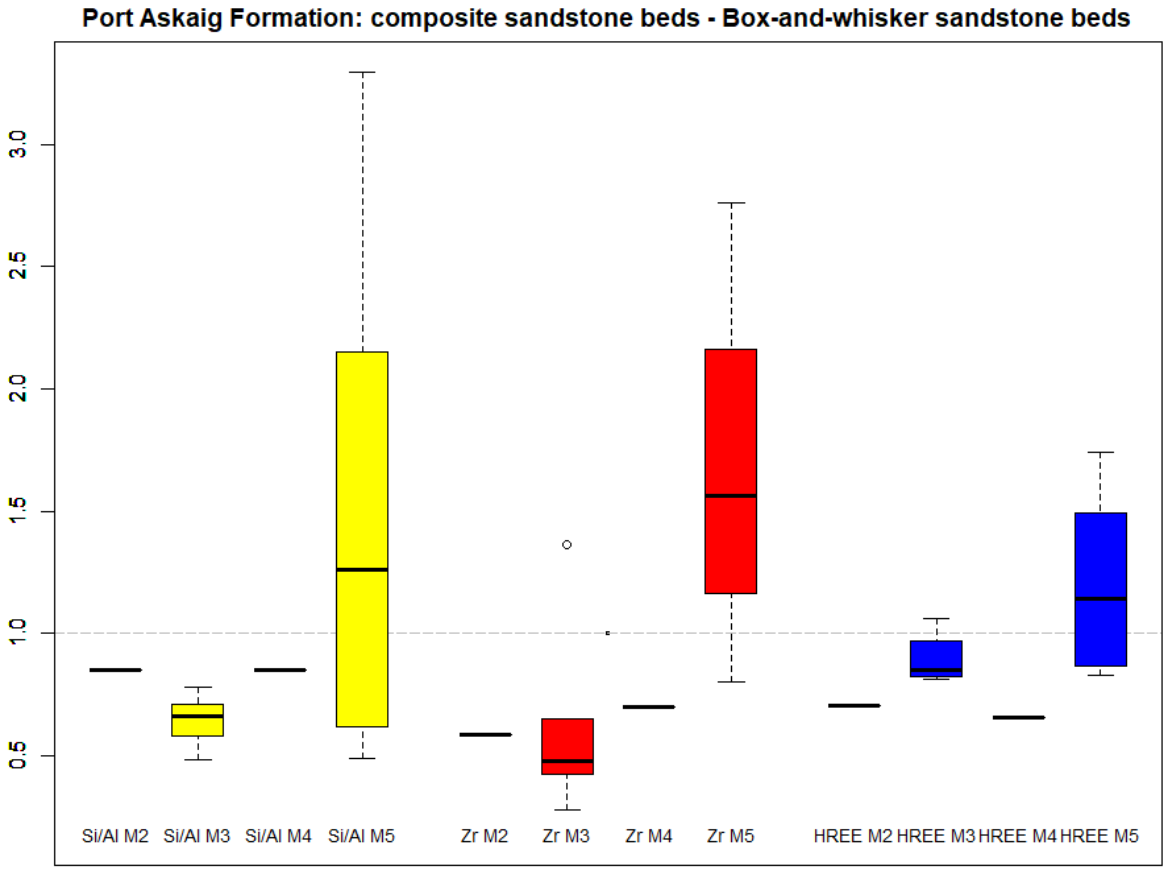

Figure 59. Box-and-whisker plot of Si/Al ratio, Zr and sum of heavy REE from sandstone beds in the PAF M2 – M5, with data from ICP dataset. The Si/Al ratios are marked yellow, Zr red and heavy REE blue and are normalized to their respective total averages. The data are separated into M2 to M5. For other comments to box-and-whisker plots, please refer to Figure 11.

The trend of several elements concentrations in Figure 60 and 61 show similar results as in the box-plots above, with increasing SiO_2 and Zr and decreasing Al_20_3 and Na_2O in M5 sandstone beds. K_2O and MgO show no distinct trends.

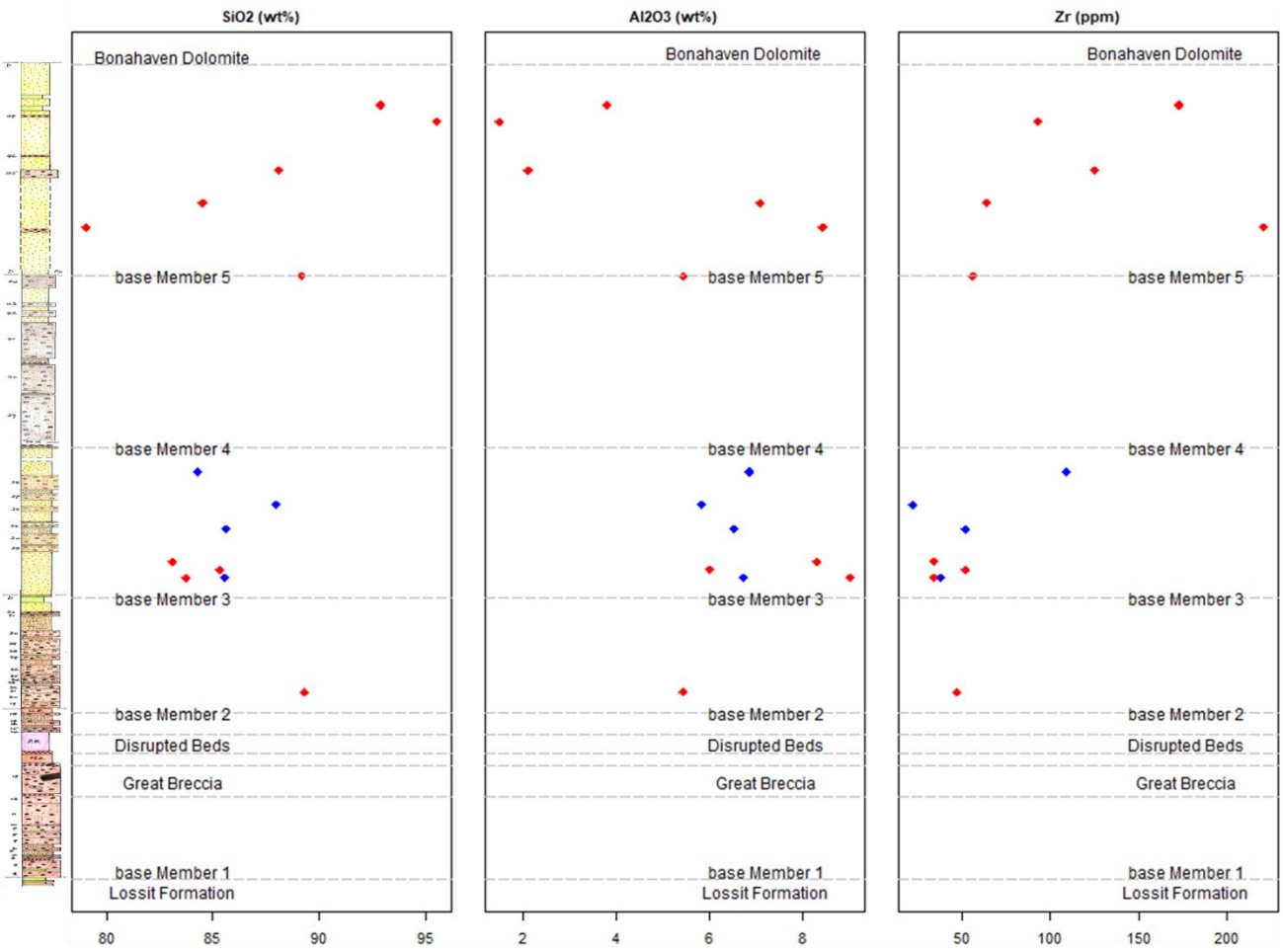

Figure 60. SiO_2, Al_2O_3 and Zr trends from ICP data for sandstone beds in the PAF M2 – M5. The concentration of each element is given on the horizontal scale. For other comments to this plot, please refer to Figure 30.

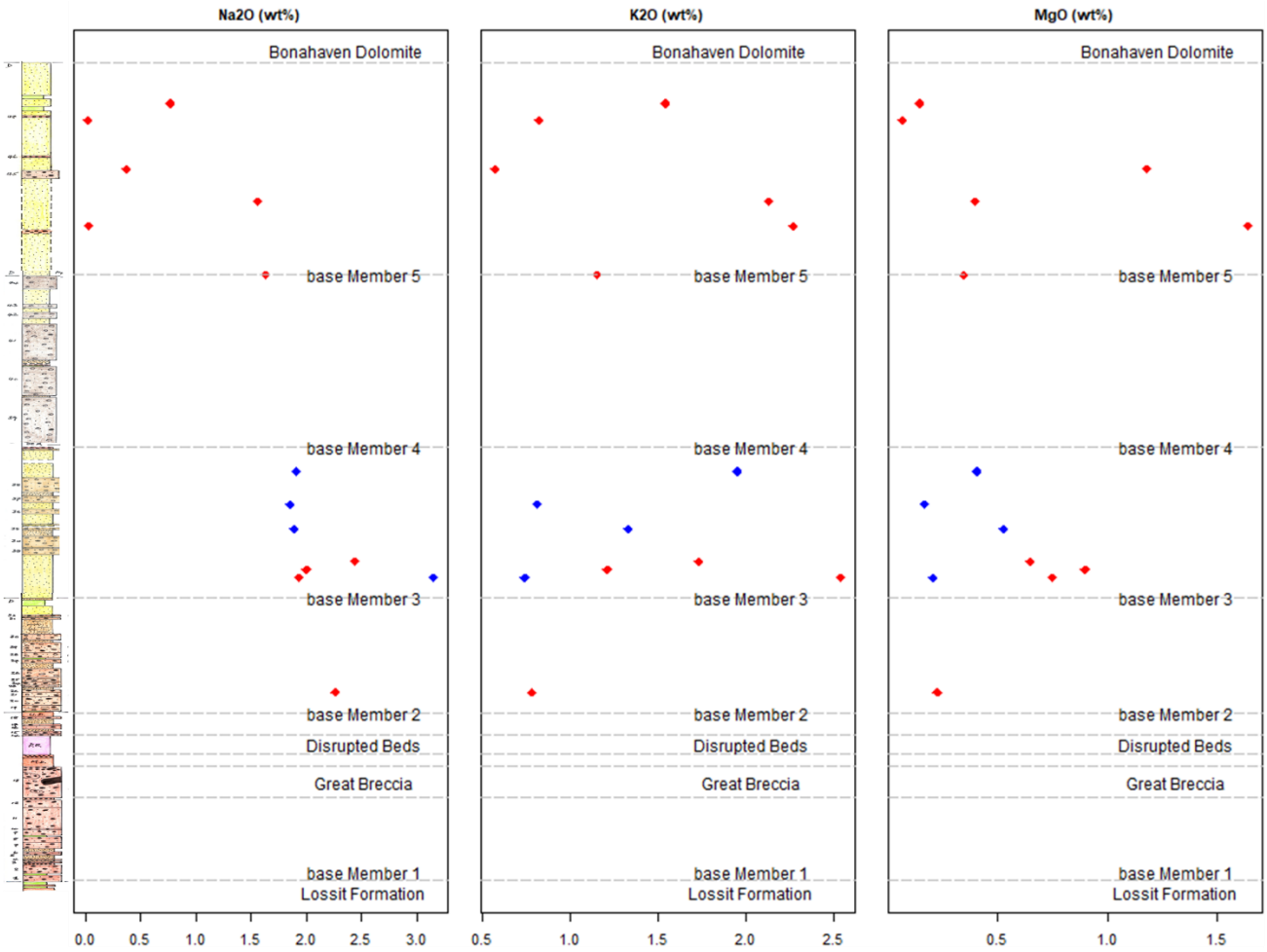

Figure 61. Na_2O, K_2O and MgO trends from ICP data for sandstone beds in the PAF M2 – M5. The concentration of each element is given on the horizontal scale. For other comments to this plot, please refer to Figure 30.

3.5 Lateral and transverse trends within diamictite beds

Sequences of portable XRF measurements were done over individual diamictite beds to investigate the possible occurrence of gradational intrabed variations. Figure 62 shows four silica trends within d1, d23, d33 and d38. Arrows are inserted to indicate possible direction of trends, but due to high variability and scattering in the XRF data the reliability of this is limited except possibly for d23. Two beds seem to indicate an upward decreasing silica content ("fining-up trend"), one an increasing and one an ambiguous trend.

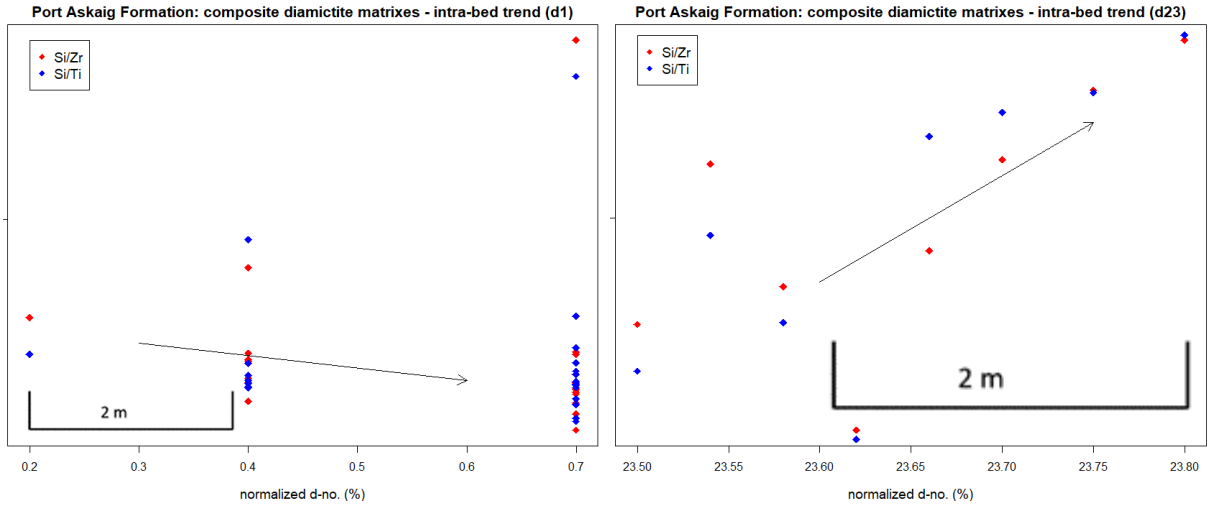

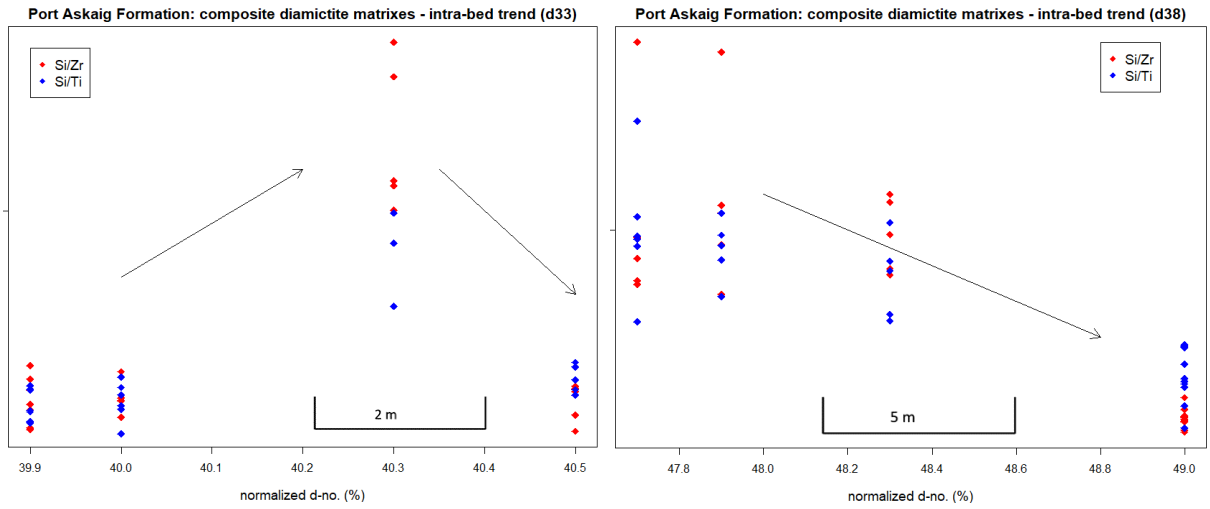

Figure 62. Intrabed trends of Si in diamictite matrix over d1, d23, d33 and d38 with data from XRF dataset. The Si data were normalized to Zr (red marks) and Ti (blue marks) to minimize effects from LE and Cl dilution and the resulting ratios were further normalized to their respective averages. The vertical scales (not shown) indicate the variation in the normalized Si to Zr respectively Ti ratios. The horizontal scale gives the normalized d-number, i.e. relative position within the diamictite bed within the PAF and the scale bars give the corresponding approximate stratigraphic height. Interpreted trends are indicated with inserted arrows.

Two transverse and one lateral intrabed measurement were also made using 3 samples for ICP analysis per bed. The standard deviation for major and some trace elements were calculated for each bed and compared with two sequences of interbed variation for close-laying beds (Table 18). The lateral intrabed trend shows consistently lower standard deviations which indicate a laterally more homogenous composition. The transverse intrabed variations are larger and of similar magnitudes as the interbed data.

		total	intra- and inter-bed standard deviation									
d-bed	direction	offset, ca (m)	SiO2	Al2O3	Fe2O3(T)	MgO	CaO	Na2O	K2O	TiO2	Zr	Rb
d30-d32	transverse	27	5%	4%	15%	25%	24%	74%	19%	1%	6%	21%
d16-d18	transverse	16	8%	4%	17%	15%	21%	20%	9%	9%	10%	8%
d41	lateral	4	0%	2%	5%	4%	32%	18%	9%	8%	4%	9%
d40	transverse	32	14%	50%	40%	45%	43%	53%	51%	55%	33%	51%
d1	transverse	3.3	10%	30%	10%	14%	16%	27%	38%	38%	27%	36%

Table 18. Variance in major elements data in diamictite matrixes from ICP dataset, measured transverse over d1 and d40 and lateral over d41 plus over three beds d16-18 and d30-32. Data in table are given as normalized standard deviations of mean concentrations calculated from three samples in each case.

The above data indicate that the matrix composition on a local vertical scale is chaotic, and that no clear gradational trends can be seen. This is believed to be consistent with a sub- or proglacial transport of glaciogenic material. However, on a larger scale over several diamictite beds and members distinct trends do exist as seen in sections 3.1 – 3.4.

3.6 Weathering indexes

3.6.1 CIA

CIA (Nesbitt and Young, 1982) was calculated using the method proposed by McLennan (1993) for estimating the CaO* (refer to review of proxies in section 1.4.1). The applied method for estimating CaO* results in an average CIA of 58 for the PAF diamictites.

A stochiometric approach was also used to assess the validity of the method used for estimating CaO*. Here OH in muscovite (based on moles K_2O) was first eliminated from LOI, with the remaining part assumed to contain only CO_2. From this the corresponding CO_2 portions related to MgO and MnO were eliminated, giving a residual assumed to come from $CaCO_3$ only. In a similar fashion Ca sitting in apatite was also eliminated from the total CaO. Provided the remaining moles CaO minus moles Ca from the stochiometric calculation of $CaCO_3$

was positive, the value was used to represent CaO*, and if negative CaO* was set to zero. This gave an average CIA value of 60 which is close to the value achieved with the method used.

According to Nesbitt and Young (1982) average shale has a CIA value of 70-75, glacial clays 60-65 and un-weathered granites and granodiorite rock 45 – 55. The CIA values from the ICP dataset for the PAF diamictite were plotted in a ternary diagram (Figure 63) and vary from matching un-weathered rock over glacial clay up to shale. Minerals were also plotted in this diagram where feldspar has a CIA of 50, muscovite about 75, illite 75-85 and kaolinite close to 100. The PAF data points show a linear weathering trend from an upper continental crust composition to muscovite. An ideal weathering path predicted from kinetic leach rates should in theory be subparallel to the A-CN join according to Fedo et al (1995) but in actual data this path is often shifted towards a more potassium-rich composition.

In addition to the above uncertainties in estimating the silicate fraction of CaO, CIA is also sensitive to variations in grain size and possible sorting during transport of the sedimentary material before deposition, as well as possible post-depositional metasomatic potassium alterations and albitization. This will be further discussed in section 4.1.

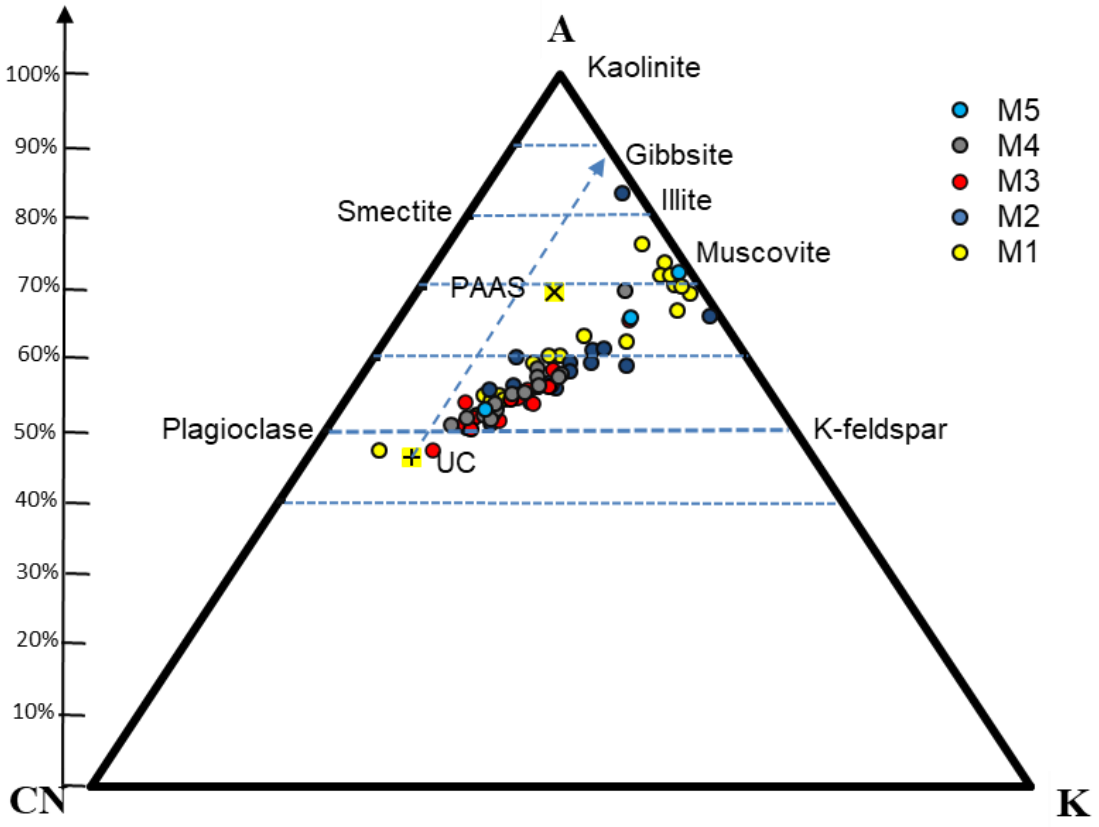

Figure 63. Ternary CIA diagram following McLennan's (1993) procedure. The vertical bar on the left side gives the CIA scale together with the dashed horizontal lines within the triangle. The vertices are marked A=mole proportion of Al-oxide, K=mole proportion of K-oxide, CN=mole proportion of Ca- plus Na-oxide. The PAF diamictite matrix data from the ICP dataset are colour coded for different members according to legend within the triangle. The ideal weathering path based on kinetic leach rates is indicated by a dashed arrow subparallel to the CN-A join. Major minerals compositions are shown together with average composition of upper continental crust (UC) and shale (PAAS) (McLennan, 2001).

The CIA level per member is shown in Figure 64. Members 2 – 4 show consistently low glacial clay values with an interquartile range of 52 – 58 (mean 56). Member 5 has a range 59 – 69 (mean 63.5) being closer to shale. Member 1 has the largest variation with an interquartile range 55 – 70 (mean 62). In Member 1 most of the variation is in the diamictites from the Great Breccia with 60% of these samples above 70.

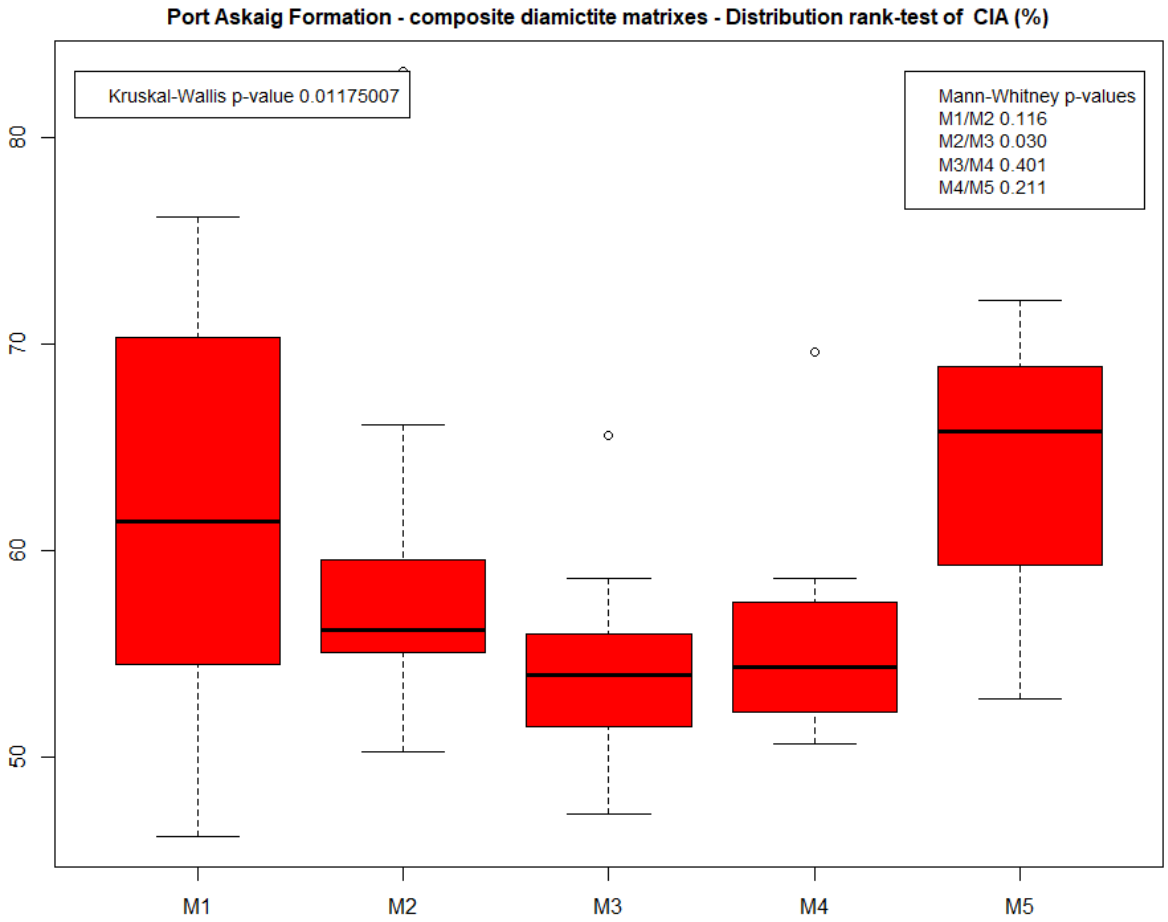

Figure 64. Kruskal-Wallis and Mann-Whitney rank-tests of CIA distribution. For comments regarding rank tests please refer to Figure 11 and regarding box-and-whisker plots to Figure 18.

3.6.2 Other weathering indexes

In addition to CIA the chemical weathering indices of PIA, CIW and STI (Price et al, 2003; Meunier et al, 2013) were also calculated from the ICP dataset (see review of proxies in section 1.4.1).

The four weathering proxies CIA, PIA, CIW and the inverse of STI were plotted over the PAFs stratigraphic column (Figures 65 and 66). They show a similar large-scale trend as CIA, with a large variation span in Member 1 including a group of data points with high values, more focused and lower values in Members 2 – 4 and then, again, higher and more variable values in Member 5. On a narrow intra-member scale, it is however more difficult to distinguish clear patterns. Time lags during accumulation and transport of the sedimentary material, including reworking and intermediate repositories, need to be considered: they would have an obvious impact on the resolution of the data.

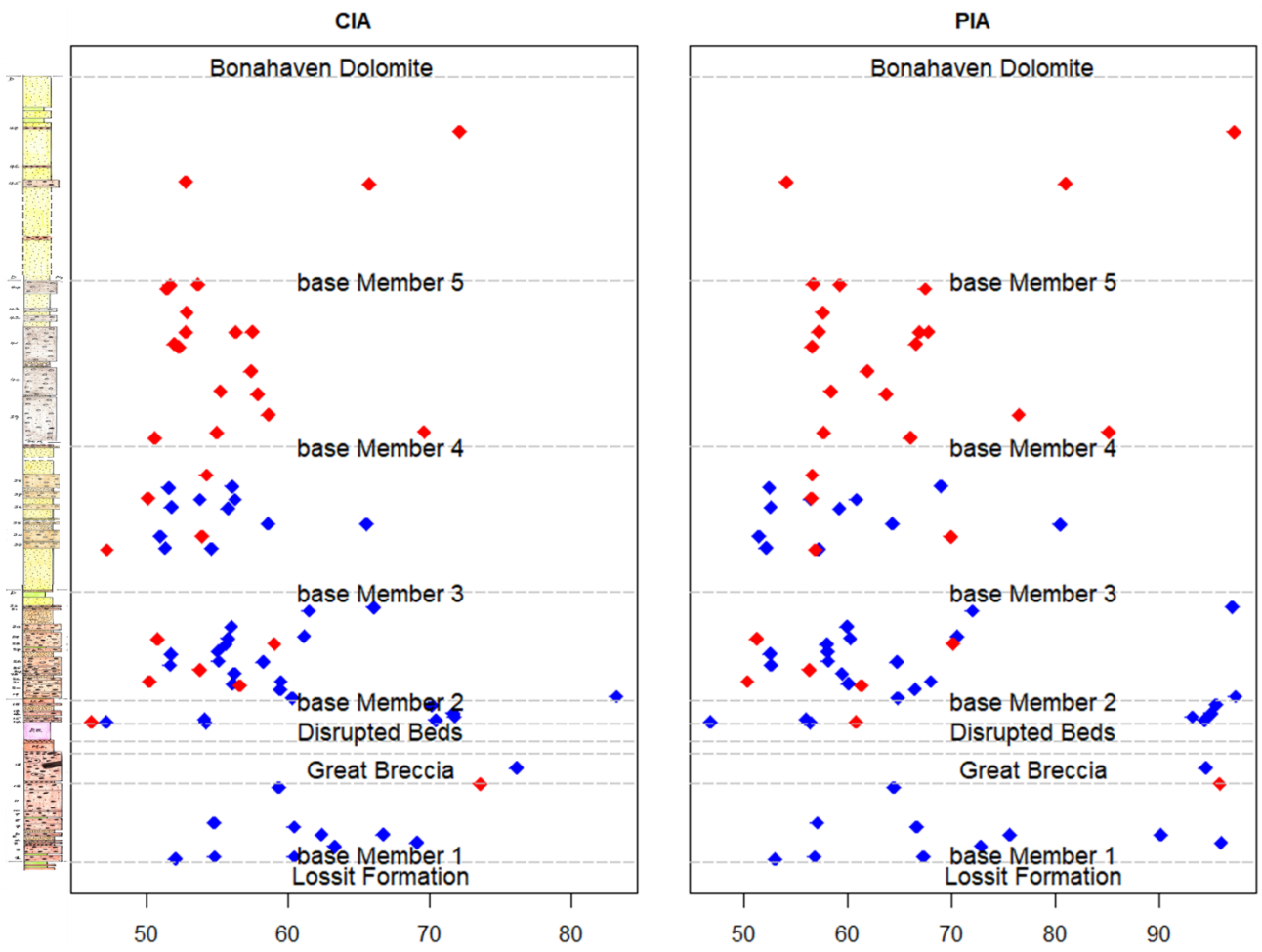

Figure 65. CIA and PIA trends from ICP data over the PAFs stratigraphic column. The CIA respectively PIA % values are given on the horizontal scale. For comments concerning the stratigraphic column and legends, please refer to Figure 30.

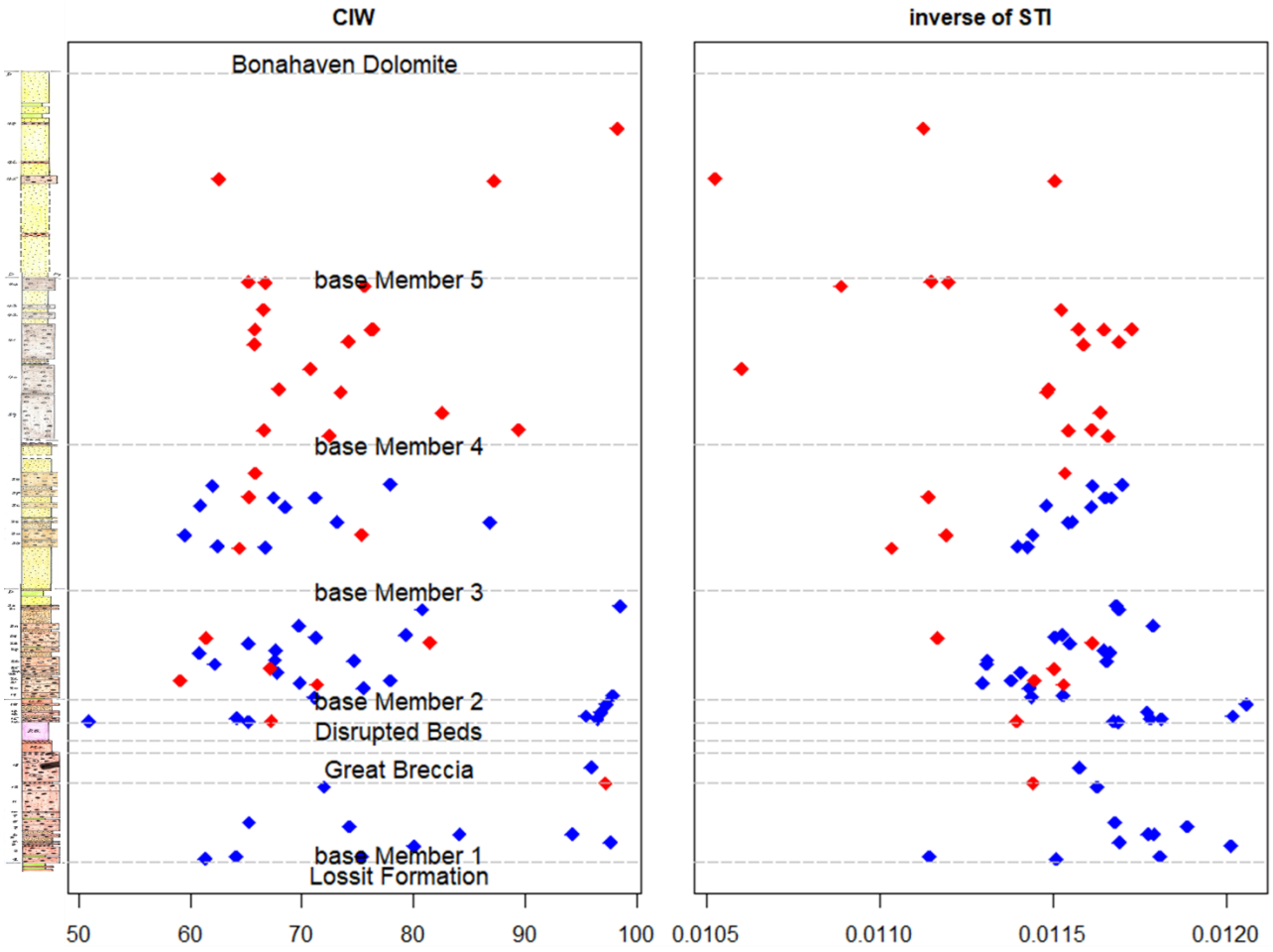

Figure 66. CIW and inverse of STI trends from ICP data over the PAFs stratigraphic column. The CIW and inverse of STI values are given on the horizontal scale. For comments concerning the stratigraphic column and legends, please refer to Figure 30.

3.7 Other palaeoclimate proxies

The degree of chemical weathering is linked to climate. The weathering trends above can thus also be taken to show the climatic variation during the deposition of the PAF. Other element ratios can also be used as indicators of palaeoclimatic variations where an alternative approach is presented below.

Aluminium and gallium are enriched in clay and especially associated with kaolinite which requires strong chemical weathering caused by a warm and humid climate. Potassium and rubidium are linked to illite which indicate a colder and/or drier climate with weaker weathering. Therefore, ratios of those elements can reflect the relative abundance of kaolinite versus illite in the sediments and thus the type of conditions prevailing during its accumulation and deposition. High Ga/Rb and low K_2O/Al_2O_3 ratios would thus indicate “kaolinitic” conditions while the opposite would be true for an “illitic” climate (Hieronymus et al., 2001; Beckmann et al., 2005). Empirical thresholds between kaolinitic and illitic conditions have been used in numerous papers on palaeoclimate (e.g. Xie et al, 2018; Xu et al, 2017; Roy & Roser, 2013; Sarki Yandoka et al., 2015). The Ga/Rb and K_2O/Al_2O_3 ratios together with the climate thresholds are presented in the binary plot in Figure 67, which indicates that the prevailing climate during the deposition of the PAF was cold and arid. Typical values for claystone and siltstone from Lopez et al (2005) are also inserted for reference.

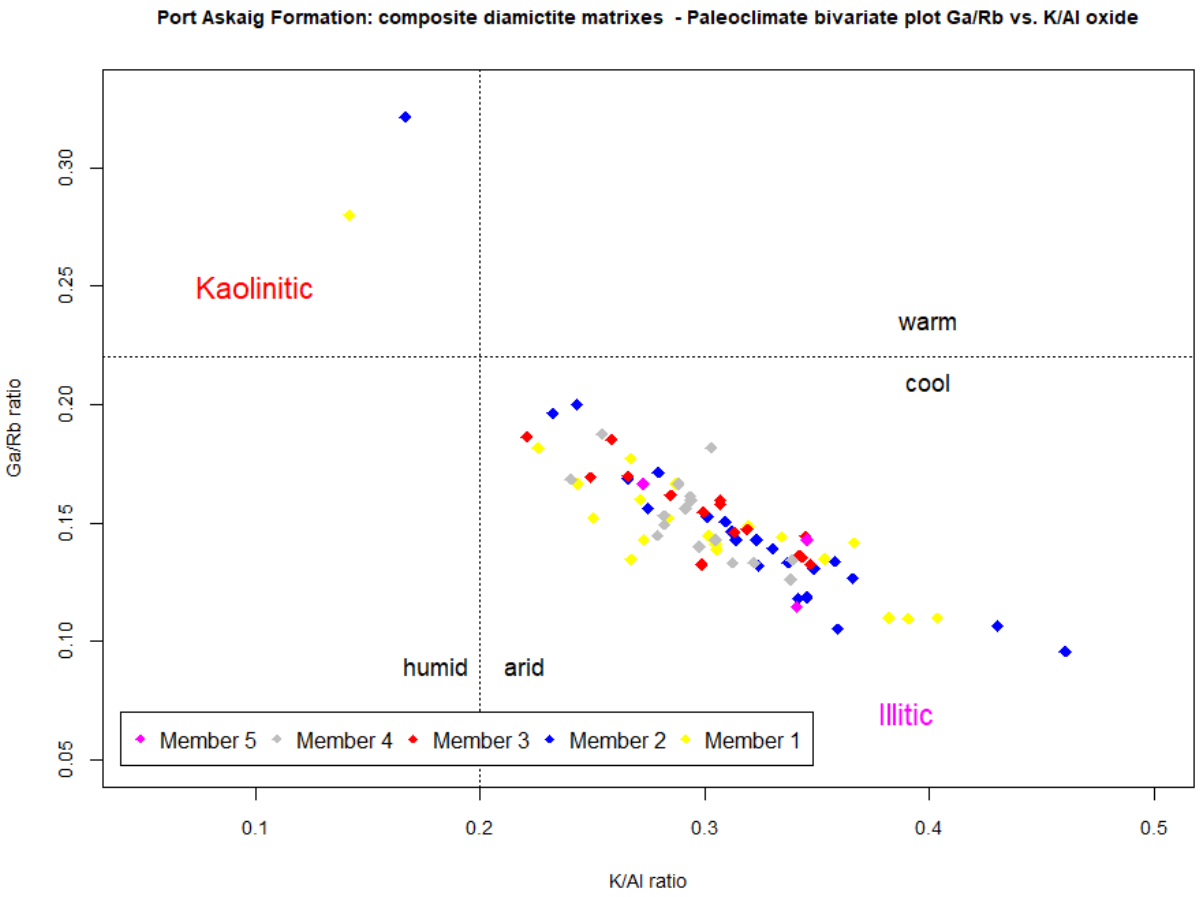

Figure 67. Biplot of K/Al versus Ga/Rb ratios. Data from the PAF ICP diamictite matrix are colour coded for different members according to the legend within the plot. Discrimination areas for different climate types are indicated by dotted horizontal and vertical lines (from Xie et al, 2018; Xu et al, 2017; Roy & Roser, 2013; Sarki Yandoka et al., 2015). Examples of K/Al ratios for claystone and siltstone are shown with vertical lines (from Lopez et al, 2005).

3.8 Provenance proxies

Herron (1988) proposed a method using geochemical concentrations to classify terrigenous sandstones and shales. The ratio SiO_2/Al_2O_3 separates the rock on a scale from quartz-arenites via intermediates to Al-rich shales while the ratio Fe_2O_3/K_2O separates lithic from feldspathic sands. A cross-plot of the logarithm of these ratios (following Podkovyrov et al, 2011 and Herron, 1988) classifies the siliciclastic component of the PAF diamictite matrixes as wacke (Figure 68), here interpreted as a poorly sorted heterogenous mix of rock fragments, quartz and feldspar, and the PAF sandstone beds as arkoses (Figure 69), here interpreted as an immature feldspar-rich sandstone.

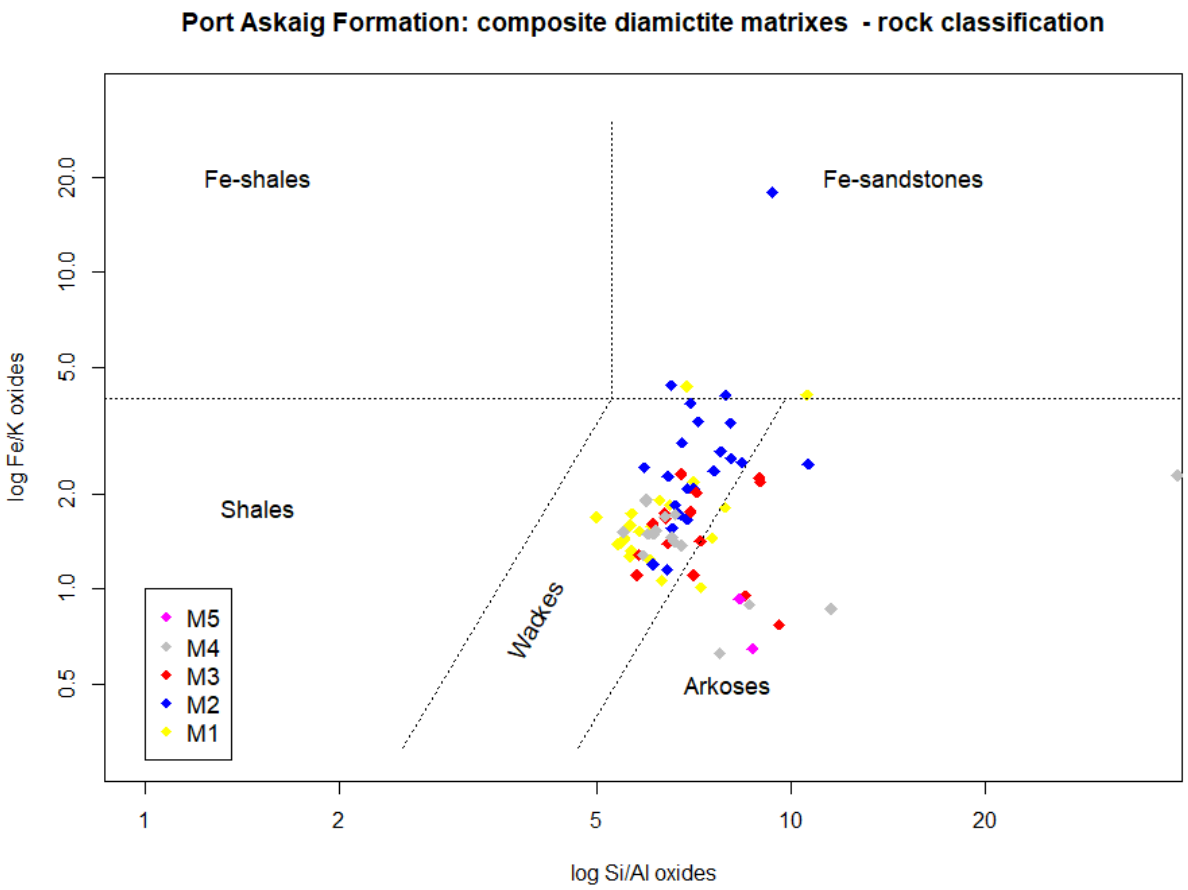

Figure 68. Discrimination diagram for classification of the PAF diamictite matrix from ICP dataset (following Podkovyrov et al, 2011 and Herron, 1988). Data are colour coded per member according to legend within the diagram. Discrimination areas within the diagram are taken from Herron, 1988.

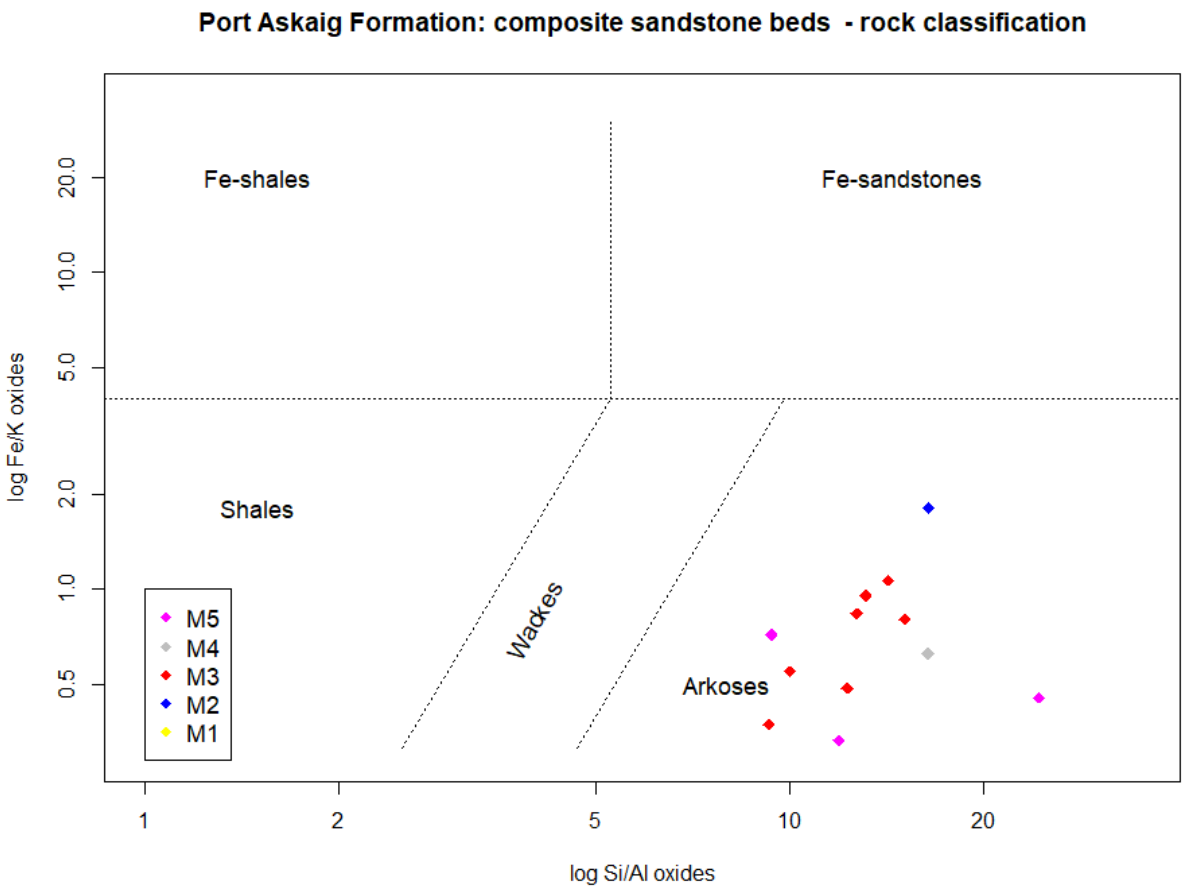

Figure 69. Discrimination diagram for classification of the PAF sandstone beds from ICP dataset (following Podkovyrov et al, 2011 and Herron, 1988). For other comments concerning the diagram, please refer to Figure 67.

4 Discussion

4.1 Early authigenesis and later post-depositional change

The matrix of the PAFs diamictite beds contains both detrital fragments and authigenic minerals. The detrital fragments are made up of small – clay, silt and sand size – particles of different rock types which glacial and glaciofluvial processes have produced and transported to their place of deposition. Their source rock can be igneous (here mostly granite and granodiorite), metamorphic (here mostly gneiss) and sedimentary (here typically carbonates as well as some sandstone). The provenance of the source rock is discussed in section 4.2.

In contrast to the detrital fragments which were transported to their place of deposition, authigenic minerals are formed in situ during and after deposition in response to geochemical processes. Authigenic minerals can be formed by chemical precipitation of minerals, by metasomatism and by the release of volatile elements. Pressure dissolution of minerals in grain-to grain contact can be facilitated by pore fluids. Metasomatism is characterized by mass transfer with interstitial brine flows acting as solvent, with an ion-by-ion replacement in mineral crystals under preservation of the original volume and shape. Volatile components such as H_2O and CO_2 can be released from minerals when pressure and temperature increase.

After deposition and when an overburden of new sediments increase temperature and pressure the deposited material first undergoes diagenesis. This includes both physical and chemical changes, such as compaction and cementation by minerals that precipitate from solution, resulting in a lithified sedimentary rock. With further increase in temperatures and pressure, the lithified sediments can undergo metamorphism. The boundary between diagenesis and metamorphism is not sharp; below metasomatism is treated under metamorphism. Authigenesis during diagenesis and later metamorphism can distort the palaeoenvironmental information contained in the geochemical record when linked to mass transfer of elements. It is therefore important to

uncover such possible authigenic and metamorphic alterations and unravel their effects to obtain a pristine signal from the dataset.

4.1.1 Present composition of main and accessory minerals

Petrographic study of thin sections confirmed that the main mineral assemblage in the matrix were carbonates, quartz, muscovite, feldspar and some amounts of biotite, pyrite and hematite. The carbonates primarily consisted of dolomite and calcite. Some accessory minerals had been identified including chalcopyrite and chlorite. Microscopy showed granophyric intergrowths and at least partial alteration of feldspar into sericite (muscovite).

A series of PCAs were done for the whole PAF and for individual members with stepwise elimination of dominating main minerals such as i) carbonates, ii) detrital elements, and/or iii) Fe_2O_3 and instead including Zr and REE as detrital indicators. Inclusions of other trace elements were also tested for different combinations. From this analysis the following inferences were made:

- The addition of Fe into the system which took place at the base of M2 (and in the Disrupted Beds as documented in Dahlgren B.Sc. thesis, 2018) was not from igneous detrital sources (PC2 in Figure 70) but through other processes. In contrast to the events which provided this ironstone beds, it is noted that the stable background Fe component which otherwise is seen in the PAF is linked to detrital components (PC3 in Figure 70) both in M1 up to and including the Great Breccia and again after mid of M2.
- Fe covaries with P within M2, but less so in other members where the PCs representing Fe (PC2 in Figure 70) and carbonates (PC1 in Figure 70) move more in tandem. This suggests that at least a portion of Fe sits in the dolomite, located in dolostone concretions. Fe could also be present in the form of siderite in concretions. Since Mg easily substitute for Fe in siderite, there should be a portion of magnesite in these concretions. Stoichiometric calculations indicate a surplus of Mg versus Ca in the upper members which can be explained by this.
- Mn generally shows high correlation (Table 19) and good correspondence with the carbonates in the PCA combinations, but also appears separate from them (PC4 in Figure 70). Interestingly Mn shows a weaker link to carbonates in M1b (d14 – d18 in M1, i.e. after the Disrupted Beds) and in M2 (Table 19), which here could indicate redox controlled precipitation. Within the carbonates Mn is believed to co-locate with Fe.
- Fe and Mn are likely to have been introduced into the dolomite beds in early diagenetic processes, similar to what has been observed in the Bonahaven Formation (Fairchild, 1985). However, high Fe and Mn concentrations in carbonates can also indicate a high degree of post-depositional alteration through flow of anoxic porewaters (Lang et al, 2016).
- Silica shows up as a unique driver in several PCs in most PCA combinations, which indicate quartz separately from siliciclastic minerals. Quartz can occur both as detrital sand grains and silica cementation released from pressure solution.
- Sodium mostly follows its own path in the PCs, and it is therefore believed to have been separately added to or detracted from the system later, e g from metasomatic processes. In several PC's Na shows up with opposite sign to K (Table 19) which could indicate substitution processes.
- Apatite which includes phosphorus is an accessory mineral in clasts in the PAF (Spencer, 1971) which in the matrix is expected to concentrate together with rutile and zircon. This is seen in M3 – M5 where PC2 (linked to P) and PC3 (linked to Ti and Zr) in Figure 70 covary. However, both P and Fe show a peak in the lower part of M2 (PC2 in Figure 70). The phosphorus wt% in M2 is 0.44 which is more than double the concentrations in the other members which are between 0.13 – 0.20 (Figure 27). Since P easily adsorbs on Fe-oxyhydroxides during precipitation, this can here indicate primary precipitated Fe.
- As expected, Sr consistently follows the carbonate elements. Sr sits in an interstitial position in the crystal structure of calcite but in aragonite substitutes for Ca (Okumura, 1986) which can explain the role of Sr as a signal of aragonitic origins.

- Zr occurs both in detrital PCs but also alone in some PCs. This could signify separate zircon crystals in the silt, possibly as indicator of sorting processes.
- Ga is consistently more aligned with Al than with other elements, which supports the view that it preferentially sits in clay.
- Mobile elements such as Rb and Sc are aligned with K and as LIL elements thus substitute for other mobile major elements.

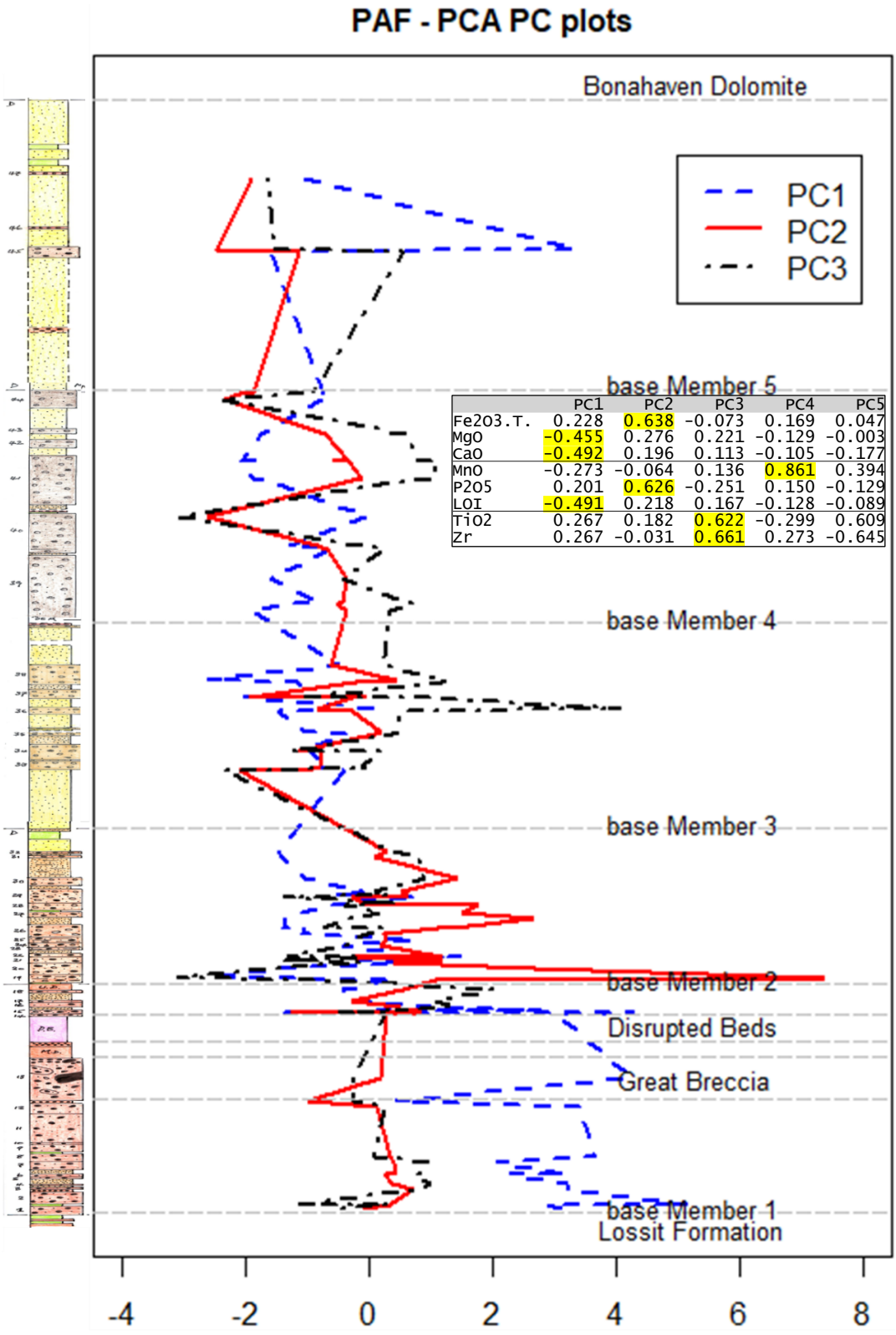

	PC1	PC2	PC3	PC4	PC5
Fe2O3.T.	0.228	0.638	-0.073	0.169	0.047
MgO	-0.455	0.276	0.221	-0.129	-0.003
CaO	-0.492	0.196	0.113	-0.105	-0.177
MnO	-0.273	-0.064	0.136	0.861	0.394
P2O5	0.201	0.626	-0.251	0.150	-0.129
LOI	-0.491	0.218	0.167	-0.128	-0.089
TiO2	0.267	0.182	0.622	-0.299	0.609
Zr	0.267	-0.031	0.661	0.273	-0.645

Figure 70. Example of principal components trends from one of the analysed PCAs. Loadings of PCs from the PCA used in this example are given in the table inserted within the plot where significant values are marked with yellow. PC1 is interpreted as controlled by carbonates, PC2 is linked to Fe and PC3 to terrigenous detrital components. Please note that the sign of PC1 is reversed in the plot to give higher values when the negative weight of PC1 score is larger. For comments concerning PCA and PC loadings, please refer to Figure 29 and Table 10.

	M1	M1a	M1b	M2	M3	M4	M5	PAF
Fe/P	0,69	0,38	0,72	0,97	0,35	0,94	1,00	0,91
Fe/Mg	-0,09	0,44	-0,20	-0,29	0,43	0,89	-0,31	-0,09
Mn/P	-0,29	-0,14	0,17	0,00	-0,43	0,21	1,00	-0,18
Mn/Mg	0,56	0,79	0,49	0,74	0,85	0,46	0,95	0,35
Mn/LOI	0,69	0,80	0,51	0,58	0,90	0,81	1,00	0,37
Na/K	-0,44	-0,42	-0,66	-0,29	-0,21	0,35	-0,23	0,08

Table 19. Correlation coefficients per member calculated for selected pairs of major elements from the PAF diamictite matrix ICP dataset. M1 is also shown divided into two parts where M1a includes diamictite beds d1 – d13 and M1b d14 – d18.

4.1.2 Diagenesis

In the early stage of diagenesis, the main processes are mechanical compaction and possible addition of authigenic primary precipitates from surface environments (such as e. g. carbonate ions and Fe- and Mn-compounds). Dolomitization of precipitated calcium carbonates also takes place relatively early. Later in the diagenetic evolution, cementation becomes the major process. The cement that binds together the detrital fragments contains chemically precipitated authigenic minerals, typically consisting of calcite, silica, hematite or siderite (Marshak, 2012). In the PAFs matrix calcite and silica precipitates have filled most cavities between grains and reduced the porosity. Pressure solution which occurs at higher pressures can play an important role in cementation. Further authigenic alteration can take place due to metasomatic processes.

Fabre et al (2013) showed in experiments that the original carbonates precipitated in the oceans under Snowball Earth conditions most likely was $CaCO_3$ in its aragonitic form, and that the change into dolomite thus was a secondary (possibly bio induced) authigenic dolomitization within a primary limestone formation. Calcium carbonate was thus the precursor of the in situ primary dolomite beds. Magnesium ions replace calcium ions during dolomitization which involves substantial recrystallization. Environments with low Ca:Mg ratio and high temperatures (about 50 °C) such as subsurface and hydrothermal environments are conducive to dolomitization (Fabre et al, 2013).

In addition to dolomitization of primary beds, increase of alkalinity can induce growth of dolomite concretions forming elongated structures following stratigraphic planes. According to Mavotchy (2016) the concentration of Fe is constant, but Mn increases with a factor of 3x within concretions, which thus would give a possibility to distinguish between primary carbonate beds and dolomite concretions.

Dissolved silica released by dissolution is re-precipitated in a variety of forms, including matrix-cement and grain replacement of allochems.

Precipitation of Fe-oxyhydroxide (ferric oxyhydroxide FeO(OH)) forms authigenic iron-rich beds. The dissolved phosphorus that was scavenged by Fe-oxyhydroxides can also be expected to have transformed into apatite in post-depositional diagenesis. Further diagenesis transforms the Fe oxyhydroxide precursor into hematite or magnetite. Hematite is an almost exclusive place for iron in late Proterozoic iron formations according to Cox et al (2013) and Halverson et al (2011), but site observations at the Disrupted Beds clearly indicate a strong magnetic presence from magnetite. Fe oxyhydroxide is unstable at elevated temperatures and can then transform to magnetite under reducing conditions.

The pyrite contained in the PAF is early diagenetic, which required the presence of organic matter, sulphate in the pore water and locally anaerobic chemical environment.

Illite is formed authigenetically during diagenesis when temperatures reach 80 – 120 °C at depth (Frey & Robinson, 1999). The precursor of illite is typically clays such as smectite or kaolinite, but which probably were available in more limited amounts in the glacial clay. Therefore, the pre-metamorphic occurrence of illite was probably linked to sericitization of feldspar.

4.1.3 Metamorphism

Metamorphism changes the mineral composition of pre-existing rocks (protoliths) through a solid-state re-crystallization without melting. This is achieved through a combination of high temperature and pressure and with help of chemically active fluids. The PAF is believed to have undergone a greenschist facies metamorphism during the Caledonian orogeny ca 460 – 480 Ma. Greenschist facies results from low temperature and moderate pressure conditions found in regional metamorphism. On Islay this reached a maximum pressure of ca 1 GPa and temperatures between 410 – 470 ^{o}C (Skelton et al, 1995 cited in Fairchild et al, 2018).

The metamorphism resulted in a major transformation of illite to muscovite during a metamorphic reaction releasing volatile species, primarily H_2O dehydration.

Potassium metasomatism is common (Fedo et al, 1995) which i. a. explains why data in a ternary CIA plot normally do not plot along an idealized weathering path but have a shallower slope deviating to the right. Different processes are involved in potassium metasomatism, for example: i) clay (e.g. kaolinite and smectite) is transformed into illite, ii) illite is transformed into muscovite, and iii) plagioclase is transformed into K-feldspar through substitution of Ca and Na. Each of these processes require the addition of potassium, but only transformation of clay – illite – muscovite will result in a net change of CIA values.

Fedo et al (1995) proposed a method to quantify the K-metasomatism in the CIA ternary diagram. Drawing a line from the K apex through each data point projecting it onto the ideal weathering path would give the pre-metasomatized CIA value according to this method. When this method was applied on the PAF CIA data the average value shifted from 58 to ca 65. However, as discussed below it is believed that most of the potassium metasomatism is related to rearrangements between feldspar and that the portion related to clay minerals converting to illite is minimal. Thus, the impact of a metasomatic overprint is expected to be limited in the PAF CIA values.

Chess-board albite has been observed in granitic diamictite clasts from d29 and upwards (A. Spencer personal communication, 2019) and in this study in thin sections from d26, and which can be a heritage from provenance sources. In addition to this, possible metasomatic albitization of the matrix has also been considered. Na has a low correlation with all detrital indicators such as Zr, Ti and REE, which suggest that sodium had been added to or subtracted from the system at a later stage, e. g. during metasomatism. PCA also indicated that Na were controlled by other processes than detrital components. However, the relative concentration of Na was low when compared to UCC and albite was only observed in thin sections from d26. Na is therefore interpreted as being released in a metamorphic process when replaced by a metasomatic influx of K from country rock. The metasomatic depletion of sodium was thereby balanced by an enrichment of potassium, now located in sericite (primarily in muscovite).

It is believed that the PAF was largely unaffected by metamorphic fluids (Skelton et al, 2019). Fluids from formations underlying the PAF (e.g. Ballygrant and Glenegadale Slate Formations) were spatially restricted to structural channels such as the axial zone of the Islay Anticline (Skelton et al, 2015). This would limit compositional change of element concentrations.

As an indicator of metasomatic fluids, mobile elements (e g Na and K) were plotted as ratios to conservative detrital elements (such as Ti respectively Zr) along the sequence of the PAF beds. A later transport of Na or K caused by metasomatism should materialize as a clear trend over the sequence of deposition. An increase (or decrease) of these mobile elements versus unaffected Ti or Zr would thus signal both the presence and the direction of a possible metasomatic fluid. Figure 71 shows a smaller decrease of sodium towards the bottom of the PAF, but is only statistically significant in relation to Ti. Potassium (Figure 71) shows a similar trend versus Ti but none for Zr. Both plots show relatively large scattering of data with significant correlation only between K and Ti. In summary, this is interpreted as a sign of weak and unevenly distributed metasomatism.

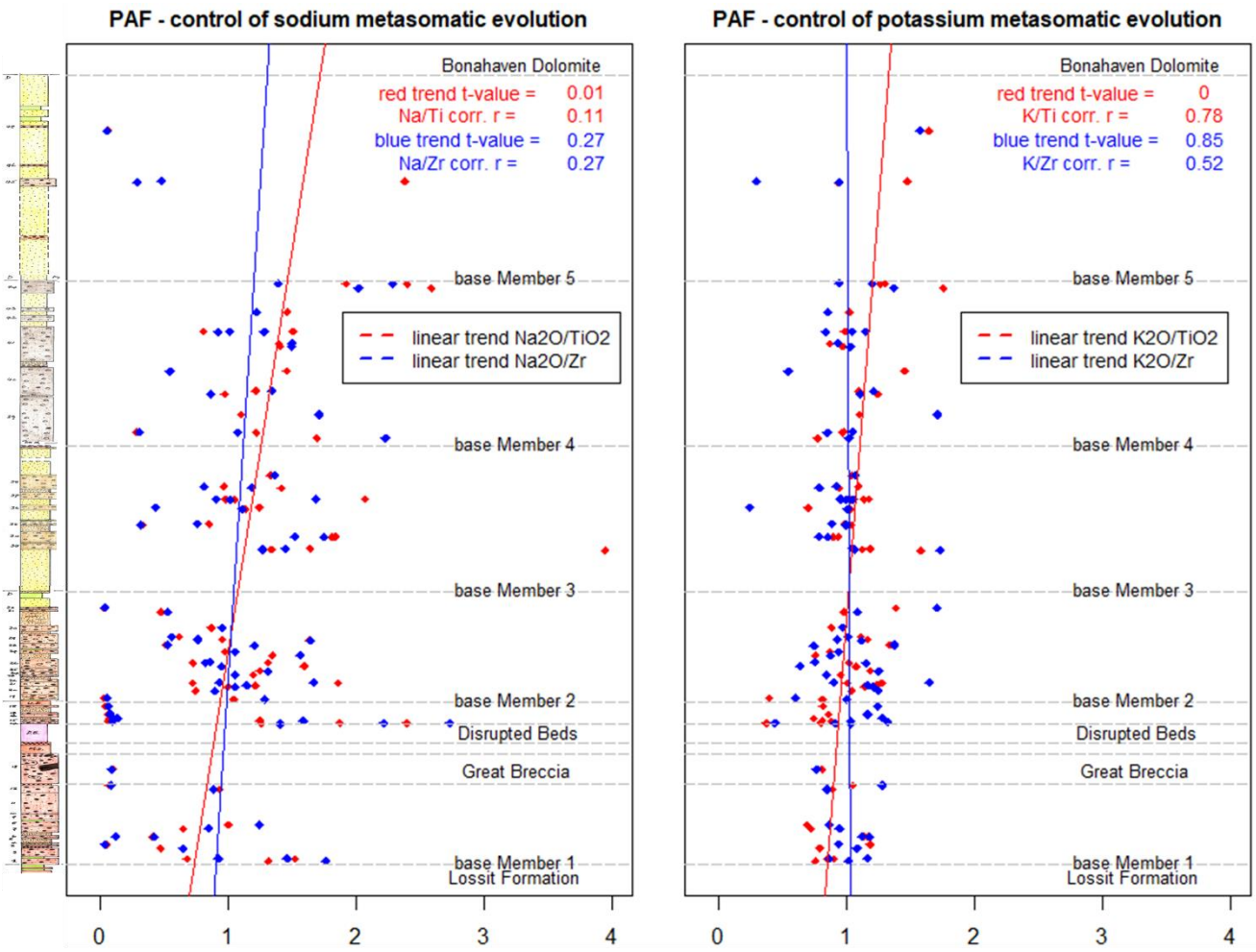

Figure 71. Trend plots for sodium and potassium as ratios to conservative elements Ti and Zr. Na/Ti and K/Ti are marked red and Na/Zr and K/Zr blue. Trend lines from linear regression are included for reference and their t-values (indicating probability that there is no trend, i.e. not any significant trend-slope) are tabulated together with their respective correlation coefficients.

4.1.4 Pre-depositional alterations

Sorting of heavy minerals can distort the geochemical signal (McLennan, 1989). REE is often found in higher concentrations within certain accessory minerals, such as zircon, allanite, sphene and monazite, which can be enriched during sedimentary processes due to their high density and resistance to weathering. The same sorting mechanism which is used in gold panning can lead to a substantial increase of these heavy minerals during fluvial transport of detrital components before deposition. Wind transport of smaller particles can also effectively sort heavier fractions, e g of glacially derived loess (Gaschnig et al, 2016). Glacial transport of till is however less likely to create this effect because of its inherent chaotic nature and is considered to provide robust averages of the bedrock sampled by the ice. The occurrence of hydraulic sorting can be checked by analysing the pattern of REE in the sedimentary material. The heaviest REE is enriched by a factor of 10^2 in zircon compared to the lightest REE when comparing to PAAS or UCC levels, and for allanite the situation is the opposite. Monazite is overall enriched in REE with a factor of up to 10^3 (McLennan, 1989). The extent of hydraulic sorting has been tested in two binary plots (Figures 72 and 73) where a chondrite-normalized ratio of light to heavy REE (here represented by La_N/Yb_N) in unaffected post-Archean rocks stays below 15 and HREE max-min ratio (here represented by Gd_N/Yb_N) lie within a band of 1 – 2 times (following McLennan, 1989). Correlations between elements tabulated in Section 3 indicate some connection between zircon and heavier REE (r=0.65 for Zr to sum HREE) and between sphene and REE (r=0.8 for Ti to sum REE), but no significant correlations for allanite (represented by large ions Ca and Sr) nor monazite (represented by P). Since the concentrations of REE and Zr in the PAF diamictites stay close to the UCC with only limited excursions, this is

together interpreted as an absence of significant general mineral sorting having taken place in the glacial PAF deposits.

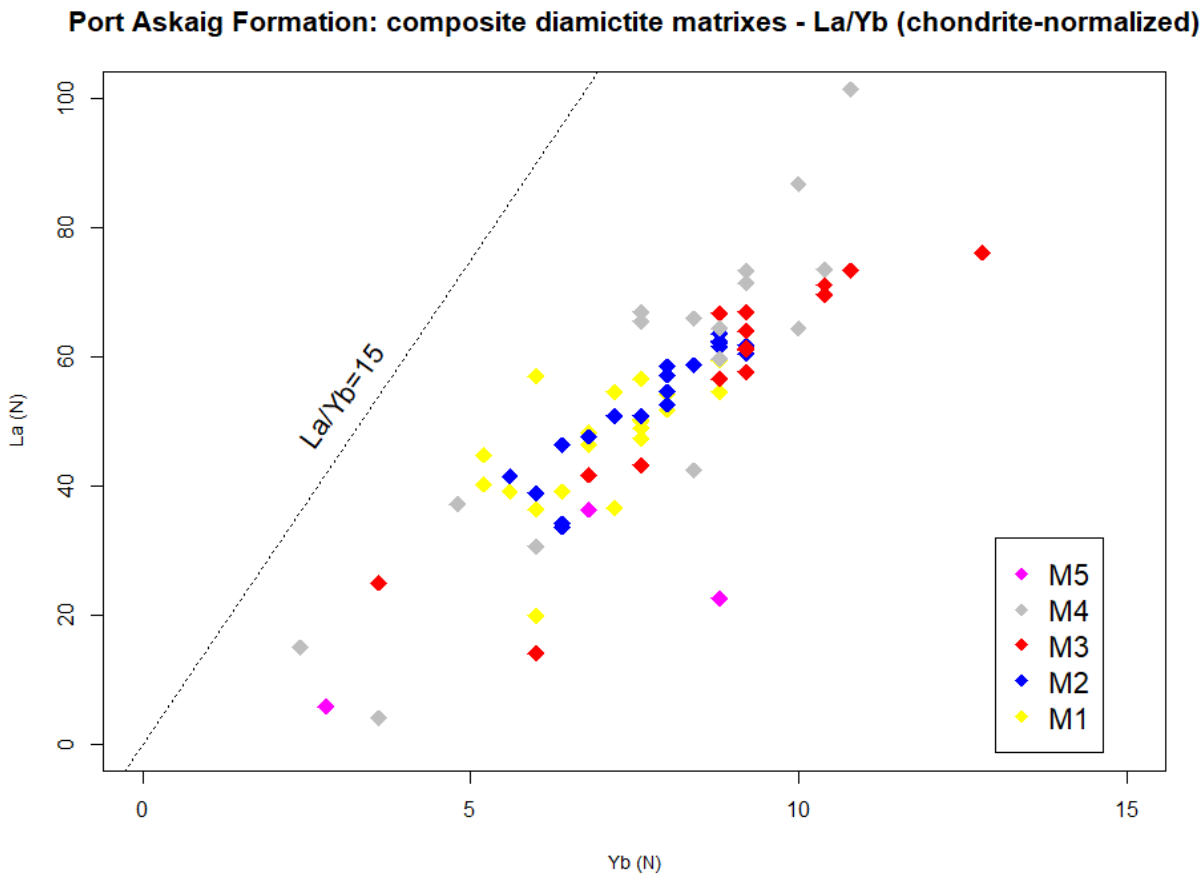

Figure 72. Test of anomalies in distribution of elements between light and heavy REE represented by an Yb_N versus La_N biplot. The PAF diamictite matrix ICP data were normalized to chondrite using norms from Evensen et al. (1978) and Schmitt et al. (1964) cited in McLennan, (1989). Data from individual members are colour coded (see legend within plot). The ratio La/Yb = 15 is inserted for reference.

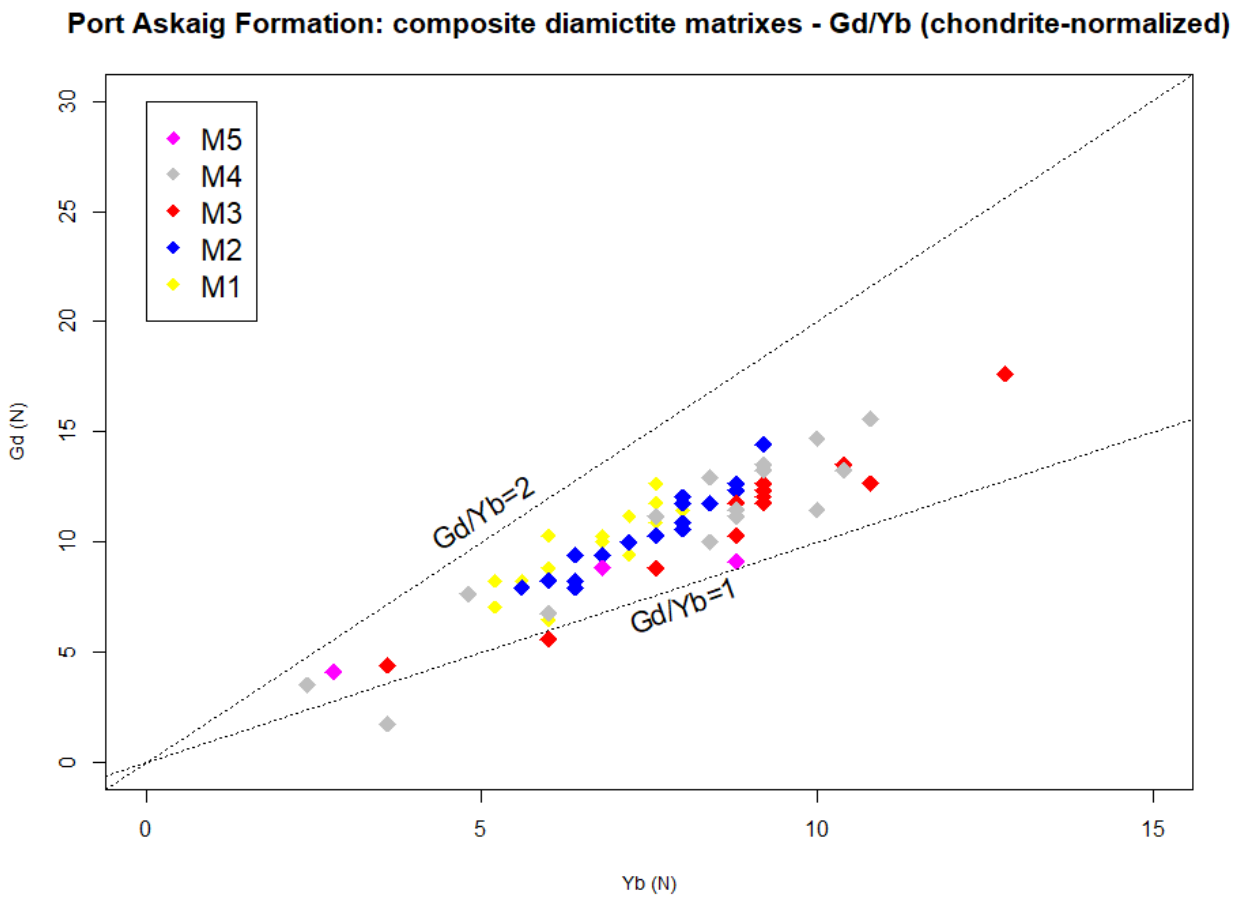

Figure 73. Test of anomalies in distribution of elements within heavy REE represented by an Yb_N versus Gd_N biplot. The PAF diamictite matrix ICP data were normalized to chondrite using norms from Evensen et al. (1978) and Schmitt et al. (1964) cited in McLennan, (1989). Data from individual members are colour coded (see legend within plot). The ratios Gd/Yb = 1 and 2 are inserted for reference.

As a further test of possible grain size influence on geochemical proxies, the correlation between CIA and the ratio between SiO_2 and Al_2O_3 as a proxy for the relation between quartz sand and clay was calculated. This gave r = -0.11 which indicates that CIA is not controlled by grain size. Due to re-crystallization of minerals studied in thin sections, the original grain sizes cannot be fully ascertained. However, the groundmass in the studied samples were typically estimated to be in the range of 0.004 – 0.01 mm. Furthermore, hydraulic sorting not only impacts the relative proportions of heavier minerals but also the distribution of grain sizes in the deposited material. Based on the absence of sorting as discussed above, absence of correlation between CIA and SiO_2/Al_2O_3 and the observed silt sized groundmass, grain size is not believed to influence the validity of the weathering proxies used in this study.

4.2 Provenance of the PAF sediments and clasts

The carbonate clasts that dominate in the lower members of the PAF are gradually replaced with granitic clasts in higher members. It would be natural to expect that these granitic stones were plucked from an igneous basement below the Dalradian Supergroup after the ice had unroofed the cover of sedimentary rock. The most obvious candidate for this would thus be the Rhinns ca 1.8 Ga old igneous complex which crops out i.a. in Islay. However, the PAF granitic clasts are believed to have an exotic origin since they cannot easily be matched with Rhinns or other known crystalline bedrock assemblages exposed in Britain nor Ireland (Fitches, 1996). The granitic clasts are thus considered to be extrabasinal as compared to the locally sourced intrabasinal carbonate clasts seen in the lower parts of the PAF. An obvious question discussed here will thus be what provenance the extrabasinal clasts have and a related question is if the PAFs diamictite matrix has the same composition and provenance as the clasts. The question about what type of process that lead to the overall switch from intrabasinal to extrabasinal clasts is addressed in section 4.3.

Spencer (1971; 1975) proposed that the source lay to the SE of the basin where the PAF was being deposited, and that the exotic material came from the southern parts of the Baltic shield. There are some but uncertain indications that the Sturtian ice moved from SE to NW (present orientation) and that the basin was sloping to the NW (Anderton, 1985; Stephenson, 2013). According to Ali (2017) referring to measurements done by Spencer (1971), the mega-clasts in the Great Breccia are dipping towards SE. Their imbrication could therefore indicate a NW ice flow (Evans et al, 2006). Furthermore, there are some petrographic similarities with the Svecofennian rock types including rapakivi type granites. The Svecofennian domain was built at 2.0-1.8 Ga by igneous rocks formed during subduction and accretion of a series of island arcs. The Svecofennian was part of the Labrador Makkovik – South Greenland Ketilidian – Southwest Scotland mobile belt with similar origin and age. At the start of the Cryogenian, Southwest Scotland was located at the triple junction of the Laurentia, Amazon and Baltica shields, with Baltica located to the SE (Li et al, 2008; Li et al, 2013).

Since this study focused on the matrix of the PAF diamictites, no samples of clasts were acquired. Therefore, geochemical data reported by Fitches et al (1996) has been used, coming from 16 clast samples from the PAF and 6 bedrock samples coming from the Rhinns complex. These clast data were compared with the new PAF matrix ICP dataset and with data from the Geological Survey of Sweden (SGU) for the geochemical composition of the Svecofennian bedrock and Swedish till derived from this bedrock. The Svecofennian bedrock composition was estimated from a random sampling of ca 50 geochemical analyses made within the geographical area of the Svecofennian domain (SGU Geolagret 2020: https://apps.sgu.se/geolagret/). The Svecofennian till composition was estimated from a dataset of till measurements (personal communication with D. Claeson, SGU, February 2020) from which a subset of 1818 analyses from the Svecofennian domain was extracted. However, the concentration of zirconium was influenced by the SGU's sampling methodology (as discussed below), which is why a Swedish general average of till (Ladenberger et al, 2020) was used in certain comparisons involving Zr.

Fedo et al (1995) proposed to use the ternary CIA plot to estimate the original pre-weathered composition of a rock. This is done by inserting a trend line through the CIA data points and extending it to intersect the K-feldspar – plagioclase join, which gives the original feldspar composition. 65 – 90% of the feldspar is plagioclase in granodiorite and in granite >35% is K-feldspar. The PAF CIA data plot (Figure 63) show an un-weathered mix of 73% plagioclase and 27% K-feldspar. The non-carbonate part of the PAFs diamictite matrix therefore has an original average composition resembling granodiorite.

Post-Archean TTG is similar to granodiorite and a major part of the late Proterozoic shields consists of TTG (tonalite – trondhjemite – granodiorite) (35%) and granite (15%) (Condie, 1993). The upper continental crust has on average the same composition as granodiorite (McLennan, 2001). Therefore, the average chemical composition for Archean and Proterozoic TTG and granite compiled by Condie (1993) were also included for comparison, as well as UCC and PAAS (McLennan, 2001).

Till gives a good composite estimate of the composition of the bedrock from which the ice sourced the material (Gaschnig et al, 2016; McLennan, 2001; Taylor & McLennan, 1995). The structure and composition of till may be impacted by the type of glacial deposition, where subglacial deposited till typically is more homogeneous and short-travelled indicating the local composition of the substrate. The two other deposition mechanisms – glacifluvial and ice rafted debris (IRD) – will potentially give a more stratified composition with possible sorting of heavier minerals. The immobile elements in till are not expected to materially change due to weathering during transport or from leaching after deposition. The Swedish till samples were taken from the C-horizon which rarely contains any organic material (C typically 0.11%), and where leaching and other environmental processes have no or very limited impact, with elements almost exclusively contained in primary minerals (Andersson et al, 2020). Till transport distances naturally vary with transport types, where glaciofluvial and especially IRD can be transported over longer distances. The finer silt fractions can be transported much further than clasts. However, studies from Finland have shown that Quaternary deposits rarely are transported longer than 20 km, but in most cases more typically 2 – 3 km (Sohlenius, 2009).

HFS elements and REE are partitioned in melts during crystallization. However, during weathering and erosion of igneous rocks they are relatively immobile and insoluble and are typically transported in terrigenous

components before sedimentation (Albarède, 2009). As seen in section 4.1.4, hydraulic sorting during transport is not expected to have changed the relative proportions of these elements in the PAFs diamictite matrix. They therefore typically reflect the composition of their original source and can therefore be used to assess provenance and tectonic settings. Th and La are more common in felsic rocks while transition metals such as Sc, V, Cr and Co are more abundant in mafic ones.

Figures 74 and 75 display two ternary discrimination diagrams La-Th-Sc, respectively Th-Co-Zr/10 (following Bhatia & Crook, 1986; Lopez et al, 2005; Xie et al 2018). In both cases the data plot within or close to the area for continental volcanic arcs. PAAS, Upper Continental Crust (UC) and average values for Archean and Proterozoic intrusive TTG rock and average Swedish till and Svecofennian bedrock are included for reference.

As seen, PAAS and UC plot close together, which confirms the assumption that that the conversion of the igneous crustal rock to shale does not change the proportions of the immobile insoluble elements used in the two ternary diagrams. It is noted that the Proterozoic TTG plots close to UC but some distance away from the Archean TTG. The PAF diamictites occupy an area between the Swedish average till and the Svecofennian rock.

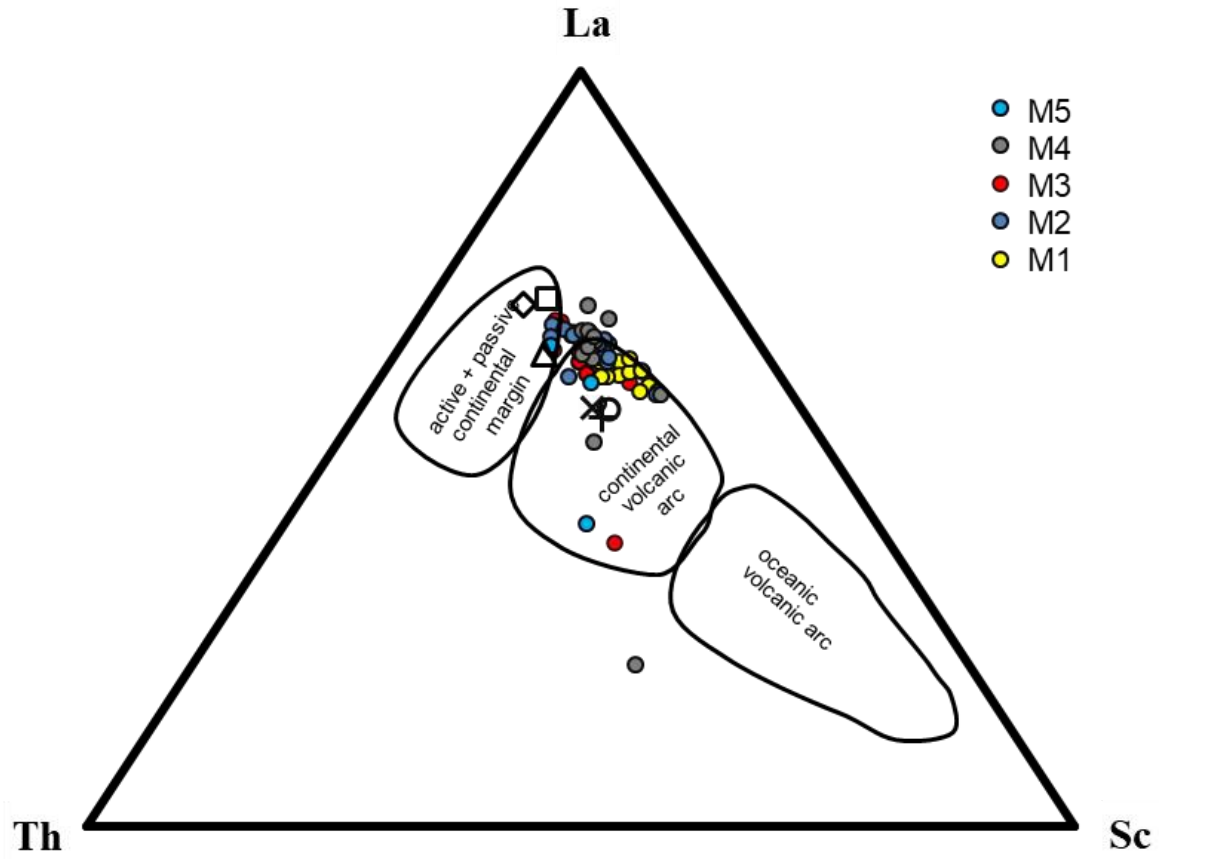

Figure 74. La – Th – Sc ternary discrimination diagram. Discrimination areas from Bhatia & Crook (1986). Legend: **X** *– PAAS (McLennan, 2001);* **+** *– UCC (McLennan, 2001); □ – Archean TTG (Condie, 1993); ○ – Proterozoic TTG (Condie, 1993); Δ – Svecofennian bedrock (SGU Geolagret, 2020);* **◊** *– Svecofennian till (SGU dataset, personal communication Claeson, 2020). Colour coded data per member for the PAF diamictite matrix from ICP dataset according to legend within plot.*

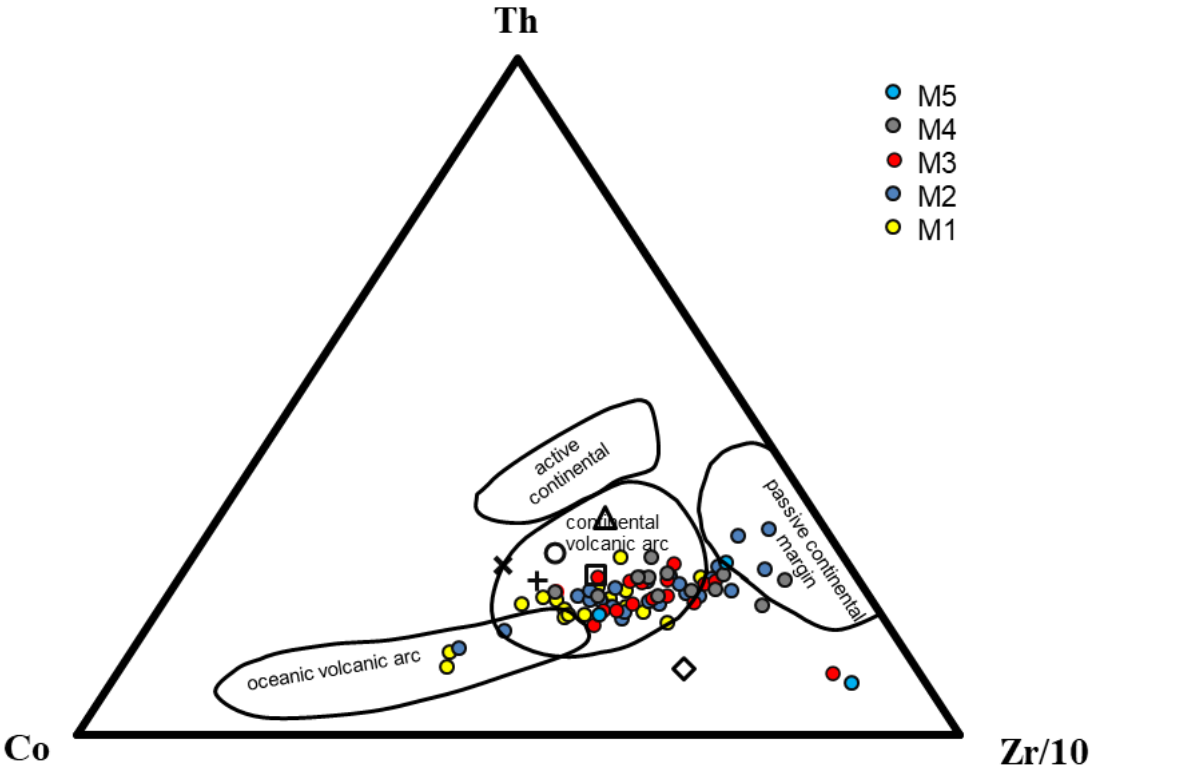

Figure 75. Th – Co – Zr/10 ternary discrimination diagram. Discrimination areas from Bhatia & Crook (1986). Legend: **X** *– PAAS (McLennan, 2001);* **+** *– UCC (McLennan, 2001);* □ *– Archean TTG (Condie, 1993);* ○ *– Proterozoic TTG (Condie, 1993);* **Δ** *– Svecofennian bedrock (SGU Geolagret, 2020);* ◊ *– Svecofennian till (Andersson et al, 2020). Colour coded data per member for the PAF diamictite matrix from ICP dataset according to legend within plot.*

In the following Figures 76 – 79, the geochemical footprint of conservative elements from REE plus Th were used to compare the PAF matrixes and clasts with the Svecofennian bedrock and till derived therefrom, and with Rhinns bedrock.

In Figure 76 following McLennan (1989) methodology, the La/Th bi-plot shows that both the PAF matrixes and clasts and the Svecofennian bedrock and till all plot within the bandwidth (1<La/Th<10) expected for post-Archean rock (McLennan, 1989) but that the Rhinns rock is clearly outside this range. Panahi & Young also (1997) used this to show that the PAF had a post-Archean provenance. However, the Archean TTG and granite also plot within this band, which suggests that the proposed use of La/Th to discriminate for age is not reliable.

The ratio La/Lu in Figure 77 provides a simple test of the slope of the REE concentrations from LREE to HREE. As was showed in Section 3.2, the REE in the PAFs matrix followed the average REE in UCC quite well without selective enrichment or depletion of HREE or LREE. Here it is noted that the PAFs clasts, the Svecofennian bedrock and post-Archean TTG and granite stay well within a band of +/-10% of the PAF matrix average. The Archean TTG and granite and the Rhinns, but also the Svecofennian till show an anomaly. This anomaly in the Svecofennian till is discussed below.

The concentration of REE and HFS elements in the till dataset received from SGU all have similar relative concentrations as those from the Svecofennian bedrock, except for Zr which has a factor 10 lower concentrations. In the sampling methodology used by SGU, it was noted that the material was sorted to include fine fractions (<0.063 mm) only. If this method also eliminated a substantial portion of the more resistant and therefore relatively larger zircon grains, this could impact the pattern of the REE in till. Zircon typically has flat neutral LREE pattern, but a steeply increasing HREE trend reaching 100 times the LREE levels (McLennan, 1989). If sorting for fine fractions excludes zircon grains, this would decrease the slope of HREE component compared to an average unsorted till. To test this assumption, the ratios Gd/Lu and La/Sm were also plotted, where Gd/Lu (Figure 78) tested for slope anomalies in the HREE part only and La/Sm (Figure 79) in the LREE part only.

It is noted that the Svecofennian till still showed an anomalous value in the HREE test but stayed on the average PAF composition in the LREE test. This indicated that the assumption that zircon was depleted in fine fractions of the Swedish till was correct, and that both the Svecofennian bedrock and the till thus have the same REE footprint as the PAFs diamictite matrix.

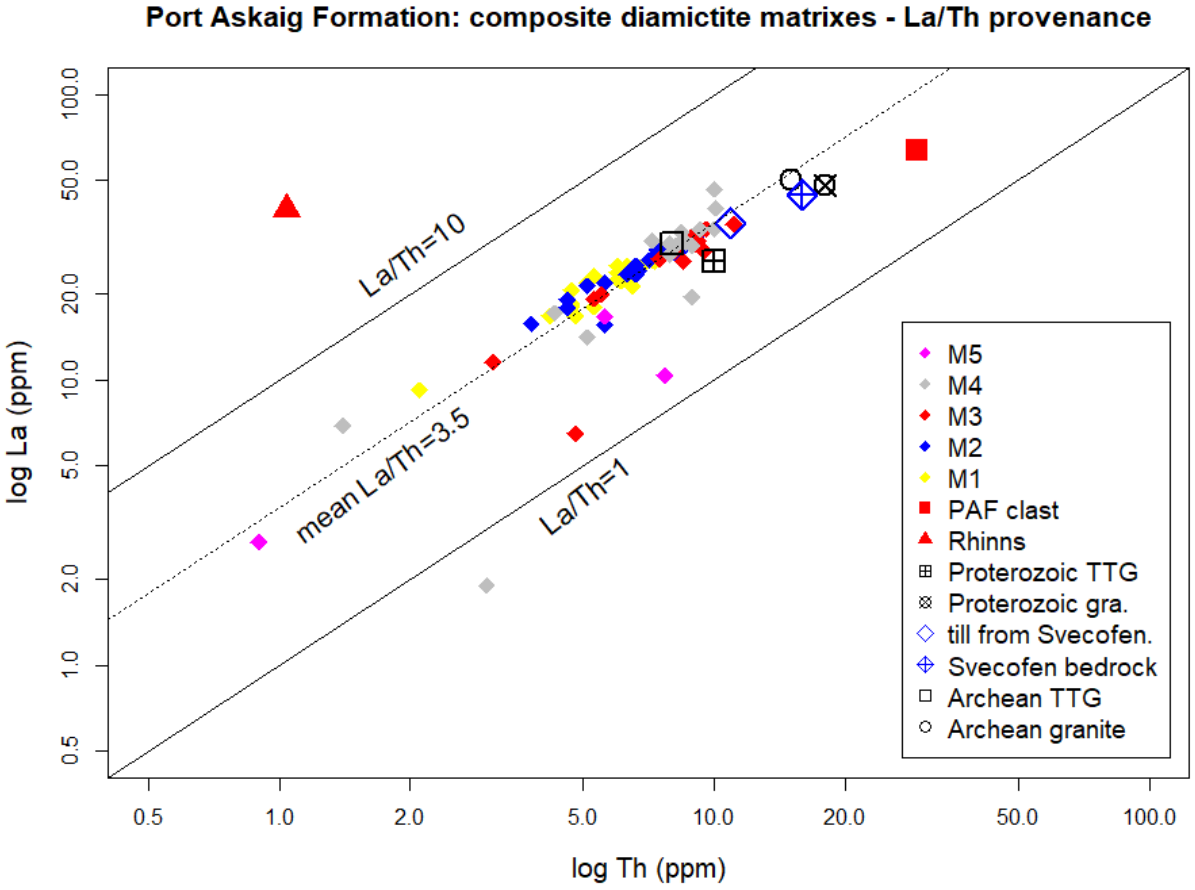

Figure 76. La/Th biplot as provenance test following McLennan (1989). Scales on both axes are logarithmic. Mean PAF value for La/Th and La/Th thresholds of 1 and 10 times are shown in the plot. Included reference data according to legend within the plot: PAAS and UCC (McLennan, 2001), Archean and Proterozoic TTG and granite (Condie, 1993), Svecofennian till (SGU dataset, personal communication Claeson, 2020), Svecofennian bedrock (SGU Geolagret, 2020), sampled data from the PAF clasts and the Rhinns bedrock (Fitches, 1996).

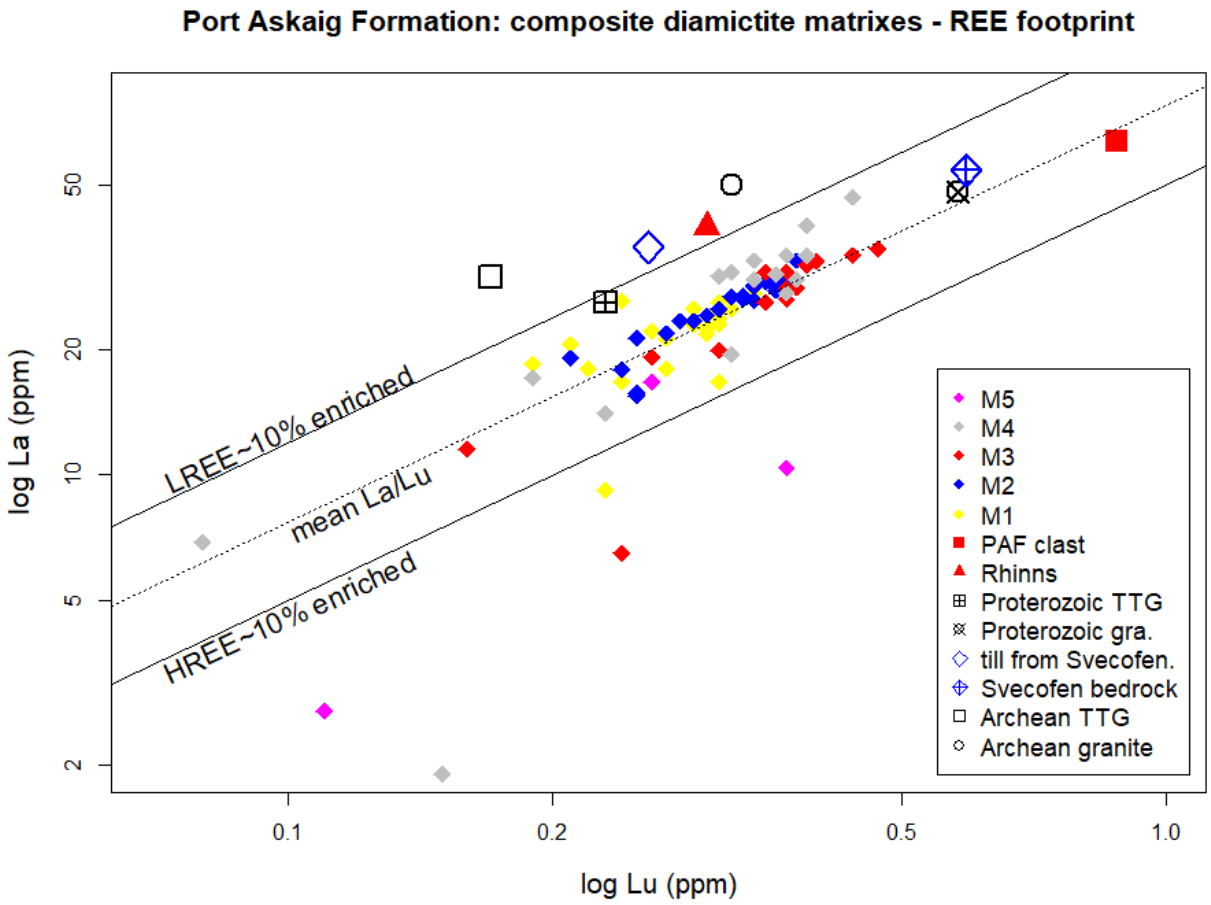

Figure 77. La/Lu biplot as test of LREE/HREE relation following McLennan (1989). Scales on both axes are logarithmic. Mean PAF value for La/Lu and +/-10% thresholds for enrichment of LREE respectively HREE relative this are shown in the plot. Included reference data according to legend within the plot: PAAS and UCC (McLennan, 2001), Archean and Proterozoic TTG and granite (Condie, 1993), Svecofennian till (SGU dataset, personal communication Claeson, 2020), Svecofennian bedrock (SGU Geolagret, 2020), sampled data from the PAF clasts and the Rhinns bedrock (Fitches, 1996).

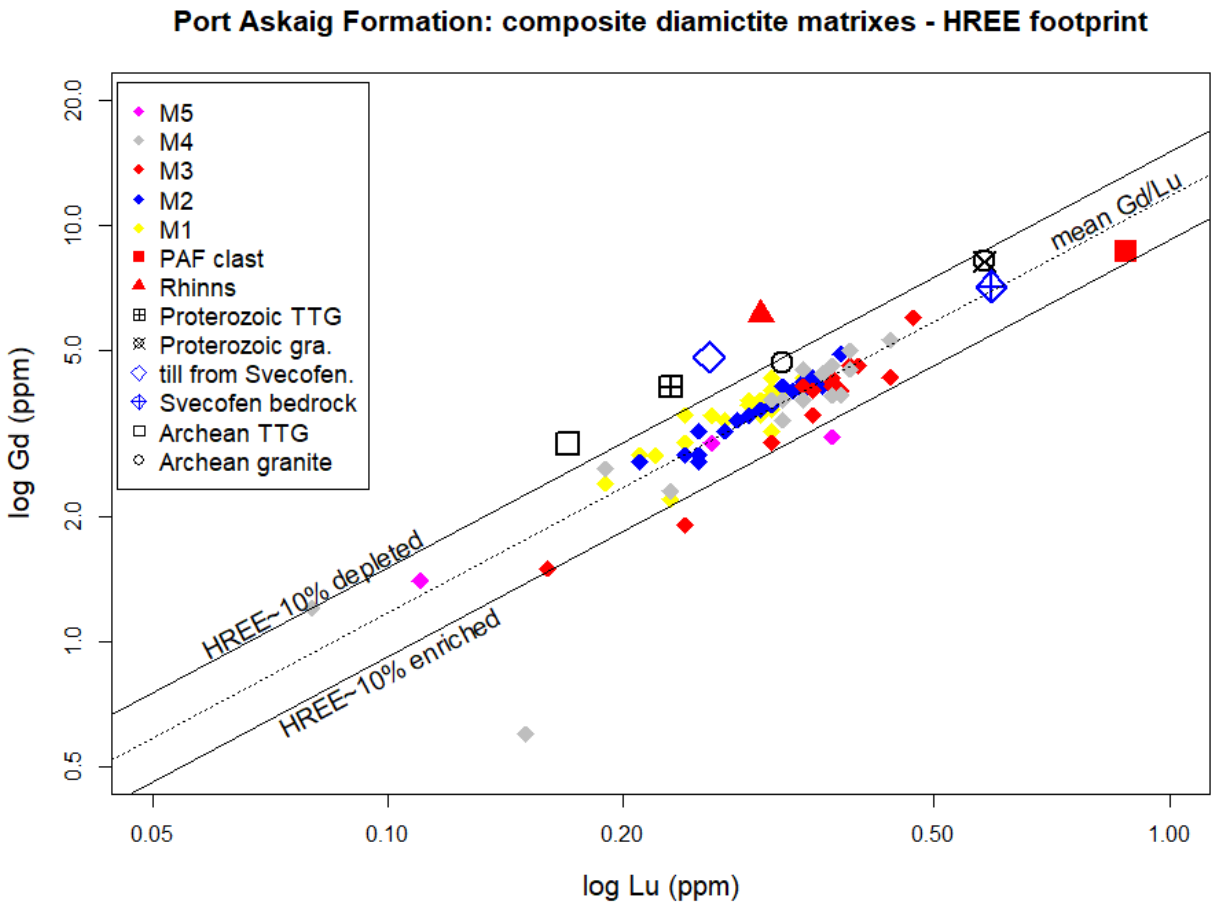

Figure 78. Gd/Lu biplot as test of HREE slope enrichment/depletion. Scales on both axes are logarithmic. Mean PAF value for Gd/Lu and +/-10% thresholds for enrichment respectively depletion of HREE slope relative this are shown in the plot. Included reference data according to legend within the plot: PAAS and UCC (McLennan, 2001), Archean and Proterozoic TTG and granite (Condie, 1993), Svecofennian till (SGU dataset, personal communication Claeson, 2020), Svecofennian bedrock (SGU Geolagret, 2020), sampled data from the PAF clasts and the Rhinns bedrock (Fitches, 1996).

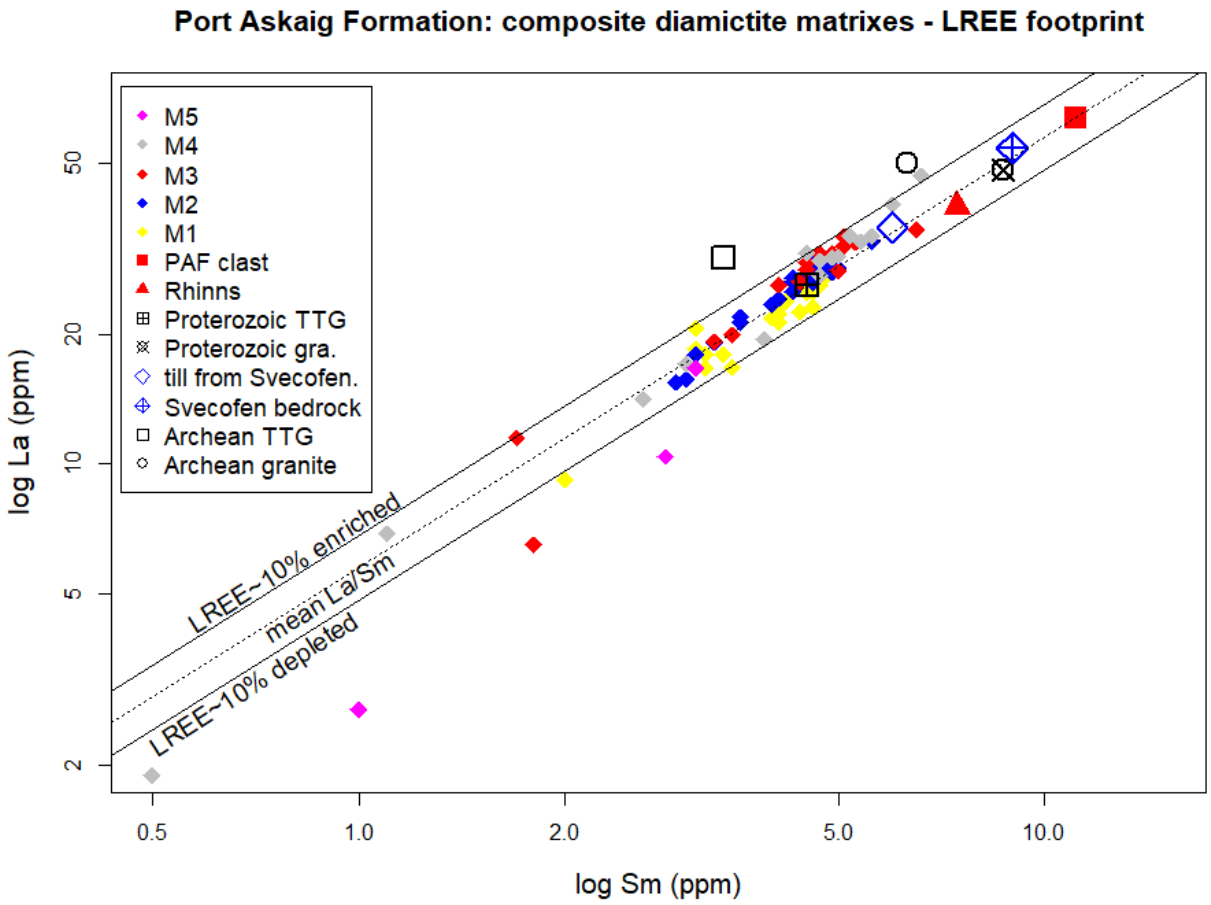

Figure 79. La/Sm biplot as test of LREE slope enrichment/depletion. Scales on both axes are logarithmic. Mean PAF value for La/Sm and +/-10% thresholds for enrichment respectively depletion of LREE slope relative this are shown in the plot. Included reference data according to legend within the plot: PAAS and UCC (McLennan, 2001), Archean and Proterozoic TTG and granite (Condie, 1993), Svecofennian till (SGU dataset, personal communication Claeson, 2020), Svecofennian bedrock (Andersson et al, 2020), sampled data from the PAF clasts and the Rhinns bedrock (Fitches, 1996).

The above interpretations regarding the provenance of the PAF can be summarized as follows:

- The diamictite matrix and clasts have the same composition and thus the same provenance, which also implies that the clasts are unlikely to be dropstones.
- CIA ternary plots indicate crystalline bedrock of granodiorite type as a source for the non-carbonatic portion of the diamictite matrix.
- The tectonic provenance of the diamictites is from a continental volcanic arcs setting, which is also the setting for the Svecofennian domain.
- The diamictites have a similar composition to the Svecofennian bedrock and till derived therefrom.
- The Baltica crustal plate was located to the SE of the PAF during the Sturtian and the direction of the ice-flow was possibly to the NW.
- As already concluded by Fitches et al (1996), the diamictites have a different composition than the samples from the Rhinns complex, which is thus not a source for the PAF material.

Therefore, the source of the extrabasinal part of the PAF diamictites could likely be the Svecofennian domain in the Baltica crustal plate.

4.3 The PAF Members – how to interpret them

As described in section 1.3.2 Spencer (1971) divided the PAF into 5 members which can be correlated over several localities. The following type of questions relating to these members are discussed in this section:

- Is the grouping into five members supported by the geochemical data or are there alternative ways to subdivide the PAF?
- How can the members be described and interpreted from a geochemical perspective and which type of processes can explain their varying compositions?
- Is Member 5 of similar type to the other members?

Spencer (1971) and Ali et al (2018) described an evolution from carbonate-dominated clasts in Member 1 to granitic silica-rich clasts in Member 5. As discussed in section 4.2, the matrix of these diamictite beds have overall the same composition as the clasts. A. Spencer and K. Chew have between 2012 and 2018 made about 200 measurements of stone types within the diamictite beds (received from A. Spencer 2019 in personal communication) and most of the ICP sampling in this study were co-located with these stone counts. This gave the possibility to make a correlation between the matrix and the clasts over the stratigraphic column of the PAF which is shown in Table 20. The Spencer & Chew (2012 – 2018) stone counts include information both about total quantity of clasts and the area they cover within each 50x50 cm measuring square. Below analysis use the number of clasts within each square from those measurements, which is here re-calculated as a percentage giving the relative mix of the quantity of clasts within each square. This supress possible influence of the relative proportion of clasts versus matrix in different locations and it was also noted that the absolute number of clasts respectively the cumulative area of clasts per square have a lower correlation with geochemical data in this study than this relative %-mix used. Thus, the matrix composition covaries better with the compositional mix of clasts than with their absolute numbers. The percentage mix of counted intrabasinal dolostone and limestone clasts correlates with the geochemical elements CaO, MgO and LOI and negatively with SiO_2. Granitic clasts correlate with SiO_2 and negatively with the carbonate elements. These correlations are even more pronounced when adding up the clasts to a total intrabasinal number. Quartzite and other extrabasinal clasts show a weak correlation with most elements, but the sum of extrabasinal clasts correlates positively with SiO_2, Al_2O_3 and Na_2O and negatively with carbonate elements.

	Dolom	Limest	OtherIntra	Tot Intra	Granite	Quartzite	OtherExtra	TotExtra	Unknown
SiO2	-0.51	-0.53	-0.37	-0.74	0.69	0.20	0.34	0.74	0.06
Al2O3	-0.36	-0.30	-0.28	-0.49	0.47	0.08	0.29	0.51	-0.05
Fe2O3.T.	0.35	-0.23	-0.21	0.13	-0.04	-0.07	-0.11	-0.09	-0.21
MnO	0.08	0.16	0.10	0.16	-0.19	0.04	-0.17	-0.20	0.19
MgO	0.51	0.42	0.23	0.67	-0.70	-0.07	-0.28	-0.68	0.04
CaO	0.41	0.62	0.50	0.73	-0.66	-0.23	-0.37	-0.73	-0.02
Na2O	-0.53	-0.23	-0.27	-0.59	0.46	0.17	0.48	0.60	0.01
K2O	-0.18	-0.27	-0.28	-0.33	0.33	0.04	0.20	0.35	-0.07
TiO2	-0.08	-0.12	-0.21	-0.16	0.17	0.04	0.11	0.18	-0.09
P2O5	0.35	-0.20	-0.15	0.16	-0.09	-0.06	-0.14	-0.14	-0.14
LOI	0.46	0.57	0.42	0.73	-0.69	-0.18	-0.36	-0.74	0.01

Table 20. The correlation coefficients between Spencer & Chew (2012 – 2018) PAF stone measurements as percentage per measuring area and the major elements in the PAF diamictite matrix in the ICP datasets. Dolom – dolomite clasts, Limest – limestone clasts, OtherIntra – other unidentified intrabasinal clasts, Tot Intra – total of intrabasinal clasts, Granite – granitic clasts, Quartzite – quartzite clasts, OtherExtra – unidentified extrabasinal clasts, TotExtra – total of extrabasinal clasts, Unknown – unidentified clasts of either intra – or extrabasinal type. Positive correlations >0.5 are marked with blue and negative correlations <-0.5 with green.

The Spencer & Chew (2012 – 2018) stone count data were also correlated with the relative distribution of lithologies in the PAF calculated from the point counting of thin sections (Table 21), which confirmed the overall correspondence between the composition of clasts versus matrixes in the PAF.

	Dolom	Limst	OtherIntra	TotIntra	Granite	Quartzite	OtherExtra	TotExtra	Unknown
CHLORITE	0.03	-0.05	-0.03	0.00	0.02	-0.11	0.09	0.01	-0.07
FELDSPAR	-0.43	-0.25	-0.23	-0.51	0.34	0.28	0.35	0.49	0.12
BIOTITE	-0.25	-0.24	-0.17	-0.35	0.29	0.15	0.20	0.36	-0.01
OPAQUE	0.13	-0.21	-0.15	-0.03	0.13	-0.02	-0.04	0.08	-0.25
QUARTZ	-0.44	-0.57	-0.30	-0.68	0.63	0.16	0.32	0.67	0.09
MUSCOVITE	-0.42	-0.44	-0.23	-0.59	0.48	0.17	0.41	0.59	0.07
CARBONATE	0.49	0.62	0.34	0.76	-0.68	-0.20	-0.41	-0.76	-0.06

Table 21. The correlation coefficients between Spencer & Chew (2012 – 2018) PAF stone measurements as percentage per measuring area and the lithologies in the PAF diamictite matrix from point counting thin sections. For other comments, please refer to Table 20.

The percentage of counted types of clasts from Spencer & Chew (2012 – 2018) stone measurements are plotted against the stratigraphic column in Figures 80 – 82, which confirms the upward increase of granitic clasts and corresponding reduction of carbonate clasts. Two very distinct events are seen in these charts where the limestone clast count drops to zero directly after the Disrupted Beds and the first appearance of granitic clasts is made at same point. An abrupt introduction of new components to the system could e.g. be caused by existing ice sheets reaching a new substratum, but the exclusion of an existing component from the system would be expected to be gradual during the ice's gradual removal and thinning out of the source and by its reworking and redeposition of lower beds (e.g. as is the case for dolomitic clasts in Figure 80).

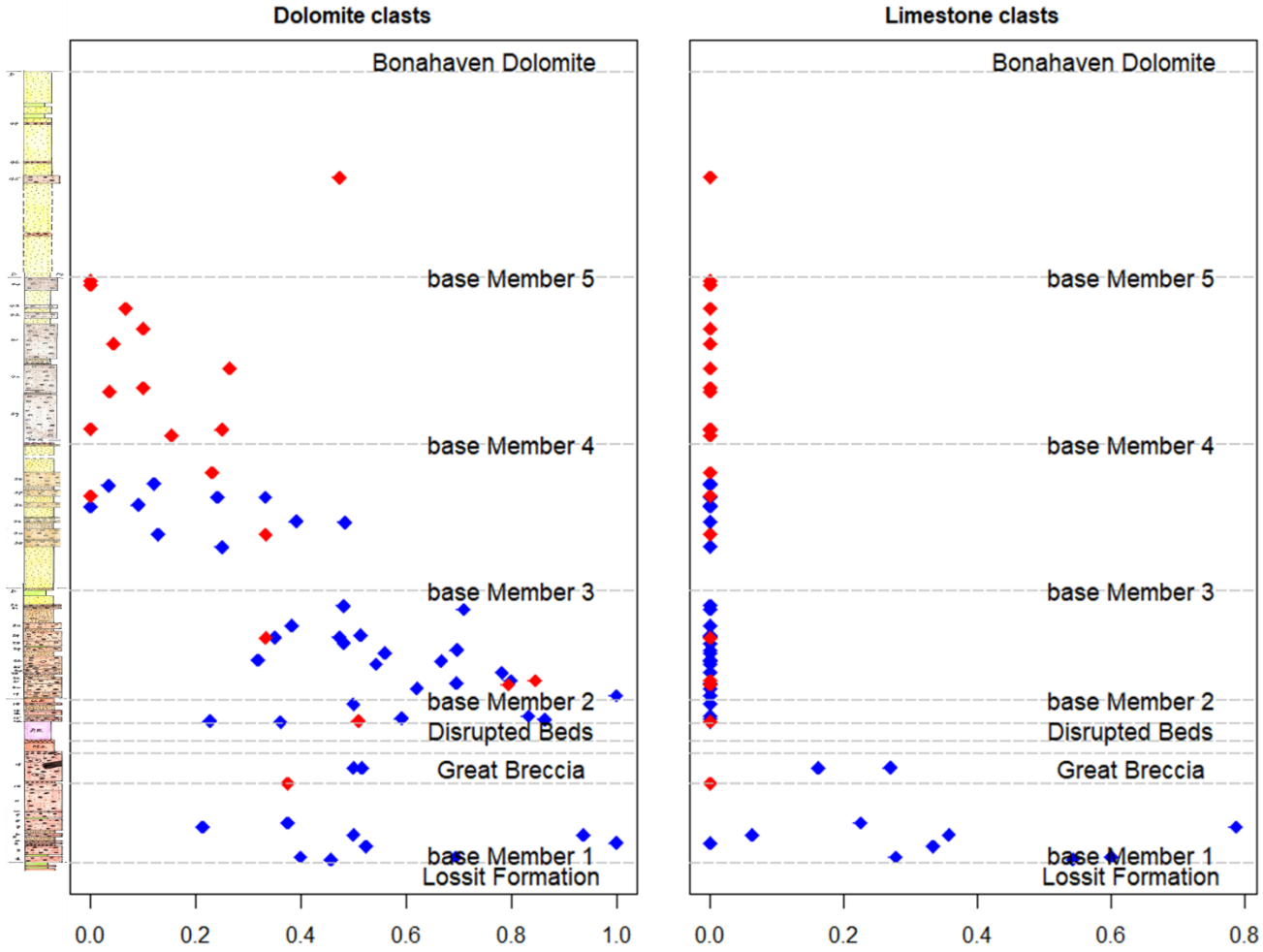

Figure 80. Trends for the relative distribution of dolomite and limestone clasts, from Spencer & Chew (2012 – 2018) stone measurements. The relative proportion (0.0 – 1.0) of the quantity of each type of clast is given on the horizontal scale. Stone measurements from the Garvellachs are marked with blue and from Islay with red. For comments regarding the stratigraphic column and its legend, please refer to Figure 30.

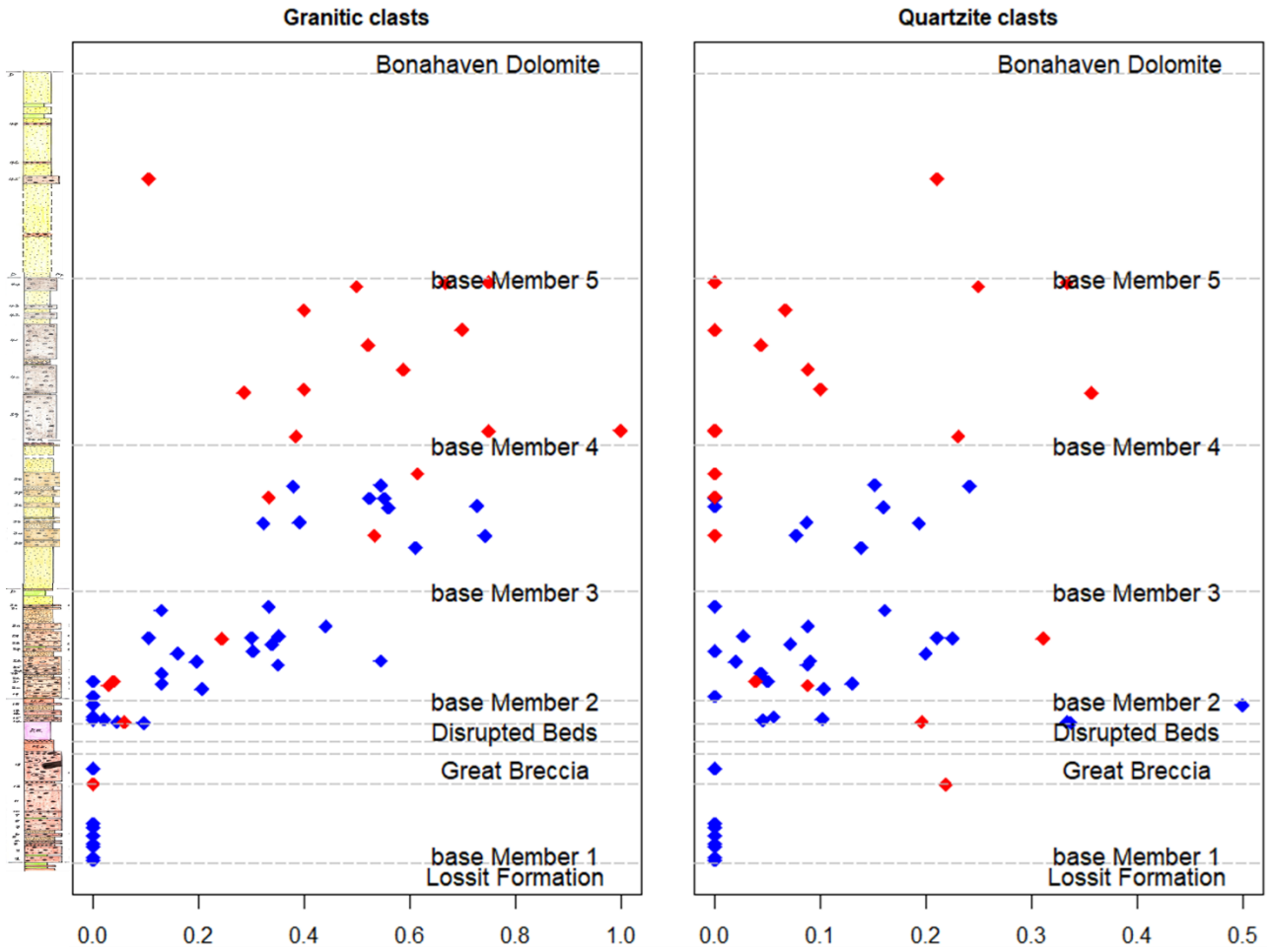

Figure 81. Trends for the relative distribution of granitic and quartzite clasts, from Spencer & Chew (2012 – 2018) stone measurements. The relative proportion (0.0 – 1.0) of the quantity of each type of clast is given on the horizontal scale. Stone measurements from the Garvellachs are marked with blue and from Islay with red. For comments regarding the stratigraphic column and its legend, please refer to Figure 30.

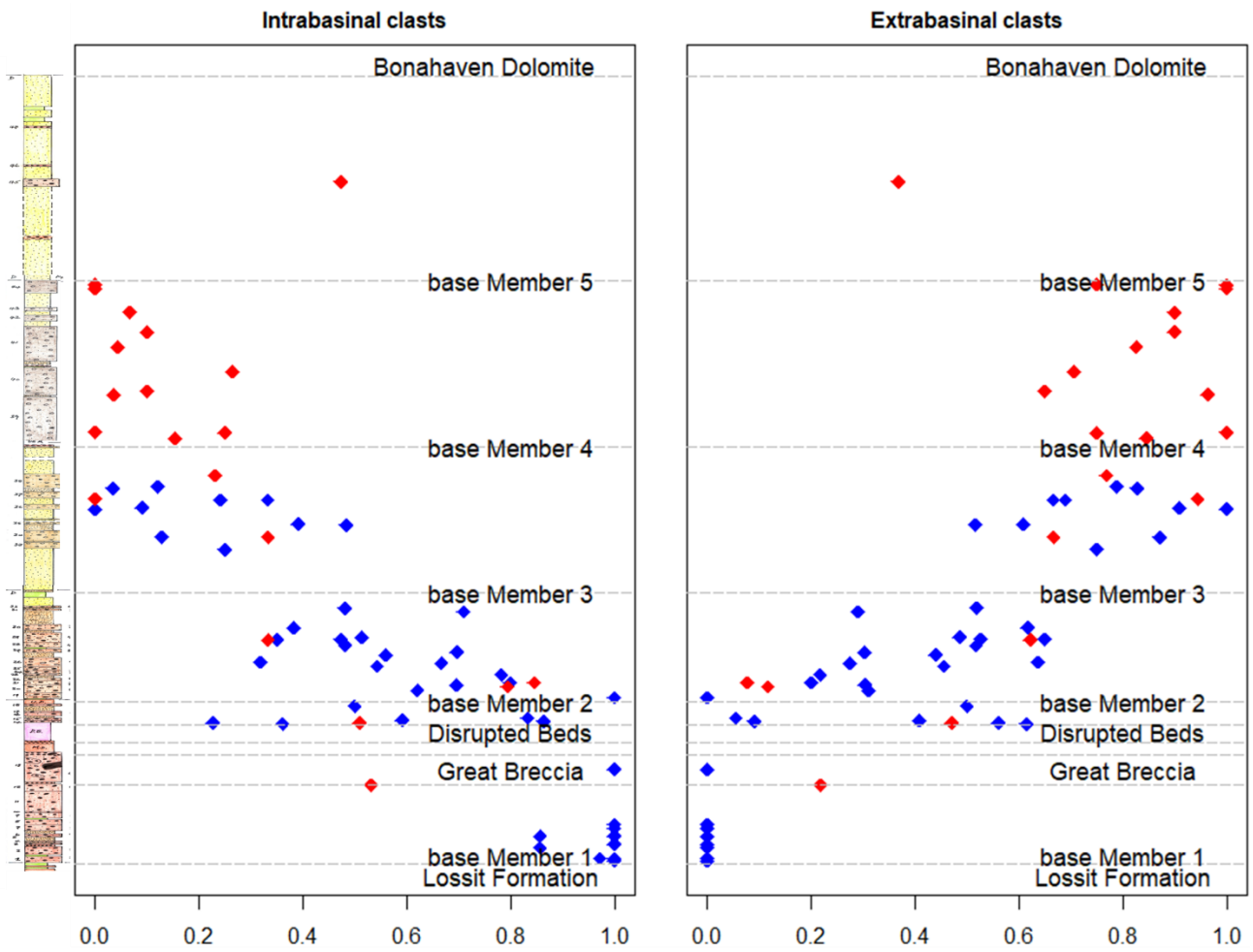

Figure 82. Trends for the relative distribution of intrabasinal and extrabasinal clasts, from Spencer & Chew (2012 – 2018) stone measurements. The relative proportion (0.0 – 1.0) of the quantity of each type of clast is given on the horizontal scale. Stone measurements from the Garvellachs are marked with blue and from Islay with red. For comments regarding the stratigraphic column and its legend, please refer to Figure 30.

The abrupt switch-off of the limestone source is also well documented in the geochemical record. CaO, MgO and the ratio CaO/MgO do not plot together in the lower part of the PAF up to and including the Great Breccia but stay well together thereafter (Figure 83). This is also evidenced by the correlation between these two elements up to and including the Great Breccia (R=0.43) and after (r=1.00) the Great Breccia. The correlation between the normalized sum of CaO and MgO versus LOI remain high throughout the PAF, which indicates that the transition just after the Great Breccia is from a mix of limestone and dolostone before to only dolostone afterwards. The limestone source area was therefore switched off after the Great Breccia.

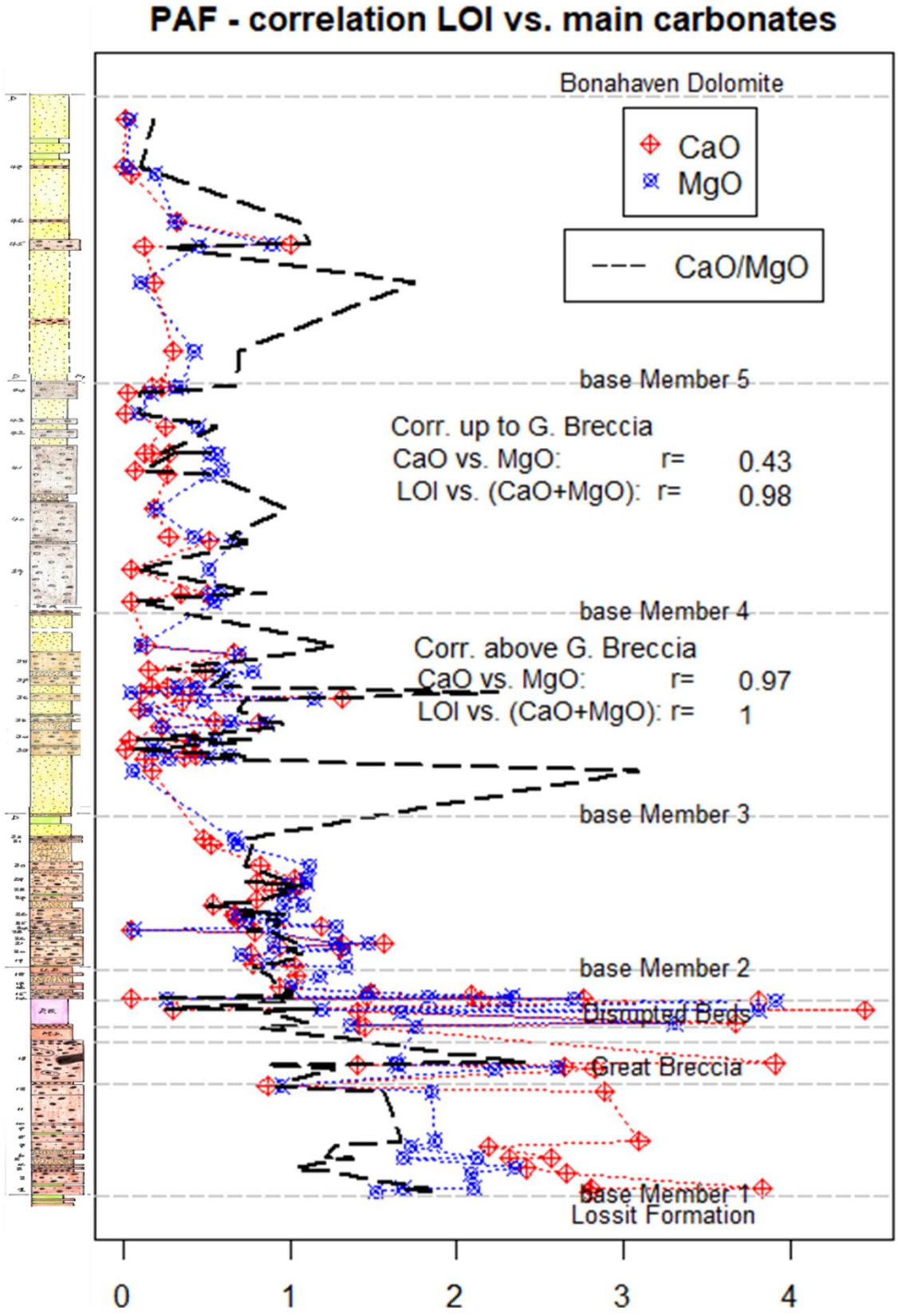

Figure 83. Trend plot showing correlation between CaO, MgO and LOI from the full ICP dataset over the five members of the PAF. LOI, CaO and MgO data are normalized to their respective mean. Correlation coefficients (r) between CaO and MgO and between LOI and the sum of CaO and MgO are tabulated in the chart. The chart shows that the diamictites contain a mix of calcite and dolomite up to and including the Great Breccia, but only dolomite above.

Since aragonite is metastable, limestone now encountered in the PAF is therefore most likely in the form of calcite. The Sr plots at moderate levels typically below UCC and never above 1000 ppm (Figure 84). High Sr content >1000 ppm in limestone is a sign that it originally was in the form of aragonite (personal communication I. Fairchild, 2020, Katz et al, 1972). Limestone transformed into dolostone does not however maintain this high Sr signature. The Neoproterozoic is believed to have had aragonitic seas due to high relative Mg/Ca ratios prevailing at that time and which favours aragonite formation over calcite (Fabre et al, 2013). Since the Sr signal is depleted and no limestone is found after the Great Breccia, this means that virtually all new limestone formed after that time was transformed into dolostone. The limestone that remained in the PAF therefore came from already existing limestone beds, most likely the Lossit Limestone, which originally was deposited in a calcite crystal form. The intriguing question what caused the sudden cut-off of that source is discussed in section 4.4.

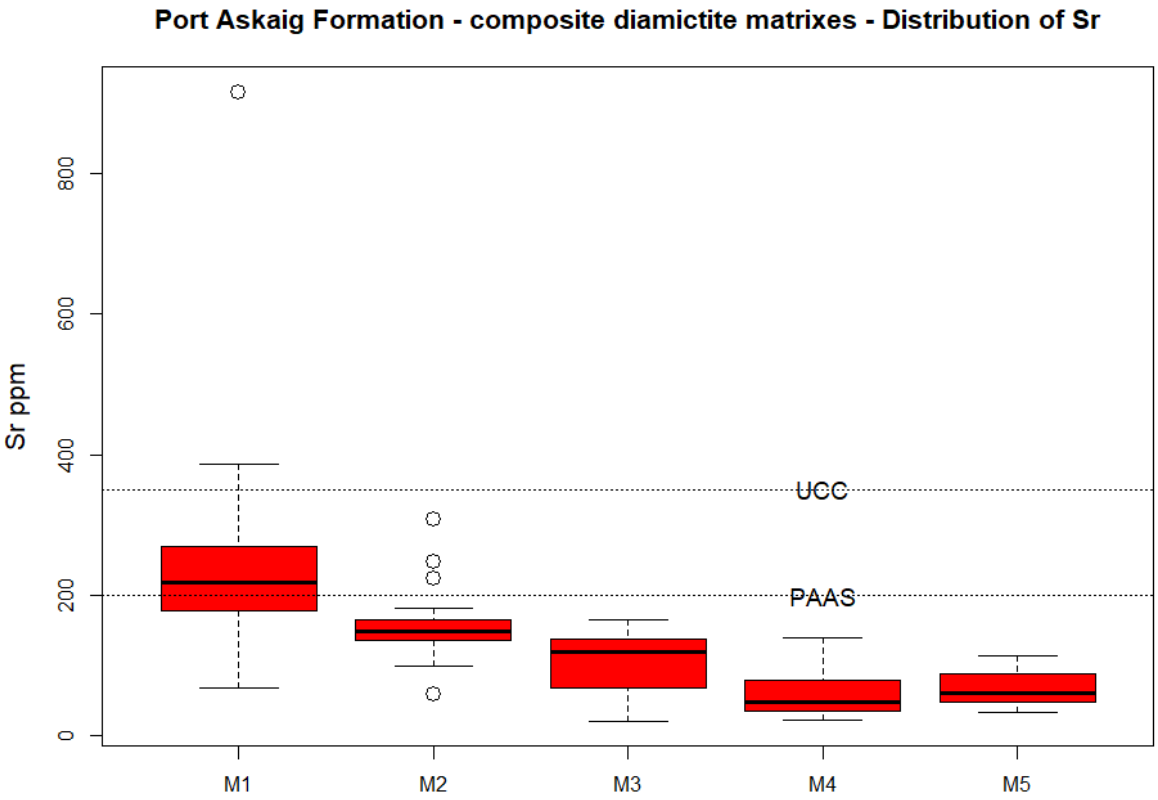

Figure 84. Box-and-whisker plot for Sr within the diamictite matrix of the PAF, based on data from the ICP dataset. Reference values for UCC and PAAS (McLennan, 2001) are shown with horizontal lines. For comments concerning box-and-whisker plots, please refer to Figure 11.

Element	Max at Member	Min at Member	Provenance
SiO_2	5	1	quartzite
SiO_2/Al_2O_3	5	1	
U	5	1	
Y/Ho	5	1	
Cr	5	1	
CIA	5	3	
Al_2O_3	4	1	arkosic sandstone
K_2O	4	1	
Rb	4	1	
Hf	4	1	
TiO_2	4	5	silty mudstone
Sc	4	5	
sum REE	4	5	
sum LREE	4	5	
V	4	5	
Na_2O	3	5	sorted detrital silt
Zr	3	5	
Th	3	5	
sum HREE	3	5	
Fe_2O_3	2	5	iron stone
P_2O_5	2	1	
MnO	1	5	carbonatic rock
MgO	1	5	
CaO	1	5	
CaO/MgO	1	5	
LOI	1	4	
Sr	1	4	

Table 22. List of location where maxima and minima of elements and combination of elements from the ICP PAF matrix dataset occurs. Location of respective maxima and minima are taken from Kruskal-Wallis boxplots included in section 3 plus a few corresponding types of boxplots for those elements and element ratios not shown in this report. A descriptive name is included for each member based on this list.

The trends of the geochemical elements were presented in section 3, which in broad terms match the stone measurements trends in above Figures 80 – 82. The upward increase in concentrations of SiO_2, Al_2O_3 and Na_2O and corresponding decrease of CaO and MgO match the respective extrabasinal and intrabasinal clasts. The trends of the major elements in the matrix thus follow the trends of the lithologies in the clasts, with a stepwise replacement of carbonates by granitic materials in the diamictite matrixes.

On a more detailed level, several trend-shifts or irregularities are seen at the level of the Disrupted Beds (SiO_2, Fe_2O_3, P_2O_5, Na_2O, CaO, MgO, LOI), and when entering M5 (Fe_2O_3, Al_2O_3, Na_2O). The SiO_2 concentrations jump up after the Disrupted Beds and then gradually increase. Fe_2O_3 and P_2O_5 are both added to the system after the Disrupted Beds and MnO has a sharp peak after the Disrupted Beds but otherwise shows a gradual slow decrease. The separate XRF dataset has the same pattern, with a stepwise increase of Si after the Disrupted Beds and again in M5 and increased levels of Fe from the Disrupted Beds and within M2.

The Kruskal-Wallis rank-tests in sections 3.1 – 3.3 showed with certainty that the geochemical compositions of the five members cannot share the same joint source or depositional process. Furthermore, the individual elements reached their respective maximums and minimums in different members and Mann-Whitney rank-tests between individual members indicated different source distributions for many of the elements. In addition to the rank-tests showed in section 3, two more tests of HFS elements typically used in provenance discrimination plots are included in Figures 85 and 86 below, giving the same conclusions. Therefore, the members likely have differences in provenances, which also supports Spencer's original grouping of the diamictite beds into 5 members. Table 22 lists some of the key elements with their respective min- and maximums and a descriptive name characterizing aspects of the provenance of each member.

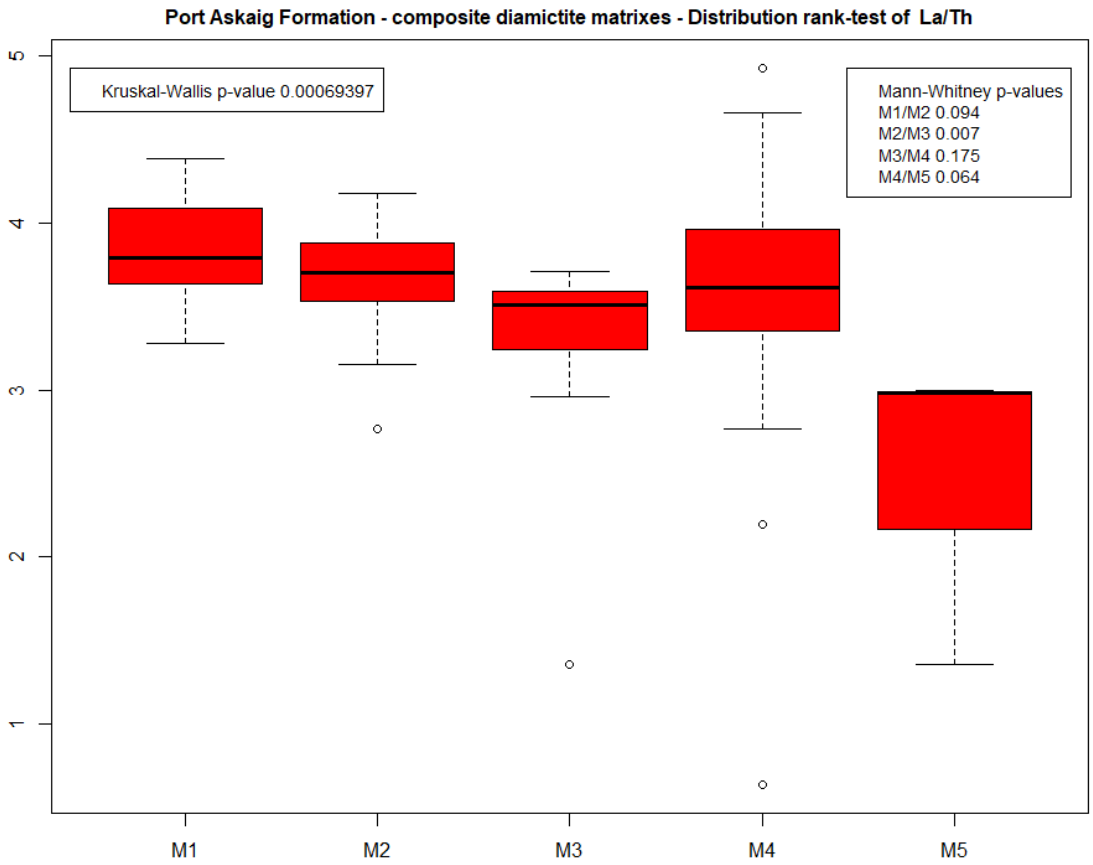

Figure 85. Kruskal-Wallis and Mann-Whitney rank-tests of the distribution of the provenance indicator La/Th. The distribution of La/Th for each member is shown in the box-and-whisker plot. The ratio between these elements' ppm concentrations is shown on the y-axis. For description of rank-test, please refer to Figure 18 and for box-and-whisker plots to Figure 11.

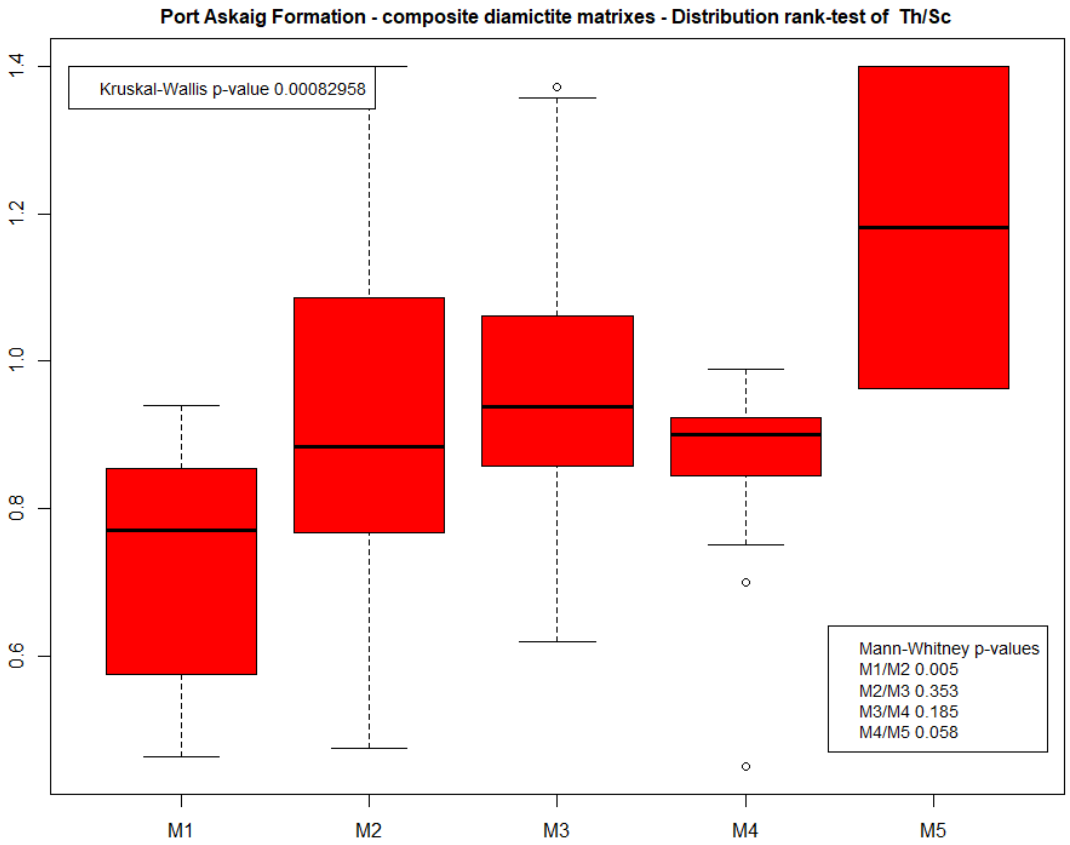

Figure 86. Kruskal-Wallis and Mann-Whitney rank-tests of the distribution of the provenance indicator Th/Sc. The distribution of Th/Sc for each member is shown in the box-and-whisker plot. The ratio between these elements' ppm concentrations is shown on the y-axis. For description of rank-test, please refer to Figure 18 and for box-and-whisker plots to Figure 11.

As will be discussed in section 4.4, the relative mix of clay and silt sized particles versus sand in the diamictite matrixes as interpreted from geochemical proxies also show a trend pattern following the original division into five members, with the sand component increasing at the border between each member and also between the Great Breccia and the Disrupted Beds in M1.

In summary, the above discussion supports Spencer's (1971) original decision to group the diamictite beds into (at least) five members and provides independent characterizations based on geochemical matrix compositions for this grouping. However, based on numerous observations, it can be argued that the Member 1 could be further divided into two sub-groups – the first (M1a) to cover the diamictite beds d1 – d13 (being the Great Breccia), and the second (M1b) starting from the Disrupted Beds, covering d14 – d18 up to and including the Upper Dolomites. As discussed above, there are multiple observations of trend-shifts between the Great Breccia and the Disrupted Beds. Limestone is removed and Fe- and P-oxides as well as granitic clasts are added to the system at this point, and some other elements (SiO_2, Na_2O) show distinct changes in patterns here. Also, CIA show an anomaly here, plotting at glacial till levels below, but as well weathered rock above this level.

Another anomaly is observed in data concerning M5. Fe_2O_3, Al_2O_3 and Na_2O show trend-shifts when entering M5, and data for several elements are more scattered within this member. The distribution of M5 data points thus shows limited resemblance with those of other members in several of the trend-plots. Figure 87 shows the REE footprints of the five members plus the sampled sandstone beds, and where M5 clearly deviates from the other members. The relative depletion of the LREE indicates a surplus of zircon within this member as compared to the more granodioritic and granitic M1 – M4. Sandstones show, as expected, significantly lower REE concentrations plus a distinct positive Eu anomaly which possibly is linked to plagioclase enrichment in this facies. Together this could imply a shift of provenance or different transport and sorting processes for the M5 material as compared to the other members. Also, considering the CIA data (where M5 on average plots close

to shale) and the conglomerate structure of the thin diamictite beds in this member, it can be questioned if this really represents a true glacial deposit.

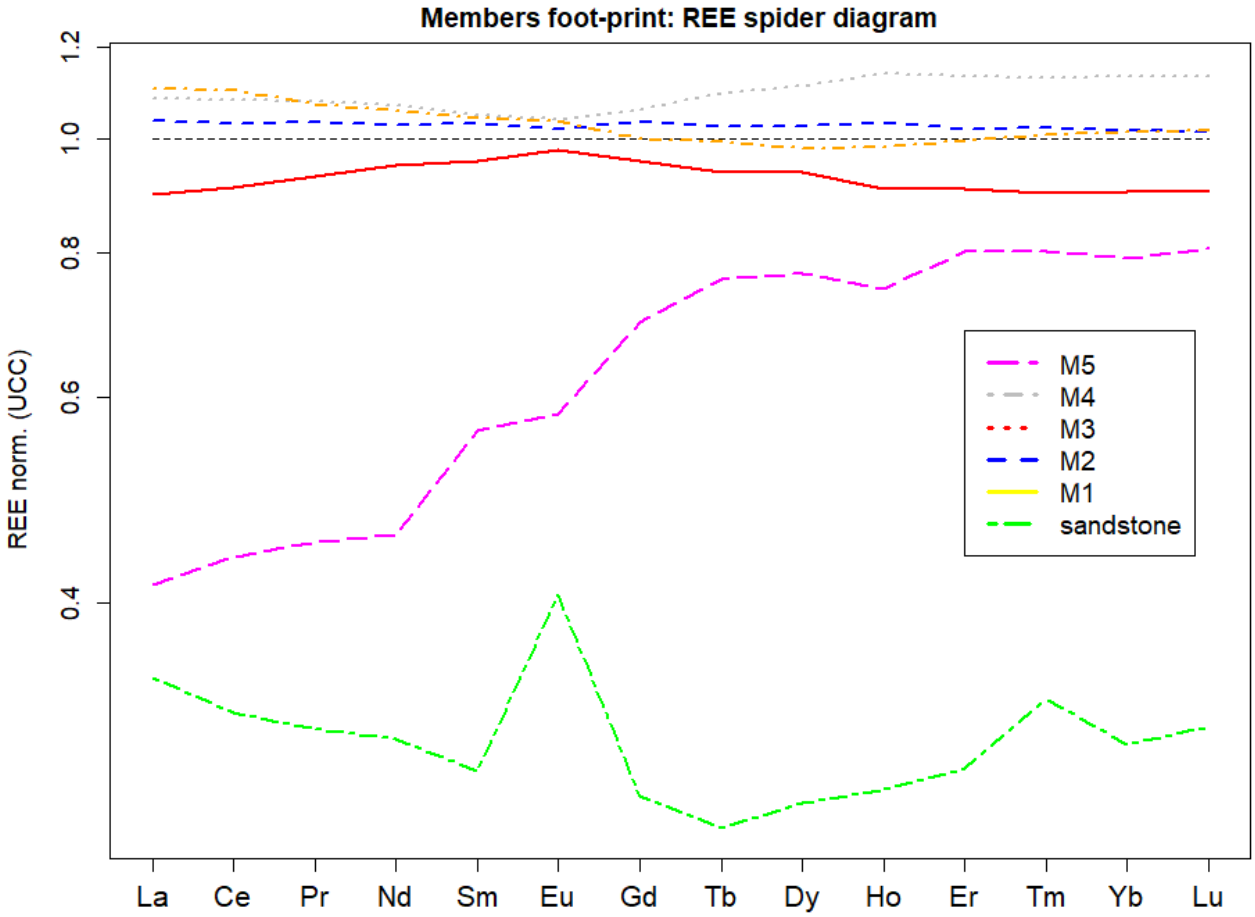

Figure 87. UCC normalized spider diagram showing the average of REE for each member and for sandstone beds in the PAF, based on the ICP dataset. The averages of diamictite members and sandstone beds are marked with dotted and dashed coloured lines (see legend in plot). The vertical scale is logarithmic. UCC standard values (McLennan, 2001) are marked with a black horizontal line at vertical position 1.0.

Changes in diamictite source compositions can i.a. depend on: i) ice reaching new strata after unroofing upper levels; ii) ice not anymore reaching certain strata after having covered it by glacial deposits; iii) change in ice flow directions; iv) change in ice transport distances (where e g IRD or glacifluvial material are more far travelled); v) tectonic change of the depositional basin (e g opening or closing certain supply alternatives); vi) tectonic change of the geographical position of the source area; vii) isostatic change of sea level (with corresponding change of the grounded ice line; or viii) any combination of these mechanisms.

In some alternatives the mechanism can cause gradual change, but in some cases also abrupt changes. They act over different time frames, where e g isostatic sea level change could operate on similar time spans as a normal glacial-interglacial cycle, while a tectonically induced change would require time spans in the range of millions of years. The original Snowball Earth model predicted a deep-frozen hiatus reaching over millions of years with a stopped hydrological cycle and non-dynamic ice sheets. Since the tectonic processes will continue during this hiatus, changes in the geometry of the depositional basin (v) and the geographical position of potential source areas (vi) will still take place. The Snowball Earth hypothesis thus predicts a major change in provenance after ending its deep-frozen stage, and this change will appear to be stratigraphically abrupt.

4.4 Depositional and palaeoenvironmental interpretation of the PAF

The diamictite matrix is composed of varied particle sizes, from fine clay sized glacial flour to silt sized particles to sand grains. The material is derived from physical erosion when the ice sheet grinds over the substrate. The

material of the glacial till is expected to contain a relatively homogenous geochemical composition, inherited from the substrate. Subglacial meltwater can both contribute to the physical erosion of the load and can also sort it after particle size and density. During the ice sheet growth phase, the glaciofluvial activity is expected to play a smaller role compared to the glacial processes, but during ice sheet meltdown it will naturally dominate.

Fluvial processes typically "wash out" the finer particles and concentrate quartz grains in the residual material. HFS elements and certain transition elements such as titanium are often concentrated in the glacially derived silt size fractions (Taylor & McLennan, 1995; López et al, 2005; personal communication I. Fairchild, 2020). These elements could therefore serve as proxies to distinguish between subglacial and glacifluvial processes, with finer silt particles indicating more subglacial erosional activity and more sand sized particles indicating more glaciofluvial activity.

The glacial cycle proxy used here includes a silt component calculated as the geometric average of moles of Ti-oxide and Zr, and a sand component taken as moles of Si-oxide contained in quartz (estimated from total moles Si-oxide minus moles Si-oxide siting in micas and feldspar approximated by 3x moles K-oxide). The ratio between these two components is shown in Figure 88. This geochemical log indicates 5 possible cycles over the PAF, with gradually increasing silt content followed by sudden reduction thereof with quartz-sand temporarily taking over. This pattern is interpreted as glacial cycles with gradual build-up of ice sheets with glacial processes dominating, followed by short episodes of rapid melting when glaciofluvial processes take over the transport of material.

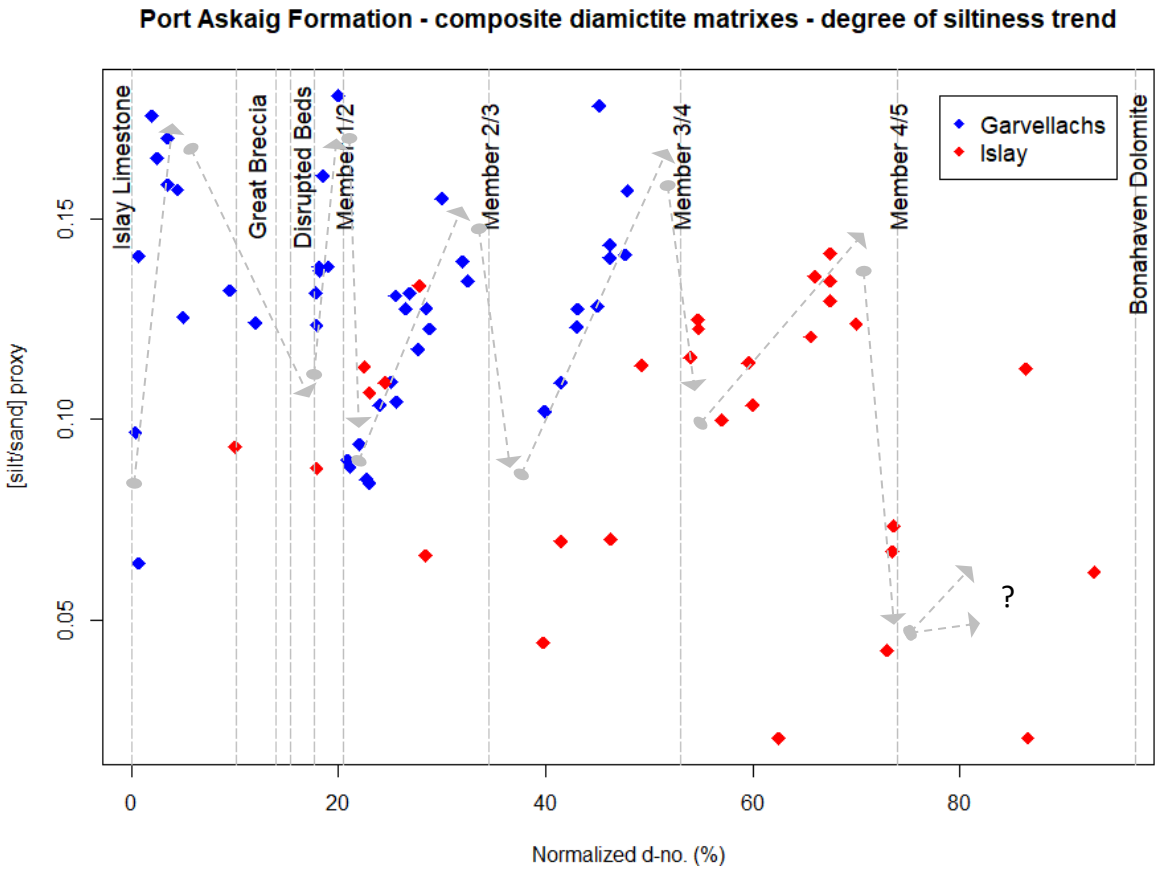

Figure 88. Trend plot for a proposed glacial cycle proxy, consisting of a ratio between silt indicators versus sand indicators. Silt sized particles are represented by the geometric average of Ti-oxide and Zr, and is expected to be linked to glacial action, while sand is represented by SiO_2 in quartz, which is expected to be linked to interglacial glaciofluvial processes. The trend is shown from left to right instead of bottom-up over the stratigraphic column, following normal presentations of proxies for Quaternary ice sheet fluctuations. The y-axis gives the relative scale of this proxy. Blue dots marks samples from the Garvellachs and red dots Islay. Gray arrows are inserted into the plot to suggest possible developments of the glacial cycles. Five glacial cycles over the duration of the deposition of the PAFs Members 1 to 4 can possibly be inferred from this plot.

The cyclical pattern of certain elements was tested with help of Fourier analysis where time and intervals of the fluctuating trend-line were transformed to frequencies and phases. The amplitude spectrum generated by the Fourier transform of the silt versus sand proxy is given in Figure 89 which indicates a periodicity of 5 cycles within this data over the height of the PAF. Fourier analysis of other elements and combination of elements typically associated with silt and clay sized fractions indicate similar results with 5 – 6 cycles, while carbonates, iron and silica and their associates give 1 – 3 cycles.

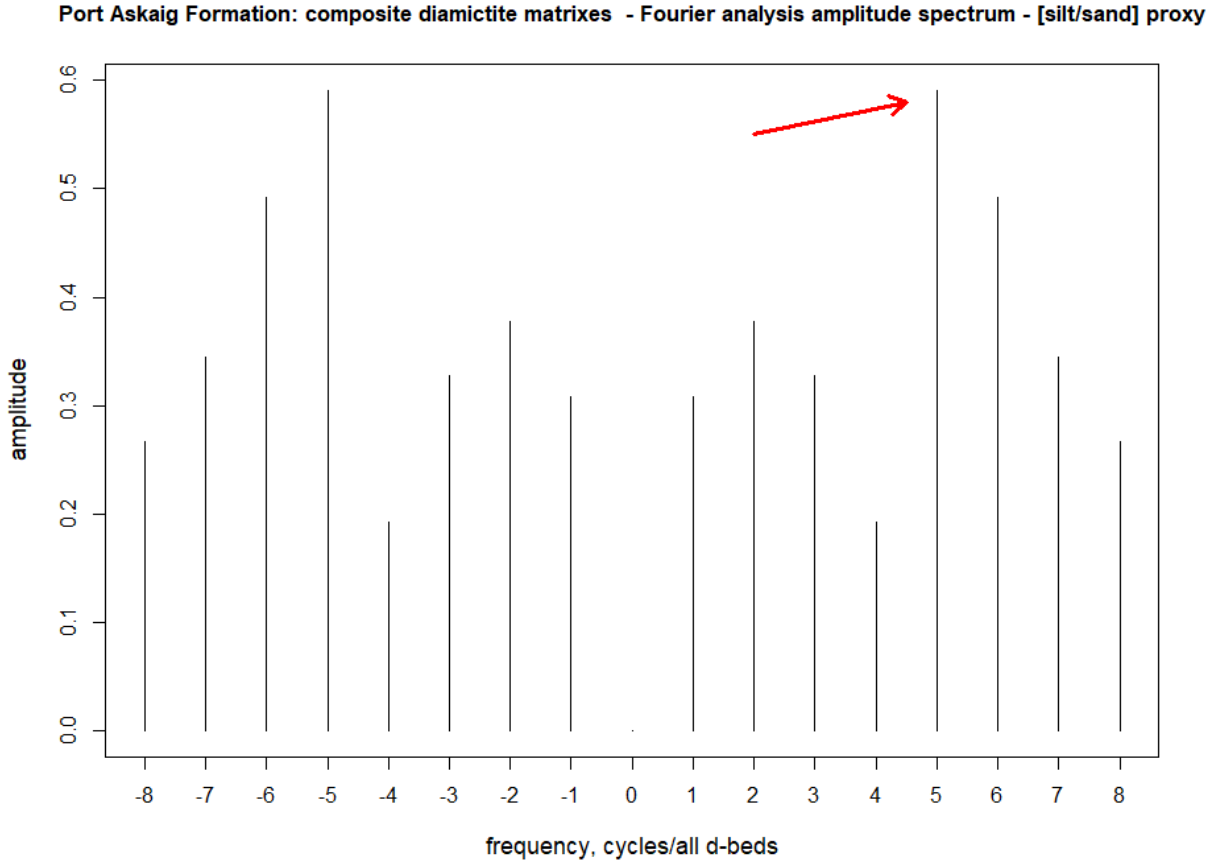

Figure 89. Fourier frequency analysis of the proposed glacial cycle proxy (geometric average of Ti-oxide and Zr versus SiO_2 in quartz). The data are first de-trended by eliminating components from a linear regression trend line (thereby eliminating sinusoids related to the "0" cycle). The relative amplitude of the frequencies from the calculated Fourier series is shown on the y-axis. The analysis generates a mirror image of positive and negative frequencies on the x-axis. This analysis shows a maximum for 5 cycles over the full height of the PAF (see red arrow).

The precipitation of carbonates forming the primary dolostone sequences are controlled by three factors: i) supply of alkalinity and Ca-ions ensuring an over-saturated water, ii) increase of water temperatures, and iii) lowering of the CO_2 partial pressure (e.g. CO_2 outgassing) (Fabre et al, 2013; Hoffman & Schrag, 2002). A flush of alkalinity and Ca-ions is expected to be delivered by melt water from the aggressive CO_2-driven chemical weathering and shallow waters will warm quickly when the ice-cover has melted and the low-latitude sun pumps energy into the ocean.

High Fe-concentration appears in the Disrupted Beds and again in Member 2 but not in between. Fe was added to the system at the Disrupted Beds (e g through precipitation in a ferruginous sea) and possibly repeated in the beginning of Member 2 (Figure 34). The high Fe_2O_3(T) concentration comes with three requisites: i) an anoxic deep sea allowing Fe(II) to be transported and accumulated, ii) limited amounts of available sulphur (H_2S), and iii) a trigger for the oxidation of Fe(II) into the magnetite or hematite precursor Fe-oxyhydroxide (Bekker et al, 2014; Hoffman & Schrag, 2002). The trigger for Fe-oxidation is at least some mixing of the water-column. However, low concentrations of manganese seem to exclude a fully oxygenated water.

Since meltwater is a common denominator for triggering both precipitation of carbonates and ironstones and since they seem to be temporally linked (the Disrupted Beds directly following the Main Dolomite and the

magnetite siltstone following the Upper Dolomite), it is thus suggested that the chemical precipitation of both Fe- and Ca-oxides are controlled by cyclical meltwater outflow events

In addition to beds of precipitated carbonates and iron, the PAF also has several other characteristics (Spencer, 1971; Ali, 2017). The diamictite beds are mostly homogenous without gradational layering except for a few places which contain fine layered marine deposited material with occasional dropstones. Most diamictite beds have a sharp and conformingly lower contact, but a few unconformities or gaps in the sequence are noted. Beds of conglomerates appear both at the top of the Great Breccia and within Member 5. Examples of subaerial exposure are common with sandstone wedges and frost shattered clasts. Interlayered sandstone beds show marine tidal cross bedding and some of the dolomite beds are primary carbonate deposits as evidenced by stromatolites.

The PAFs larger stratigraphic record thus provides clear evidence of changing sea levels, including subaerial features, tidal sandstones, varved silt beds, IRD (drop stones) and precipitation of carbonates and iron-rich beds. Several competing processes will participate in the control of the relative sea level. Melting of continental glaciers alternatively isostatic loading from new growing continental glaciers, subsidence of a rifting basin and thermal expansion of a mixed warming ocean after the snowball Earth will all contribute to a sea level rise. In a similar fashion, isostatic rebound after deglaciation and sea water transferred into new continental glaciers will contribute to a lower relative sea level. Furthermore, detrital and chemical sedimentation will gradually fill up the accommodation space. Table 23 contains tentative estimates of some of these factors, the purpose of which is to focus the discussion of the depositional environments of the PAF (not taking definite stand on their absolute values). A qualitative conclusion can be made from this table: tectonic- and glacial-related factors are of different magnitudes and will thus not “compete” in a sea-level modulation (Lambeck, 2014).

	sea level change rate (m/kyr)	total sea level change (m)	total duration (kyr)
ice-sheet meltdown	200	+320	1.6
ice-sheet build-up	20	-280	14
isostatic rebound initial	20	-210	10.5
isostatic rebound later	5	-70	14
isostatic loading	20	+320	16
thermal ocean expansion	1	+40	40
basin subsidence	0,1	+1,000	10,000

Table 23. Estimates of processes which impact relative sea level, including resulting rate of change (m/kyr), assumed absolute impact (m) and the time (kyr) during which the process is expected to operate. A typical average glacier height of 750 m would depress the crust with ca 280 m assuming a crust density of 2.7 g/cm3. This would add ca 320 m to the sea when melting, assuming 30% of Earth surface covered by continental glaciers. Height of the ice-sheet is reduced compared to Quaternary conditions and rates accelerated, considering the low latitude position. The ratio for ice build-up to meltdown duration has been chosen to 10:1 and the length of a glacial cycle to ca 16 kyr to a Milankovitch Neoproterozoic precision cycle. Holocene isostacy rates give initially 8-20 m/kyr and later 1-2 m/kyr (Schlager, 1999). Thermal expansion of ocean waters after termination of Snowball Earth is taken from Hoffman et al (2017). Basin subsidence varies, but examples from Namibia (Hoffman & Schrag, 2002) states 0.065 m/kyr and Bosscher & Schlager (1993) give a range of 0.02 – 0.2 m/kyr. The duration of the basin subsidence was arbitrarily chosen to indicate effect of a continuous multi-million years rifting.

Quaternary ice sheets have a saw-tooth pattern with gradual build-up over a longer period followed by a rapid melting phase. The build-up phase is not linear but includes shorter oscillations with a waxing and waning ice sheet. The melting is accelerated by the gravitationally driven flow lubricated by a warm based ice. Large outflows of meltwater both erode underlaying sediments and create large freshwater plumes stratifying the ocean thereby changing the chemistry of the sea. The build-up and subsequent meltdown of the ice sheets cause both eustatic and isostatic sea level changes.

Results from the CIA analysis in section 3 indicate significantly higher variations (SD=12) in values from d13 to d18 compared to the lower beds d1 to d12 (SD=5) and 6 out of 10 data points in d13 – d18 had values above 70. Panahi & Young (1997) noted quite high CIA values (mean 73 compared to 62 in this study) in M1 compared to a mean of 64 within M2 – M3 (where this study has a mean of 56). Panahi & Young had thus generally higher values in their study compared to this, but which can be explained by different methods in estimating the

siliciclastic component of Ca (CaO*). Panahi & Young did this by methodology outlined by Dreimanis (1962) while this study used the method proposed by McLennan 1993. It is noted that the CaO* component in the Panahi & Young study is set to zero in 17 of 18 of their samples. If CaO* were set to zero in this study the average CIA in both M1 and M2-3 would increase by 6 units. Panahi & Young interpreted the difference between M1 and M2-3 values as a legacy from an old sedimentary cover in M1 that had gone through an earlier weathering cycle. The data in this study do not contradict this interpretation but add the possibility that there was a new event of focused chemical weathering occurring at and just after the Great Breccia.

The interpretation below (Table 24) of the paleoenvironmental conditions that resulted in the deposition of the PAF is built on the following assumptions and interpretations of observations:

- The dynamic phases of the PAFs glacial cycles are assumed to operate in similar ways to the Quaternary, with saw tooth patterns including gradual and oscillating build-up cycles followed by rapid meltdowns.
- The entry into the Snowball Earth stage is interpreted to be through one glacial build-up cycle with primarily cold-based ice allowing sharp basal diamictite contacts without erosional features.
- The Great Breccia is interpreted as the final step in this glacial build up before entering the long Snowball Earth hiatus, at which time the eustatic sea level drop had placed previous deposits into subaerial permafrozen positions.
- The geochemical trend-shifts seen between the Great Breccia and the Disrupted Beds as discussed in section 4.3, including the abrupt change of diamictite source area documented by the switch-off of the supply of limestone, are interpreted to require a process on a tectonic time scale and were thus linked to the Snowball Earth hiatus.
- The large differences in CIA data, with high values after the Great Breccia as compared with earlier parts of M1, are interpreted to be caused by aggressive CO_2 induced chemical weathering when the icehouse condition was finally broken.
- The exit from the Snowball Earth icehouse is interpreted to be through a series of possibly 5 major melting events of short durations, intermixed with somewhat longer periods when the ice managed to recover control.
- Features in the PAF which are used to correlate the 5 glacial cycles are based on the following observations: i) primary carbonate beds, ii) ironstone layers in siltstone beds and similar types of gradational siltstone beds, iii) unconformities (interpreted to indicate major meltwater outwashes, similar to jökulhlaups), iv) tidal sandstone beds, and v) geochemical indicators of variations in silt size particles versus sand size particles in the diamictite matrixes.
- Each major melting event created large freshwater plumes of cold meltwater, with an assumed increase of alkalinity and oxygen allowing both carbonates and Fe-oxyhydroxide to precipitate, as observed in the Main and Upper Dolomite, respectively in the Disrupted Beds and magnetite siltstone.
- The freshwater plumes generated by each major melting event are assumed to have led to Heinrich events causing the ice sheets to temporarily return.
- The rifting caused by Rodinia breakup is assumed not to have started at the onset of the Sturtian glaciation and basin subsidence rate is assumed to have been negligible during the initial part of the Snowball Earth hiatus and only starting in earnest toward the end of that period.
- The isostatic lowering of the basin during the period preceding the start of the first melting cycle is assumed to be of similar magnitude as the eustatic sea level decrease caused by the total water stored in continental glaciers.
- The exit from the Snowball Earth pan-glaciation is assumed to take place during a relatively short time period where the varying subaerial and subaqueous depositional palaeoenvironments evidence in the PAF after the Great Breccia primarily are interpreted to be caused by a combination of fast isostatic and eustatic changes, but not tectonically driven basin subsidence.
- Assuming that the glacial cycles during the exit from Snowball Earth were controlled by Milankovitch orbital precession forcing leads to the conclusion that the exit took place within at most 100,000 years with an average deposition rate of 10 m per 1,000 years (matching examples, cited in Hogan et al,

2020, of glacial sediment fluxes with hundreds of meters thick depositions at the ice margin during the last glacial retreat).

formation / member	description	interpretation of ice sheet development	interpretation of ice sheet status	G-no	interpreted event	dimate
Bonahaven Dolomite	dolomite					warm
M5	tidal sandstone		questionable if ice sheets recahed sea level	?		temperate ?
	d47				possibly conglomerates (wave washed beach type)	
	tidal sandstone	?				
	d45 - d46				possibly conglomerates (wave washed beach type)	
	tidal sandstone					
M4	d44				interpreted from its geochem signature	warm (?)
	tidal sandstone			G5		
	d39 - d43		oscillating warm based ice, gradual build up of ice sheets			cold / arid
M3	unconformity				glacial erosion	
	tidal sandstone		rapid meltdown	G4		warm
	d33 - d38		oscillating warm based ice, gradual build up of ice sheets			cold / arid
M2	tidal sandstone			G3		temperate
	rhytmically laminated siltstone				rhytmic meltwater depositions	
	unconformity		rapid meltdown		jökulhlaup type outwash	warm
	d19 - d32		oscillating warm based ice, gradual build up of ice sheets			cold / arid
M1b	magnetite siltstone		rapid meltdown	G2	Fe-oxyhydroxide precipitation in meltwater plymes	temperate
	Upper Dolomite (primary)				carbonate precipitation in meltwater plymes	warm
	unconformity				jökulhlaup type outwash	
	d14 - d18		oscillating warm based ice, gradual build up of ice sheets			cold / arid
	Disrupted Beds		rapid meltdown	G1	Fe-oxyhydroxide precipitation in meltwater plymes	temperate
	Main Dolomite (primary)				carbonate precipitation in meltwater plymes	warm
	erosion surface				jökulhlaup type outwash	
Snowball Earth	>10^7 yrs hiatus		cold based ice		interpreted from geochem trend shifts	a deep frozen Earth
M1a	d13 (Great Breccia)		oscillating warm based ice, gradual build up of ice sheets			cold / arid
	Islay unconformity				glacial erosion or jökulhlaup type outwash	
	d1 - d12					
Lossit Formation	limestone/dolostone					warm

Table 24. A palaeoenvironmental interpretation of the deposition of the PAF. The separation of M1 into two parts is based on discussion in section 4.3. G-no is the number of the five glacial cycles indicated in Figures 88 and 89. Identification and stratigraphic position of glacial markers given in column "description" are taken from Spencer (1971) and Ali (2017).

It is thus proposed that the PAF was deposited during 5 glacial cycles (here referred to as G1 – G5) starting with gradual build-up of ice sheets followed by rapid meltdowns, and where G1 was unique in the sense of containing the multimillion years hiatus of the Snowball Earth event. G1 thus include d1 to d13 (the Great Breccia), the >10 Ma hiatus, the Main Dolomite including the underlaying erosional surface to the Great Breccia and ending with deposition of the Disrupted Beds; G2 starts with the soft sediment deformation of the Disrupted Beds, continues through d14 – d18 and ends with an unconformity followed by the Upper Dolomite and an iron-rich siltstone bed; G3 starts with the soft sediment deformation of the Fe-siltstone bed, continues through d19 – d32 and ends with an unconformity followed by a laminated siltstone bed and tidal sandstones; G4 goes through d33 – d38 and ends with tidal sandstones; G5 starts with a glacial erosion unconformity, continues through d39 – d43 and ends in tidal sandstones; the continuation possibly describe the final tapering out tail of the overall pan-glaciation.

The above model addresses i.a. two questions which have seemed to contradict a Snowball Earth interpretation of the PAF. The large number of diamictite beds in the PAF, requiring dynamic ice sheets, seem incompatible with deposition under deep-frozen hydrological conditions during the Snowball Earth hiatus. The above interpretation implies that they instead were primarily deposited during one rapid entry (d1 – d13) and a

shorter exit phase over a few glacial cycles (d14 – d47), with limited or no activity during the actual Snowball Earth.

The deposition of the PAFs 1100 m thick succession of beds required a persistent balance between rates of accommodation space and sediment supply. It seems unlikely that this balance would have been maintained during a full Snowball Earth event, also during the paused sediment supply under the multimillion years hiatus. Above interpretation does not require an ongoing basin subsidence during the entry into and initial part of the Snowball Earth, and accommodation space created by rifting starting towards the later part of the Snowball Earth hiatus is assumed to suffice.

5 Conclusions

Based on the study of ICP measurements from 100 samples, XRF measurements from 134 locations and 101 thin sections from the 47 diamictite and other selected non-glacial beds in the 1100 thick PAF the main findings are these:

- The trends of the major elements follow as expected the trends of the lithologies, with a gradual replacement of carbonates by granitic materials in the diamictite matrixes, and several trend-shifts or irregularities can be seen at the level of the Great Breccia / the Disrupted Beds (SiO_2, Fe_2O_3, P_2O_5, Na_2O, CaO, MgO, LOI) and when entering M5 (Fe_2O_3, Al_2O_3, Na_2O).
- A Principal Components Analysis (PCA) also confirms the main trend with a gradual replacement of carbonates by siliciclastic material, but also shows the influence of quartz sand versus silt and the inclusion of Fe not linked to detrital components.
- Correlation analysis confirms that REE in the diamictite matrixes are controlled by detrital components and have no legacy from ocean chemistry.
- Trend analysis of trace elements shows as expected that Sr decreases with carbonates and that Cr increases with silica upwards, but also gives hints of an upward-increasing intra-member “sawtooth” trend in M2, M3 and M4 for V, Zr, Rb and possibly for Ga, Th, Y.
- The sandstone samples show a significant positive Eu anomaly indicating plagioclase enrichments during sediment sorting.
- Kruskal-Wallis and Mann-Whitney rank-tests, comparing the distribution of chemical elements between the PAF members, indicate that most elements in different members do not originate from the same source or depositional process.
- The geochemical patterns of elements in both the diamictite matrix and sandstone are distinctly different in M5 compared to the other members.
- CIA values calculated from the diamictite matrix ICP samples show consistently low glacial clay values in Members 2 – 4 (interquartile range 52 – 58) and a value closer to shale in Member 5 (interquartile range 59 – 69), but large variations in Member 1 (interquartile range 55 – 70) with most of the variation with higher values starting from the Great Breccia and upwards.
- The geochemical log indicates 5 possible cycles over the PAF, with gradually increasing silt content followed by sudden reduction thereof with quartz-sand temporarily taking over.

The detailed interpretations which can be suggested based on these findings and further analysis herein are these:

- Geochemical overprints from early authigenesis and later post-depositional changes including sediment sorting were limited and are deemed not to have had an influence on the validity of the weathering- and other geochemical proxies used in this study.
- The siliciclastic portion of the diamictite matrix has a granodioritic provenance originating from a continental volcanic arcs setting.
- The diamictites have a similar composition to the Svecofennian bedrock and Swedish till derived therefrom.
- The diamictites have a different composition than the Rhinns complex, which is thus not a source for the PAF material.

- The limestone source for the diamictite matrix was abruptly switched-off directly after the Great Breccia, which required some special type of event since the exclusion of an existing component from the system normally would be expected to be gradual during the ice's gradual removal and thinning out of a source-type and by its reworking and redeposition of lower beds containing such sourced deposits.
- This study supports Spencer's (1971) original grouping of diamictite beds into members, but also argues that Member 1 could be further divided into two sub-groups – M1a to cover the diamictite beds d1 – d13 (up to and including the Great Breccia), and M1b starting from the Disrupted Beds, covering d14 – d18 up to and including the Upper Dolomites.
- Member 5 clearly deviates from the other members in its geochemical footprint, implying a shift of provenance or different transport and sorting processes for the M5 material, which raise the question if this member really represents a true glacial deposit.

Some general interpretations can also be suggested:

- The source of the extrabasinal part of the PAF diamictites is the Svecofennian domain in the Baltica crustal plate located palaeogeographically to the southeast of the PAF.
- The PAF was deposited during 5 glacial cycles starting with gradual build-up of ice sheets followed by rapid meltdowns, and where the first cycle was unique in the sense of containing the multimillion years hiatus of the Snowball Earth event. The Great Breccia is interpreted as the final step in this first glacial build up. The exit from the Snowball Earth icehouse is interpreted to be through a series of possibly 5 major melting events of short durations, intermixed with somewhat longer periods when the ice managed to recover control.

6 Acknowledgements

This thesis is made as a part of the Master's Degree Programme in Geological Sciences, provided by the Department of Geological Sciences, Stockholm University. The author would like to thank Prof. Alasdair Skelton not only for excellent support as supervisor for this thesis project, but also for being an inspirational and engaging teacher of geology and setting the example for what scientific work is all about. The generous support and thought-provoking questions provided by co-supervisors Dr Anthony M. Spencer, Hafrsfjord, Norway and Prof. Ian J. Fairchild, University of Birmingham have strongly contributed to the development of the ideas presented in this thesis, although possible erroneous interpretations are entirely of the authors own doing.

Dr Anthony M. Spencer spent a considerable amount of time with the author during fieldwork in the Garvellachs and Islay, giving invaluable guidance and insight into the stratigraphy of the PAF. Additionally, the author would like to thank Alasdair MacLachlan for providing safe boat transport to and between the Garvellachs islands.

Extensive help and support were given by numerous other contributors, where only a few can be mentioned here: Prof. Bruce K. Levell, University of Oxford, Dr Dick Claeson, Geological Survey of Sweden and fellow post graduate students Mirren Green and Patrick Casey, Stockholm University.

7 Recommendations for future studies

The palaeoenvironmental interpretation presented in this report is i.a. based on the assumption that the glacial – interglacial conditions are reflected in the variation in clay-, silt- and sand sized particles in the PAF diamictite matrixes. Data from the geochemical logs were here used as proxy for variations in particle sizes. As an alternative to this, it is proposed that a systematic documentation of the groundmass versus larger mineral grains can be achieved by doing a particle size point count of thin sections.

8 Appendix with supplementary data

Supplementary data to this report consisting of the PAF geochemical logs will be provided upon request from the author.

9 References

Albarède F., 2009. Geochemistry, An introduction (second edition): Cambridge, Cambridge University Press, 342 p.

Ali, D.O., 2017. Evolution of the Cryogenian Port Askaig Formation in Scotland: PhD thesis submitted to the University of London for the degree of Doctoral of Philosophy, 275 p.

Ali, D.O., Spencer, A.M., Fairchild, I.J., Chew, K.J., Anderton, R., Levell, B.K., Hambrey, M.J., Dove, D. & Le Heron, D.P., 2018. Indicators of relative completeness of the glacial record of Port Askaig Formation, Garvellach Islands, Scotland: Precambrian Research, v. 319, p. 65 – 78.

Andersson, M., Ripa, M. & Smith, C.A., 2020. Geokemisk kartering i västra Bergslagen: SGU-rapport 2020:01, p. 93.

Anderton, R., 1985. Sedimentation and tectonics in the Scottish Dalradian: Scottish Journal of Geology, v. 21, p. 407 – 436.

Arnaud, E. & Eyles, C.H., 2002. Catastrophic mass failure of a Neoproterozoic glacially influenced continental margin, the Great Breccia, Port Askaig Formation, Scotland: Sedimentary Geology, v. 151, p. 313 – 333.

Arnaud, E. & Eyles, C.H., 2006. Neoproterozoic environmental change recorded in the Port Askaig Formation, Scotland: Climatic vs tectonic controls: Sedimentary Geology, v. 183, p. 99 – 124.

Beckmann, B., Flögel, S., Hofmann, P., Schulz, M. & Wagner, T., 2005. Orbital forcing of Cretaceous river discharge in tropical Africa and ocean response: Nature, v. 437, p. 241 – 244.

Bekker, A., Planavsky, N.J., Krapez, B., Rasmussen, B., Hofmann, A., Slack, J.F., Rouxel, O.J. & Konhauser, K.O., 2014. Iron formations: Their origins and implications for ancients seawater chemistry: Treatise on Geochemistry, 2nd ed., p. 561 – 628.

Benn, D.I. & Prave, A.R., 2006. Subglacial and proglacial glaciotectonic deformation in the Neoproterozoic Port Askaig Formation, Scotland: Geomorphology, v. 75, p. 266 – 280.

Benn, D.I., Le Hir, G., Bao, H., Donnadieu, Y., Dumas, C., Fleming, E. J., Hambrey, M.J., McMillan, E.A., Petronis, M.S., Ramstein, G., Stevenson, C.T.E., Wynn, P.M. & Fairchild, I.J., 2015. Orbitally forced ice sheet fluctuations during the Marinoan Snowball Earth glaciation: Nature Geoscience, v. 8, p. 704 – 708.

Bhatia, M. & Crook, K., 1986. Trace element characteristics of graywackes and tectonic setting discrimination of sedimentary basins: Contributions to Mineralogy & Petrology, v. 92, p. 181 – 193.

Bosscher, H. & Schlager, W., 1993. Accumulation rates of carbonate platforms: The Journal of Geology, v. 101, p. 345 – 355.

Clift, P.D., Wan, S. & Blusztajn, J., 2014. Reconstructing chemical weathering, physical erosion and monsoon intensity since 25 Ma in the northern South China Sea: A review of competing proxies: Earth-Science Reviews, v. 130, p. 86 – 102.

Cohen, K.M., Finney, S.C., Gibbard, P.L. & Fan, J.-X., 2013 (updated May 2019). The ICS International Chronostratigraphic Chart, Episodes 36, p. 199-204.
URL:http://www.stratigraphy.org/ICSchart/ChronostratChart2019-05.pdf

Condie, K.C., 1993. Chemical composition and evolution of the upper continental crust: Contrasting results from surface samples and shales: Chemical Geology, v. 104, p. 1 – 37.

Cox, G.M., Halverson, G.P., Minarik, W.G., Le Heron, D.P., Macdonald, F.A., Bellefroid, E.J. & Strauss, J.V., 2013. Neoproterozoic iron formation: An evaluation of its temporal, environmental and tectonic significance: Chemical Geology, v. 362, p. 232 – 249.

Crockett, R., 2019. A Primer on Fourier Analysis for the Geosciences (first edition): Cambridge, Cambridge University Press, 176 p.

Dahlgren, M., 2018. A sedimentological study of Cryogenian glacial-interglacial cycles recorded by the Port Askaig Tillite Formation on Islay, Scotland: BSc thesis submitted to the Stockholm University, 47 p.

de Jayawardena, U.S. & Izawa, E., 1994. A new chemical index of weathering for metamorphic silicate rocks in tropical regions: A study from Sri Lanka: Engineering Geology, v. 36, p. 303 – 310.

Donnadieu, Y. & Ramstein, G., 2002. Is high obliquity a plausible cause for Neoproterozoic glaciations?: Geophysical Research Letters, v. 29, no. 23, p. 42-1 – 42-4.

Dreimanis, A., 1962. Quantitative gasometric determination of calcite and dolomite by using chittick apparatus: Sedimentary Petrology, v. 32, p. 520 – 529.

Dunbar, G.B., Naish, T.R., Barret, P.J., Fielding, C.R. & Powell, R.D., 2008. Constraining the amplitude of late Oligocene bathymetric changes in Western Ross Sea during orbitally-induced oscillations in the East Antarctica Ice Sheet: (1) Implications for glacimarine sequence stratigraphic models: Palaeogeography, Palaeoclimatology, Palaeoecology, v. 260, p. 50 – 65.

Earle, S., 2015. Physical Geology: published by BCcampus, Victoria, B.C., p. 719.

Marshak, S., 2012. Earth – Portrait of a Planet (Fourth Edition): published by W.W. Norton and Company, New York.

Evans, D.J.A, Phillips, E.R., Hiemstra, J.F. & Auton, C.A., 2006. Subglacial till: Formation, sedimentary characteristics and classification: Earth-Science Reviews, v. 78, p. 115 – 176.

Eyles, C.H., 1988. Glacially- and tidally-influenced shallow marine sedimentation of the late Precambrian Port Askaig Formation, Scotland: Palaeogeography, Palaeoclimatology, Palaeoecology, v. 68, p. 1 – 25.

Eyles, N. & Januszczak, N., 2004. 'Zipper-rift': a tectonic model for Neoproterozoic glaciations during the breakup of Rodinia after 750 Ma: Earth-Science Reviews, v. 65, p. 1–73.

Fabre, S., Berger, G., Chavagnac, V. & Besson, P., 2013. Origin of cap carbonates: An experimental approach: Palaeogeography, Palaeoclimatology, Palaeoecology, v. 392, p. 524 – 533.

Fairchild, I.J., 1985. Petrography and carbonate chemistry of some Dalradian dolomitic metasediments: preservation of diagenetic textures: Journal of the Geological Society, v. 142, p. 167 – 185.

Fairchild, I.J. & Kennedy, M.J., 2007. Neoproterozoic glaciation in the Earth System: Journal of the Geological Society, v. 164, p. 895 – 921.

Fairchild, I.J., Bonnand, P., Davies, T., Fleming, E.J., Grassineau, N., Halverson, G.P., Hambrey, M.J., McMillan, E.M., McKay, E., Parkinson, I.J. & Stevenson, C.T.E., 2016. The late Cryogenian warm interval, NE Svalbard: Chemostratigraphy and genesis: Precambrian Research, v. 281, p. 128 – 154.

Fairchild, I.J., Spencer, A.M., Ali, D.O., Anderson, R.P., Anderton, R., Boomer, I., Dove, D., Evans, J.D., Hambrey, M.J., Howe, J., Sawaki, Y., Shields, G.A., Skelton, A., Tucker, M.E., Wang, Z. & Zhou, Y., 2018. Tonian-Cryogenian boundary sections of Argyll, Scotland: Precambrian Research, v 319, p. 37 – 64.

Fedo, C.M., Nesbitt, H.W. & Young, G.M., 1995. Unraveling the effects of potassium metasomatism in sedimentary rocks and paleosols, with implications for paleoweathering conditions and provenance: Geology, v. 23, p. 921 – 924.

Fitches, W.R., Pearce, N.J.G., Evans, J.A. & Muir, R.J., 1996. Provenance of late Proterozoic Dalradian tillite clasts, Inner Hebrides, Scotland, *in*: Brewer, T.S. (ed.), 1996, Precambrian Crustal Evolution in the North Atlantic Region, Geological Society Special Publication No 112, p. 367 – 377.

Frey. M. & Robinson, D., 1999. Low-Grade Metamorphism: published by Wiley-Blackwell, 328 p.

Gaschnig, R.M., Rudnick, R.L., McDonough, W.F., Kaufman, A.J., Valley, J.W., Hu,Z., Gao, S. & Beck, M.L., 2016. Compositional evolution of the upper continental crust through time, as constrained by ancient glacial diamictites: Geochimica et Cosmochimica Acta, v. 186, p. 316 – 343.

Graf Jr, J.L., O'Connor, E.A. & van Leeuwen, P., 1994. Rare earth element evidence of origin and depositional environment of Late Proterozoic ironstone beds and manganese-oxide deposits, SW Brazil and SE Bolivia: Journal of South American Earth Sciences, v. 7, p. 115 – 133.

Halverson, G.P., Wade, B.P., Hurtgen, M.T. & Barovich, K.M., 2010. Neoproterozoic chemostratigraphy: Precambrian Research, v. 182, p. 337 – 350.

Halverson, G.P., Poitrasson, F., Hoffman, P.F., Nédélec, A., Montel, J.-M. & Kirby, J., 2011. Fe isotope and trace element geochemistry of the Neoproterozoic syn-glacial Rapitan iron formation: Earth and Planetary Science Letters, v. 309, p. 100 – 112.

Harnois, L. & Moore, J.M., 1988. Geochemistry and origin of the Ore Chimney Formation, a transported paleoregolith in the Grenville Province of southeastern Ontario, Canada: Chemical Geology, v. 69, p. 267 – 289.

Herron, M.M., 1988. Geochemical classification of terrigenous sands and shales from core or log data: Journal of Sedimentary Petrology, v. 58, p. 820 – 829.

Hieronymus, B., Kotschoubey, B. & Boulegue, J., 2001. Gallium behavior in some contrasting lateritic profiles from Cameroon and Brazil: Journal of Geochemical Exploration, v. 72, p. 147 – 163.

Hoffman, P.F., Kaufman, A.J., Halverson, G.P. & Schrag, D.P., 1998. A neoproterozoic Snowball Earth: Science, vol. 281, p. 1342 – 1346.

Hoffman, P.F. & Schrag, D.P., 2002. The snowball Earth hypothesis: testing the limits of global change: Terra Nova, vol. 14, p. 129 – 155.

Hoffman, P.F., Halverson, G.P., Domack, E.W., Maloof, A.C., Swanson-Hysell, N.l. & Cox, G.M., 2012. Cryogenian glaciations on the southern tropical paleomargin of Laurentia (NE Svalbard and East Greenland), and a primary origin for the upper Russøya (Islay) carbon isotope excursion, Precambrian Research, v. 206-207, p. 137 – 158.

Hoffman, P.F., Abbot, D.S., Ashkenazy, Y., Benn, D.I., Brocks, J.J., Cohen, P.A., Cox, G.M., Creveling, J.R., Donnadieu, Y., Erwin, D.H., Fairchild, I.J., Ferreira, D., Goodman, J.C., Halverson., G.P., Jansen, M.F., Le Hir, G., Love, G.D., Macdonald, F.A., Maloof, A.C., Partin, C.A., Ramstein, G., Rose, B.E.J., Rose, C.V., Sadler, P.M., Tziperman, E., Voigt, A. & Warren, S.G., 2017. Snowball Earth climate dynamics and Cryogenian geology-geobiology: Science Advances, v. 3, p. 1 – 43.

Hogan, K.A., Jakobsson, M., Mayer, L., Reilly, B.T., Jennings, A.E., Stoner, J.S., Nielsen, T., Andresen, K.J., Nørmark, E., Heirman, K.A., Kamla, E., Jerram, K., Stranne, C., & Mix, A., 2020. Glacial sedimentation, fluxes and erosion rates associated with ice retreat in Petermann Fjord and Nares Strait, north-west Greenland: The Cryosphere, v. 14, p. 261–286.

Jakobsson, M., Backman, J., Murray, A. & Løvlie, R., 2003. Optically Stimulated Luminescence dating supports central Arctic Ocean cm-scale sedimentation rates: Geochem. Geophys. Geosyst., v. 4(2), p. 11.

Jakobsson, M., Andreassen, K., Bjarnadottir, L.R., Dove, D., Dowdeswell, J.A., England, J.H., Funder, S., Hogan, K., Ingolfsson, O., Jennings, A., Larsen, N.K., Kirchner, N., Landvik, J.Y., Mayer, L., Mikkelsen, N., Möller, P., Niessen., F., Nilsson, J., O'Regan, M., Polyak, L., Nörgaard-Pedersen, N. & Stein, R., 2014. Arctic Ocean glacial history: Quaternary Science Reviews, v. 92, p. 40 – 67.

Katz, A., Sass, E. & Starinsky, A., 1972. Strontium behavior in the aragonite-calcite transformation : An experimental study at 40 – 48°C: Geochimica et Cosmochimica Acta, v. 86, p. 481 – 196.

Klaebe, R.M., Smith, M.P., Fairchild, I.J., Fleming, E.J. & Kennedy, M.J., 2018. Facies-dependent $\delta^{13}C$ variation and diagenetic overprinting at the onset of the Sturtian glaciation in North-East Greenland: Precambrian Research, v., p. 96 – 113.

Kleine, B.I., Zhao, Z. & Skelton, A.D.L., 2016. Rapid fluid flow among fractures at greenschist facies conditions on Syros, Greece: American Journal of Science, v. 316, p. 169 – 201.

Ladenberger, A., Carlsson, M., Andersson, M., Bergman, S., Uhlbäck, J., Ohlsson, S-Å., Smith, C., Morris, G. & Arvanitidis, N., 2016. Till geochemistry in southern Norrbotten: SGU-rapport K 561, p. 68.

Lang, X., Shen, B., Peng, Y., Huang, K., Lv, J. & Ma, H., 2016. Ocean oxidation during the deposition of basal Ediacaran Doushantuo cap carbonates in the Yangtze Platform, South China: Precambrian Research, v. 281, p. 253 – 268.

Lambeck, K., Rouby, H., Purcell, A., Sun, Y. & Sambridge, M., 2014. Sea level and global ice volumes from the Last Glacial Maximum to the Holocene: PNAS, v. 111, no. 43, p. 15296 – 15303.

Li, Z.X., Bogdanova, S.V., Collins, A.S., Davidson, A., De Waele, B., Ernst, R.E., Fitzsimons, I.C.W., Fuck, R.A., Gladkochub, D.P., Jacobs, J., Karlstrom, K.E., Lul, S., Natapov, L.M., Pease, V., Pisarevsky, S.A., Thrane, K. & Vernikovsky, V., 2008. Assembly, configuration, and break-up history of Rodinia: A synthesis: Precambrian Research, v. 160, p. 179 – 210.

Li, Z.-X., Evans, D.A.D. & Halverson, G.P., 2013. Neoproterozoic glaciations in a revised global palaeogeography from the breakup of Rodinia to the assembly of Gondwanaland: Sedimentary Geology, v. 294, p. 219 – 232.

López, J.M.G., Bauluz, B., Fernández-Nieto, C. & Oliete, A. Y., 2005. Factors controlling the trace-element distribution in fine-grained rocks: the Albian kaolinite-rich deposits of the Oliete Basin (NE Spain): Chemical Geology, v. 214, p. 1 – 19.

Marshak, S., 2012. Earth – Portrait of a Planet (Fourth Edition): published by W.W. Norton and Company, New York.

Mavotchy, N.O., El Albani, A., Trentesaux, A., Fontaine, C., Pierson-Wickmann, A-C., Boulvais, P., Riboulleau, A., Ngombi Pemba, L., Pambo, F. & Gauthier-Lafaye, F., 2016. The role of the early diagenetic dolomitic concretions in the preservation of the 2.1-Ga paleoenvironmental signal: The Paleoproterozoic of the Franceville Basin, Gabon: C. R. Geoscience, v. 348, p. 609 – 618.

McLennan, S.M., 1993. Weathering and Global Denudation: The Journal of Geology, v. 101, p. 295 – 303.

McLennan, S.M., 1989. Geochemistry and Mineralogy of Rare Earth Elements, *in*: Lipin, B.R. & McKay, G.A. (eds.), 1989, Reviews in Mineralogy, v. 21, The Mineralogical Society of America, p. 169 – 200.

McLennan, S.M., 2001. Relationships between the trace element composition of sedimentary rocks and upper continental crust: Geochemistry, Geophysics, Geosystems – G3, v. 2, p. 24.

Meunier, A., Caner, L., Hubert, F., El Albani, A. & Prêt, D., 2013. The weathering intensity scale (WIS): An alternative approach of the chemical index of alteration (CIA): American Journal of Science, v. 313, p. 113 – 143.

Naish, T.R., Woolfe, K.J., Barret, P.J., Wilson, G.S., Atkins, C., Bohaty, S.M., Bucker, C.J., Claps, M., Davey, F.J., Dunbar, G.B., Dunn, A.G., Fielding, C.R., Florindo, F., Hannah, M.J., Harwood, D.M., Henrys, S.A., Krissek, L.A., Lavelle, M., van der Meer, J., McIntosh, W.C., Niessen, F., Passchler, S., Powell, R.D., Roberts, A.P., Sagnotti, L., Scherer, R.P., Strong, C.P., Talarico, F., Verosub, K.L., Villa, G., Watkins, D.K., Webb, P-N. & Wonik, T., 2001. Orbitally induced oscillations in the East Antarctic ice sheet at the Oligocene/Miocene boundary: Nature, V. 413, P. 719 – 723.

Nesbitt, H.W. & Young, G.M., 1982. Early Proterozoic climates and plate motions inferred from major element chemistry of lutites: Nature, v. 299, p. 715 – 717.

Okumura, M. & Kitano, Y., 1986. Coprecipitation of alkali metal ions with calcium carbonate: Geochemica et Cosmochemica Acta, v. 50, p. 49 – 58.

Olympus Innov-X Delta User Manual, PN_103201, Rev_A: June/2010.

O'Regan, M., King, J., Backman, J., Jakobsson, M., Päilike, H., Moran, K., Heil, C., Sakamoto, T., Cronin, T.M. & Jordan, R.W., 2008. Constraints on the Pleistocene chronology of sediments from the Lomonosov Ridge: Paleoceanography, v. 23, p. 1 – 18.

Panahi, A. & Young, L.G.M., 1997. A geochemical investigation into the provenance of the Neoproterozoic Port Askaig Tillite, Dalradian Supergroup, Western Scotland: Precambrian Research, v.85, p. 81 – 96.

Parker, A., 1970. An Index of Weathering for Silicate Rocks: Geological Magazine, v. 107, p. 501 – 504.

Prave, A.R., Fallick, A.E., Thomas, C.W. & Graham, C.M., 2009. A composite C-isotope profile for the Neoproterozoic Dalradian Supergroup of Scotland and Ireland: Journal of the Geological Society, v. 166, p. 845 – 857.

Podkovyrov, V.N., Grazhdankin, D.V. & Maslov, A.V., 2011. Lithogeochemistry of the Vendian Fine-Grained Clastic Rocks in the Southern Vychegda Through: Lithology and Mineral Resources, v. 46, p. 427 – 446.

Price, J.R. & Velbel, M.A., 2003. Chemical weathering indices applied to weathering profiles developed on heterogenous felsic metamorphic parent rocks: Chemical Geology, v. 202, p. 397 – 416.

Rooney, A.D., Strauss, J.V., Brandon, A.D. & Macdonald, F.A., 2015. A Cryogenian chronology: Two long lasting synchronous Neoproterozoic glaciations: Geology, v. 43, p. 459 – 462.

Roy, D.K. & Roser, B.P., 2013. Climatic control on the composition of Carboniferous-Permian Gondwana sediments, Khalaspir basin, Bangladesh: Gondwana research, v. 23, p. 1163 – 1171.

Ruddiman, W.F., 2014. Earth's Climate – Past and Future (third edition): New York, W. H. Freeman and Company, 445 p.

Sarki Yandoka, B.M., Abdullah, W.H., Abubakar, M.B.; Hakimi, M.H. & Adegoke, A.K., 2015. Geochemical characterisation of Early Cretaceous lacustrine sediments of Bima Formation, Yola Sub-basin, Northern Benue Trough, NE Nigeria: Organic matter input, preservation, paleoenvironment and palaeoclimatic conditions: Marine and petroleum geology, v. 61, p. 82 – 94.

Sawaki, Y., Kawai, T., Shibuya, T., Tahata, M., Omori, S., Komiya, T. Yoshida, N., Hirata, T., Ohno, T., Windley, B.F. & Maruyama, S. 2010. $^{87}Sr/^{86}Sr$ chemostratigraphy of Neoproterozoic Dalradian carbonates below the Port Askaig Glaciogenic Formation, Scotland: Precambrian Research, v. 179, p. 150–164.

Schlager, W., 1999. Scaling of sedimentation rates and drowning of reefs and carbonate platforms: Geology, v. 27, p. 183 – 186.

Sellén, E., Jakobsson, M. & Backman, J., 2008. Sedimentary regimes in Arctic's Amerasian and Eurasian Basins: Clues to differences in sedimentation rates: Global and Planetary Change, v. 61., p. 275 – 284.

SGU Geolagret 2020: https://apps.sgu.se/geolagret/

Skelton, A.D.L., Graham, C.M. & Bickle, M.J., 1995. Lithological and structural controls on regional 3-D fluid flow patterns during greenschist facies metamorphism of the Dalradian of the SW Scottish Highland: Journal of Petrology, v. 36, p. 563- 586.

Skelton, A., Lewerentz, A., Kleine, B., Webster, D. & Pitcairn, I., 2015. Structural channeling of Metamorphic fluids on Islay, Scotland: Implications for Paleoclimatic reconstruction: Journal of Petrology, v. 56, p. 2145 – 2171.

Skelton, A., Löwhagen, L., Fairchild, I.J., Boyce, A., Mörth, C.-M., Siegmund H., Webster, D. & Spencer, A.M., 2019. Stable isotopes of oxygen and hydrogen in meteoric water during the Cryogenian Period: Precambrian Research, v. 320, p. 253 – 260.

Sohlenius, G., Lax, K. & Ladenberger, A., 2009. Kan SGUs data användas för att uppskatta moränens transportlängd?: Sveriges geologiska undersökning SGU-rapport 2009:26, 25 p.

Spencer, A.M., 1971. *in*: Late Pre-Cambrian glaciation in Scotland. Memoir of the Geological Society of London, 112 p.

Stephenson, D., Mendum, J.R., Fettes, D.J. & Leslie, A.G., 2013. The Dalradian rocks of Scotland: an introduction: Proceedings of the Geologists' Association, v. 124, p. 3 – 82.

Taylor, S.R. & McLennan, S.M, 1995. The geochemical evolution of the continental crust: Reviews of Geophysics, v. 33, p. 241 – 265.

Webster, D., Anderton, R. & Skelton, A., 2017. A guide to the geology of Islay (second edition): Ringwood Publishing, Glasgow, 178 p.

Wilson, G.S., Levy, R.H., Naish, T.R., Powell, R.D., Florindo, F., Ohneiser, C., Sagnotti, L., Winter, D.M., Cody., R., Henrys, S., Ross, J., Krissek, L., Niessen, F., Pampillio, M., Scherer, R., Alloway, B.V., Barret, P.J., Brachfeld, S., Browne, G., Carter, L., Cowan, E., Crampton, J., DeConto, R.M., Dunbar, G., Dunbar, N., Dunbar, R., von Eynatten, H., Gebhardt, C., Giorgetti, G., Graham, I., Hannah, M., Hansaraj, D., Harwood, D.M., Hinnov, L., Jarrad, R.D., Joseph, L., Kominz, M., Kuhn, G., Kyle, P., Läufer, A., McIntosh, W.C., McKay, R., Maffioli, P., Magens, D., Millan, C., Monien, D., Morin, R., Paulsen, T., Persico, D., Pollard, D., Raine, J.I., Riesselman, C., Sandroni, S., Schmitt, D., Sjunneskog, C., Strong, C. P., Talarico, F., Taviani, M., Villa, G., Vogel, S., Wilch, T., Williams, T., Wilson, T.J. & Wise, S., 2012. Neogene tectonic and climatic evolution of the Western Ross Sea, Antarctica – Chronology of events from the AND-1B drill hole: Global and Planetary Change, v. 96-97, p. 189 – 203.

Xie, G., Shen, Y., Liu, S. & Hao, W., 2018. Trace and rare earth element (REE) characteristics of mudstone from Eocene Pinghu Formation and Oligocene Huagang Formation in Xihu Sag, East China Sea Basin: Implications for provenance, depositional conditions and paleoclimate: Marine and Petroleum Geology, v. 92, p. 20 – 36.

Xu, Q., Ma, Y., Chen, Z., Liu, B., Song, X. & Wang, Y., 2017. Geological and geochemical characterization of lacustrine shale: A case study of the Jurassic Da'anzhai member shale in the central Sichuan Basin, southwest China: Journal of Natural Gas Science and Engineering, v. 47, p. 124 – 139.

Young, G.M., 2002. Geochemical investigation of a Neoproterozoic glacial unit: The Mineral Fork Formation in the Wasatch Range, Utah: Geological Society of America Bulletin, v. 114, p. 387 – 399.